Mechanical Systems in Nanometre Metrology

Stuart T. Smith

A Dissertation submitted for the Degree of Doctor of Philosophy

School of Engineering Science,

University of Warwick, Coventry

Acknowledgements

Firstly, I should like to express my appreciation to my supervisors, Dr's D. K. Bowen and D. G. Chetwynd, for their continual support and encouragement without which this project would not have been possible. I also wish to acknowledge the support of Dr A. Franks and Mr K. Lindsey of the National Physical Laboratory (Teddington) for allowing me to participate in their work as part of a CASE studentship award. Thanks are due to Dr G. R. Fischer of Monsanto Industries (Milton Keynes) for his time and help in the processing of silicon components.

The development of the Scanning Tunelling Microscope was taken from the idea stage to reality by the draughting skills of Mr J. Roe and the patience and machining skills of Mr. C. Major of the University's Engineering Workshops. Laboratory work has been carried out in the Department of Micro-engineering and Metrology under the supervision of Mr R. Bridgeland.

The National Physical Laboratory (Teddington) is to be thanked for the financial support that it has shown over the last two years of this project. Manufacture of Nanosurf 2 was carried out in the Engineering and Glass workshops at this institute.

Finally, I should like to thank Ani for the understanding that she has shown throughout the period of the research project.

Summary

The work reported in this thesis was carried out in the School of Engineering Science, University of Warwick, between October 1984 and October 1987.

Chapter 1 contains a review of recent developments in instrumentation that require both manipulation and measurement over the range 0.1-100nm. The instruments considered are the Scanning Tunnelling Microscope (STM), Stylus techniques, X-ray interferometry and x-ray microscopy. The rest of the thesis presents the design and assessment of a novel STM incorporating an X-ray interferometer, an ultra-high precision stylus measuring instrument and an x-ray microscope two axis specimen translation stage.

Chapters 2 and 3 present an assessment of different mechanisms for the production of rectilinear motions having parasitic errors of better than 1nm. Theoretical and experimental investigations into monolithic parallel spring systems based on a notch type hinge and long range slideways based on a polymeric bearing sliding on a polished glass prism are presented. Optimisation of a soleniod magnet force transducer is presented as a drive technique for the former device, whilst a mechanically non-influencing feedscrew drive is described for the latter system.

A stylus based measuring instrument, called "Nanosurf 2", that incorporates the polymeric slideway is presented in chapter 4. The performance of this system has been assessed and the results are presented in the following chapter.

The linearity and accuracy of an electromagnetically driven, single crystal silicon, monolithic spring make it a suitable for use as the translation mechanism in a Scanning Tunnelling Microscope. Consequently, a three-axis spring has been constructed to generate the translations required for imaging. An X-ray interferometer is built into the probe axis to facilitate absolute calibration. This work is preceeded by an investigation into the generation of complex shapes in this brittle material.

Finally, the current status of this work is reported with the presentation of initial experimental results.

Table of Contents

Chapter 1: Instrument systems and mechanisms in Nanotechnology

1.1 Introduction

The object of this thesis is to present the results of a three year period of study during which investigations were carried out into a number of different systems involving measurements in the nanometer region. All of the systems considered have been designed for metrological purposes, although it will be shown later that there are many other applications. The instruments presented all operate on similar metrological principles. That is, a transducer is positioned at a point on the surface under investigation. The specimen is then traversed along a reference plane and subsequent variations in output are monitored. In all cases, for optimum results, the specimen must be moved in a plane considerably better than the transducer resolution. To achieve this for ultra-high resolution transducers, elastic design techniques have been employed and are covered in chapter 2. The systems that have been examined to a greater or lesser degree are

1. X-ray microscopy
2. Stylus techniques
3. Combined Scanning Tunnelling Microscopy (STM) and X-ray interferometry.

These are listed in order of increasing importance to this thesis. The object of this chapter is to introduce some of the fundamental principles and give the reader a rough idea of the practical realisation of these instruments.

1.2 X-ray microscopy

The x-ray microscope presently being produced at the National Physical Laboratory has a number of similarities to the more conventional scanning electron microscope only in this instance it is the specimen that is scanned. The object is illuminated and then enlarged by a

focusing system onto an image plane. This is an x-ray image as opposed to a photograph that has been enlarged using optical or other techniques. Because of the low unit decrement of x-rays, the focal distance of a conventional transmission lens becomes impractically large and reflection techniques must be employed. This lens consists of a hollow cone having an on-axis profile of an ellipse followed by a hyperbola. This is commonly known as a Wolter type 1 microscope. The focused beam passes through the specimen and is monitored by a scintillation counter. The specimen is then raster scanned to form an x-ray image. Because of the small wavelength of x-rays (0.1-30nm), the optic will require nanometer and subnanometer dimensional accuracy, stability and surface finish, (Franks, 1977). This is being manufactured in the nanotechnology unit of the National Physical Laboratory using high precision lapping and polishing techniques. The design of the specimen scanning stage will be presented in chapter 6. Displacement is obtained by deflection of an elastic spring using an electromagnetic force transducer. All of this must be housed in a vacuum system to reduce atmospheric absorption.

The advantages of an x-ray microscope system are summarised by Franks, 1977,

"the three factors which make x-ray microscopy an attractive technique are the resolution, which is potentially higher than the optical microscope, the ability to examine internal structure of materials which appear opaque in both optical and electron microscopes and the ability to provide an analysis of the elements present in the specimen.."

A general schematic diagram of the x-ray microscope system is shown in figure 1.1.

1.3 Stylus techniques

Stylus techniques were developed during the 1940 war as a means of quality control, (Whitehouse, 1974). This is a follower surface measurement technique whereby a diamond point, or stylus, is contacted and then drawn across the surface under examination. The motion of this stylus relative to a fixed reference is then used as a quantitative measurement of the surface finish and profile of the specimen. The stylus motion is usually detected by an inductive transducer, although laser pick-up, piezo-electric and capacitance methods are being employed in some of the modern systems, (Garratt, 1979).

The wavelength characteristics of the complete system will be a function of tip geometry, reference accuracy and stability, electronic high and low pass filters, tip surface interactions and the stylus dynamics. In a majority of applications the local surface "roughness" is the only parameter that is required. This is because roughness values are related to contact conditions between two surfaces and thus wear rates, running-in times etc, Greenwood and Williamson, 1966. This roughness profile will also permits the calculation of many other performance related diagnostics as well as information about the processes or mechanisms that create the surface, (Thomas, 1975, Whitehouse, 1985).

The high frequency filter characteristic due to stylus tip geometry is unavoidable although resolution can be enhanced by using expensive and delicate fine tip radius diamonds, (Radhakrishnan, 1970). The high frequency characteristic may also be reduced by a tendency to shear local sharp asperities. Scanning electron micrographs of ploughing tracks under high loads (200mg) are shown in the paper of Guerrero and Black, 1972. The load range usually employed during stylus measurements is in the range 4-100mg and it will be shown in chapter 7 that the pressures produced by a standard Vickers indentation hardness test will induce significant surface damage at loads of a few grammes for hard, brittle materials such as glass and Si. The limitation of lower wavelength capability is governed by the reference accuracy and stability. Stability is over both the sampling time and the instrument's expected life span if accuracy is to be assessed. The sampling time is a function of the stylus dynamics and these are usually relatively slow to avoid the high stiffnesses required to improve response times. An easier way of obtaining stable performance is to make use of the modern high stability materials such as Zerodur and Invar. These materials were thus used to create a stylus measurement system capable of assessing surface finish and profile of the x-ray optics mentioned in the preceding section (vertical resolution ≈2nm over 50mm and a sampling time of 20mins). The design and characterisation of this instrument, known as Nanosurf 2, will be presented in chapters 4 and 5.

Using a mapping technique developed by M. Stedman, 1987, the performance of a instrument can be represented by mapping its measurement limitations. This results in a closed curve that is bounded by its vertical and horizontal range and resolution, horizontal reference datum

and, in the case of contact/near contact measuring instruments, the probe geometry. Such a map representing a number of stylus instruments including Nanosurf 2 has been reproduced in figure 1.2.

The reasons for using a stylus instrument are that it is purely mechanical and not susceptible to changes in optical or electronic surface properties, the output is in the form of a voltage proportional to the surface variations and is thus amenable to signal processing/ computerisation and the mechanical tip-surface interface will evict soft contaminating layers that have little influence on contact mechanisms.

1.4 The x-ray interferometer

X-ray interferometry is a technique capable of monitoring displacements of up to 0.2mm with an accuracy greater than 10pm, Hart, 1968, Bowen et al, 1985, Becker and Seyfried, 1987. This instrument can be considered as a moire´fringe displacement transducer with the grating being in the form of the lattice planes of a high purity single crystal. A schematic diagram of an x-ray interferometer system is shown in figure 1.3 reproduced from the paper of Bonse and Hart, 1965, where this technique was initially presented. The instrument comprises three equidistant Bragg reflecting wafers with the lattice planes parallel to within ≈1nrad. X-rays are diffracted through the beam splitter (S) emerging as a double beam at the appropriate Bragg angle. These two beams then pass through the mirror (M) whereby they recombine within the analyser crystal (A). This sets up a standing wave having spatial periodicity equal to the reflection plane spacing (commonly denoted as the scalar d_{hkl}). If perfect alignment and rectilinear motion of the analyser relative to the splitter and mirror can be obtained, then a motion of d_{hkl} will result in a variation in intensity of the output beams (R and T) corresponding to one moir´e fringe. This is totally independent of the x-ray wavelength. The lattice spacing of the cubic silicon crystal is given by the equation

$$d_{hkl}=\frac{a}{\sqrt{h^2+k^2+l^2}} \qquad (1.1)$$

Where a is the lattice constant. It is possible to measure this value by external monitoring of the analyser displacement. Using a He-Ne laser measurement system Becker et al, 1981, 1982,

have determined this value to be 543102.018±0.034fm. Thus for a [220] reflection the lattice spacing is 0.1920171nm.

Having established the validity of the interferometer principle Hart, 1968, suggested its use as a ruler having sub angstrom resolution. His interferometer was a monolithic single crystal structure with an in-built linear spring mechanism to enable the displacement of the analyser blade. Attached to this was a weaker spring that could be deflected by a micrometer to provide the required driving force. The ratio of the spring stiffnesses was 10^5:1 giving an output displacement of 0.2nm for a micrometer motion of 20μm. Shortly after this Deslattes, 1969, produced an interferometer comprising two separated crystals mounted on a brass linear spring system. The design aspects of some linear springs will be examined in more detail in chapter 2. In this system the analyser is driven by a micrometer through a reduction lever having a displacement ratio of 1000:1. Fringe contrast was maintained for displacements of up to 20μm. A similar system was developed by Nakayama et al, 1981, with a piezo-electric drive replacing the micrometer. This could obtain displacements of 100μm with fringe contrasts variations again implying parasitic rotations of less than 10^{-8}rad in the critical axis. Using this system Deslattes could determine the value of Avagadro's constant to within 1.05ppm (N_A=6.0220943×$10^{23}mol^{-1}$).

Since this early work, a number of interferometer systems have been developed based on both the monolithic and the two crystal systems. In all of these systems the analyser displacement is carried out by a Jones type rectilinear spring, Jones, 1951. This is obviously a useful technique but is likely to be rather limited by the parasitic errors incurred by large distortions. Using these spring systems a piezo electrically driven displacement of 200μm has been reported with a two crystal system, Becker, 1987. To avoid some of the problems associated with the thermal characteristics of the spring materials, Alemanni et al, 1986, have constructed in linear spring from the ultra low expansion glass ceramic Zerodur. Again using a piezo electric drive, fringe contrast could be maintained for a displacement of 50μm. In all of these two crystal systems, elaborate and sensitive tilt mechanisms were necessary to obtain the required alignment between the analyser and the two other blades. This problem can be reduced or even eliminated by producing the whole interferometer from a single crystal monolith. This has been pursued by Chetwynd et

al, 1983, for the calibration of microdisplacement transducers. In this system the analyser linear spring is driven by an electromagnetic force transducer. This drive system provides accurate linear displacements of up to 20nm with a resolution and accuracy of better than 10pm, Bowen et al, 1985. Hysteresis could not be detected and the accuracy was limited by the electronics rather than the mechanical system. This transducer will be examined in more detail in chapter 2.

From the above discussion it is clear that x-ray interferometer techniques are capable of achieving displacements of up to 200μm or more with an accuracy of better than 1 part in 10^6. Also it is found that for small displacements, the electromagnetically driven single crystal linear spring system can operate in open loop fashion to create accurate displacements with a resolution that is probably better than 10pm

1.5 The scanning tunnelling microscope

The scanning tunnelling microscope is a follower type of instrument possessing a number of similarities to stylus techniques. A probe is positioned in close proximity to the surface under investigation. This usually consists of a tungsten wire electrode possessing a very fine point at the end near to the surface. A voltage (V) is applied across the gap and the resistance (R) is then used as a monitor of the tip to surface distance (hereafter called the emitter spacing s). For large separation distances, the current across this gap can be described by the Fowler-Nordheim theory and in simplified form can be expressed by the equation, Fowler and Nordheim, 1928, Young, 1966,

$$J=(1.54\times10^{-6}F/\psi)e^{(-6.83\times10^{7}\psi^{3/2}\upsilon(y))/F} \quad (A/cm^2) \tag{1.2}$$

Where F is the field strength (V/cm), J is the current density, ψ is the work function and υ is a slowly varying function of ψ. Assuming that the field (voltage) at the emitter varies inversely as the 3/2 power of emitter separation and that voltages can be measured to 1 part in 10^5, then the least detectable displacement (Δz_o) is given by, Young, 1966,

$$\Delta z_o=2z_o[(z_o/r_o)^{1/2}-1]\times10^{-5} \tag{1.3}$$

Where r_o and z_o are the emitter radius and nominal emitter spacing respectively, see figure 1.4. From this equation it can be seen that the resolution increases with a decrease in the emitter

spacing to create a psuedo self magnifying magnifying glass.

This principle was then developed into a surface profile measuring instrument that was called a "Topografiner", Young, Ward and Scire, 1972. In this system a tungsten probe is mounted on piezo-electric translation stages that are capable of positioning in the three cartesian axes. The specimen is moved into close proximity to the probe using a differential micrometer. To reduce electronic and mechanical noise, the whole system is then put into an ultra-high vacuum (10^{-10}Torr). Feeding a constant current across the emitter spacing, the probe could then be scanned in the X-Y plane. The spacing and thus the voltage variations are then used to servo the z-axis piezo to maintain a constant separation. This results in a faithful follower where the product of the piezo electric constant and the applied voltage are a quantitative measure of surface profile. Using this instrument, surface profiles could be mapped with vertical and horizontal resolutions of 3 and 400nm respectively. Typical values for the emitter spacing, voltage and current are 15nm, 50-60v and 10^{-7}A.

If the emitter spacing is reduced still further (<2nm), a quantum mechanical effect known as "tunnelling" will become the predominant conduction mechanism. In the Fowler-Nordheim electric emission region, the potential barrier is lowered by the large applied voltages. Tunnelling is influenced by the number of electronic states on the positive electrode and thus the current density becomes a linear function of the applied voltage for a fixed separation. A solution of Schrodinger's equation to yield the current density of electrons tunnelling through a thin insulating layer between two electrodes was first proposed by Holm, 1951, with a complete solution given by Simmons, 1963. The current density can be obtained by the general expression

$$J=J_o\left[\bar{\psi}e^{(-A\bar{\psi}^{1/2})}-(\bar{\psi}+eV)e^{(-A(\bar{\psi}+eV)^{1/2})}\right] \tag{1.4}$$

Where

$$A=(4\pi\beta\Delta s/h)(2m)^{1/2} \tag{1.5a}$$

$$J_o=\frac{e}{2\pi h(\beta\Delta s)^2} \tag{1.5b}$$

$$\bar{\psi}=\frac{1}{\Delta s}\int_{s_1}^{s_2}\psi(z)dz \tag{1.5c}$$

Where

m = mass of electron

e = charge of electron

h = Planck's constant

ψ = work function of metal electrode

ψ_o = height of rectangular barrier

An energy diagram for two electrodes separated by an insulating gap is shown in figure 1.5. Equation (1.4) can be visualised as the net current flow due to the flow of electrons from left to right and vice versa the magnitude of which is given by the left and right hand components of the equation. The value for the average barrier height will be altered by the image force. The shape of this image force reduced barrier is difficult to predict and will result in large errors in work function calculations under certain conditions. It has been shown that the error in the measured work function due to an assumption of a constant rectangular barrier can be greater than 300% for small emitter spacings (<0.3nm) and tip radii, Binnig, 1984. At larger separations corresponding to that which would normally be used for imaging (≈1nm) the barrier potential approaches that predicted by classical image potential theories, Willis et al, 1985. In the paper of Binnig, 1984, it is pointed out that

> ".. the logarithmic derivative of the tunnel current is nearly independent of the electrode separation, and is determined by the barrier height at large distances. This is an important result for application of STM to surface chemistry because $\partial ln I / \partial s$ is a direct measure of the work function..."

This also implies the metrological property that the sensitivity of the logarithm of the current to the emitter spacing remains relatively constant. Thus in most practical systems the current passes through a logarithmic amplifier. From the above equation it can be seen that a 1v/decade amplifier will give a sensitivity of 10v/nm. Thus the use of the rectangular barrier model can yield close approximations to the work function. The current density for a rectangular barrier and low applied voltage is given by, Simmons, 1963,

$$J=[3(2m\psi_o)^{1/2}/2s](e/h)^2Ve^{(-(4\pi s/h)(2m\psi_o)^{1/2})} \quad (1.6)$$

Inserting values for the constants yields the equation

$$J=3.16\times10^{10}\psi_o^{1/2}(V/\Delta s)e^{-1.025\Delta s\psi_o^{1/2})} \quad (1.7)$$

where s is measured in angstrom units. This expression is found to predict the current-voltage characteristic of the tunnelling probe and thus a relationship can be assumed of the form

$$I\approx constant\times Ve^{(-As\Phi^{1/2})} \quad (1.8)$$

where Φ is the average work function of the two electrodes. Typically the current is in the region of a few nanoamperes with the voltage measured in the region of a few tens of millivolts. Differentiating equation (1.8) with respect to the emitter spacing gives

$$\frac{\partial \ln I}{\partial s}\Big/_V = -A\Phi^{1/2} \quad (1.9)$$

In the constant current mode errors in the predictions are often incurred due to non-linearities introduced by field emission at large separation and the lowering of the barrier close to the Fermi level at small separations, Willis et al, 1985. In Young's paper, the onset of this phenomena was clearly observed at separations of ≈2nm. This was the first observation of direct metal-vacuum-metal tunnelling although tunnelling through aluminium oxide films of known thickness had been previously measured, Fischer and Giaver, 1961. Since then the tunnelling characteristics of a lead probe approaching a lead surface at a rate 0.2nm/hr has been investigated by Thompson and Hanrahan, 1976. This was achieved by a thermal drive in which the components in the measurement loop of the apparatus were designed for a mismatch in thermal expansion coefficients. Consequently, heating or cooling the instrument resulted in a change in the electrode spacing. Although the tunnelling phenomena could be observed, mechanical and electronic noise and stability precluded the use of the Topografiner in the tunnelling mode.

Ten years later a working system was presented by Binnig and his co-workers, (Binnig et al, 1982). This system consisted of a piezo-electric z-axis displacement stage and a piezo-electric "louse" for coarse positioning. The tungsten probe being driven by the louse with the platinum specimen translated in the z-axis. The louse is a piezo electric plate that has three feet. These feet can be electrostatically clamped or unclamped to a reference surface. Using a sequence of clamp-

ing and unclamping these whilst simultaneously expanding and contracting the plate, it is possible to obtain a virtually unlimited motion with a resolution of approximately 10nm, Binnig and Rohrer, 1982, Mamin et al, 1985. Electronic noise was reduced by improving the hardware and isolating the instrument in a high vacuum. Mechanical vibration susceptibility has been reduced by increasing the stiffness of the components and by magnetic levitation of the instrument on superconducting coils. This whole instrument is in turn mounted on a system of elaborate sprung isolation devices.

Having obtained probe separation stabilities in the region of tens of picometers per minute, a second system was constructed along similar principles whereby the probe could be translated in the three axes using perpendicular piezo stacks. It was also found that vibration isolation could be adequately obtained using metal springs with a viton spacer at each end to filter out high frequency elastic waves. In some systems eddy current damping has been added. This formed the basis of a complete imaging system that has been adopted by all subsequent STM's. The louse is also widely used although a number of systems have been developed utilising either a feedscrew or feedscrew and lever, see for example Coombs and Pethica, 1985, van der Walle et al, 1985, Drake et al, 1986, Gerber et al, 1986, Smith and Binnig, 1986).

Over the five year period since the first presentation of the working system there has been considerable development in both the design and application of this instrument. This has also provided a greater understanding of the tunnelling mechanism as well as direct verification of a number of physical principles. In the following paragraphs, some of the developments will be outlined in a rough chronological order. The theories pertaining to this technique are outside the scope of this text. However, detailed analyses on the theory of STM can be found in the papers of, Feuchtwang et al, 1983, Garcia et al, 1983, Tersoff and Hamann, 1985, Bruinsma and Bak, 1986.

In early 1982, Binnig et al, presented the first topographical maps of both $CaIrSn_4$ and Au(110) surfaces. In these images, monoatomic steps could be clearly resolved. It was also proposed that resonant tunnelling could be examined using this technique. Later on in this same year,

a topograph of the 7×7 reconstruction on Si(111) clearly showing individual atom sites over two complete rhombohedral unit cells was presented also by Binnig and Rohrer. The next year, 1983, saw some further work by Binnig and his coworkers in which examination of these surfaces helped to clarify the theoretical models of this reconstruction. It was also shown that work function variations and thus the presence of different constituents on a surface can be detected and located. The original microscope was then modified for use at liquid helium temperatures, Elrod et al, 1984. Copper blocks used for eddy current damping became too conductive at these temperatures causing high coupling and were thus over damped. These had to be replaced by a suitable aluminium alloy. Additional isolation had to be mechanically introduced during cooling. Also, because the piezo electric coefficient is reduced at this temperature the louse was found to be unreliable and was replaced by an electromagnetically driven micropositioner. This is described in the paper of Smith and Elrod, 1985. Using this method the superconducting gap in Nb_3Sn could be studied.

The following year, 1985, saw a marked increase in the number of publications outlining design and applications for this technique. Sonnenfeld et al, 1985, using an electromagnetic squeezer developed by Moreland and Hansma, 1983, were able to observe a tunnelling current between silver and silicon in atmospheric air. The ability to use air as the insulating barrier is confirmed in the paper of Garcia et al, 1985. In this work the STM has been used, in air, to measure the surface roughness of metrological gauge blocks. A calculation of the number of molecules in the operating volume yields a value of $\approx 10^{-2}$ which means that it should work as if it is in a vacuum anyway. The noise introduced by molecules hitting the probe will introduce noise. However this was found to happen at a rate of $\approx 10^{10}$/s and was outside the bandwidth of the instrument and thus did not effect performance. In May of that year, Baro et al, 1985, reported the tunneling of electrons through biological specimens mounted on a conducting surfaces. In this paper they shown an image of a virus taken under 0.1% glycerol. It was found that noise conditions in air or fluids was not significantly greater than that found in ultra high vacuum.

If the voltage is raised above the work function then the classical turning point occurs at a position midway between the two electrodes. Beyond this point, the field emission current sets up

a standing wave that that will be manifest as oscillations in current with either gap distance or bias voltage. These are caused by

> "..interference between incident and reflected electrons in the positive kinetic energy of the electron gap.."

Although these oscillations could be detected by Binnig, 1982, these waves have been generated, measured and compared with the predictions of Schrodingers equation by Becker et al, 1985. This implies the possibility of using this gap distance interferometrically. It is also pointed out by Binnig et al, 1985, that small changes in conductivity will occur in the presence of surface adsorbates. The implications of this are that if a stability of greater than 0.001nm can be achieved then the STM can be used as a spectroscopic tool to identify and study these adsorbates.

As the tunneling probe is moved into close proximity to the surface, there is a possibility that the tip will contact an insulating particle or even an oxide layer. The probe will then be driven further towards the surface causing the two surfaces to distort. This will continue until either another probe asperity comes within tunnelling distance or the oxide layer is sufficiently penetrated. In this instance the probe surface separation will be related to the elastic properties of the material and scanning will be unreliable because it is no longer a non contacting process. This model proposed by Coombs and Pethica, 1985, has been shown to be a possible explanation of anomalous barrier heights (this may also be caused by the image forces, Willis et al, 1985) and curiously high surface slopes, implying asperities ten atoms high and monoatomically wide.

Increases in stiffness and stability of new designs meant that they had become less sensitive to external vibrations. Thus systems were found to operate satisfactorily with viton spacers as isolation, Gerber et al, 1986, and then to a system with virtually no isolation at all, Smith and Binnig, 1986.

In this year, Binnig et al, 1986, introduced the idea of the Atomic Force Microscope (AFM). In this system, a tip, mounted onto a thin cantilever beam, is brought into close proximity to the surface under examination. At small separations there will be an attraction caused by van der Waals forces that will tend to deflect the beam. This has previously been measured directly by

Tabor, 1969. The deflection of this beam is then monitored with a tunneling probe. In the initial system forces as low as 10^{-10}N could be detected. The surface is then scanned under the tip and the beam deflection and thus tip surface force kept constant by servo control in the z-axis. The advantage of this system is that insulating materials can be examined whilst the preliminary results indicate that similar resolution to STM is achievable whilst operating in air. This was at the time approximately 1nm and 0.15nm horizontal and vertical resolution with a drift rate of less than 0.4nm/min and a response time down to 0.3ms, van de Walle, 1985.

Scan lengths for these topographs is normally in the region of a few hundreds of nanometers. In the examination of optical surfaces, Dragoset et al, 1986, obtained a scan area of greater than $5\mu m^2$. To obtain these traverses, corrections had to be applied for non-linearities in the piezo translation devices.

The production of probe tips is a rather ill defined process. Techniques include cutting a tungsten wire with engineers snips, grinding and electrochemical etching. The mechanical processes give a rough point with a high density of asperities. These operate on the assumption that there will be one asperity higher than the rest that will operate as the probe. This does seem to be successful but raises the question as to whether the same asperity is in operation if rough surfaces are being studied. Electrochemically etching these rods in a 1N KOH solution can yield a smoother point having radius of 1μm or less, Dragoset et al, 1986. This is more likely to have a single high asperity although little attention has been given to the form of the probe tips. However, Kuk and Silverman, 1986, found that tip structure could be examined in situ using Field Ion Microscopy (FIM) techniques. This technique can also be used to produce tips of known structure. Using this method of assessment it has been shown that for high resolution, tips having atomic asperities must be used and that the tip structure remains unaltered by the scanning process. Common to the previous probe production processes is the need to clean the surface to remove any oxide layers. This usually passing a high (μA) current across the gap. It is also shown that this process can radically alter the tip characteristic resulting in a change in the probe resolution. However the use of ion beam milling for the removal of oxide layers has been found to reliably produce usable probes with no apparent loss in resolution and possibly a slight enhancement,

Biegelsen et al, 1987.

It has recently been shown that probes can be used to mechanically work the surface under examination. A specimen having a thin (≈20nm) oxide layer over a conducting substratehas been examined with an STM. The probe is pushed through the oxide layer until a tunneling current is detected. Then it is traversed across the specimen whilst a tunneling current is maintained and thus ploughing through the oxide layer. This was found to produce a track ≈20nm wide, McCord and Pease, 1987. On the other hand, Becker et al, 1987, found that by applying a high voltage across the barrier of a W-Ge barrier it is possible to pick up a single atom on the end of the probe. This could then be moved to a different position and redeposited by a reversal of this potential.

A number of other recent investigations using the STM has been; an examination of the granular structure of Nd-Fe-B permanent magnet materials, Corb et al, 1987, imaging of semiconductors under aqueous environments, Sonnenfeld et al, 1987, and a topographical map of photoconductive semi insulating GaAs whilst being illuminated by both a 150W halogen lamp and a 5mW HeNe laser, van de Walle et al, 1987.

A coarse positioning stage has been devised whereby the specimen table is mounted on an oscillating stage that can be driven by a piezo electric translator. The oscillation consists of a sharp pulse followed by a slow reverse traverse. If the wave form is correct then due to inertial forces, the table will slip in the one direction only, Pohl, 1987. Steps of 0.2-0.04μm have been achieved with loads of up to 1kg.

All of these achievements have not been without complication. In the paper of Dragoset et al, 1986, motions of greater than a few hundred nanometers were found to introduce "substantial non-linearities" that required "corrections" before images could be produced. This implies an unreliable image and also a loss of accuracy. This poses possible problems in the calibration of such devices. Calibration is usually performed by measuring a known step height or it is carried out prior to experimentation. For a long traverse or if the z-axis piezo is extended during the scan large errors may result.

An assessment of these translation devices by Drake et al, 1985, indicates that other sources

of error may be present. Using the STM they were able to obtain images in air, oil and liquid nitrogen. Images having atomic resolution could only be obtained under liquid nitrogen conditions. This is possibly due to the thermally stable, highly damped environmental conditions. The thermal effects of this instrument will depend on both the thermal piezo-electric coefficient and the thermal expansion and thermal capacitance mismatches throughout the measurement loop (i.e. length of connection between specimen and probe tip). For a well controlled environment the piezo-electric coefficient is going to be stable to a very slight fraction of a percent. The dynamic thermal effects are difficult to assess whereas the static effect will be a measure of the thermal mismatch around the loop. Drake assesses this to have a value of approximately 5×10^{-6}/k. For a miniature system having a loop of 2cm (say) the thermal coefficient of approximately 100nm/k could be expected. However, Drake could not not measure this quantity because of the overiding effects of creep. This is measured as the change in the piezo-electric coefficient upon application of a voltage over a given time. This phenomena has been recognised by a lot of workers in this field and can cause a change in the piezo-electric coefficient by as much as 33% over a period of 15min or less. As with other creep mechanisms this effect diminishes with time but will increase the uncertainty in calibration of these devices especially for long duration measurements.

Because of the linearity, accuracy and stability of the silicon single crystal monolithic x-ray interferometer, it was decided to use this as a three dimensional translation stage for use as an STM. This also provides an inherent calibration and real space feedback monitoring facility with potential accuracy of 10pm or less. This is also a monolithic sructure with a thermal expansion coefficient coincidently close to that of tungsten. Thus a mismatch coefficient of 10^{-8}/k may be expected with the high conductivity of silicon providing enhanced insensitivity to dynamic thermal variations. The main object of this thesis has been to design and manufacture such a system with a view to utilising these favourable characteristics. The design, manufacture and testing of this instrument are presented in chapters 2,6,7 & 8.

Figure 1.1: Schematic diagram of x-ray microscope

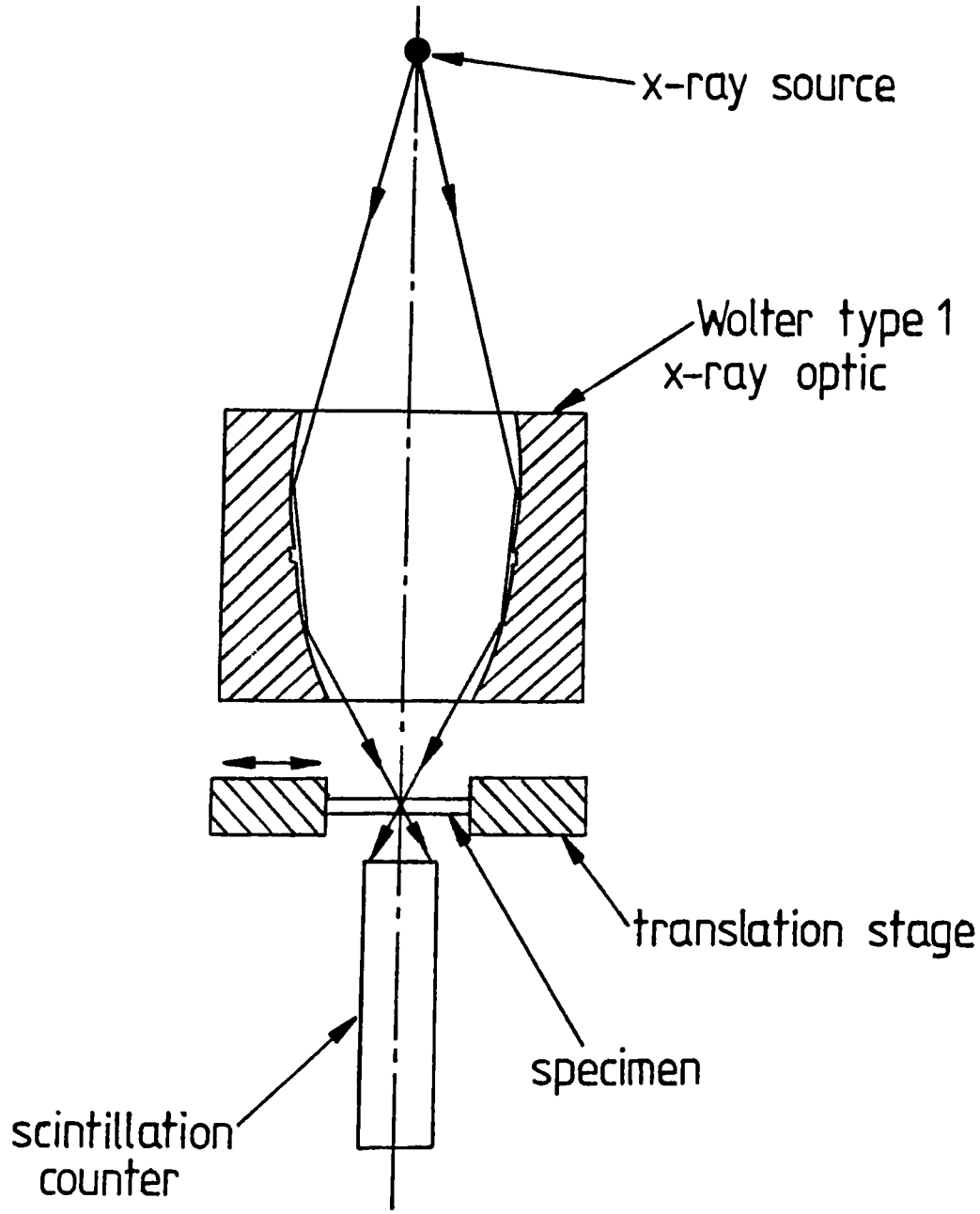

Figure 1.2:Performance characteristics of some stylus instruments

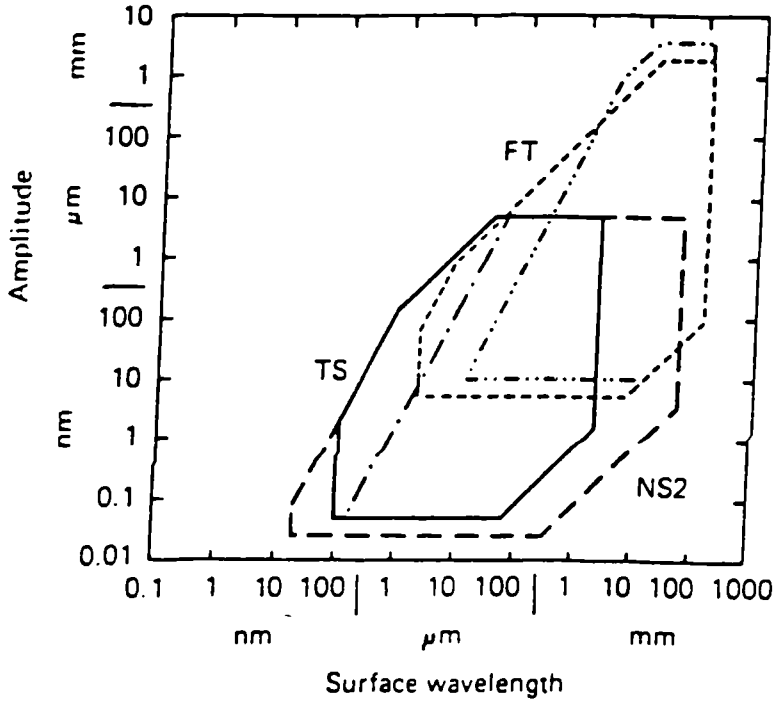

TS,Talystep:——chisel stylus

·—·-standard stylus

NS2,Nanosurf 2

FT,Form Talystep:----standard stylus

··—··-ball stylus

Figure 1.3:An x-ray interferometer

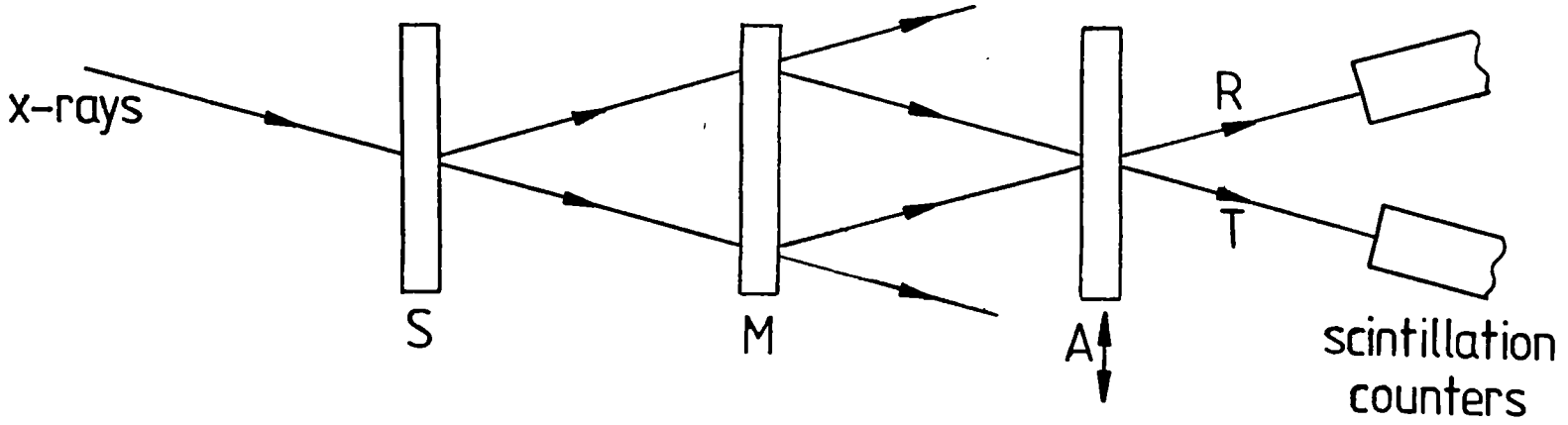

Figure 1.4:Scanning probe system

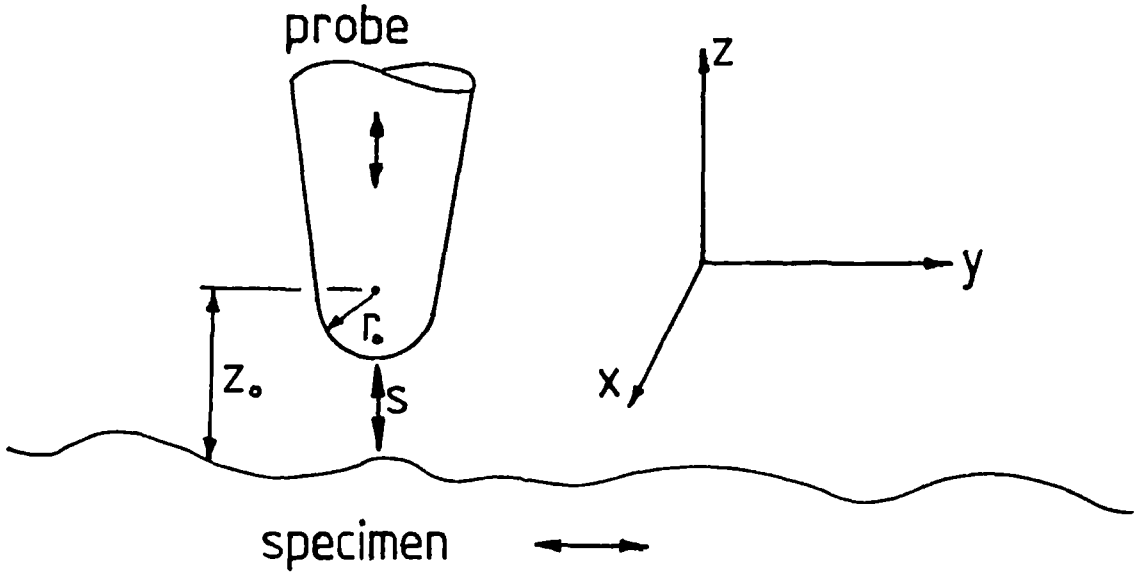

Figure 1.5:Potential energy diagram for an electron between two electrodes

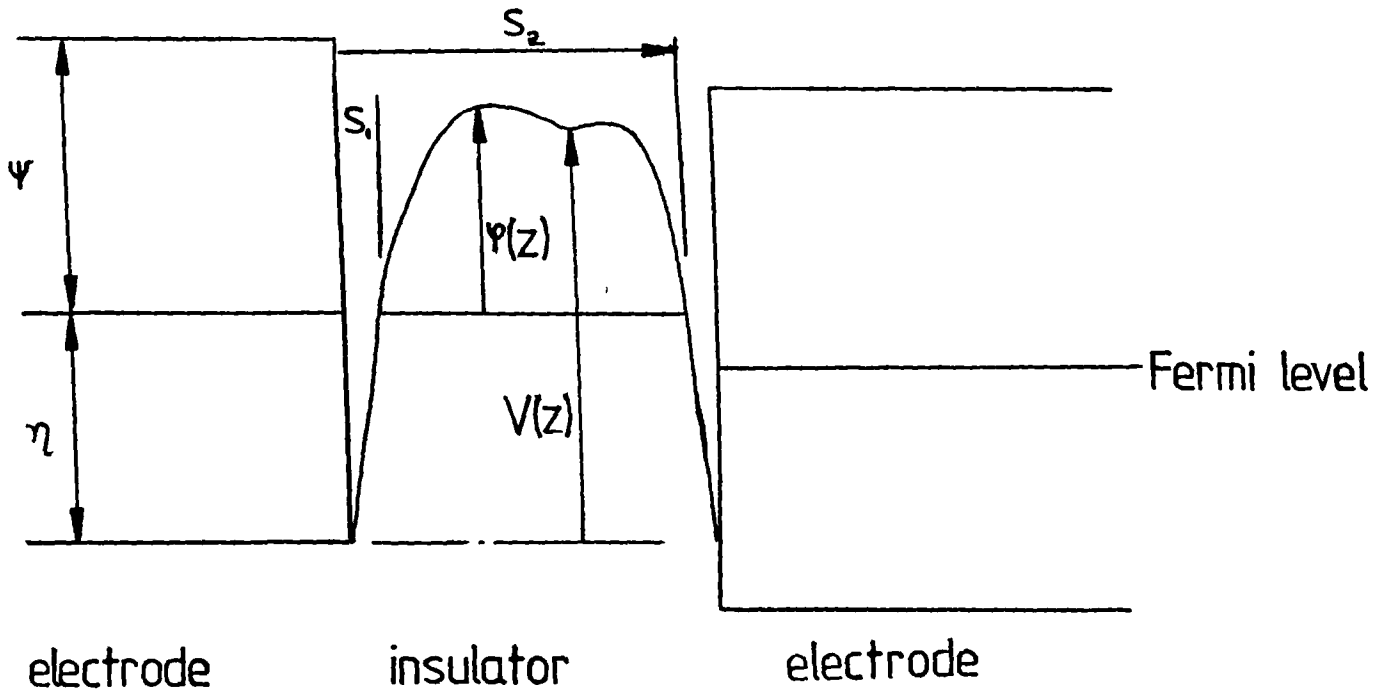

Chapter 2: An assessment of elastic design for use as a precision reference motion

2. Introduction

Elastic flexure devices have been in use for possibly hundreds of years and were well established in 1897 with the Emery Testing Machine, Gibbons (1935). Since then these techniques have been used to advantage in a wide variety of precision instruments, such as; gravimeters, tiltmeters, optical slit mechanisms and capacitance micrometry, (Jones 1952, 1962, 1967, 1968 & 1973), optical interferometry, Hill and Bruce (1961), x-ray interferometry, (Hart, 1968, Chetwynd et al, 1983, Becker et al, 1987 and Alemanni et al, 1986), and the Marsh tensile testing machine, (Marsh, 1961). These instruments are representative of a number of possible flexure device variations on which a good bibliography is given by Geary (1954, 1960) and Sydenham (1981, 1984). The object of this chapter is to present information for the design and assessment of rectilinear spring mechanisms such as those used in the design of the Scanning Tunneling Microscope presented in chapter 5. Jones (1951), has shown that well designed spring systems may possess parasitic errors not exceeding 2μm over displacements of 10mm or more. This implies a linearity of better than 1 part in 5000. It has been shown in chapter 1 that this ratio can be greater for smaller displacements.

Rectilinear spring systems are traditionally fabricated from individual components. This inevitably gives rise to cumulative errors resulting from machining tolerances, thermal expansion mismatch, mechanical interfaces, stress concentrations in the regions around fixtures and construction inaccuracies, Jones (1950, 1956). If, however, the spring is machined from a single

monolith, the above considerations become either non-existent or dependent upon machine tool characteristics only. The repeatability and describability of modern CNC machine tools makes them ideally suited for the manufacture of these mechanisms.

There are two distinct types of rectilinear spring. These are the notch type hinge and the leaf spring, figure 2.1. Compliance of the notch type hinge is a result of the thin web that remains after two holes have been drilled closely together. This configuration is often used for monolithic devices because of the ease of manufacture. The leaf spring arrangement is self evident from figure 2.1.

A consideration common to both of these devices is materials selection. This subject will be discussed in the proceeding section, whereafter, each configuration will be considered in turn.

2.1. Materials selection

Table 2.1 is a review of the properties of some materials that may be important for use in precision instrumentation. Selection of a material to be suitable for use as a monolithic spring will be influenced by four main design considerations. These are:-

1. Response of system.
2. Stability of deflection.
3. Magnitude of elastic distortion.
4. Cost.

2.1.1. Response of system

This section is based on a previous study of material properties by Chetwynd (1987). The upper velocity at which displacements of a spring mechanism can occur will be related to the resonant frequency. If the structure is considered as a simple spring/mass system, then the fundamental frequency (ω) will be governed by the relationship:-

$$\omega = K\sqrt{E/\rho} \tag{2.1}$$

K is a function of the spring geometry and will be independent of the material that is used. Thus, for the above equation, it can be seen that dynamic properties are enhanced by an increase

in the ratio of elastic modulus (E) to density (ρ). From table 2.1, it can be seen that silicon is the most suitable material followed by zerodur and fused quartz. Mild steel, Dural and Invar have a ratio four or five times that of silicon and would be expected to have less than half the response time.

A lower limit to the response of the spring system will be determined by thermal characteristics of the material. If heat input to a material is conducted in the absence of any release other than that due to the material's own heat capacity, then the unsteady diffusion equation is given by:-

$$\frac{\partial T}{\partial t}=\frac{K_t}{C_v}\nabla^2 T=\frac{K_t \rho}{C_p}\nabla^2 T=D\,\nabla^2 T \qquad (2.2)$$

where

T = temperature

t = time

C_p = specific heat at constant pressure

C_v = specific heat at constant volume

K_t = thermal conductivity

The value D is called "diffusivity" and can be considered as a measure of the response to a thermal spike. A high diffusivity corresponds to an inability of the material to maintain a temperature gradient for a protracted period of time. This implies two complementary material characteristics. A material with a high diffusivity will settle to a steady state condition very quickly, whereas a low diffusivity implies insensitivity to rapid thermal fluctuations. A material cannot have the best of both worlds. With reference to table 2.1, it can be seen that silicon has the highest value of 9.71×10^{-5} with standard dural being of a less but similar value. The most thermally insensitive are the glassy materials with invar being an intermediate between these two extremes. The temperature change at a given time and distance away from a thermal input in a particular solid will depend on the square root of its diffusivity. If a rod of material is subjected to a temperature increase at one end, the magnitude of the temperature at the other end at a given

time will be approximately ten times higher in silicon than in Zerodur for rods of the same length.

2.1.2. Stability of deflection

A spring system is deflected by applying a force to distort the compliant members. For open loop control of such a system, the determination of displacement is dependent upon an accurate knowledge of both the driving force and stiffness. Drive systems will be discussed in section 2.4. It will be shown later in this chapter that the stiffness is linearly related to the elastic modulus (E) of the material. This property will fluctuate with temperature and for small variations can be represented by the thermal coefficient of elasticity (γ_t). Clearly, it is an undesirable property and should be minimized if at all possible. From table 2.1 it can be seen that Elinvar (or the equivalent Nispan-C) is the lowest of these values and with correct pretreatment can be zero within a limited temperature band. The value of 100×10^{-6} for S_i is that measured along the c_{11} elastic tensor, McSkimin (1953). This implies errors of approximately 0.1%/k. For many metals this value will be around 0.3-4%/k.

2.1.3. Magnitude of elastic distortion

The position of a point within a material is directly related to temperature by the expansion coefficient (α_t). Zerodur is a glass ceramic that has a temperature coefficient of the order 10^{-8} over a narrow temperature band rising to approximately five times this value over a bandwidth of 50k. This material will be discussed more fully in chapter 4. Fused quartz has a coefficient of 5.5×10^{-7} with Invar being approximately twice this value. Silicon and elinvar have coefficients that are approximately twice the value of Invar. Dural has a relatively high expansion coefficient that is an order of magnitude greater than that of silicon.

Hysteresis is a phenomena that is well known in metals and will lead to a cumulative errors directly related to the stress and thus displacement. This effect is only apparent upon returning the spring to a rest position. It may be avoided by operating the spring in a manner such that this position is not approached. The high purity and crystallinity of silicon has been proven to leave it with a mechanical hysteresis at levels of <10pm at room temperature, Siddons, 1978. This has the

effect of doubling the range of the spring system.

The functional limitations to displacement magnitudes are governed by mechanical failure. Hysteresis, yield and fatigue are related properties of ductile materials. Due to these phenomena, the performance of ductile materials (mainly metals) will deteriorate with use. The brittle materials, however, are more likely to either operate very well or not at all i.e. they break. Thus as long as acceptable stress levels are not exceeded, the quality of performance will be maintained. The strength of brittle materials has been shown to be governed by initial surface imperfections, Griffiths (1920), Marsh (1963). These imperfections are usually introduced at the manufacturing stage and will have a marked influence on the strength of a component. Lawn et al (1981), show that the strength of silicon can be degraded by an order of magnitude after a sharp indenter has been applied to its surface under a load of 1N. It is possible to reduce this effect by removal of the damaged surface using an appropriate etchant. Glass and glass ceramics suffer additional strength degradation due to hydrogen embrittlement, Cuthrell (1979).

2.1.4. Cost.

The cost of a monolithic spring system is governed by the material and labour costs. The cost of the standard glasses and metals considered in table 2.1 are relatively similar and are insignificant in relation to labour. The cost, at present, of the more exotic materials climbs steadily as Invar 0.1p/g=0.8p/cm^3, Zerodur 0.3p/g=0.76p/cm^3 and silicon 25p/g=57.5p/cm^3. Costing for metal springs is standard engineering practice and will be dependent on time and tooling. Brittle materials, however, require a lot of expertise and non-conventional tooling. The author is not aware of any manufacturers or workshops with the capability to produce both accurate and intricate shapes from these materials on a jobbing basis. Thus machining of glass and silicon may still be considered a specialist process. Finishing processes such as etching and polishing must also be carried out if mechanically reliable devices are to be produced. The production of springs from brittle materials can only be carried out as a labour intensive project requiring the use of high speed diamond tooling.

2.2. The notch type rectilinear spring

The simplest form of monolithic spring traverse, a plain parallelogram movement based on a four bar kinematic chain, has the disadvantage of intrinsic parasitic motion perpendicular to the traverse direction. Using two such motions in a compound design (see figure 2.2) will eliminate this error.

The compound spring consists of two platforms, the primary (A) and the secondary (B), supported on flexible legs (C,D,E and F). The primary platform is driven in the x-direction by the appropriate technique. In the results presented in chapter 6 a feedscrew and wobble-pin drive was used for initial experimentation of these devices with electromagnetic drives being utilized for the more accurate applications, see section 2.4. A displacement of this platform will cause distortion of the "necked hinges" of the platform support legs. Because the bending strength of these hinges is considerably less than the rest of the structure, all other distortions are considered insignificant. Assuming further, that all hinges have equal stiffness, the displacement ratio of primary to secondary platform relative to the base will clearly be 2:1. If this ratio is maintained then it is reasonable to expect greater linearity than for the simple case. To ensure that this ratio obtained a lever system can be applied between the two platforms, Jones, 1956. This is known as "slaving", see figure 2.4. To test this hypothesis, simple, double and slaved compound monolithic parallel springs were produced. The double compound spring is two simple compound springs joined together about the x-axis in the z-plane, see figure 2.3. This design, based upon a symmetrical stress distribution, utilizes elastic averaging to reduce the effect of machining errors (in the length of any of the legs or in the stiffness of any of the webs) on the linearity of motion. This principle can be indefinitely extended, by increasing the number of parallel platform support legs above the minimum of two. The kinematic overconstraint of this will act to ensure a primary secondary displacement ratio of 2. This overconstraint is acceptable as any errors in manufacture will be compensated by elastic deformations provided that tolerances are within acceptible limits. It is also expected that the symmetrical design will improve immunity to temperature gradients, especially those along the axis of motion.

The compliance of the necked hinge indicates that an analysis of its bending strength will help to create some design rules for these devices. A closed form analysis of the stress distribution within a necked hinge is rather complicated, Ling, 1952, Paros, 1965. However, using the finite element methods available on PAFEC 75 software, empirical stress/strain relationships have been developed. The finite element mesh used in this analysis is shown in figure 2.5. By analyzing a number of different geometries of hinge, a formula analogous to that for a simple cantilever beam has been obtained. The angle (θ) rotated by a particular hinge due to an applied bending moment (M) can be represented by

$$\theta=\frac{2KMR}{EI_{zz}} \tag{2.3}$$

Where:-

$I_{zz}=ht^3/12$

t = thickness of web

h = depth of web

R = radius of holes for web

The value for the constant K has been determined by carrying out six analyses with values of the ratio R/t varying between 1 and 5. The angle of twist for a given bending moment has been calculated using a linear elastic finite element analysis. Rearranging equation (2.3), values for the constant K are obtained. This has been plotted in figure 2.6 against the radius/thickness ratio. Using linear regression techniques the variation of the constant K with the radius/thickness ratio has been matched to a hyperbolic equation of the form

$$y = a/x + b$$

The match has a corrected coefficient of determination of 0.9926. and a standard error of 0.01. From this analysis an approximate equation for the angular constant is given by

$$K\approx 0.565\frac{t}{R}+0.166 \tag{2.4}$$

For a given bending moment, the maximum stress (which occurs at the outside edge of the thinnest part of the web) is determined from the equation

$$\sigma_{max}=\frac{6MK_t}{t^2h} \tag{2.5}$$

The stress concentration factor K_t can be found graphically (Peterson (1974)) or from the approximation

$$K_t\simeq\frac{2.7t+5.4R}{8R+t}+0.325 \tag{2.6}$$

Use of equations (2.3) and (2.5) will determine the required drive force and the maximum stress for a given displacement. Off axis loading of the platform will induce additional moments about the necked hinge. In the case of a y-axis load, these moments will be additive and will effectively increase the stiffness of the pair of support legs in tension and reduce the stiffness of the pair of support legs under compression. This effect will alter the platform displacement ratio and may also lead to catastrophic failure if extreme loads are encountered.

Thermal expansion does not effect the position of the primary platform if there is a uniform temperature change or a y-plane gradient. This is because motion of the primary platform due to expansion of the legs (C & D) will be compensated by an equal and opposite expansion of the legs (E & F). This reasoning also applies to leaf type springs. Parasitic motion will occur, however, if unsteady temperature gradients exist in the x- or y-planes. From the materials selection considerations, duralumin was chosen as the most suitable material for initial experiments into these devices, see section 2.6.

Machining tolerances of spring elements other than the necked hinge require only sufficient rigidity is maintained so as not to deflect significantly under the applied loads. From equation (2.3) the stiffness of a compound spring is given by

$$\lambda=\frac{EI_{zz}}{KRL^2} \tag{2.7}$$

Where L = length of platform support legs

Inconsistent values of the second moment of area (I_{zz}) will introduce non-symmetrical stresses within the structure, possibly resulting in inherent parasitic errors. In an elastic system the platform displacement characteristics will remain linear, no matter how crude the machining. However, the drive axis may no longer be colinear with platform motion. To ascertain changes in

stiffness due to machining tolerance it is important to evaluate changes in the second moment of area. Assuming the worst case of cross section tapering, as in figure 2.7, the second moment of area is given by

$$I_{zz}=\int y^2 dA=\frac{h}{12}(t^3+3t^2\psi h+4t(\psi h)^2+2(\psi h)^3) \tag{2.8}$$

Where

ψ = angular machining error (Rad).

The second moment of area for a positioning error (δ) becomes (figure 2.7b)

$$I_{zz}=\frac{h(t+2\delta)^3}{12} \tag{2.9}$$

The errors in stiffness are minimized by maximizing the thickness t and the effect of angular errors is reduced by minimizing the web depth h. The effect of elastic averaging is as follows. If the sum of stiffnesses of the hinges of legs E and F in figure 2.2 is equal to the sum of stiffnesses of legs C and D then the motion remains linear even though the overall calculated stiffness may be in error. If the double arrangement is used, then even this criterion for linear motion may be relaxed provided that the webs do not buckle, and the linkage bars are very stiff in comparison to the webs; the effect of web stiffness errors is only to alter the stress in the linkage bars. Angular errors (ψ) will introduce a secondary moment M_y at each web pivot. In most cases the effect of these moments will again be to change the stresses in the linkage bars rather than to affect the motion of the table, hence they effectively cancel.

Following the work of Jones, 1951, the z-axis angular pitch (θ_z) due to positioning errors of a web in the x- and y-axis on a simple parallel spring can be approximated by

$$\theta_z=\delta_x x^2/2L^2b \text{ or } x\delta_y/Lb \tag{2.9}$$

where

b = web spacing

x = x-axis deflection of platform

δ_y = y-axis machining error

δ_x = x-axis machining error

The direction of motion of the primary platform will, in general, be the direction of least stiffness. This will contain the lowest natural frequency and also the highest dynamic amplification. To estimate the resonant frequencies of a compound rectilinear spring it is convenient to use the lumped model shown in figure 2.8. The two fundamental modes can be found by solving the quadratic equation

$$\omega_n^4-\omega_n^2\left\{2\lambda\left[\frac{1}{M_A}+\frac{1}{M_B}\right]+2\frac{\lambda}{M_B}\right\}+4\frac{\lambda^2}{M_AM_B}=0 \qquad (2.10)$$

M_A = mass of platform A

M_B = mass of platform B

This holds for the simple parallel spring if the mass of platform B is made equal to zero. Inserting values for a compound spring used in assessment experiments, frequencies of 56 and 140Hz were calculated. Sand was then placed on this spring and low amplitude vibrations applied to its support. The two lowest resonant frequencies observed were at 52 and 130Hz corresponding to a 10% error that is near to the experimental accuracy.

Maxwell 1897, stated that one of the main assets of elastic mechanisms is that they are friction and wear free. An unfortunate side effect is a large dynamic amplification factor that will render them particularly sensitive to mechanical vibrations transmitted from foundations or airborne sources. Most of the materials likely to be used will have low intrinsic damping. If possible, it is desirable to apply external damping mechanisms such as viscous, electro-magnetic or interfacial energy dissipation. An increase in stiffness will attenuate disturbances but will also limit the displacement range. This range is increased if the ratios R/t and material yield stress/elastic modulus are increased.

2.3. Parametric equations governing the simple leaf type rectilinear spring

2.3.1. The equations of Plainevaux (1956)

This section outlines the mathematical analysis developed by Plainevaux, 1956, for the characterization of the simple leaf type rectilinear spring. Upon deflection of the primary

platform, each spring member will deform in the manner shown in figure 2.9. The differential equation of moments for this beam is given by

$$EI\frac{d^2X}{dY^2}+PX=M_o-F_oY \tag{2.11}$$

The coordinate Y is measured parallel to the axis of the undistorted leg and the deflection X is perpendicular to Y and parallel to the applied force F. Using the dimensionless groups

$$y=\frac{Y}{L}\ ;\ 4\beta_l^2=\frac{PL^2}{EI}\ ;\ \psi_l=\frac{FL^2}{EI}\ ;\ m_o=\frac{M_oL}{EI} \tag{2.12}$$

equation (2.11) becomes

$$\frac{d^2X}{dy^2}+4\beta_l^2X=L(m_o-\psi y) \tag{2.13}$$

The boundary conditions are

$$@\ y=0, X=\frac{dX}{dy}=0\ \ \&\ \ @\ X=\delta,\ \frac{dX}{dY}=\frac{dX}{ldy}=\tan\theta$$

Solving equation (2.13) for the above boundary conditions gives the following equations

$$X=\frac{\psi L}{8\beta_l^3}(sin(2\beta y)-2\beta y)+\frac{m_oL}{4\beta_l^2}(1-cos(2\beta y)) \tag{2.14a}$$

$$\frac{\delta}{L}=\frac{\psi}{8\beta_l^3}(sin(2\beta)-2\beta)+\frac{m_o}{4\beta_l^2}sin(2\beta) \tag{2.14b}$$

$$\tan\theta=\frac{\psi}{4\beta_l^2}(cos(2\beta)-1)+\frac{m_o}{2\beta}sin(2\beta) \tag{2.14c}$$

The change in height (λ_l) of the beam is given by (Plainevaux, 1956):-

$$\lambda_l=\int_0^L(1+(dX/dy)^2)dy-L\ =\frac{1}{2L}\int_0^1(dX/dy)^2dy \tag{2.15}$$

Substitution of (2.14a) into (2.15) gives an expression for the determination of the change in height of the platform, figure 2.9. Making the substitution $\alpha_l=4\beta_l^2/\pi^2$ equations (2.14) and (2.15) can be expressed in dimensionless form and represented by the series:-

$$\frac{M_AL}{EI}=4\tan\theta\left\{1-\frac{\pi^2\alpha_l}{30}-\frac{11\pi^4\alpha_l^2}{25200}\cdots\right\}-6\frac{\delta}{L}\left\{1-\frac{\pi^2\alpha_l}{60}-\frac{\pi^4\alpha_l^2}{8400}\cdots\right\} \tag{2.16a}$$

$$\frac{FL^2}{EI}=-6tan\theta\left\{1-\frac{\pi^2\alpha_l}{60}-\frac{\pi^4\alpha_l^2}{8400}\cdots\right\}+12\frac{\delta}{L}\left\{1-\frac{\pi^2\alpha_l}{10}-\frac{\pi^4\alpha_l^2}{8400}\cdots\right\} \tag{2.16b}$$

$$\frac{M_oL}{EI}=-2tan\theta\left\{1+\frac{\pi^2\alpha_l}{60}+\frac{13\pi^4\alpha_l^2}{25200}+\cdots\right\}+\frac{6\delta}{L}\left\{1-\frac{\pi^2\alpha_l}{60}-\frac{\pi^4\alpha_l^2}{8400}\cdots\right\} \tag{2.16c}$$

$$\frac{\delta}{L}=\frac{\tan^2\theta}{15}\left\{1+\frac{11\pi^2\alpha_l}{420}+\frac{\pi^4\alpha_l^2}{1200}+\cdots\right\}-\frac{\delta}{10L}\tan\theta\left\{1+\frac{\pi^2\alpha_l}{70}+\frac{\pi^4\alpha_l^2}{4200}\cdots\right\}$$

$$+\frac{3}{5}\left[\frac{\delta}{l}\right]^2\left\{1+\frac{\pi^2\alpha_l}{420}+\frac{\pi^4\alpha_l^2}{25200}\cdots\right\} \tag{2.16d}$$

If the load case is tension then α_l is replaced by $-\alpha_l$. Ignoring the pitching terms in equations (2.16), it is convenient to use the following parametric equations for initial design purposes

$$\delta=\frac{F_o L^3}{12EI}\phi_l(\alpha_l) \tag{2.17a}$$

$$\lambda_l=\frac{3}{5}\frac{\delta^2}{L}\chi_l(\alpha_l)=\frac{L^5}{240}\left[\frac{F_o}{EI}\right]^2\psi_l(\alpha_l) \tag{2.17b}$$

$$M_o=\frac{6EI\delta}{L^2}\frac{\tau_l(\alpha_l)}{\phi_l(\alpha_l)}=\frac{F_o L}{2}\tau_l(\alpha_l \tag{2.17c}$$

The functions ϕ, ψ, χ, τ & η are reproduced in figures 2.10 to 2.19. These are computed from the series

$$\phi_l(\alpha_l)=1+\frac{\pi^2\alpha_l}{10}+\frac{17\pi^4\alpha_l^2}{1680}+\frac{31\pi^6\alpha_l^3}{30240}\cdots \tag{2.18a}$$

$$\psi_l(\alpha_l)=1+\frac{17\pi^2\alpha_l}{84}+\frac{31\pi^4\alpha_l^2}{1008}+\frac{691\pi^6\alpha_l^3}{166320}\cdots \tag{2.18b}$$

$$\chi_l(\alpha_l)=\frac{\psi_l(\alpha_l)}{\phi_l^2(\alpha_l)} \tag{2.18c}$$

$$\eta_l(\alpha_l)=\frac{\tau_l(\alpha_l)}{\phi_l(\alpha_l)}=1-\frac{\pi^2\alpha_l}{60}-\frac{\pi^4\alpha_l^2}{8400}-\frac{\pi^6\alpha_l^3}{756000}\cdots \tag{2.18d}$$

Plainevaux has shown that if the applied load is small then the optimum drive position is mid way between the platform and base. However, it is often more convenient to apply the load directly to the centroid of the platform. If the load on the platform (v) is perpendicular to the drive direction, see figure 2.9b, then the pitching angle (θ) can be approximated by the expression

$$\theta=\left[\frac{\delta}{L}\right]^3\frac{12\left[1-\frac{vL^2}{120EI}\right]}{350\left[\frac{b}{L}\right]^2} \tag{2.19}$$

2.3.2. Axial deflection of a slender column under an axial load

This section presents an equation to enable the designer to calculate an approximate value for the change in height (λ_l) of a deformed slender column under an axial load (P) in terms of the original length (L) and the deflection (δ). The governing equation for a slender column is given by, figure 2.20 :-

$$EI\frac{d^4y}{dx^4}+P\frac{d^2y}{dx^2}=0 \tag{2.20}$$

The boundary conditions from figure 2.20 are given by

$$y(0)=y'(0)=y'(s)=0 \quad \& \quad y(s)=-\delta$$

Substituting these conditions into eqn 2.20 and solving for y gives

$$y=\frac{\delta}{2}\left\{\cos\left[\frac{\pi x}{s}\right]-1\right\} \tag{2.21}$$

Assuming that the length of the beam remains the same in its distorted condition as it would undistorted under load, the distance s is given by the integral

$$L=\frac{2s}{\pi}\int_0^{\frac{\pi}{2}}\left[1+K^2\sin^2\eta\right]^{\frac{1}{2}}d\eta=\frac{2s}{\pi}(1-K^2)^{\frac{1}{2}}E\left[\frac{K^2}{1-K^2},\frac{\pi}{2}\right] \tag{2.22}$$

Where

$\eta=\pi x/s$

$k=\pi\delta/2s<<1$

$E=$ the elliptic function

neglecting terms of the order K^4, equation (2.22) becomes

$$L=s(1-K^2)^{\frac{1}{2}}\left[\frac{K^2}{4(1-K^2)}-1\right]^2 \tag{2.23}$$

Squaring equation (2.23) and solving for s gives

$$s^2=\frac{\left[L^2+\frac{5\pi^2\delta^2}{8}\right]+\left\{\left[L^2+\frac{5\pi^2\delta^2}{8}\right]^2-4\left[L^2\pi^2\delta^2+\frac{25\pi^4\delta^4}{256}\right]\right\}^{\frac{1}{2}}}{2} \tag{2.24}$$

From this equation, the change in height of the platform is given by

$$\lambda_l = L - s \tag{2.25}$$

2.4. Drive techniques

Having designed a flexure, it is important to choose the correct drive for a specific application. The common considerations for selection of an appropriate drive are range, resolution, temperature stability, time stability, linearity and stiffness. This section will briefly review some of the drive techniques that are relevant to this study.

2.4.1. The hydraulic drive

Hydraulic drives are used because of the very high fluid pressures and thus stiffnesses that can be achieved. These systems can have a very high power/weight ratio and are not limited to short displacements. For a hydraulic cylinder used as a piston drive the resolution is limited by leakage and in consistencies in the properties of material interfaces. However, using laser interferometric feedback, accuracies of greater than 0.2μm over a 100mm traverse have been achieved, Ido et al, 1981. A system that effectively attenuates the range and enhances resolution is the poisson pusher. Here the pressure is used to squeeze a steel cylinder perpendicular to the direction of traverse, Hu and Chetwynd, 1987. This will introduce a strain in this direction. The ratio of the two perpendicular stresses is related by piossons ratio (v). The stiffness of this system is very high and displacement resolution is determined by the thickness of the steel (or other material) cylinder. The displacement range/resolution ratio is determined by the pressure range/resolution. Thermoelasticity and expansion will limit the open loop fidelity of this device. The cost of these systems can be prohibitively high and feedback is essential if high resolution is to be achieved. Leakage may cause problems in high vacuum applications.

2.4.2. Feedscrew mechanisms

These are a widely used and relatively cheap technique for obtaining displacements of up to 1m or more. If a smooth continuous motion is required, this will prove to be adequate in the majority of applications. Care must be exercised to avoid the pitch of the thread being superimposed in the motion of the driven platform. A non-rotating shank and decoupling between driver and device are essential if this is to be achieved. The accuracy of drive will always be a function of the pitch errors. This can be improved if a compliant nut is used, Stanley, 1968. Fine positioning can again be achieved by squeezing the threads perpendicular to the drive direction and utilizing the Poissons ratio effect. This has been used to obtain a fixed adjustment with a resolution of 0.1nm, Jones, 1967. If motions that include reversal of direction are required, backlash and material interface problems will preclude their use at the nanometre level.

2.4.3. The friction drive

The drive mechanism is simply a rod clamped between two rollers. Rotation of these clamps will induce a displacement, the magnitude of which depends on the smallest obtainable angular increment and the roller radius. This method is not restricted to short range displacements and accuracies of better than 0.1μm are obtainable, Reeds (1985).

2.4.4. Piezo-electric transducers

If a voltage is applied to a crystalline material that has no centre of symmetry, then the change in polarisation changes the dipole moment arm introducing a dimensional change. This can be used to create a very stiff drive having displacements of up to 100μm with resolution in the region of 0.1nm or less, Scire, 1978. This appears to be limited by the electronics rather than the piezo material itself. These devices have a high thermal expansion coefficient and creep is well known as a major problem. Over a period of a few minutes this can be as large as 33%, Drake, 1986. This can be compounded by a tendency to bend. Precautions are often necessary with the high electric fields that are required (100 - 2000v). Again it can be seen that, for absolute accuracies, feedback is necessary.

2.4.5. The electromagnetic drive

The electromagnetic drive is a force transmission transducer. This will consist of a magnet centered along the axis of a coil. These are not in mechanical contact. A current applied to the coil will induce a force on this magnet. If the magnet is attached to an elastic device, a displacement will be produced that is linearly related to this force. For small displacements, the force, and thus displacement, is linearly related to the current. Although not mechanically contacting, this system will generate heat that can be transferred to the elastic member via convection and radiation. The stiffness of this drive is governed by the stiffness of the elastic flexure being driven. The range resolution ratio is limited by the electronics, but the magnitude of distortion should remain significantly below the dimensions of the coil or nonlinearities will result. This system combined with a single crystal silicon flexure has been used in x-ray interferometry for some time

as a drive system. Its excellent precision and freedom from hysteresis at displacements $<10pm$, Siddons (1978), make it ideal for use as an STM probe. Thus design rules for the optimization of coil parameters and calculation of the forces generated are presented in this next section.

2.5. The design of the electromagnetic force transducer

The magnet/coil system used in the following analysis is shown schematically in figure 2.21. The magnet (usually samarium/cobalt) is attached to a flexure's primary platform and is surrounded by a solenoid coil that is attached to a fixed datum. A current applied to this coil will induce an axial field (H) given by the equation (Montgomery, 1963, 1969)

$$H_x(x/a_1)=H_x(0)\left\{\frac{F(\alpha_c,\beta_c+x/a_1)+F(\alpha_c,\beta_c-x/a_1)}{2F(\alpha_c,\beta_c)}\right\} \tag{2.26}$$

Where $F(\alpha_c,\beta_c)$ is the well known Fabry factor given by:-

$$F(\alpha_c,\beta_c)=\beta_c \ln\left\{\frac{\alpha_c+(\alpha_c^2+\beta_c^2)^{1/2}}{1+(1+\beta_c^2)^{1/2}}\right\} \tag{2.27}$$

and

$$H_x(0)=\frac{n\lambda_c IF(\alpha_c,\beta_c)}{a_1 2\beta_c(\alpha_c-1)} \tag{2.28}$$

Where

n=number of turns on coil

ρ=resistivity of winding material

a_1=inside radius of coil

a_2=outside radius of coil

$\alpha_c=a_2/a_1$

l=length of coil

$\beta_c=l/2a_1$

λ_c=packing factor of coil

I= current (A)

To determine values of the field factor for points outside of the coil the principle of superposition applies:-

$$F\left\{\alpha_c,\beta_c-\frac{x}{a_1}\right\}=-F\left\{\alpha_c,\frac{x}{a_1}-\beta_c\right\} \text{ for } \frac{x}{a_1}>\beta_c.$$

To relate the field along the central axis to force imparted on a magnet within that coii, it is important to review some of the fundamental aspects of magnetism. A bar magnet can be conveniently modelled as a rod of material containing a discrete pole of strength m at each end. If one of the poles is placed in a field of strength H (the field at the other pole being negligible) the force on that pole is given by (see Hadfield, 1962, Spreadbury, 1949)

$$F=Hm \tag{2.29}$$

In the design being considered here, the axis of the pole-pair of the magnet is taken to lay along the axis of the field. It is assumed that there is no radial field. This approximation is justified because the radial variation is slow at the coil axis. Also, with the short magnets considered here only a small torque would be produced and the mechanism being driven is much stiffer in torsion than translation. If the poles are positioned at potentials v_n and v_s a distance dx apart, the potential energy of the magnet (ψ) is

$$\psi=mdx\frac{(v_n-v_s)}{dx} \tag{2.30}$$

The value mdx is experimentally determined and is known as the moment (M) of the magnet. For small fields the magnetic moment is given by

$$M=B_{rem}V_m \tag{2.31}$$

B_{rem} = Remanence

V_m = Volume of magnet

If the distance between the poles is small, equation (2.31) becomes

$$\psi=M\frac{dv}{dx}=MH \tag{2.32}$$

The force on the magnet (F) is given by

$$F=M\frac{dH}{dx} \tag{2.33}$$

If, however, magnetization or demagnetization is significant (a soft magnet), the susceptibility will be finite and is often expressed as a constant (K_s) for small field variations. For this case, the moment of the magnet can be expressed as

$$M = VJ = KVH \tag{2.34}$$

Substitution of equation (2.34) into (2.32) and differentiating, equation (2.33) becomes

$$F = 2KVH\frac{dH}{dx} \tag{2.35}$$

Equations (2.29), (2.33) and (2.35) give the force on a magnet positioned with its pole axis concurrent with that of the solenoid coil. If use is made of a hard saturated magnet in moderate fields demagnetization will be minimal and the effects of Barkhaussen jumps, hysteresis and equation (2.35) can be ignored. Equation (2.33) has been found to accurately model the drive devices used in the experiments described here.

Any coil will possess the properties of both inductance (L) and resistance (R_c). For a cylindrical uniform current density coil, the resistance is given by

$$R_c = \frac{\pi\rho(\alpha_c+1)n^2}{a_1\lambda_c(\alpha_c-1)2\beta_c} \tag{2.36}$$

The inductance is related to the resistance of the coil by the equation

$$L = a_1^2 R_c \lambda_c \frac{\phi_c(\alpha_c,\beta_c)}{\rho} \tag{2.37}$$

The function ϕ is plotted in figure 2.22 (see Montgomery, 1963). From this equation it can be seen that the ratio L/R_c is constant for a given coil geometry and windings material.

If, for example, the coil is to be used in an ultra-high vacuum (UHV) system (as would be the case for tunnelling probe applications) the temperature will be determined by the radiation effect. For an input power W (watts) the steady state temperature (T_s) is governed by the relationship:-

$$W = A_s\kappa(T_s^4 - T_A^4) \tag{2.38}$$

Where:-

$A_s \approx a_1^2\pi((\alpha_c^2-1)+4\alpha_c\beta_c)$ =surface area of coil

κ=Stefan Boltzmann constant =56.7×10^{-9} W/m^2k^4

T_A=ambient temperature

To reduce thermal fluctuations of the coil drive it is necessary to maximize equation (2.38) for a given coil power consumption.

The field at the centroid of the coil ($H_x(0)$) can be expressed in terms of power by the equation:-

$$H_x(0)=\frac{F(\alpha_c,\beta_c)}{(2\pi\beta_c(\alpha_c^2-1))^{1/2}}(W\lambda_c/\rho a_1)^{1/2} \tag{2.39}$$

The graphs of figure 2.23(a & b) show contours of maximum axial field slope against the normalized half length (β_c) and outer radius (α_c) of the coil. The parameters that have been held constant in this analysis are; a_1=0.007m, $\rho=100\times10^{-9}$ Ωm, W=2.0W. Comparison of this figure with contours of coil surface area (figure 2.24) indicate that geometry factors in the region α_c=2.0 and β_c=1.0 will constitute a good design.

2.6. The dynamic characteristics of an electromagnetically driven linear spring system

From the previous analysis it is clear that (for small displacements of the magnet) the force experienced by a magnet within an energized coil is proportional to the applied current (I), i.e

$$F=K_1I \tag{2.40}$$

The constant K_1 is a function of the position of the magnet along the axis of the coil and can be determined from equation 2.33.

The motion of the primary platform for a given input force, as modeled in figure 2.21, is governed by the relationship:-

$$F=m\frac{d^2x}{dt^2}+b\frac{dx}{dt}+\lambda x \tag{2.41}$$

Where:-

m= mass of platform

b= damping factor

λ= spring stiffness

Assuming that the platform is initially at rest, equation (2.41) can be rearranged in terms of displacement (x) and expressed in Laplace transform notation by:-

$$X(s)=\frac{F(s)/m}{s^2+2\zeta\omega_n s+\omega_n^2} \tag{2.42}$$

Where:-

$\omega_n=\sqrt{\lambda/m}$ =natural frequency (rad/s)

$\zeta=b/2\sqrt{\lambda m}$ =critical damping factor

Combining equations (2.40) and (2.42), the output displacement for any input current can be obtained. It is common when driving inductive loads to use an input voltage (v) instead of current to avoid large voltages associated with rapidly changing input demands. The voltage/current relationship for a coil is given by:-

$$v(t)=i(t)R_c+L\frac{di(t)}{dt} \tag{2.43}$$

Again, assuming that initial conditions are zero, equation (2.43) can be rearranged in terms of current (I) and expressed in Laplace transform notation as:-

$$I(s)=\frac{V(s)}{R_c+Ls}=\frac{V(s)/L}{T+s} \tag{2.44}$$

The constant $T(=R_c/L)$ can be obtained from equation (2.37). To obtain a linear traverse of the spring platform, it is postulated that a voltage ramp be applied to the coil of the form:-

$$v(t)=K_2t \text{ or } V(s)=K_2/s^2 \tag{2.45}$$

Substituting equations (2.45),(2.44) and (2.40) into (2.42) the platform displacement is given by:-

$$X(s)=\frac{K_1K_2/Lm}{s^2(T+s)(s^2+2\zeta\omega_n s+\omega_n^2)} \tag{2.46}$$

The real time solution of equation (2.46) is given by:-

$$x(t)=A+Bt+Ce^{-Rt/L}+\frac{Ee^{-\zeta\omega_n t}}{\omega_n\sqrt{1-\zeta^2}}\sin(\omega_n\sqrt{1-\zeta^2}.t)$$

$$\cdots+De^{-\zeta\omega_n t}\cos(\omega_n\sqrt{1-\zeta^2}.t) \tag{2.47}$$

Where:-

$$A=\frac{-K_1K_2(2\zeta T+\omega_n)}{T^2\omega_n^3Lm}$$

$$B=\frac{K_1K_2}{TLm\,\omega_n^2}$$

$$C=\frac{K_1K^2}{T^3Lm\,(\omega_n^2/T+T-2\zeta\omega_n)}$$

$$D=\frac{K_1K_2(4\zeta^2\omega_n-2\zeta T-\omega_n)}{T\omega_n^3Lm\,(2\zeta\omega_n-T-\omega_n^2/T)}$$

$$E=\frac{K_1K_2(2\zeta^2T-4\zeta^3\omega_n-T+3\zeta\omega_n)}{T\omega_n^2Lm\,(\omega_n^2/T+T-2\zeta\omega_n)}$$

It can be seen from this equation that there will be transient errors from an ideal path associated with the constants C ,T ,E & D and a steady state error of magnitude A. The response $x_s(t)$ of this system to a voltage step of magnitude K_2 can be obtained by differentiating equation (2.47). The solution of this is given by:-

$$x_s(t)=A'+B'e^{-Rt/L}+C'e^{-\zeta\omega_n t}\cos(\omega_n\sqrt{1-\zeta^2}.t)$$
$$\cdots+\frac{D'}{\omega_n\sqrt{1-\zeta^2}}e^{-\zeta\omega_n t}\sin(\omega_n\sqrt{1-\zeta^2}.t) \qquad (2.48)$$

Where:-

$$A'=\frac{K_1K_2}{T\omega_n^2Lm}$$

$$B'=\frac{K_1K_2}{T^2Lm\,(2\zeta\omega_n-T-\omega_n^2/T)}$$

$$C'=\frac{K_1K_2(2\zeta\omega_n-T)}{\omega_n^2TLm\,(T+\omega_n^2/T-2\zeta\omega_n)}$$

$$D'=\frac{K_1K_2(2\zeta^2\omega_n-\zeta T-\omega_n)}{\omega_nTLm\,(T+\omega_n^2/T-2\zeta\omega_n)}$$

If for the ramp motion the coil current is used as a monitor of displacement the apparent motion ($x_m(t)$) is given by:-

$$x_m(t)=\frac{F}{\lambda}=\frac{K_1i(t)}{\lambda}=\frac{K_1K_2t}{\lambda R}-\frac{K_1K_2}{\lambda LT^2}(1-e^{-Rt/L}) \qquad (2.49)$$

The measurement error ($e_m(t)$) is then determined as the difference between apparent and actual displacement i.e;

$$e_m(t)=x(t)-x_m(t)=G+He^{-Rt/L}+De^{-\zeta\omega_n t}\cos(\omega_n\sqrt{1-\zeta^2}.t)$$
$$\cdots\frac{Ee^{-\zeta\omega_n t}}{\omega_n\sqrt{1-\zeta^2}}\sin(\omega_n\sqrt{1-\zeta^2}.t) \qquad (2.50)$$

Where:-

$$G=\frac{-2\zeta K_1K_2}{\omega_n^3TLm}$$

$$H=\frac{K_1K_2(2\zeta\omega_n-T)}{T^2\omega_n^2Lm\,(T+\omega_n^2/T-2\zeta\omega_n)}$$

In this case, the steady state error is independent of inductance although it will determine the rate at which a constant error will be obtained. This point will be discussed in the results section.

If an input current of the form $I=K_2t$ is used the first order transfer function of equation (2.44) can be ignored and equation (2.46) becomes:-

$$X(s)=\frac{K_1K_2}{ms^2(s^2+2\zeta\omega_n s+\omega_n^2)} \tag{2.51}$$

Equation (2.51) can be solved to yield the result:-

$$x(t)=A''(1-e^{-\zeta\omega_n t}\cos(\omega_n\sqrt{1-\zeta^2}.t))+B''t$$
$$\cdots+\frac{D''e^{-\zeta\omega_n t}}{\omega_n\sqrt{1-\zeta^2}}\sin(\omega_n\sqrt{1-\zeta^2}.t) \tag{2.52}$$

Where:-

$$A''=\frac{-K_1K_2 2\zeta}{\omega_n^3m}$$

$$B''=\frac{K_2K_2}{\omega_n^2m}$$

$$D''=\frac{K_1K_2(2\zeta-\omega_n)}{\omega_n^3m}$$

There is a steady state error of magnitude A'' as well as the exponentially decaying transients. The above analysis enables the prediction of overshoot displacements, settling times and steady state conditions for for both ramp and step coil demands. This is of particular interest for digital systems where motions are generated from a number of discrete steps. These predictions are of particular interest in the scanning tunnelling microscope where a large overshoot can result in contact and the possibility of damage to the probe. In all of these analyses it is clear that the error is reducible by reducing the constants K_1,K_2 and m and increasing the inductance (L) and the stiffness (λ).

Table 2.1

material	E (GPa)	K_t ($Wm^{-1}K^{-1}$)	α (K^{-1})	ρ (kgm^{-3})	C ($Jkg^{-1}K^{-1}$)	D (m^2s^{-1})	ρ/E ($kgN^{-1}m^{-1}$)	γ ($kPaK^{-1}$)
aluminium(Dural)	71	180	270×10^{-7}	2800	900	714×10^{-7}	40	
bronze	100	180	170 "	8800	360	570 "	84	
fused quartz	73	1.3	5·5	2200	840	7·0	30	
Invar	145	16	9·0	8000	500	40	55	
mild steel	210	63	150	7860	420	190	37	-280
Ni-Span-C (Elinvar)	145	16	30	8000	500	40	55	0
silicon	190	157	23	2300	700	975	12	
Zerodur	91	1.64	0·5	2530	820	8	28	

Figure 2.1: Simple rectilinear spring systems

a)The leaf type spring

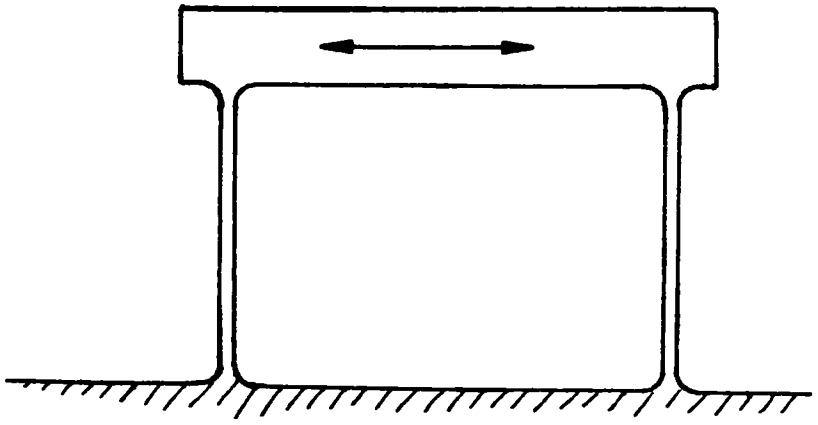

b)The notch type spring

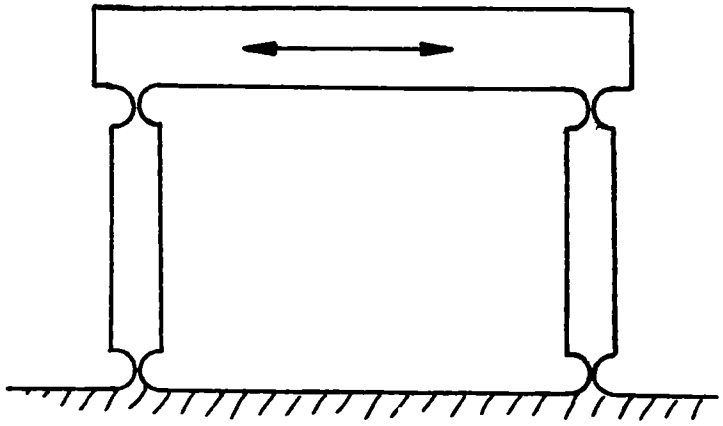

Figure 2.2:The compound rectilinear spring

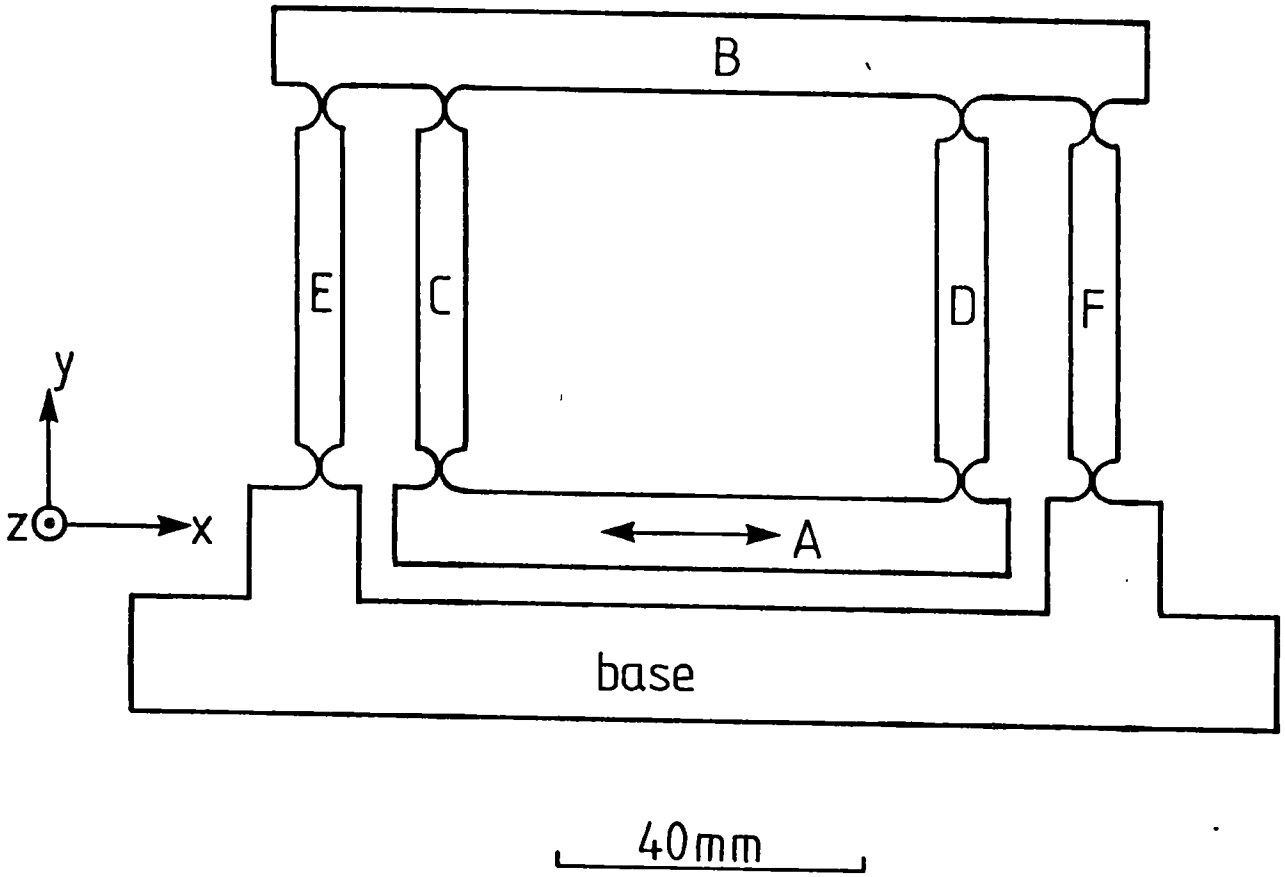

Figure 2.3

The double compound rectilinear spring

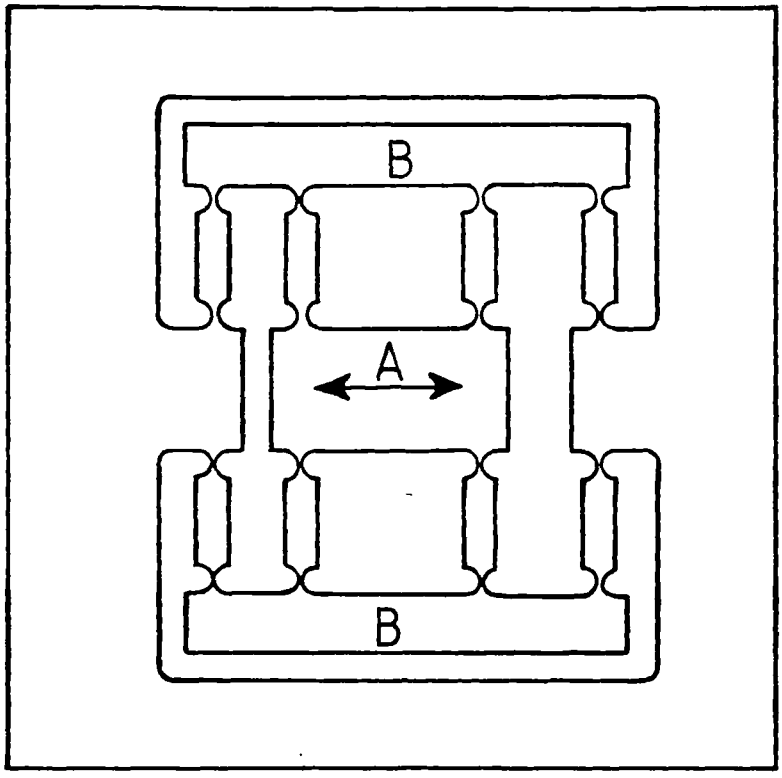

Figure 2.4:The slaved compound rectilinear spring

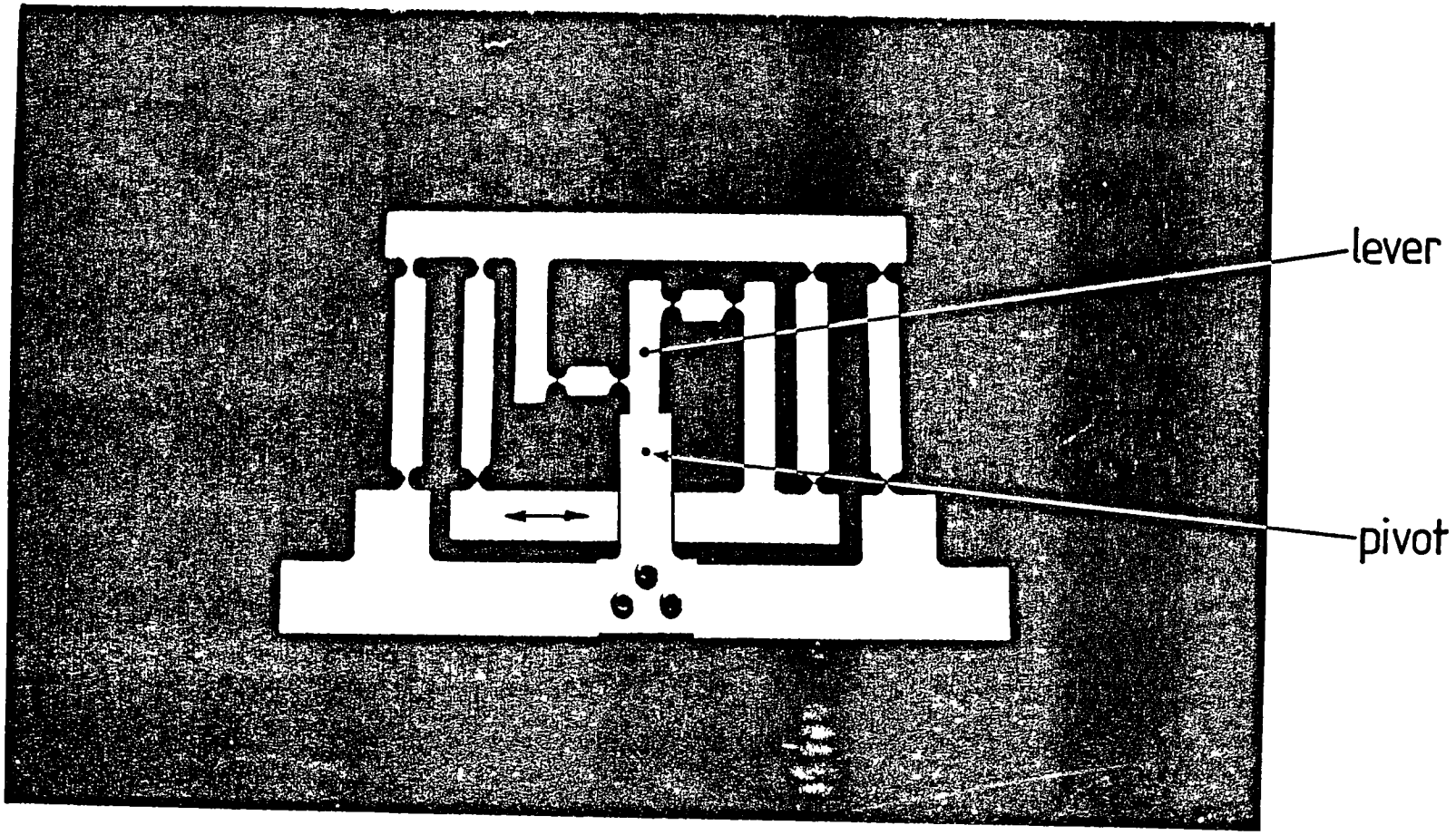

Figure 2.5:Mesh for finite element analysis of the web type hinge

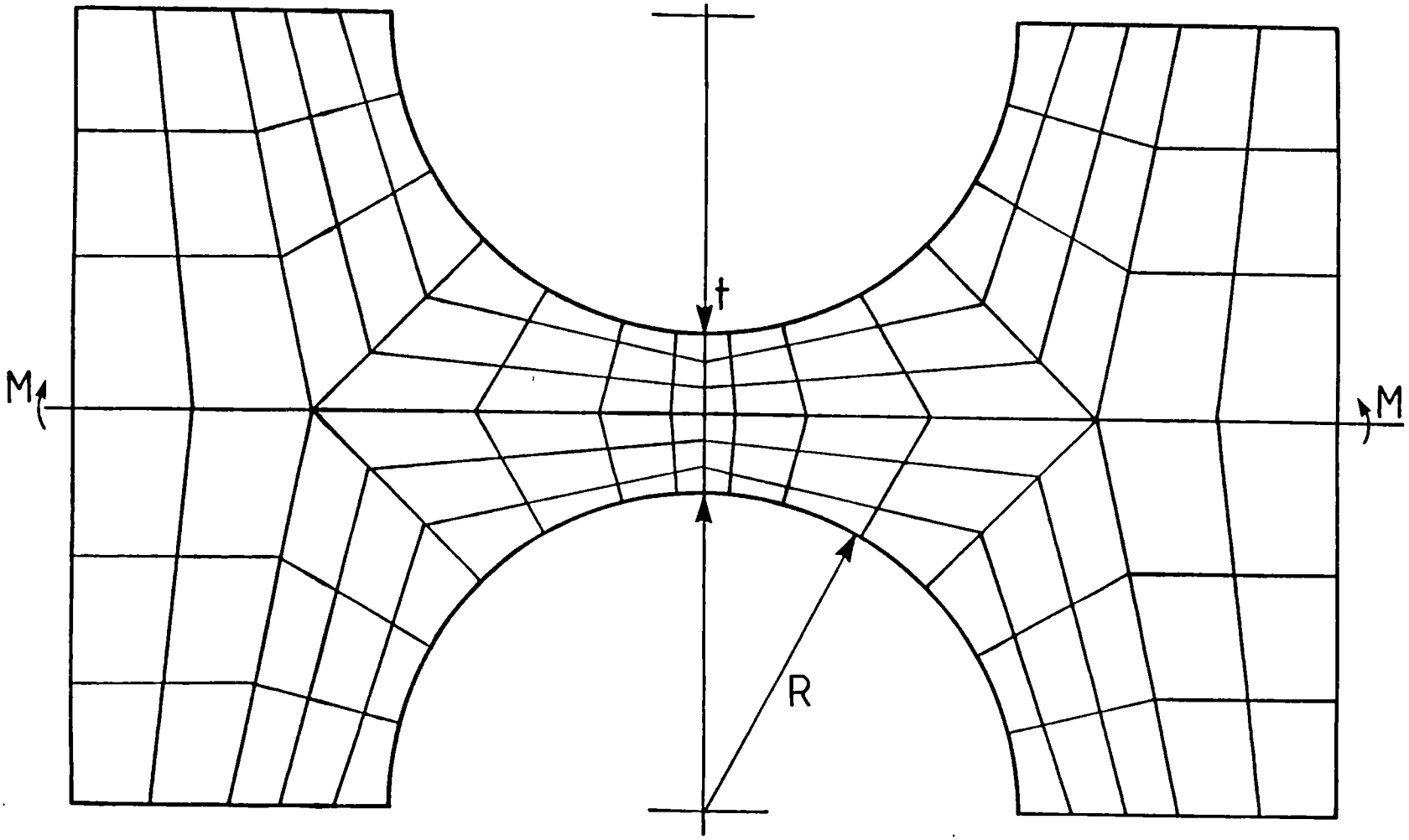

Figure 2.6:The angular constant K

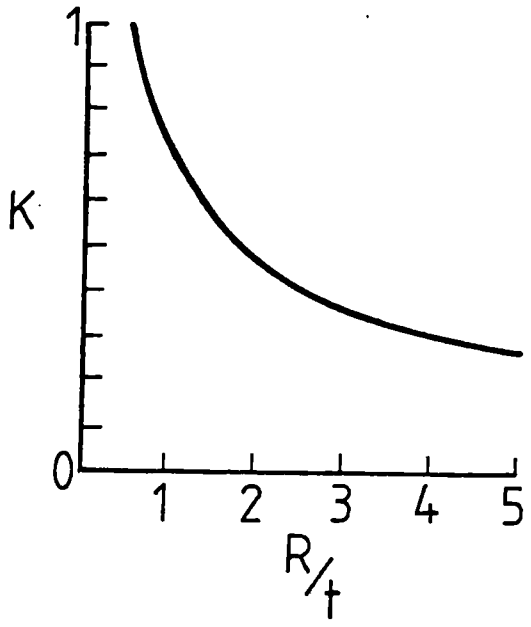

Figure 2.7

Cross section of the web hinge

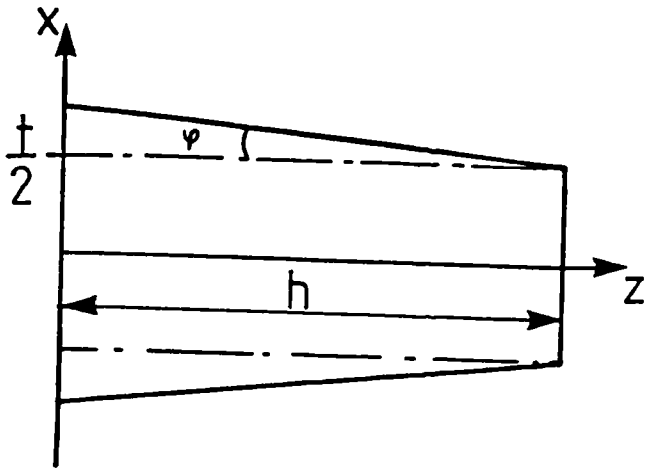

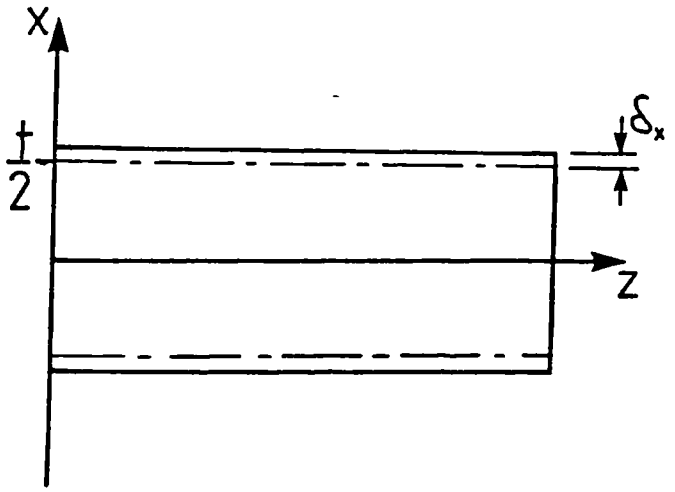

Figure 2.8

Lumped model for the compound spring

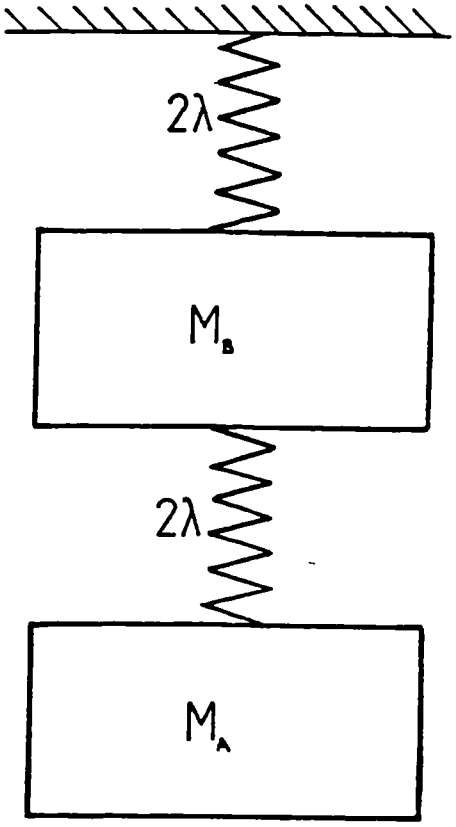

Figure 2.9: Free body diagram for the leaf spring type parallel flexure

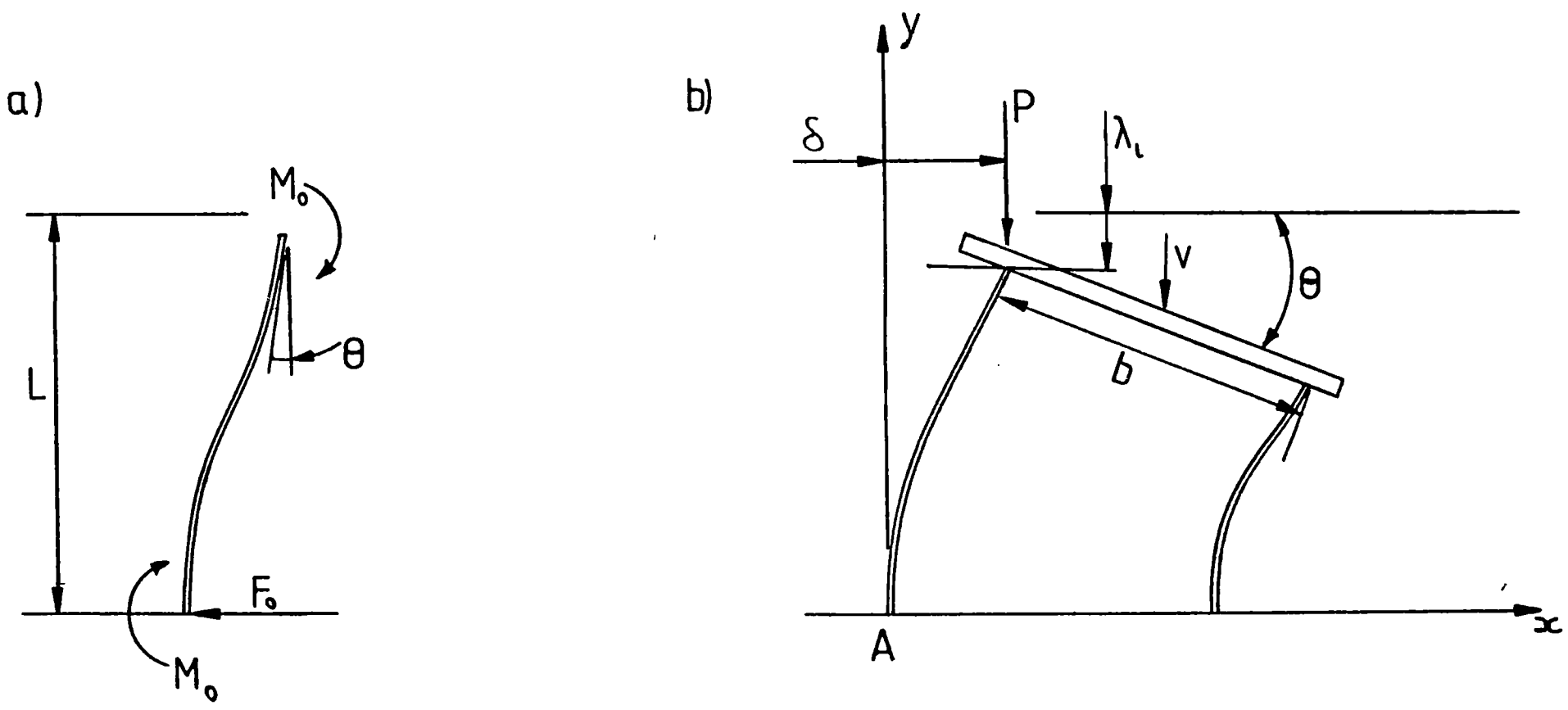

Figure 2.10:The function ϕ against α for a beam in tension

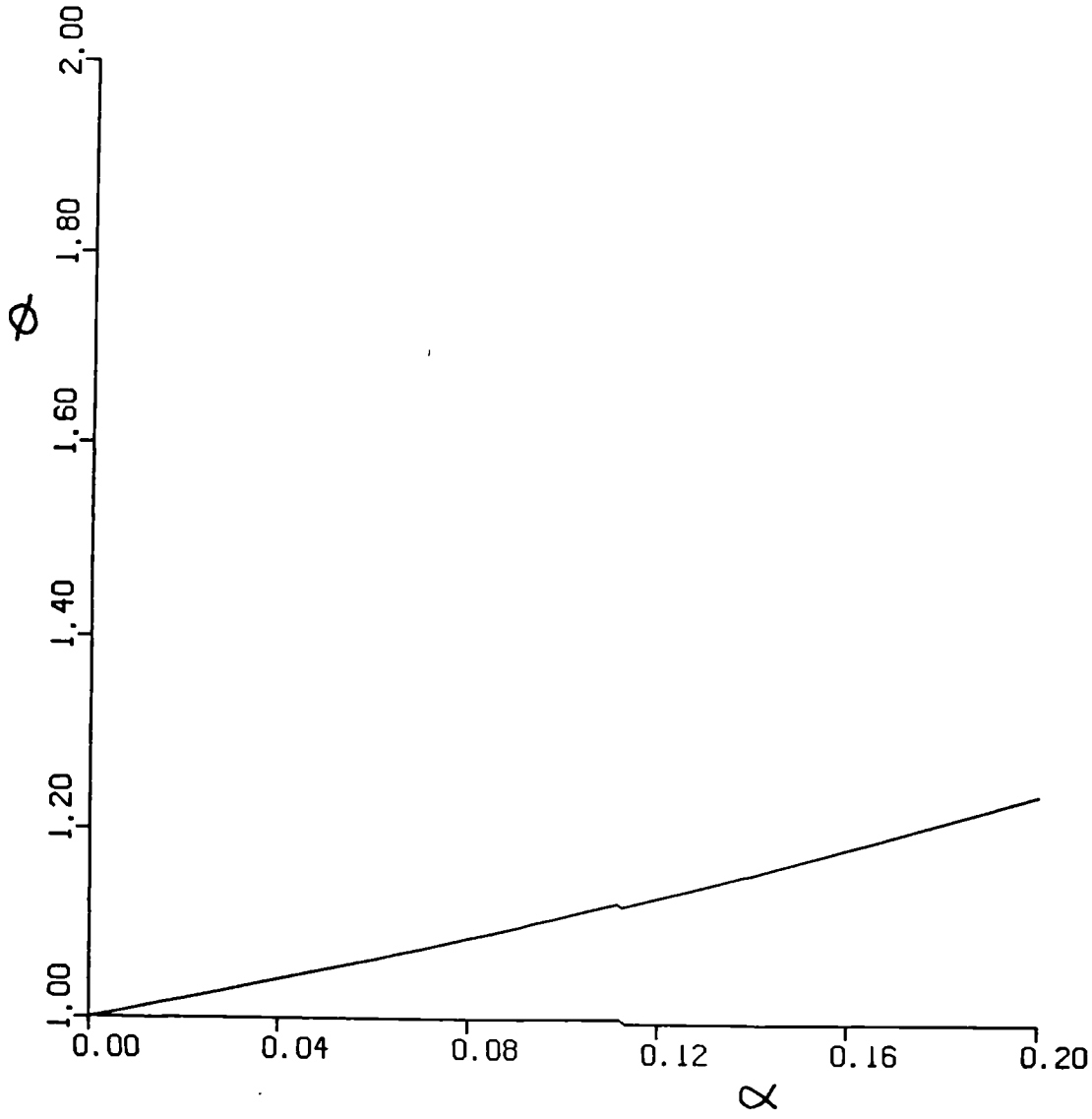

Figure 2.11:The function ψ against α for a beam in tension

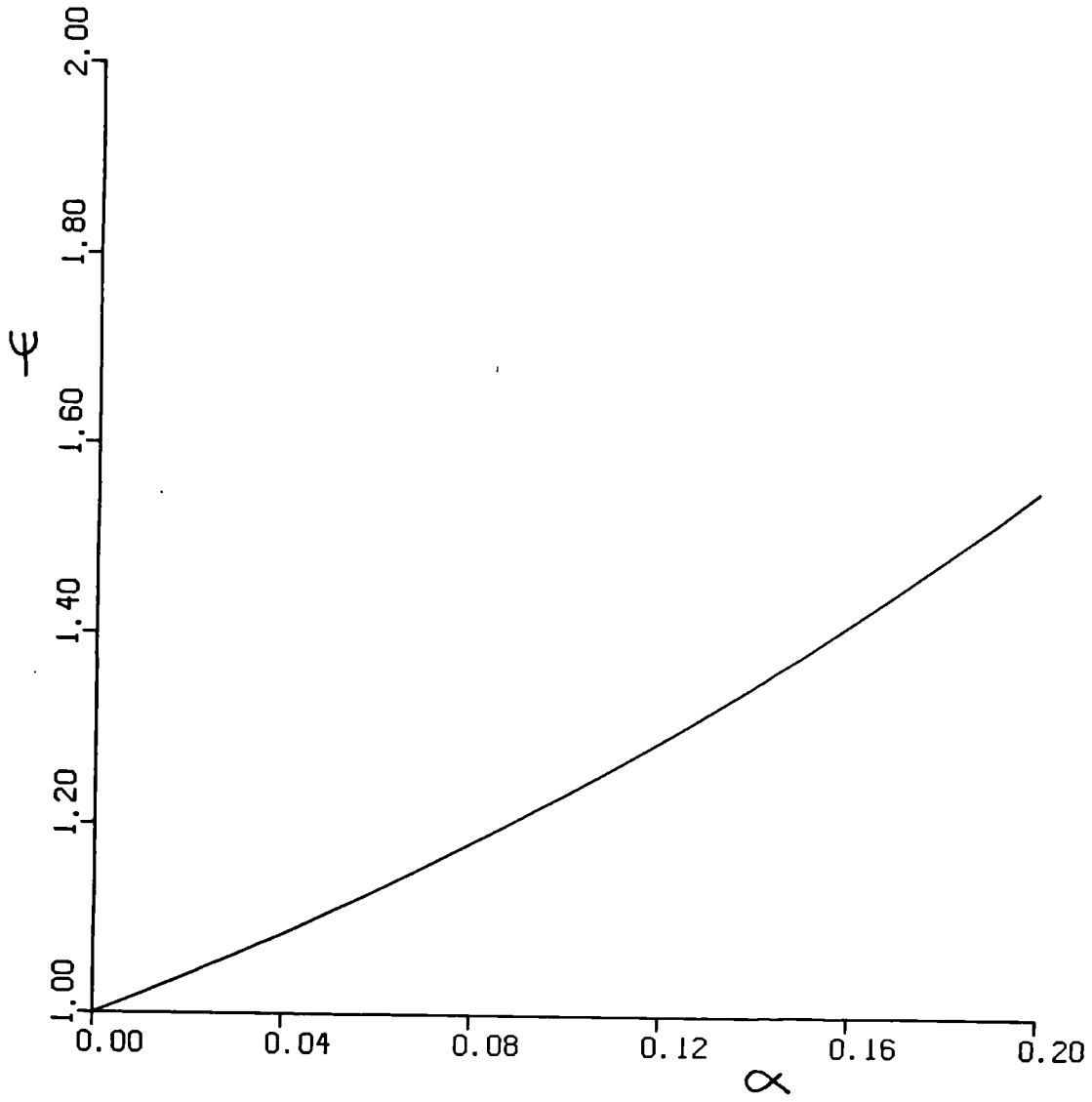

Figure 2.12:The function χ against α for a beam in tension

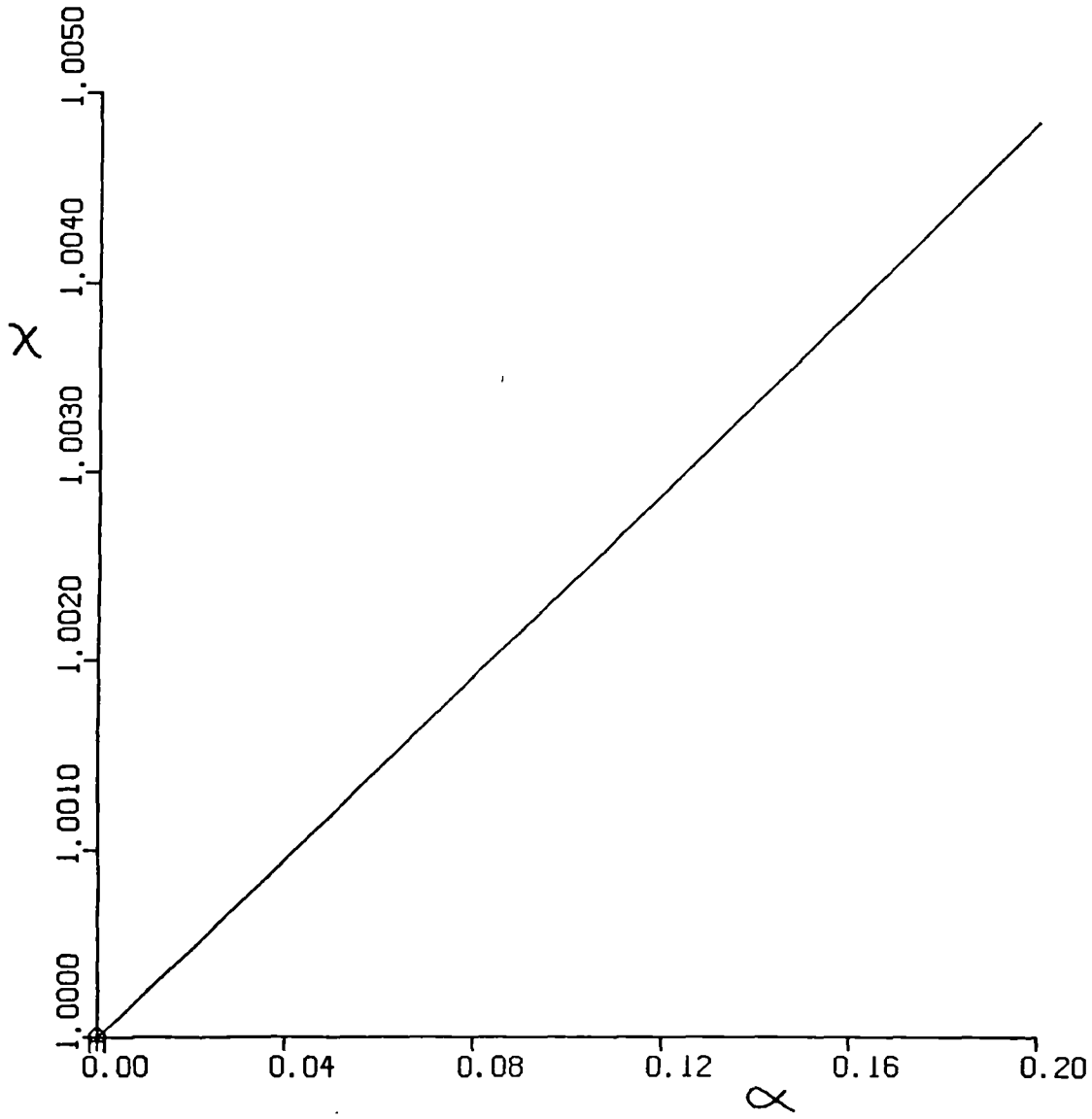

Figure 2.13:The function τ against α for a beam in tension

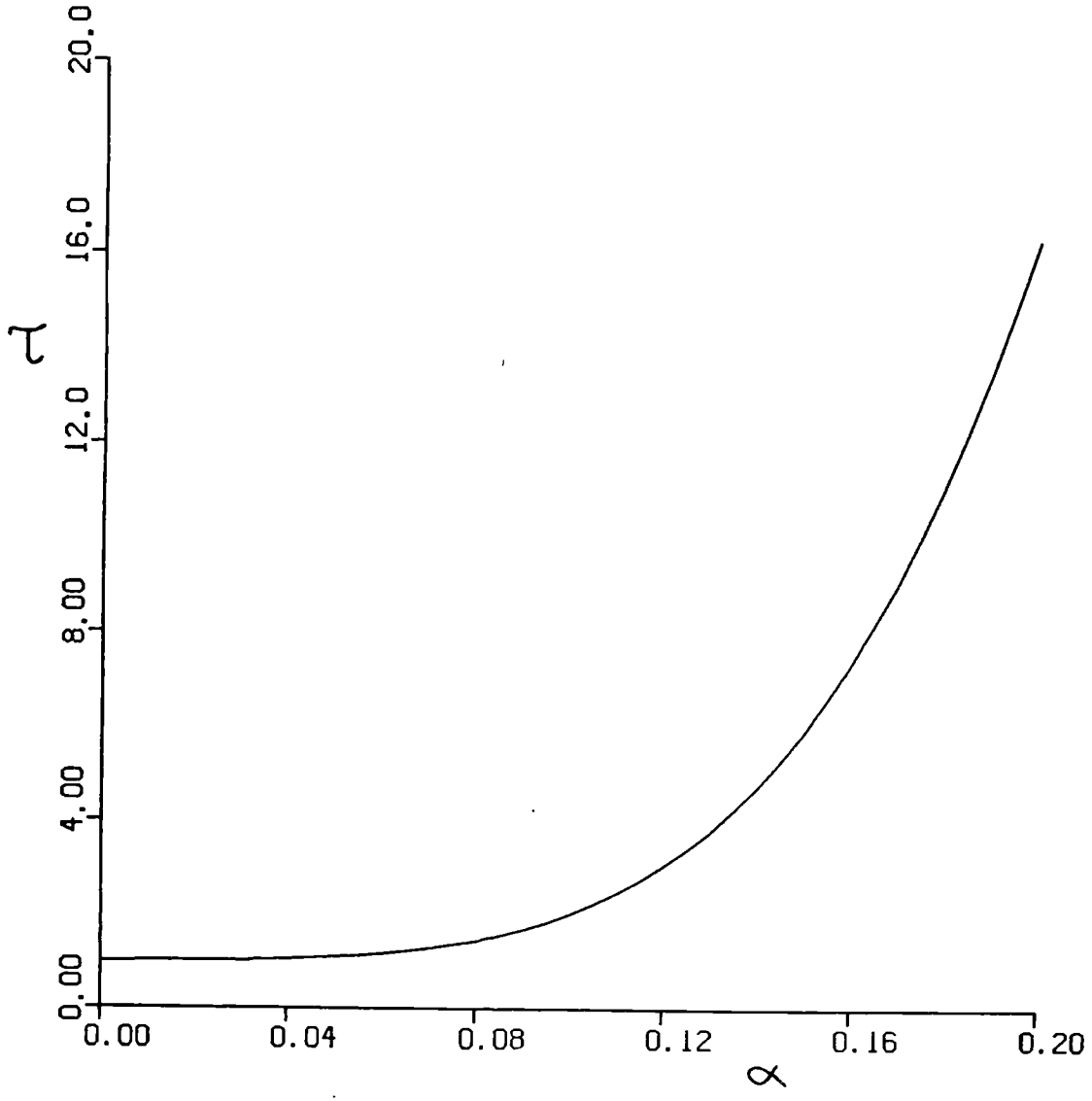

Figure 2.14:The function η against α for a beam in tension

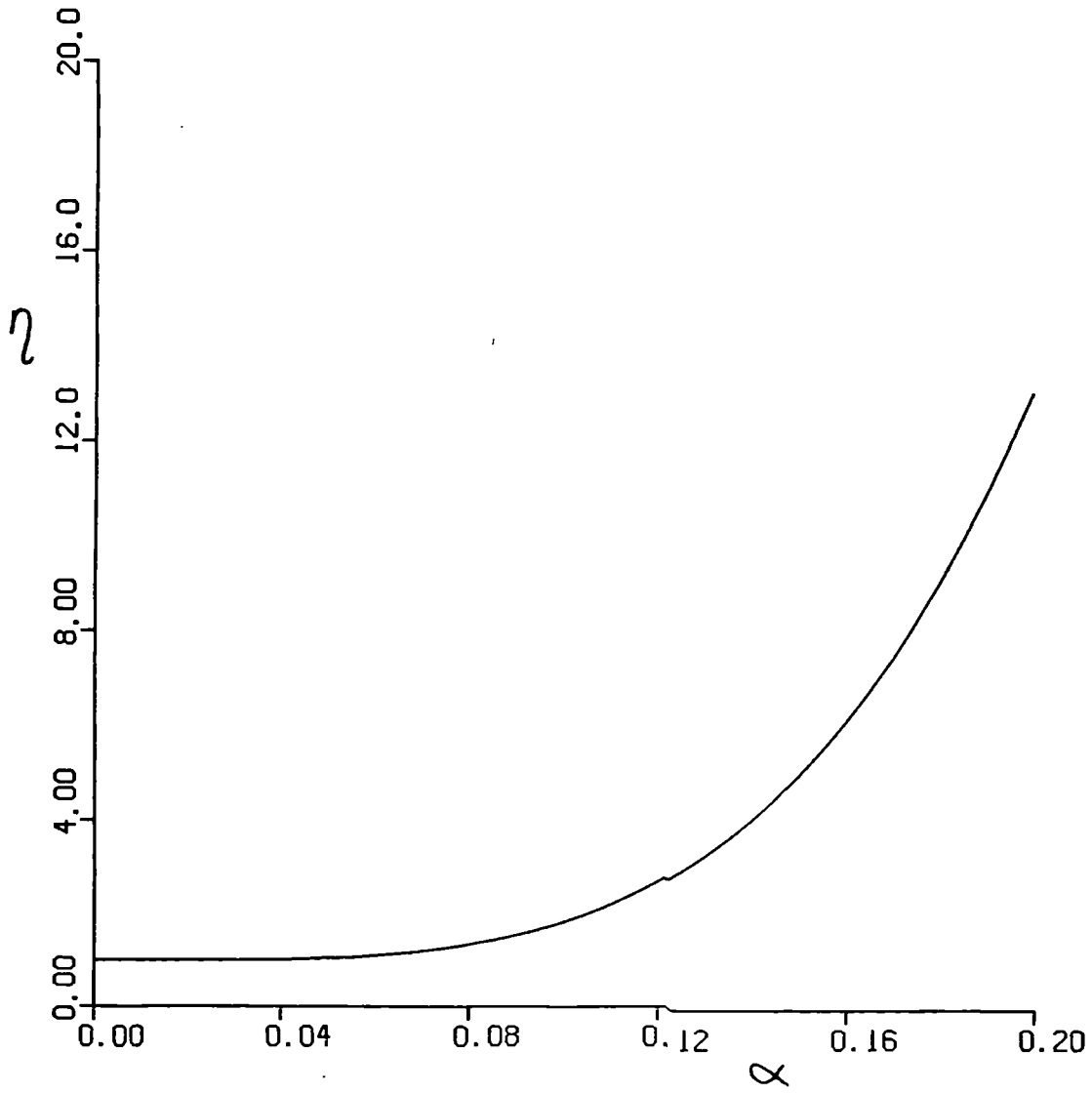

Figure 2.15:The function ϕ against α for a beam in compression

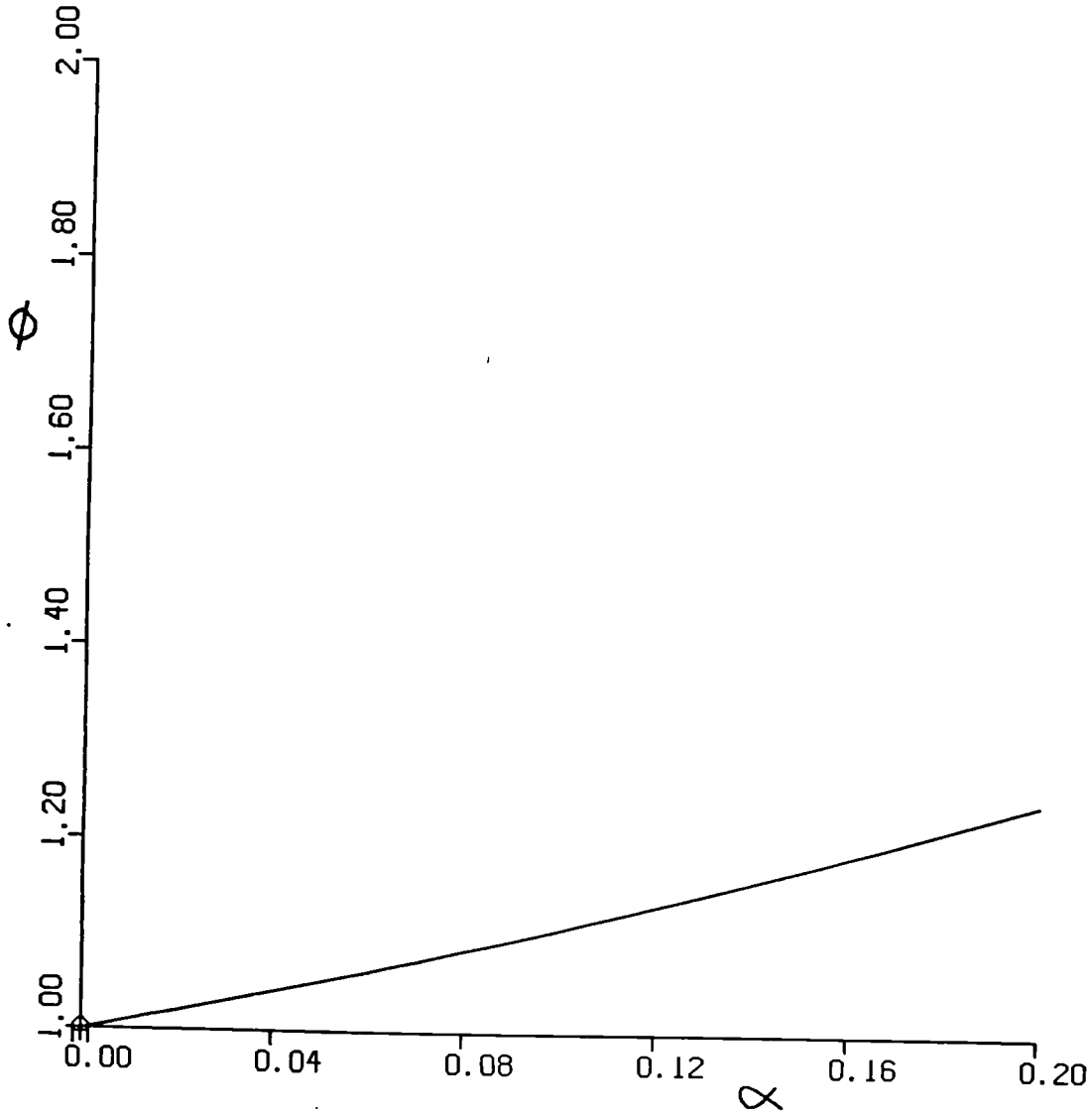

Figure 2.16: The function ψ against α for a beam in compression

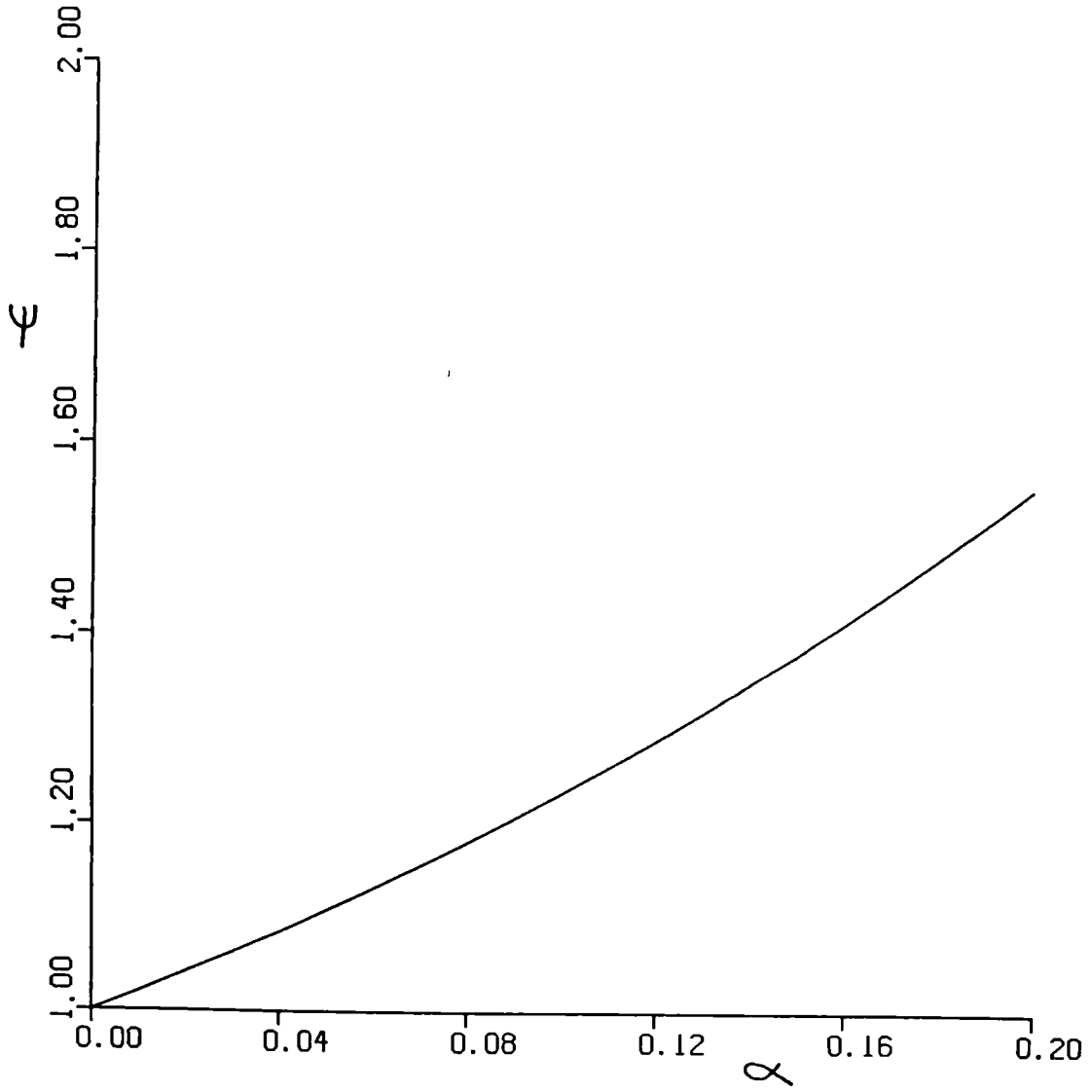

Figure 2.17:The function χ against α for a beam in compression

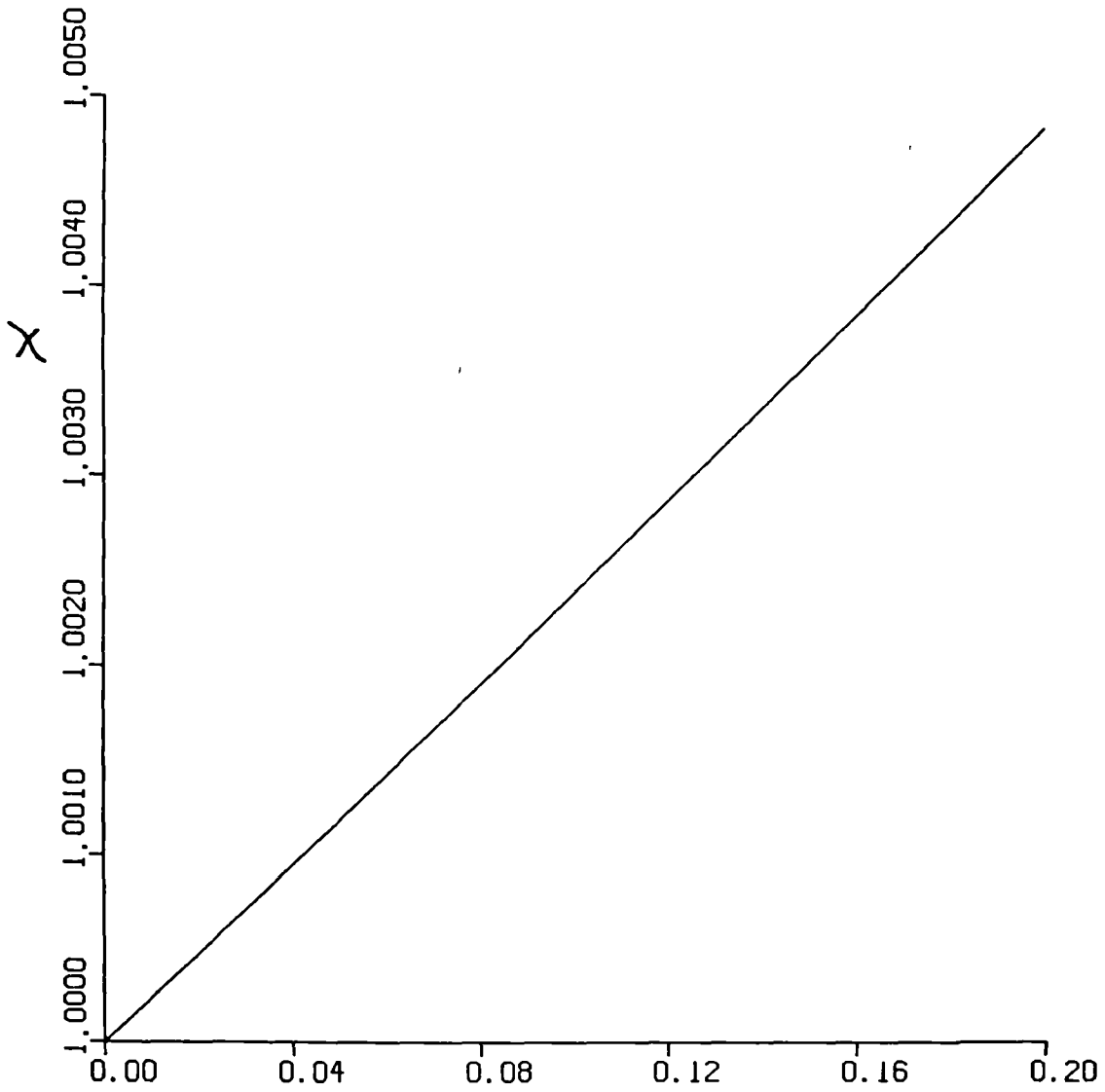

Figure 2.18:The function τ against α for a beam in compression

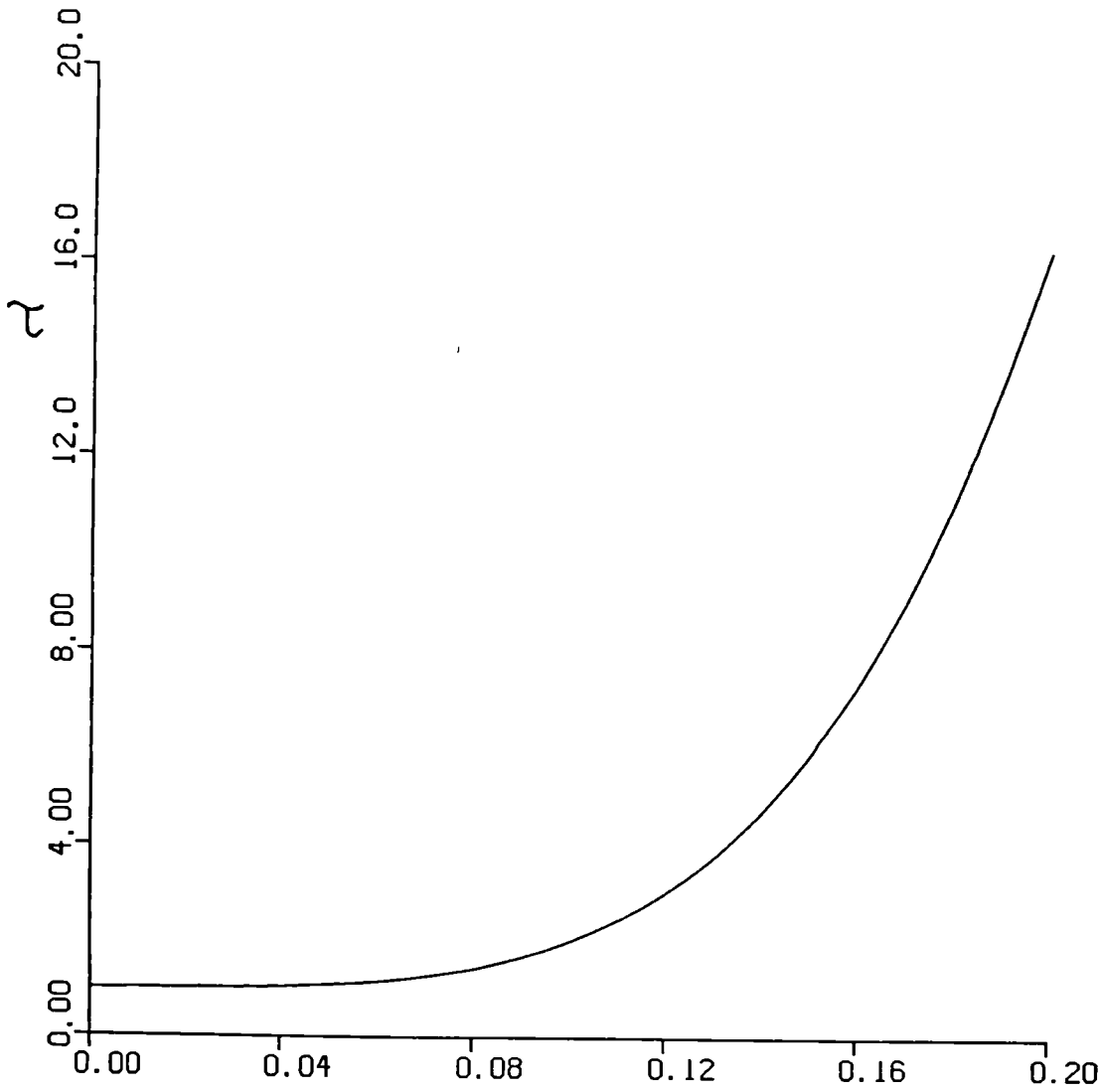

Figure 2.19: The function η against α for a beam in compression

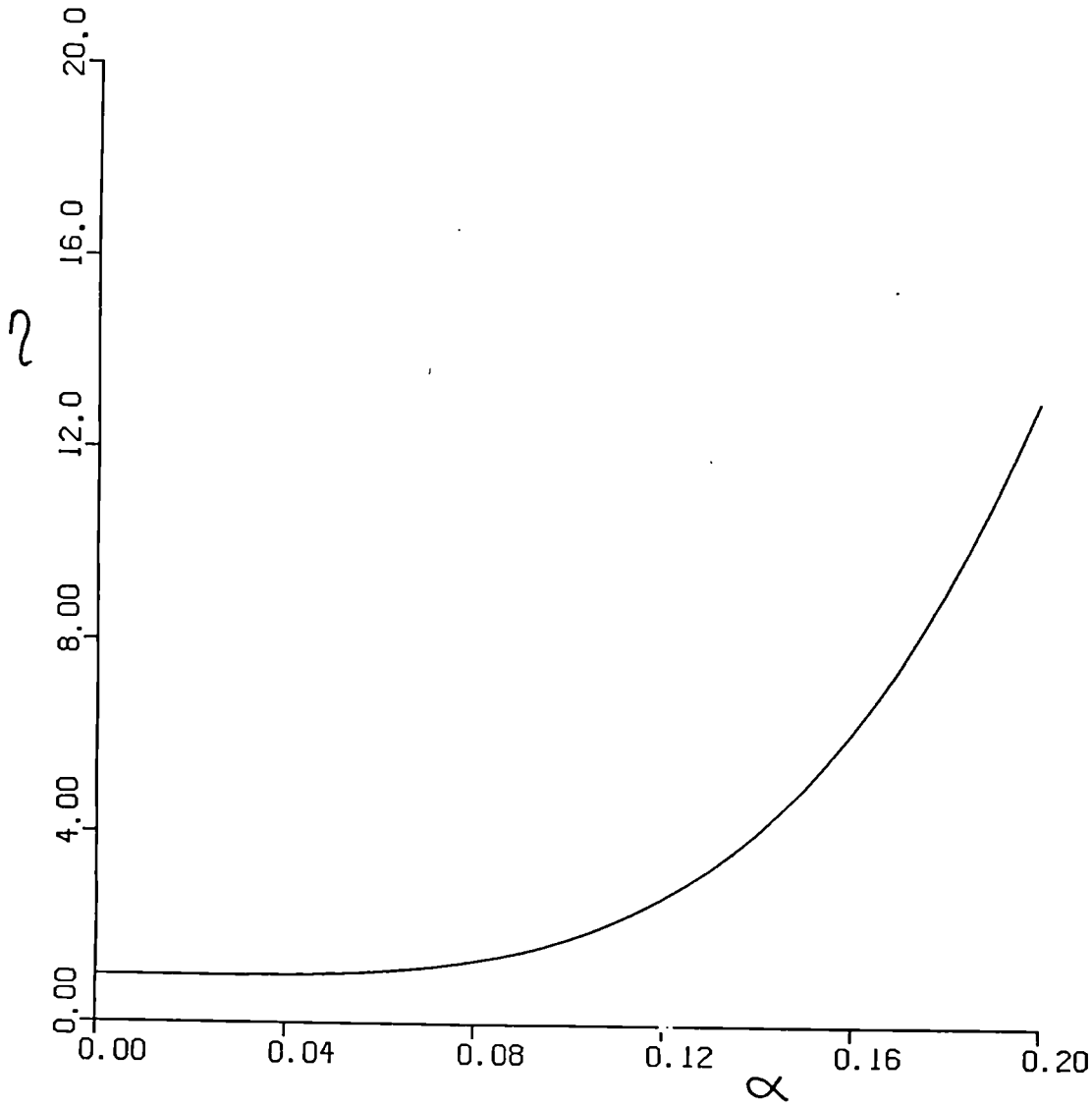

Figure 2.20: The deflected slender column

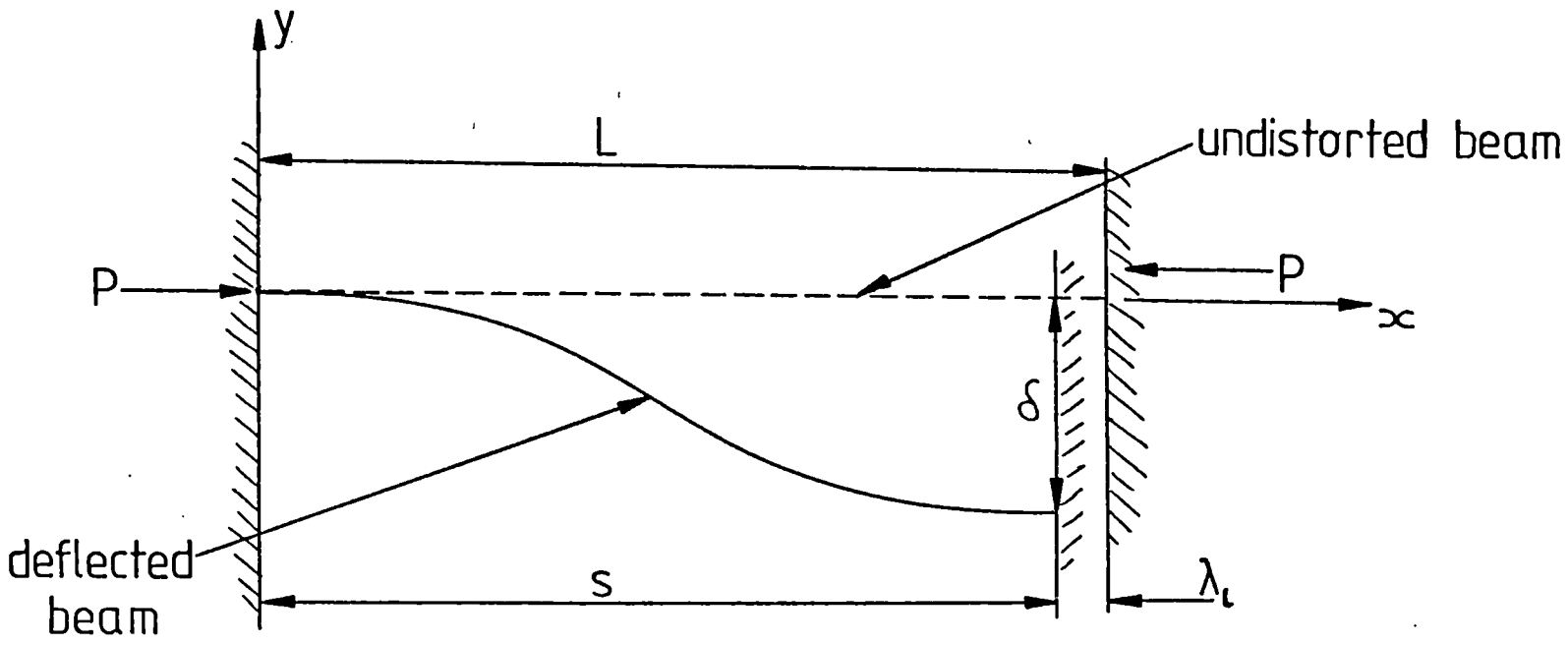

Figure 2.21

a)The linear drive

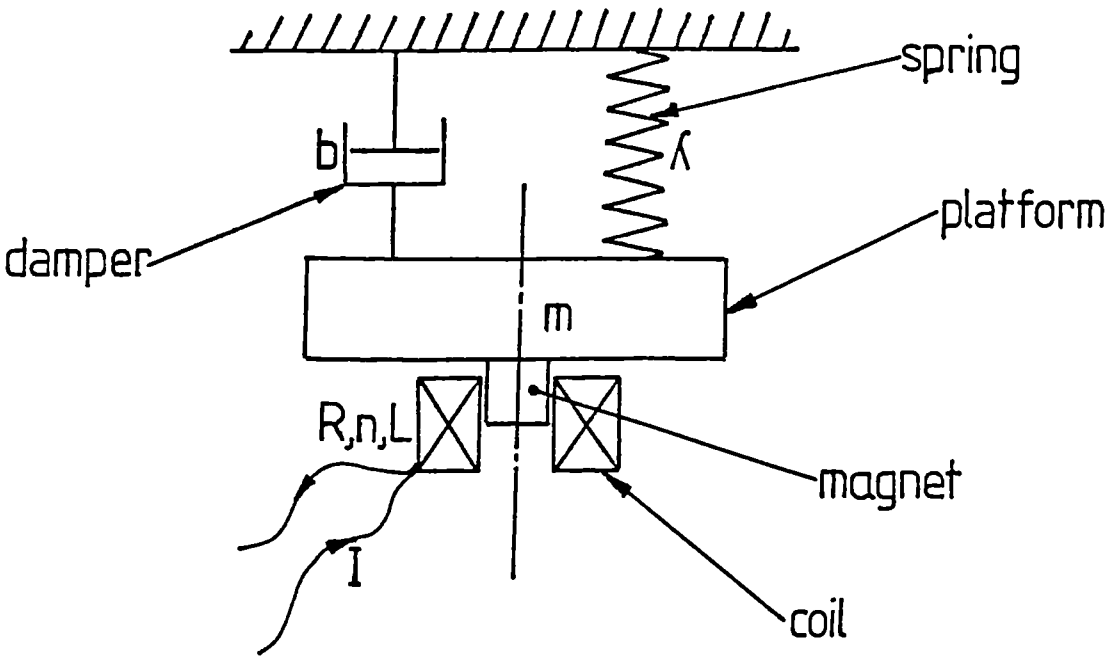

b)Coil geometry

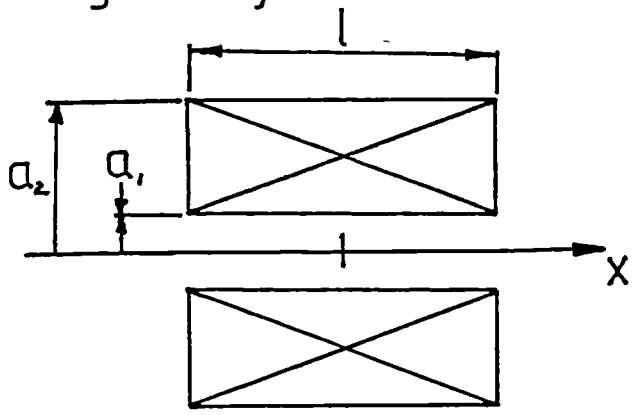

Figure 2.22: The inductance factor ϕ

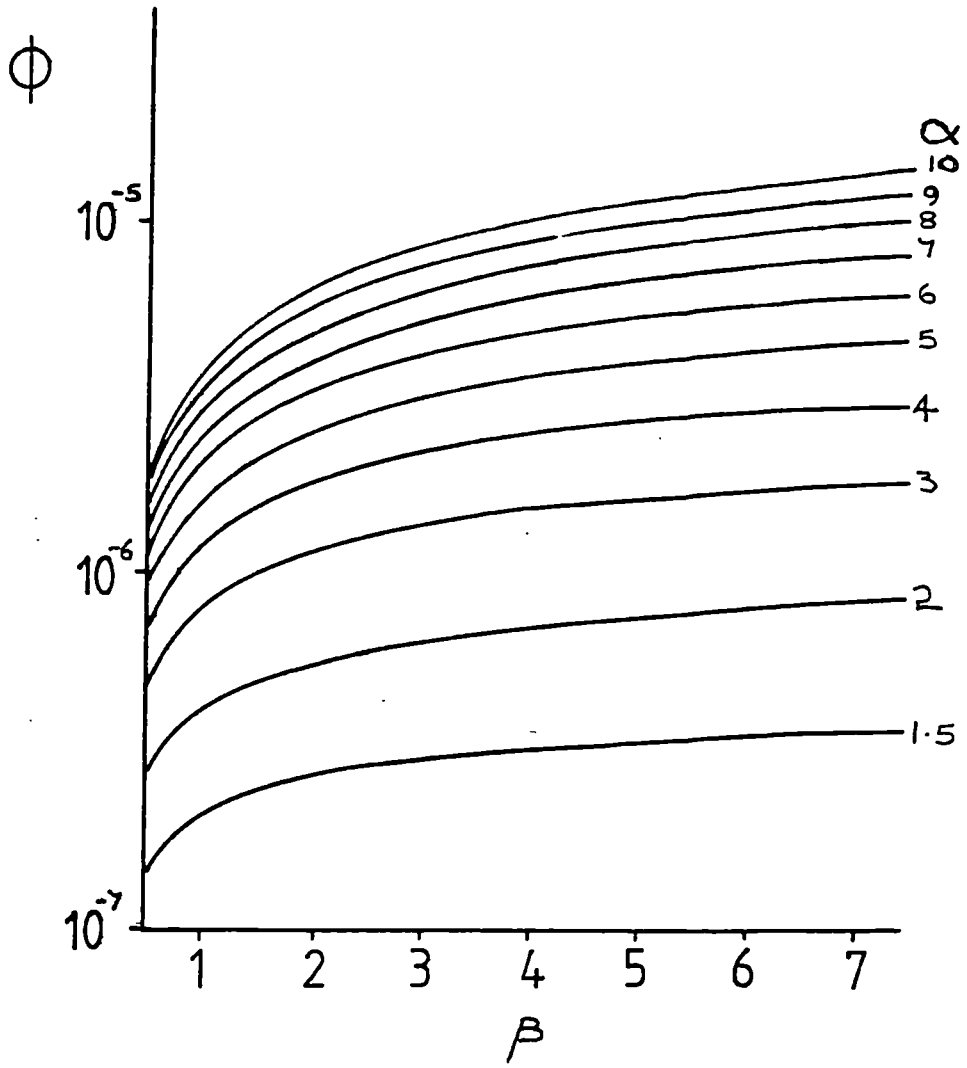

Figure 2.23a:Contours of maximum field slope against coil geometry

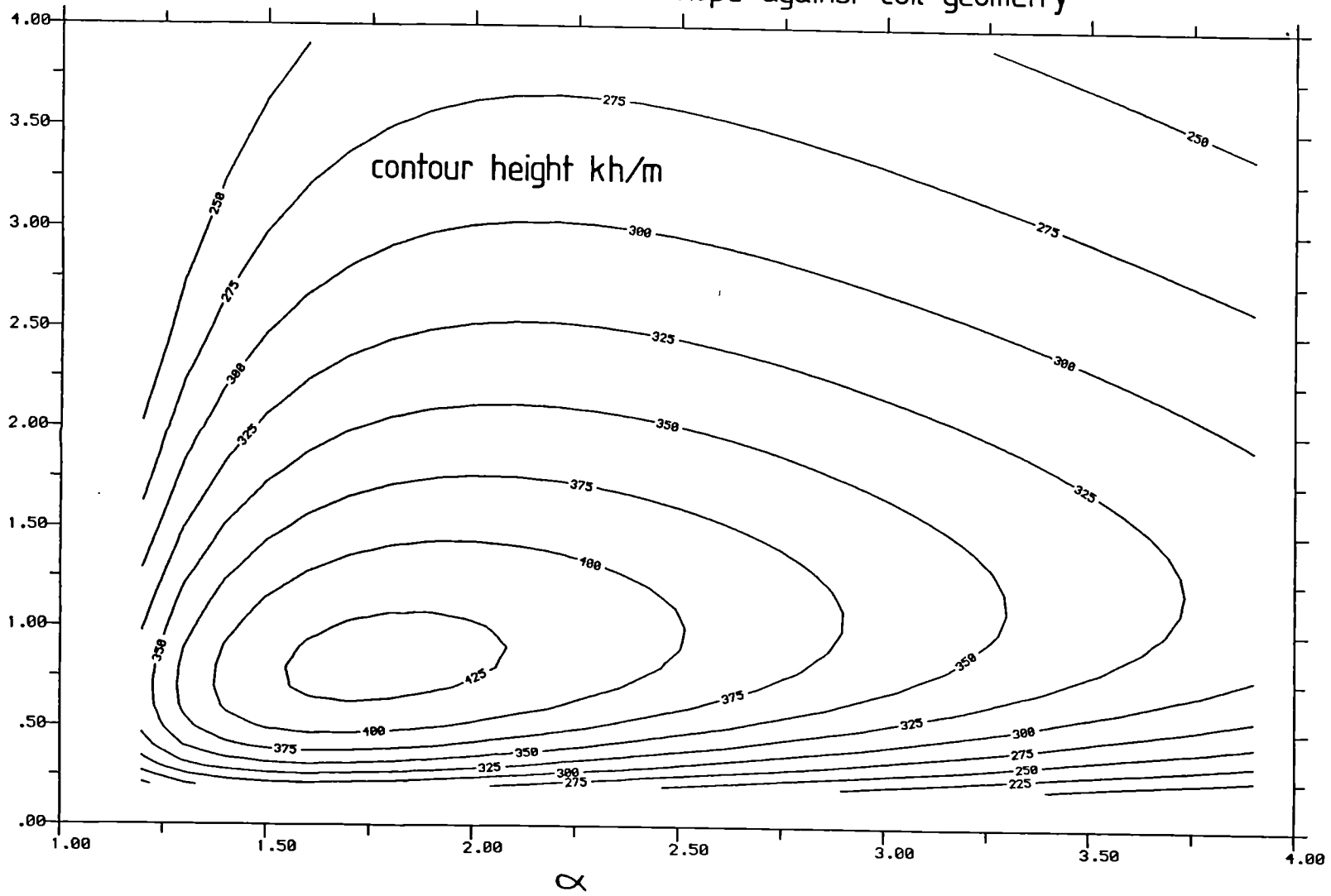

Figure 2.23b:Isometric plot

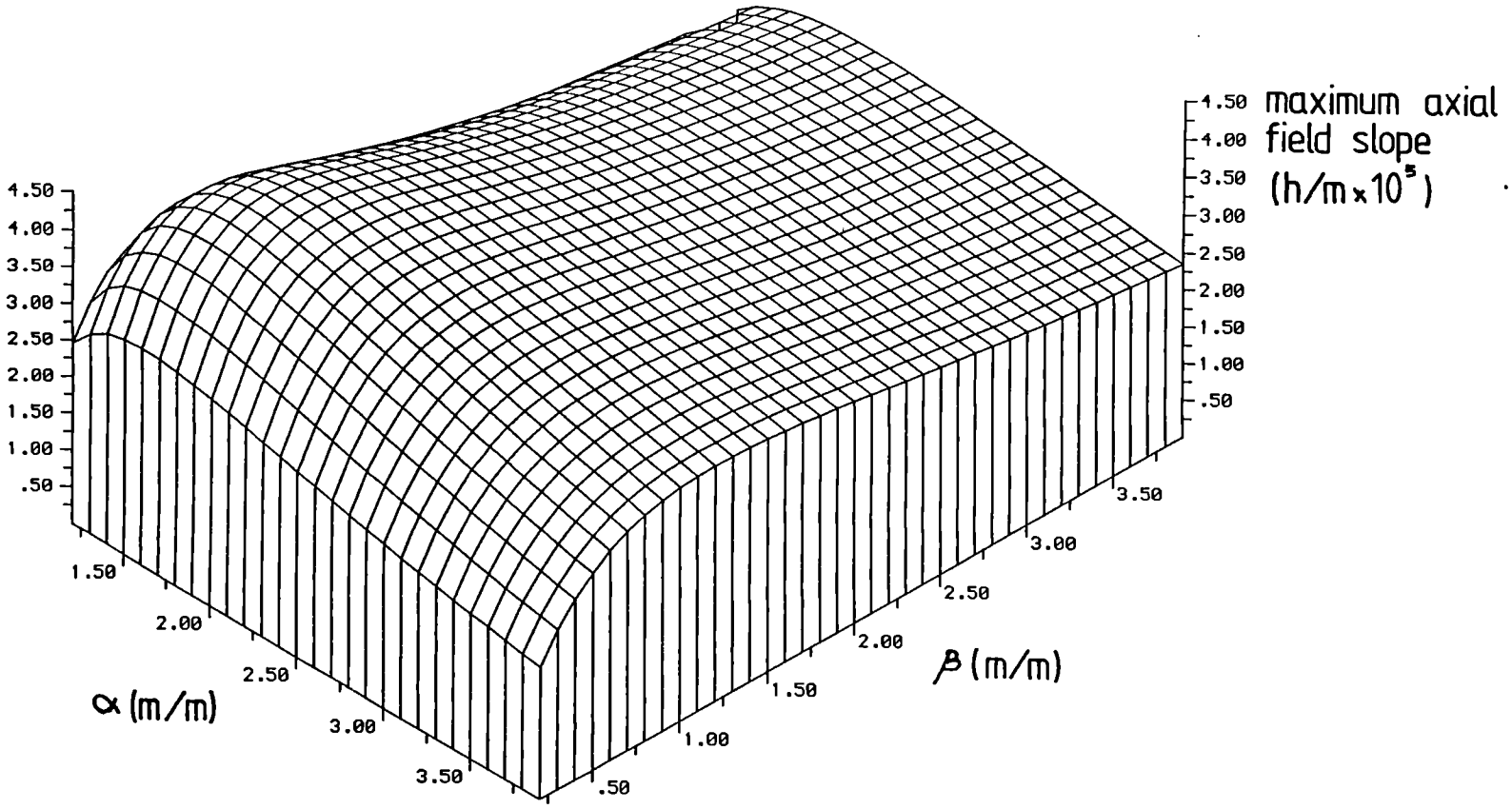

Figure 2.24:Surface area of coil corresponding to previous figure

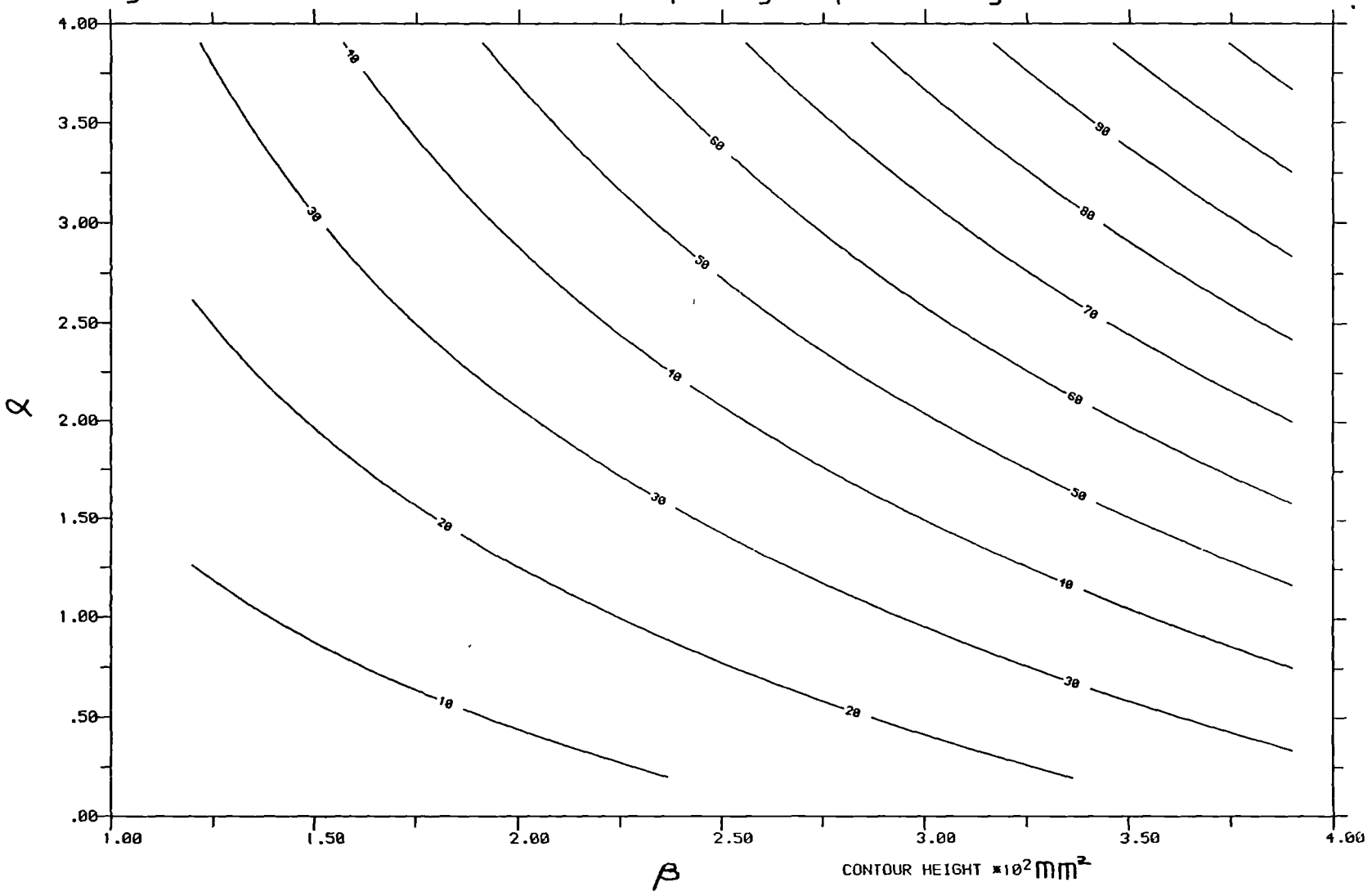

Chapter 3: The design of a slideway system for use as a precision reference motion

3.0 Introduction

It is necessary, before commencing this chapter, to define the general requirements of a reference motion and the specifications in terms of dimensional stability and accuracy.

A reference motion is initially required for use in fine instrument mechanisms. It had been proposed that motions of up to 50mm length with a reproducibility of approximately 1 nm (10^{-9}m) be obtained. The traverse length (λ) is a measure of the limit of useful diagnostics obtainable for any particular surface (i.e. roughness and waviness). For smaller values of λ ($\approx$1mm) linear motions with accuracies of the order 0.1nm vertical/50nm lateral or less are required. It is considered that a low friction mechanism will reduce the magnitude of the forces applied to the system. For long range reference motions elastic design techniques are impractical and may be readily discarded. The remaining techniques to be considered are:-

1. Dry, plain rubbing bearing.
2. Elastohydrodynamic bearings.
3. Hydrostatic bearings (externally pressurised).

These will be briefly discussed in reverse order (order of considered merit) to give some reasons for the final design philosophy that was adopted.

3.1 Hydrostatic bearing systems

These systems consist of highly conforming surfaces with a small separation maintained by applying pressurised fluid between the two. The fluid used to separate the two surfaces can be

either pneumatic or hydraulic. The latter fluid will involve large bulk and cost, viscous drag, viscosity index, fluid recycling, vibration transmitted by the pumping equipment (even with accumulators in the system) and thermal expansion effects of the fluid. Because of these difficulties this system is not considered further. A pneumatic system has the distinct advantage of a very low friction coefficient with a relatively high stiffness. The other distinct advantage is a contamination free fluid medium that is readily available in a majority of modern workshops. Pneumatic hydrostatic bearings have been used in stylus instrumentation to record surface variations with an accuracy of around 100 nm over 25 mm traverse distances, (Sayles et al, 1976).

Although the stiffness of an air bearing is high it is exceedingly non-linear and will tend to exhibit low damping factors, (Gross, 1962). For light loads the stiffness varies approximately as a square law with the film thickness. This power law will increase with load (decreasing film thickness). The consequences of increasing load on the system may give rise to distortions that may not be insignificant on a nanometer scale. This stiffness may involve fairly high transmission of external vibrations as well as the problems associated with internally generated noise (turbulence, Helmholtz resonance, unsteady air supply). With the necessity of very thin films, high conformity and complexity of geometry(i.e contouring fluid exit regions), the choice of materials is economically restricted to ductile (usually metallic) varieties. This may introduce problems of thermal stability due to the relatively high expansion coefficient. Both of the above systems are not vacuum compatible.

3.2 Dry And Lubricated Bearing Materials

In this category of bearing system there are three distinct sub divisions:-

1. A low modulus, dry, low μ bearing material (PTFE, ultra-high molecular weight polyethylene (UHMWPE), etc.). This will be sliding on a very smooth glass or glass ceramic surface. It might be advantageous to incorporate a lubricant/solvent to reduce the shear strength of the contacting interface (i.e. polyacetal and silicone oil (20cs)).
2. Elastohydrodynamic lubrication.

3. An all solid interface with the surfaces coated with MoS_2 or graphite.

Again, these three categories will be discussed in reverse order. This is the considered order of merit for this particular application.

3.2.1 The Friction Of Lamellar Solids (see Bowden and Tabor)

The two main dry bearing materials that appear suitable for this application are graphite or molybdenum disulphide (MoS_2).

a) Graphite

As with MoS_2, the low coefficient of friction (μ=0.1) is attributed to sliding of one laminae over another. To facilitate this mechanism it is essential that the laminae assume a preferred orientation and it has been determined that the angular orientation of the basal planes corresponds to the angle of friction.

b) Molybdenum Disulphide

This material will also exhibit a low friction coefficient ($\mu \approx 0.1$) and will retain this value under vacuum conditions (unlike graphite). The coefficient of friction will increase if contaminants are introduced ($\mu \approx 0.22$ for "moist" nitrogen) and thus optimum results can only be obtained upon maintenance of a "clean" low humidity environment. This lubricant is applied either as a solid/resin mix glued to the surface or applied in powder form with a selvyt cloth. There have also been recent investigations by N.C.T. (National Centre for Tribology) into sputtered MoS_2 coatings. In powder or solid form there is a need for a certain amount of keying into the parent surface. If the counterface is a highly polished flat then any keying by the extreme hardness in the basal plane (6.5 Mohs) will invariably result in a certain degree of damage. Additionally, this hard thin layer may not average out any slideway imperfections and might possibly enhance any periodicities present on both carriage and slideway (these periodicities are very difficult to eliminate, Lindsey, 1973) with highly polished surfaces. For the above reasons it was considered that this lubrication system only be investigated upon inadequate performance of other mechanisms.

3.2.2 Elastohydrodynamic Lubrication

Elastohydrodynamic lubrication is the hydrodynamic lubrication that is maintained through a combination of viscous effects and elastic deformation of the interface in sliding contact. The elastic distortion will occur with extreme pressure conditions or if low elastic modulus materials are used. Calculation of the hydrodynamic forces at very low velocities are rather unreliable and have not been specifically modeled to this situation. However, it is important to note that this form of lubrication can persist at velocities orders (1 - 2) of magnitude below that predicted by hydrodynamic theory, Hooke, 1972, Archard, 1975, Cudworth, 1976. This point must be taken into account when interpreting frictional data of lubricated polymer systems.

3.2.3 Dry friction and/or boundary lubrication

The frictional properties of a low modulus, polymeric materials appear very favourable. The wear rates are very low and the friction coefficient will remain smooth under fairly constant conditions. To investigate the applicability of this system it will be necessary to review the relevant theory of polymer bearing systems, and in particular, the frictional and wear properties of polytetrafluoroethylene (PTFE).

3.2.3.1 Dry Friction

If P represents the average pressure that a material can withstand and W is the total load on that material, then for a purely plastic material the static area of contact (A) is be given by, (Pascoe, 1956, Bowers, 1953):-

$$A=\frac{W}{P} \tag{3.1}$$

By analogy with the friction of metallic contacts, the force (F) required to shear the junctions formed over this contact area is:-

$$F=As=\frac{Ws}{P} \tag{3.2}$$

where s is the shear strength of the junction that has formed.

The above equation assumes that the materials are clean and that the shear strength and flow

pressure remain constant (this is not exactly true for polymers, Adams, 1963). It has been established that the coefficient of friction is more likely to follow a power law of the form:-

$$\mu \alpha W^{-\beta} (0<\beta<0.33) \tag{3.3}$$

This implies an intermediate behaviour showing both plastic (β=0) and elastic (β=0.33) contact characteristics. For a spherical pad rubbing against a flat surface (or equivalently, two crossed cylinders) Pascoe, 1956, found equation (3.3) to be more accurately expressed for nylon by the equation :-

$$\mu = K W^{-0.26} D^{0.52} \tag{3.4}$$

where D is the diameter of sphere.

This equation is independent of temperature, time, velocity, composition and bulk geometry. All of these factors will effect the value of the friction coefficient that is obtained in any one experiment.

Junction growth, as found in metallic friction, is not considered to occur with polymer friction. This is demonstrated by the correlation between the increase in contact area due to creep and the value of the static friction coefficient.

Primary creep will also effect the friction coefficient as this is synonymous with hysteresis and the elastic recovery rate. This effect implies an increase in contact area with a decrease in speed. The strain due to creep is a function of time and the total displacement will depend on the length (or thickness) of the material under load. Tabor, 1957/58, postulates that elastic recovery effects will not be significant if values for the velocity of sliding are of the order of a hundredth of the width of apparent contact. In the experiments to be discussed in the following sections, the width of contact was observed through the polished glass counterface to be approximately 1-2 mm. With velocities less than 0.01 mm/s all experiments were well within this criterion. Thus it is reasonable to expect that, after running-in, the kinetic friction will approach static friction as velocities tend to zero (no junction growth theory), (see Tanaka, 1984).

The materials under main consideration were ultra-high molecular weight polyethylene (UHMWPE) and polytetrafluoroethylene (PTFE). These have previously been shown to have a

very low friction at dry bearing interfaces. The immediate problem was to attach thin films of UHMPE (<50 μm) to a sliding surface. It was found that thin films could be shaved from a solid using an ordinary wood plane but attempts to adhere these to a surface were, at best, unreliable. The use of thicker slabs of this material was considered inappropriate because of creep and thermal expansion effects ($\alpha_t \approx 10^{-4}/k$). PTFE however can be obtained in the form of Glacier DU bearing material. This is a composite of PTFE and lead that has been keyed into a porous brass subsurface. This is then bonded to mild steel. The thickness of protruding PTFE is of the order 20 μm for older material and less for modern varieties. The expansion coefficient of this combination is roughly $15 \times 10^{-6}/k$

3.2.3.2 Polymer Lubrication

Lubrication of polymers can be explained by various mechanisms including; adsorption, plasticisation or hydrodynamic/elastohydrodynamic effects, (Rubenstein, 1961, Fort, 1962, Cohen, 1966). The force required to initiate the sliding of a lubricated interface is given by the general equation:-

$$F = A(\alpha s_0 + (1-\alpha)s_L) \tag{3.5}$$

Where:-

s_0=Shear strength of the polymer

s_L=Shear strength of the lubricant

α=Fraction of the true area at which polymer/counterface contact occurs.

The bracketed term in equation (3.5) is known as the effected shear strength (S_E). If P is the hardness pressure or flow pressure of the polymer under an applied load (W), the coefficient of friction is given by equations (3.1 & 3.5):-

$$\mu = \frac{\alpha s_0}{P} + \frac{(1-\alpha)s_L}{P} \tag{3.6}$$

From this equation it can be seen that the friction coefficient can be reduced by a reduction in α, s_0, s_L and/or increasing P.

One mechanism by which α may be reduced is that of adsorption. Rubenstein, 1961, postulates that the separation between two surfaces will increase with adsorption of a lubricant into the polymer or counterface surface. This separation appears to increase with increasing chain length of molecule in a homologous series (chain length is roughly proportional to viscosity). This effect, however, will diminish as the chain length increases to a size where adsorption becomes improbable. Lubricants can reduce the performance of a polymer bearing by weakening inter-chain forces which may lead to an increase in the wear rate. This wear mechanism is thought to be either high transfer and removal or surface fatigue related to solubility/wettability (for a complete discussion see Lancaster, 1984, Atkins, 1984, Ellison, 1954, Senior, 1971). Adsorption may also enhance hydrodynamic/elastohydrodynamic lift-off, (Tabor, 1957, Fort, 1962). This effect can appear to be dominant under the right conditions at velocities of around 0.1mm/s. This implies that unless very low velocities have been used, interpretation of results from polymer lubrication investigations must be approached with caution. These parameters may additionally depend upon the surface finish of the counterface.

The adsorption or absorption of a lubricant into the surface of a polymer may bring about the onset of plasticisation. The immediate effect of this will be a reduction in s_0 without a significant change in P. The interface will then consist of a thin, soft intermediate layer between the polymer/counterface surface. The effect of adsorption have been observed during dwell tests to give a low friction coefficient ($\approx$0.1) that can persist for an extended duration without the need for any added lubricant. The most attractive polymer/lubricant combination at high velocity ($\approx$0.5m/s) is that of polyacetal with either silicone oil (20cs) or Di-2-ethylhexyl sebacate. The friction reduces from 0.3 to 0.1 and a reduction in the wear rate two orders of magnitude can be obtained, (Lancaster, 1984). For these reasons it was considered important to investigate the frictional properties of a polyacetal(POM) silicone fluid combination at very low velocities (i.e. boundary lubrication). The bearing pads used in this investigation were Glacier DX. This material is of a similar composition to the Glacier DU only there is a POM surface layer $\approx$200μm thick.

Plasticisation may have a deleterious effect if diffusion into the bulk of the polymer causes a marked reduction of P. This can lead to an increase in the friction or even catastrophic failure.

3.3 The sliding mechanism of dry PTFE

It has been well established that the sliding interface of PTFE consists of a thin (10-40nm), highly oriented film. The orientation of this film, which occurs over a large temperature and velocity range, can be clearly seen in electron diffraction patterns to be parallel to the direction of sliding (see Mackinson, 1964, Steijn, 1968, O'Leary, 1967, Pooley, 1972). The wear of this interface will possibly be a result of deposition and removal or a gradual transfer of layers similar in nature to the spreading of a deck of playing cards. These mechanisms imply a fairly low wear rate. However, Makinson & Tabor observered that there is a transition between high and low friction as either sliding velocity is increased or the temperature is reduced. This transition is attributed to:-

> "...the viscous force to shear the film increases until a stage is reached where the shear force exceeds the strength of the boundaries between crystals or grains"

This implies a rapid increase in wear above a critical speed or temperature. This sudden increase in wear has been observed by Tanaka, 1973, although the friction coefficient exhibited a more continuous change. This mechanism requires a strong adhesion to the parent surface, a view disputed by Steijn, 1968, who attributes film formation and fibril structure purely to low shear stress and inter granular strength.

Another wear mechanism is that of delamination of surface films due to frictional heating. This results in interface stresses between the film and polymer caused by anisotropic thermal expansion mismatch and dilatation due to the α–β phase transformation at 292-296 kelvin, (Hornbogen, 1983, Lhymn, 1986). This mechanism is explained by the drawing of a thin film into thin bands or fibrils in which the local temperature is increased due to frictional heating. The result of this temperature increase is a bubble formation perpendicular to the direction of sliding. Decohesion of these bubbles will then form wear debris. This may account for the sudden increase in wear rate at high sliding speeds. Irradiation of PTFE (50Mrad) can reduce the phase transition temperature by a few degrees and improve the wear rate, (McLaren and Tabor, 1965). It is unclear as to whether this is caused by suppression of bubble formation or the bulk alteration of

material properties, mainly an increase in hardness. However this will cause a marked alteration of the polymers frictional characteristics considered undesirable for this particular application.

It is considered that the wear of PTFE at low sliding velocities will be comparable with other polymer systems (10^{-8} cm/cm). This wear rate was monitored at velocities greater than $1mm/s$ (load=1kg) and thus may not be relevant to this investigation, (Tanaka, 1973). The predicted wear for a full traverse is of the order $0.5nm$ which is within the design specification. However, if the wear process is linear, the errors induced will be reduced considerably. The friction coefficient will also be low.

3.4 Experimentation

3.4.1 Apparatus

The procedure for measurement of frictional properties of the aforementioned polymeric materials is shown in figure 3.1. The sliding mechanism consists of five polymeric pads (5 d.o.f. kinematic constraint) attached to a carriageway. This carriage could then be slid along the optical glass prismatic slideway with velocities ranging from 0.01-0.0005 mm/s. The mass of the carriage (plus specimen) was 1400 gms. The carriage is driven by a non-rotating micrometer with a ball trapped between two flats (WC anvil and slip gauge) to reduce drive "influence". The force required to push the carriage could be monitored using the four gauge, temperature compensated strain gauge bridge. To ascertain the viability of the polymer/glass slideway as a precision reference motion, a supersmooth superflat ULE silica specimen was placed directly onto the carriage and surface fluctuations were monitored using a "Talystep" stylus transducer. The leveling stage was required to obtain parallelism to less than 0.1 sec of arc. This mechanism, as well as the slideway configuration are explained more fully in chapter 6. The central two thirds of the specimen are flat to approximately 10nm with variations less than 0.1nm (i.e. $R_a < 0.1$nm). The outputs from the strain-gauge bridge and "Talystep" were simultaneously monitored by a Hewlett-Packard 9836 computer via an 98640A ADC. Instrument noise and thermal drift are shown in figure 3.2. The results of these experiments could then be either displayed or printed. This system is a modification of the "Nanosurf", Lindsey, 1985.

3.4.2 Procedure

The strain gauge bridge was switched on for approximately twelve hours to allow the temperature to stabilise. The force characteristics were then calibrated using calibrated masses. The five polymeric pads measured approximately 4mm × 4mm square. These were ultrasonically cleaned in carbon tetrachloride and glued to the carriage using a two part epoxy adhesive. To obtain a high degree of averaging the pads were initially used flat. This will result in a high conformity with the interface. The pads were glued in-situ to ensure this conformity. The angular discrepancy between the carriage and slideway was measured using a Hilger and Watts Clinometer and errors could not be detected to within 1 min of arc.

Three different experiments were performed:-

1. The friction of POM dry and lubricated under high conformity conditions. The silicone oil was applied by rubbing the pads with a saturated cotton wool bud and allowing this to "soak" for 24 hours. The excess oil was then removed with a "kimwipe". The experimental results shown in all figures are a representative sample of a total of approximately 100 experiments.
2. The dry friction of PTFE under high conformity conditions.
3. The dry friction of ≈ 30cm diameter spherical PTFE pads. The pads were prepared by pressing 5mm diameter blanks into a roughly spherical shape using a 7.5cm rad punch against polypropylene. These were then shaped using a "glass file". Between each experiment the interface surfaces were cleaned using carbon tetrachloride.

3.5 Results

3.5.1 The friction of dry and lubricated Polyacetal

From the graphs of figures 3.3-3.6 it can be seen that the friction coefficient of a polymer/silicone/glass interface is consistently of the order 0.3 with a slightly higher static friction coefficient of 0.33. The "ramp up" to the maximum friction is due to the compliance of the drive/carriage interface. Over a velocity range 20:1 the frictional characteristics of this system

have remained relatively constant. The smoothness of friction is reflected by the output of the "Talystep". This shows a disturbance of around 15-20nm which settles down to a smooth motion after approx 20μm of traverse. This characteristic is independent of traverse speed.

This friction coefficient is considerably higher than that obtained at increased speeds (v=500mm/s, μ=0.1). The same experiment was repeated using a dry acetal slider. This, surprisingly, exhibited a reduced friction coefficient (μ=0.2) and stick slip was very slight (see figure 3.7). The initial disturbance to this system was greatly reduced and perturbations of the order 5-10nm were generally recorded over the complete velocity range. The temperature of all experiments was maintained within the range 293-293.5 kelvin.

3.5.2 The friction of PTFE under high conformity conditions

This system has a very high friction coefficient ($\mu_k \approx 0.3$)
with a static coefficient approaching 0.5. From the graphs of figures 3.8 and 3.9 it can clearly be seen that for these high frictional forces there is a marked correlation between friction and the uniformity of the precision motion.

3.5.3 The dry friction of ≈30cm diameter PTFE spherical pads

The graphs of figure 3.10 (a & b) show the running-in characteristics of the 30 cm spherical pads. The initial peek is usually attributed to the initial orientation of the interfacial film. The second peek is an anomaly. Figure 3.10b shows the start up and continuous friction of a "run-in" system. The friction coefficient for this system is 0.1. After further running in (1m traverse) the precision reference motion characteristics were measured (figure 3.11). This shows that start up perturbations were of the order 3 nm and this performance could be obtained over the complete range of velocities. The system has been recalibrated and checked after a three day period to verify these results.

3.6 Discussion

The boundary lubrication of a polyacetal/silicone system appears to be very ineffectual at these very low sliding velocities (if not detrimental). If, as was mentioned, there is a

hydrodynamic/elastohydrodynamic contribution then the film thickness will be directly proportional to velocity. In this case there must be a certain cut-off point at which the lubrication is completely squeezed out leaving a "dry" contact. This squeezed out oil will also contribute to the friction coefficient by retention in the pockets introducing viscous shear forces. The slightly higher friction in the lubricated condition may be explained by the mechanism of plasticisation. This plasticisation may result in reducing the flow pressure and thus increasing the contact area. Although perturbations with the POM/ silicone are relatively small the system is rather unpredictable and has a disturbing stick-slip characteristic. The effect on the carriage, as monitored by the "Talystep", is caused by the center of inertia of the carriage being offset to the center of friction and the line of action of the micrometer drive. The later designs incorporate a balancing system for the carriage. Other problems with a POM system is the fact that very thin films are difficult to obtain and this makes it correspondingly difficult to avoid the stick-slip phenomena (assuming this to be a consequence of creep). A thick film may also be a major contribution to thermal instabilities ($\alpha_t \approx 3\times10^{-5}/k$).

The relevance of high conformity is unknown but various experiments have shown that friction does tend to increase with reductions in load, surface finish and velocity. All of these parameters may be significant in the experiments with highly conforming surfaces and may explain why the ultimate in friction coefficients was obtained.

To try and overcome these problems the PTFE pads were made to a spherical shape. This was to increase the load on the polymeric material at the expense of averaging over macroscopic distances. Additionally, to reduce the effects of creep, the PTFE was thinned down to the brass subsurface using a spherical glass "file". The drawing of the thin film over the brass spherulites could be observed under a microscope as a dulling of the brass after a short traverse. In this instance the coefficient of friction dropped to a value of 0.1 after an initially high value ($\approx$0.2) (figure 3.10). This suggests that an orientated film was initially formed by a drawing process. Stick-slip, although present after long rest periods (12 hours), was very small and virtually undetectable for shorter creep periods. The disturbing influence of the initial start up was minimal (<5nm) and microscopic averaging appears adequate (figure 3.11 and 3.12). This averaging is a

consequence of the thin interfacial film (possibly 10nm) against a surface of roughness of approximately 1nm R_a.

Figure 3.1: Schematic view of friction measurement apparatus

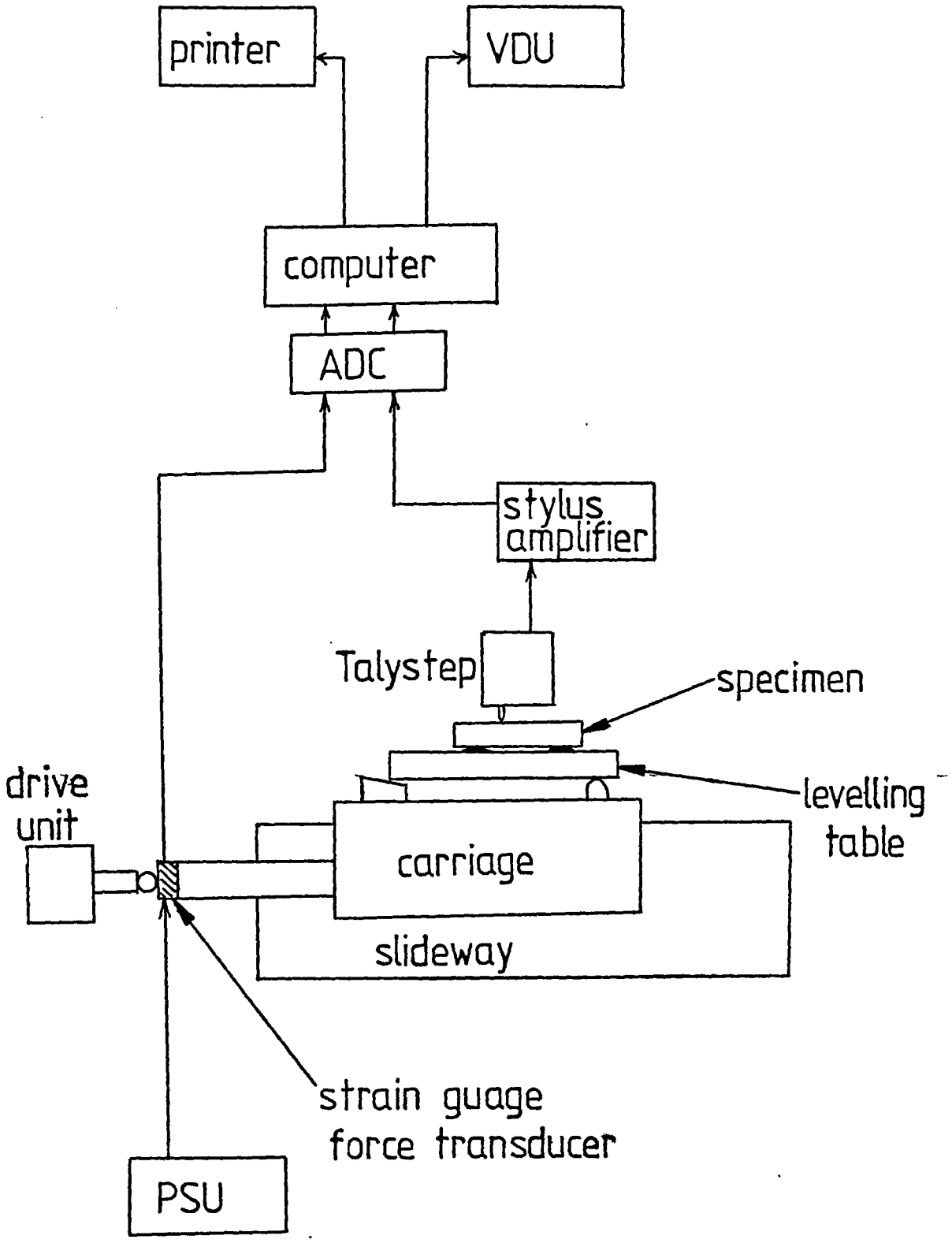

Figure 3.2

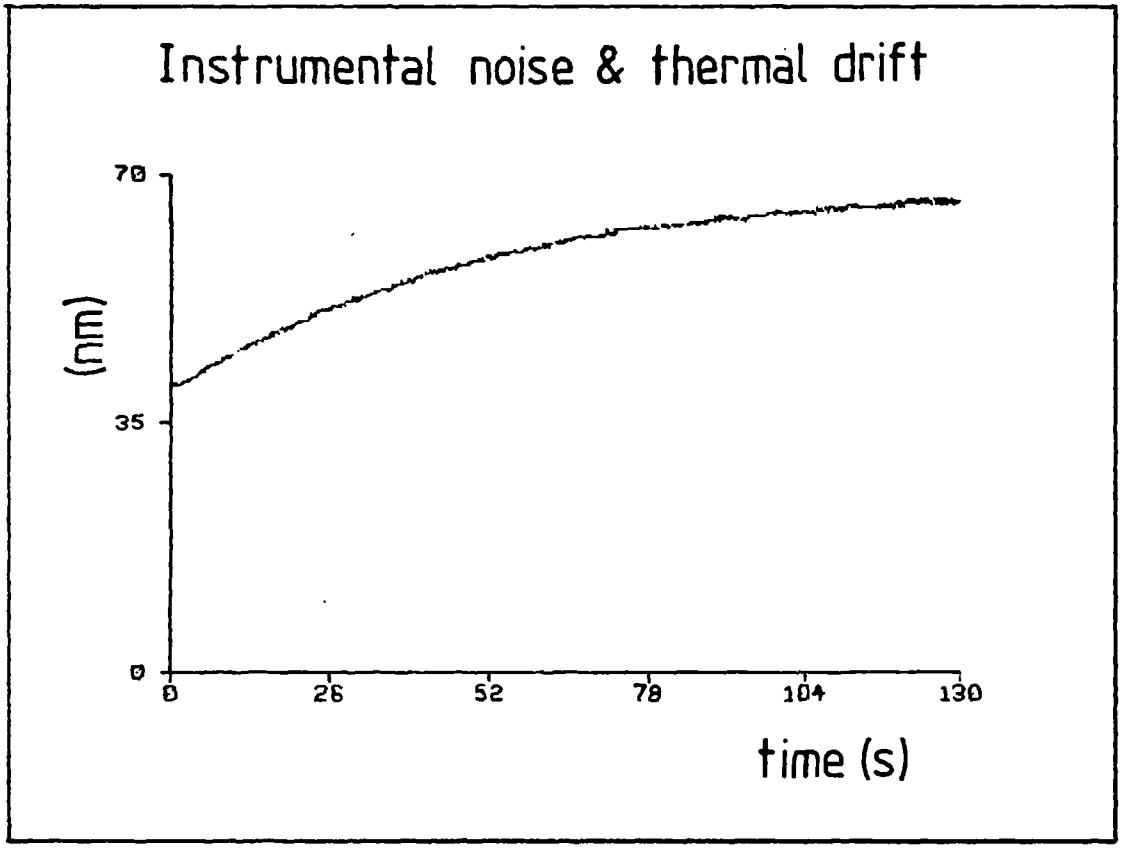
Instrumental noise & thermal drift
70
35
0
(nm)
0
26
52
78
104
130
time (s)

Figure 3.3:Friction characteristics of acetal at low velocity

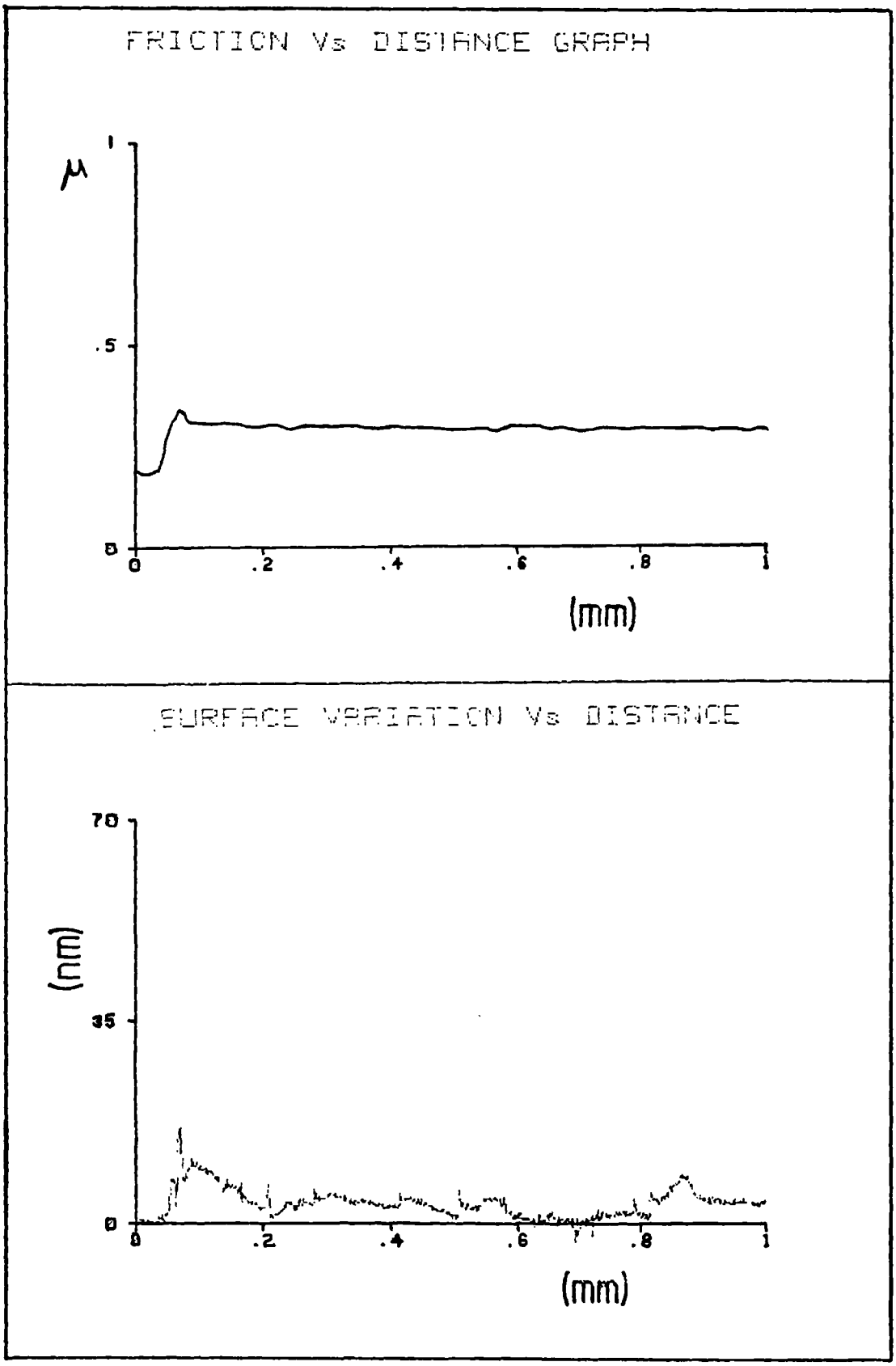

v=0.01 (mm/s)
η=20cs

Figure 3.4: Friction characteristics of acetal at low velocity

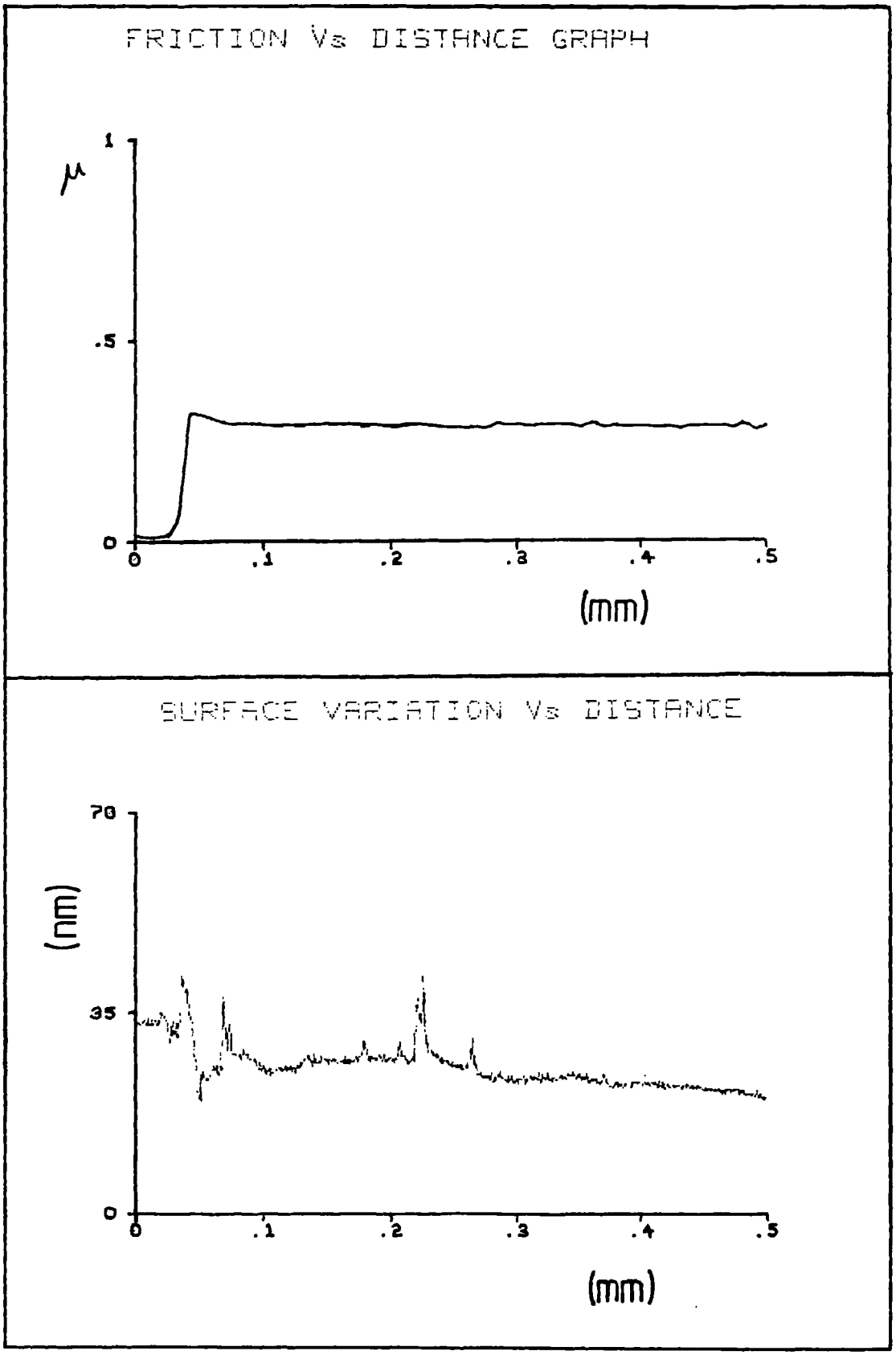

v = 0.005 (mm/s)

η = 20cs

Figure 3.5: Friction characteristics of acetal at low velocity

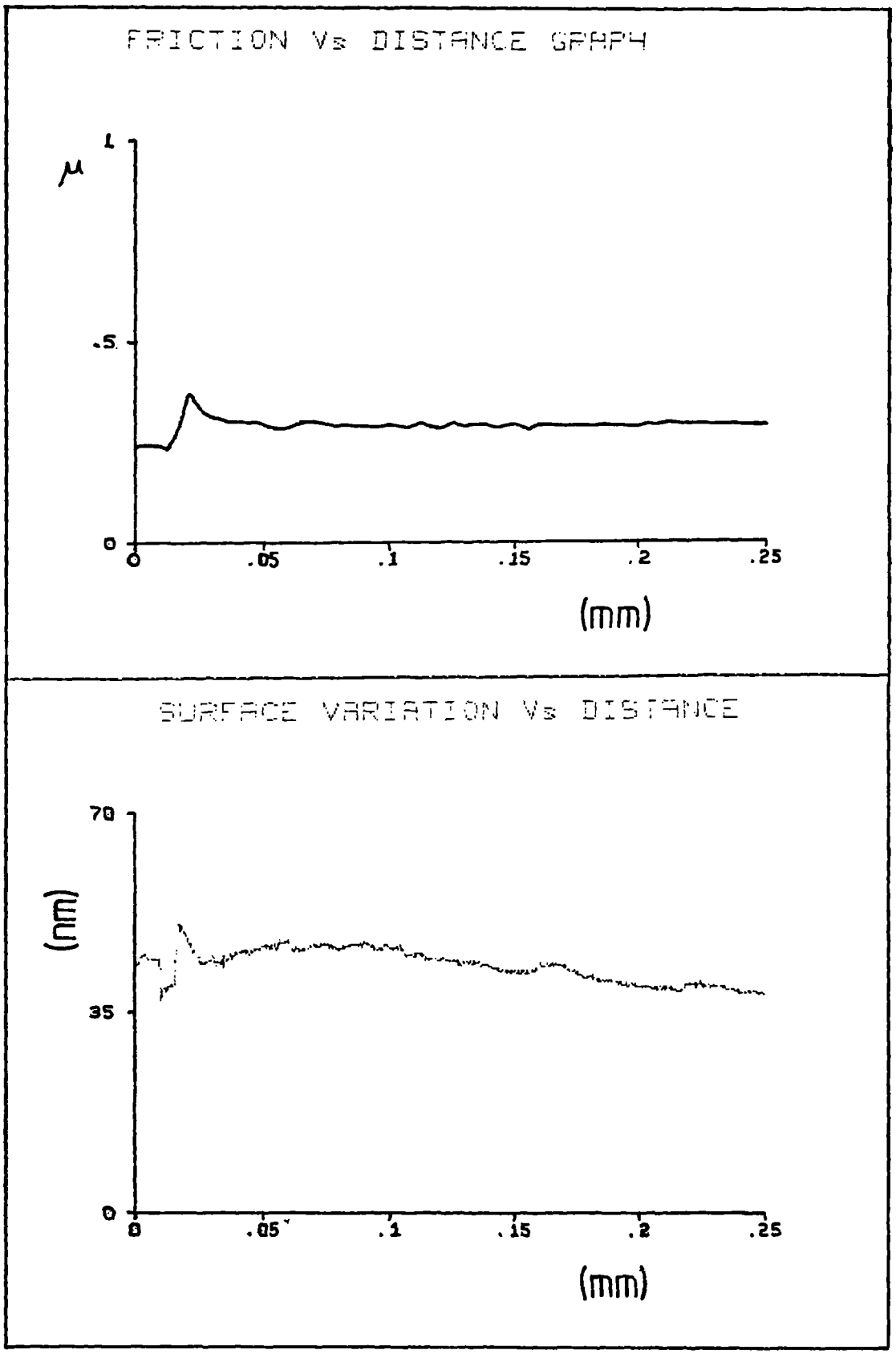

v=0.0025 (mm/s)

η=20cs

Figure 3.6: Friction characteristics of acetal at low velocity

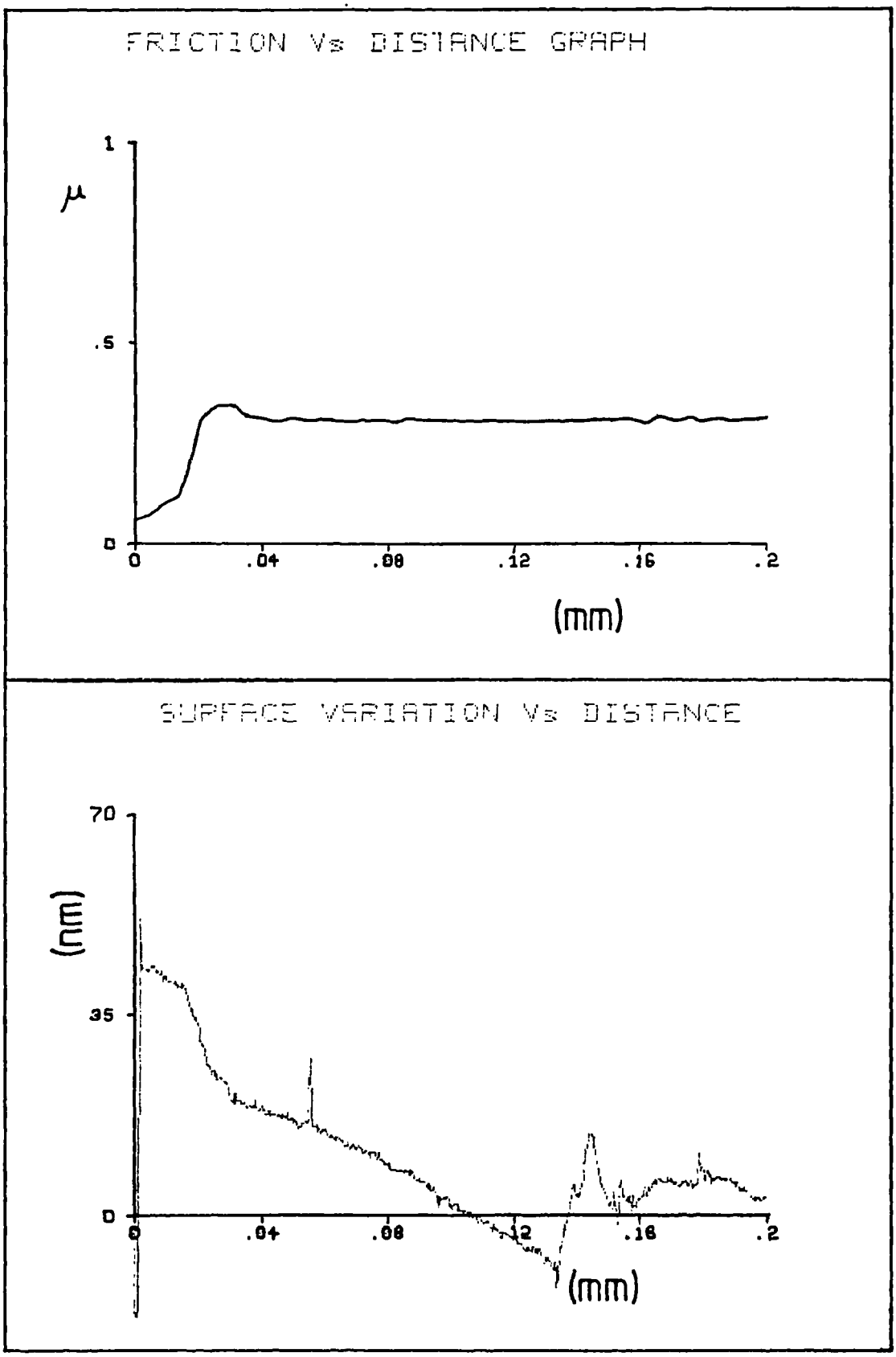

v=0.0005 (mm/s)

η=20cs

Figure 3.7: Friction characteristics of acetal at low velocity

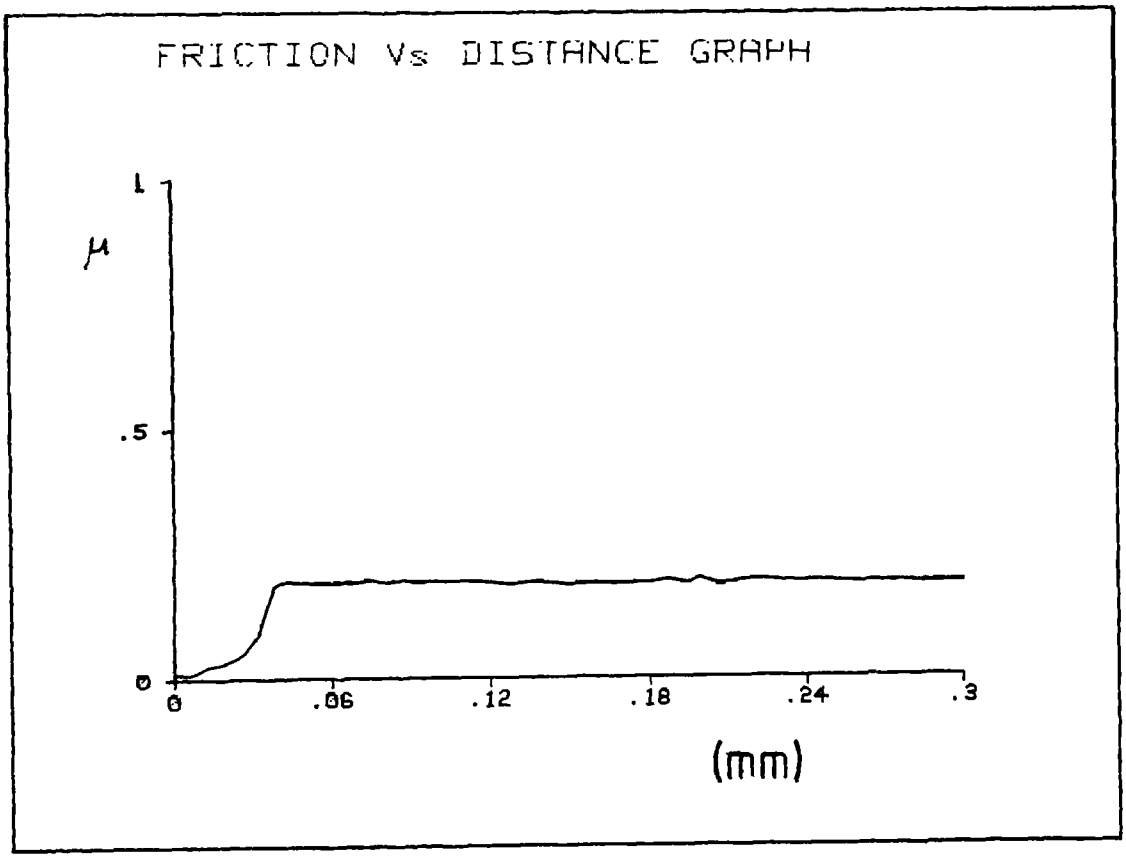

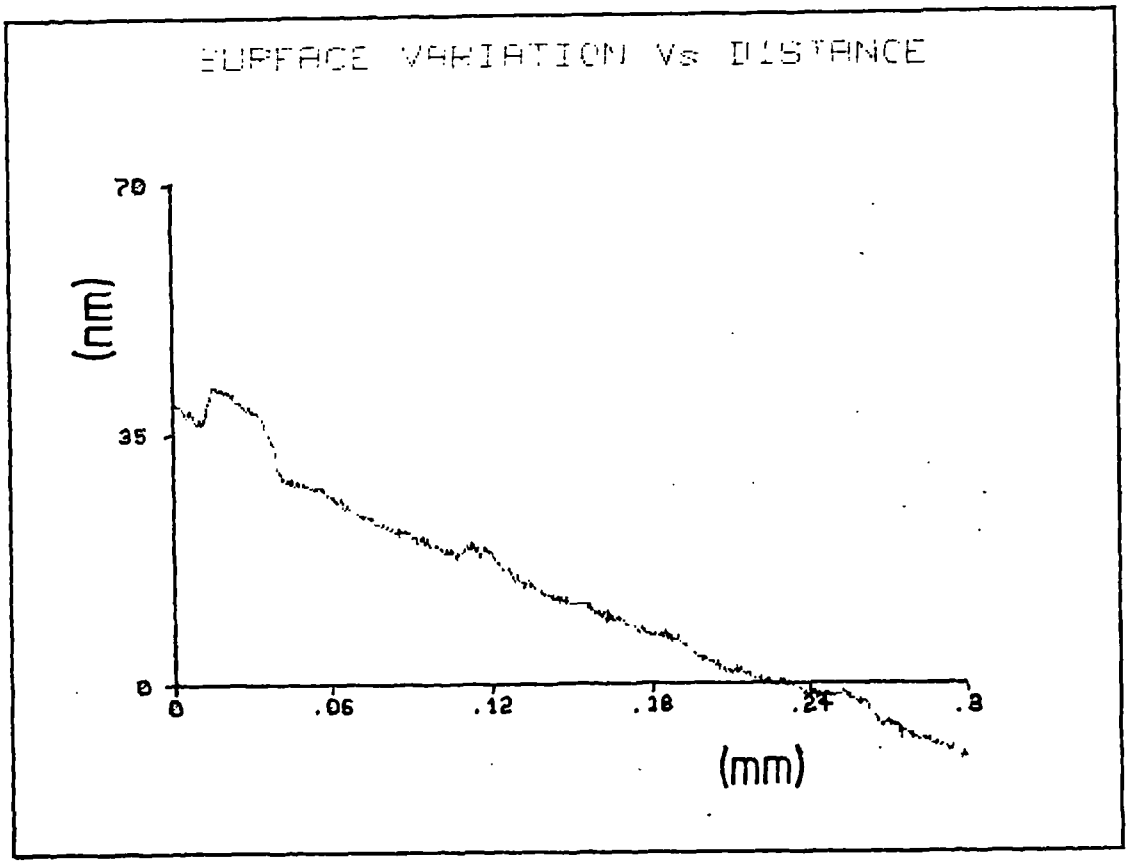

v=0.0025 mm/s

Figure 3.8: Friction characteristics of PTFE at low velocity

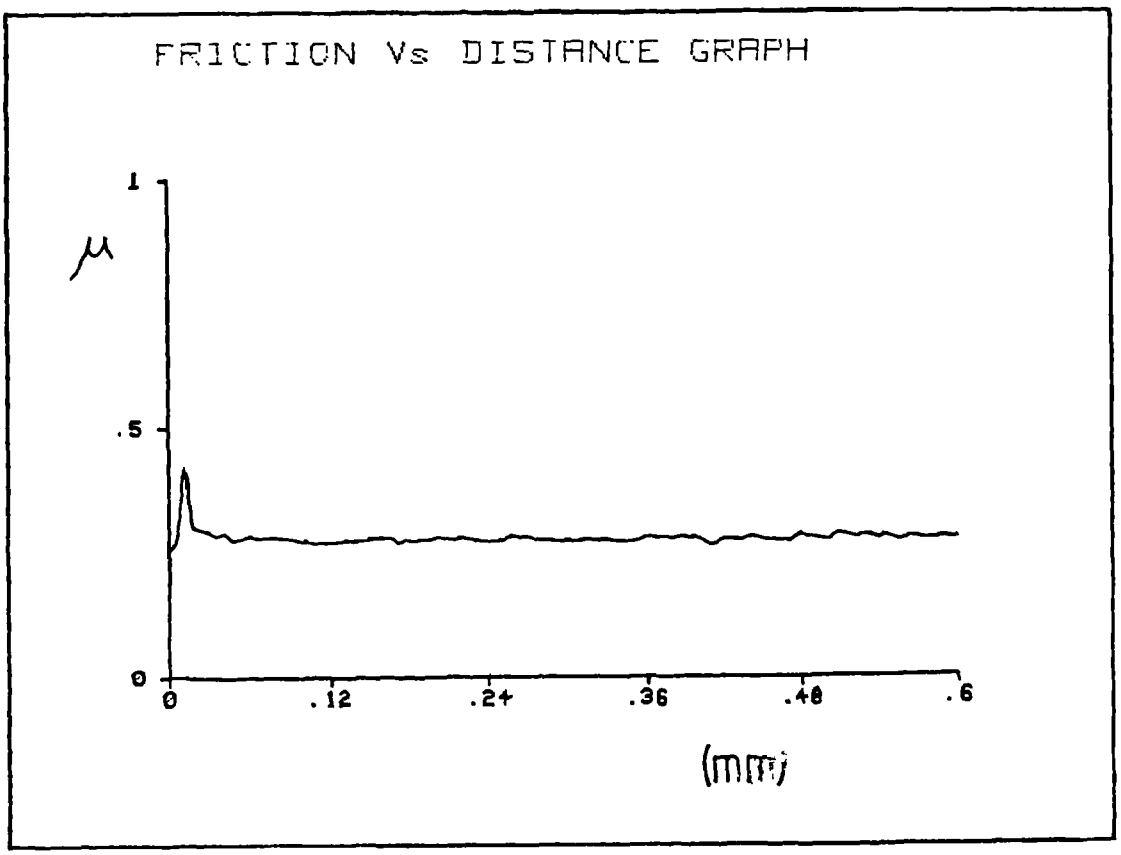

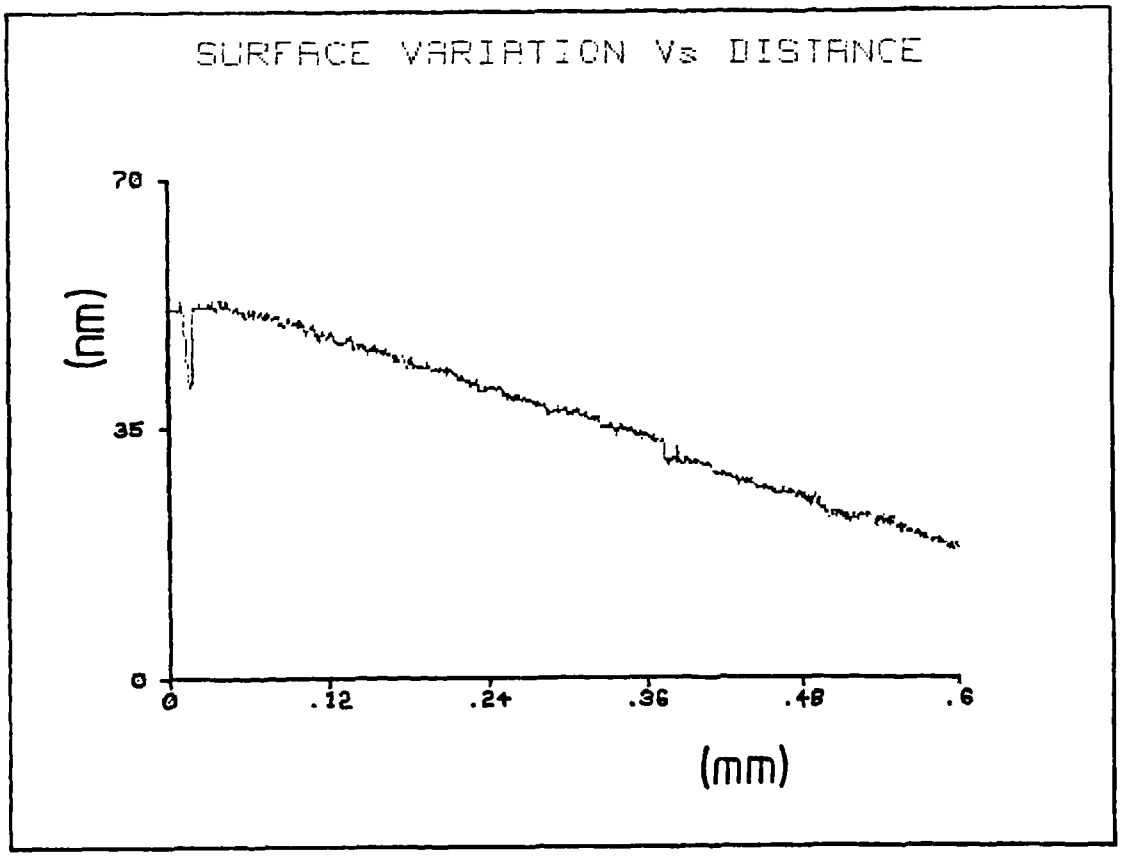

v=0.005 (mm/s)

Figure 3.9: Friction characteristics of PTFE at low velocity

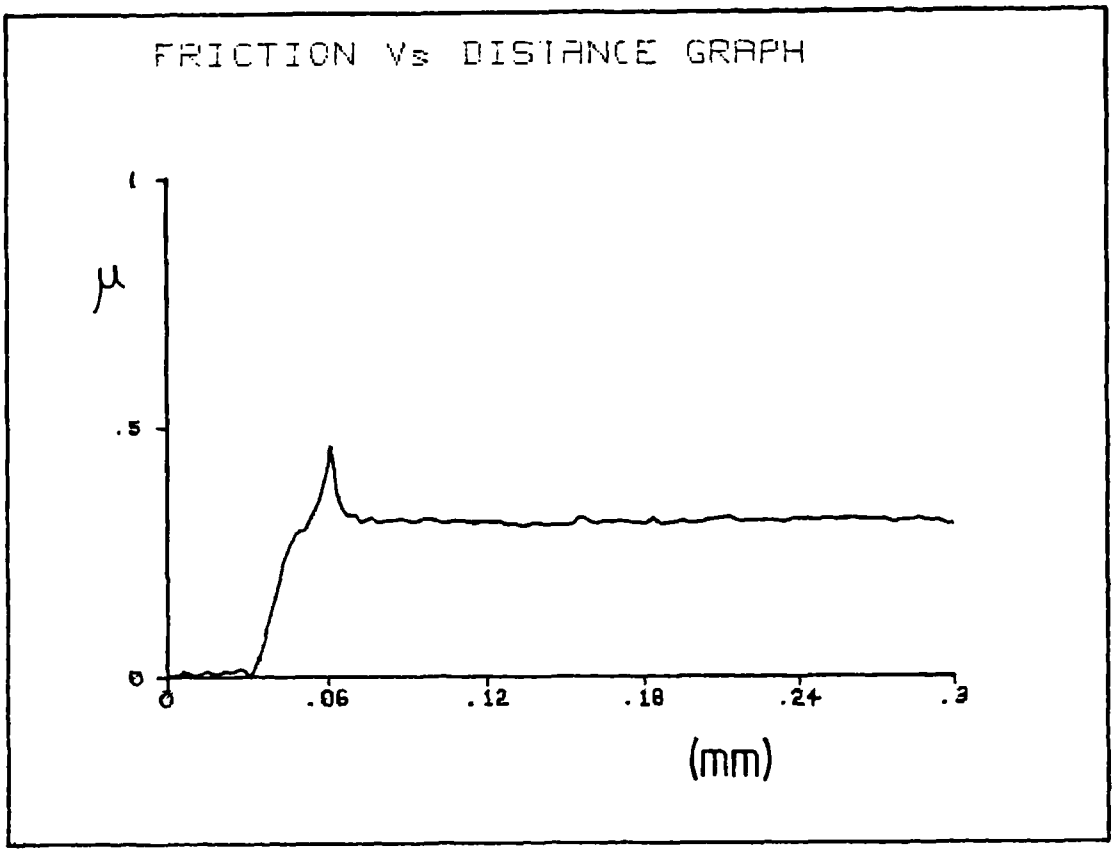

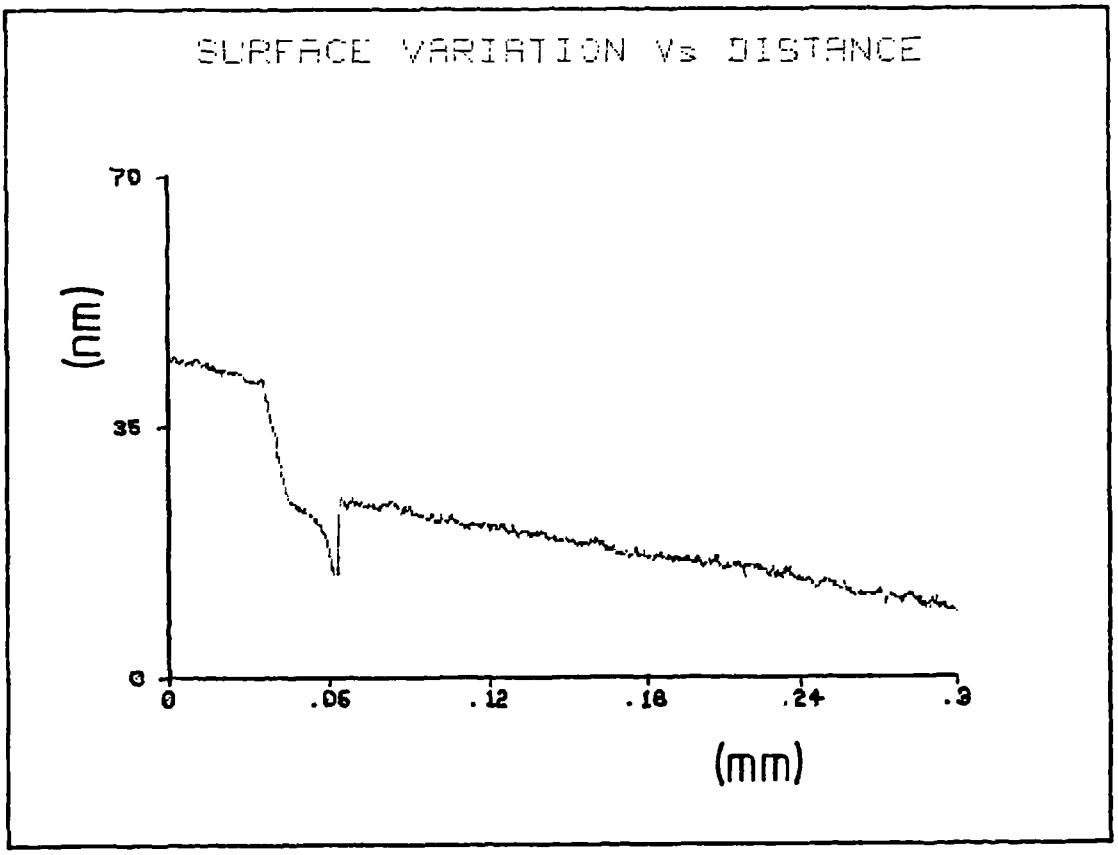

v=0.0025(mm/s)

Figure 3.10: Running-in characteristics of spherical PTFE pads at low velocity

a)

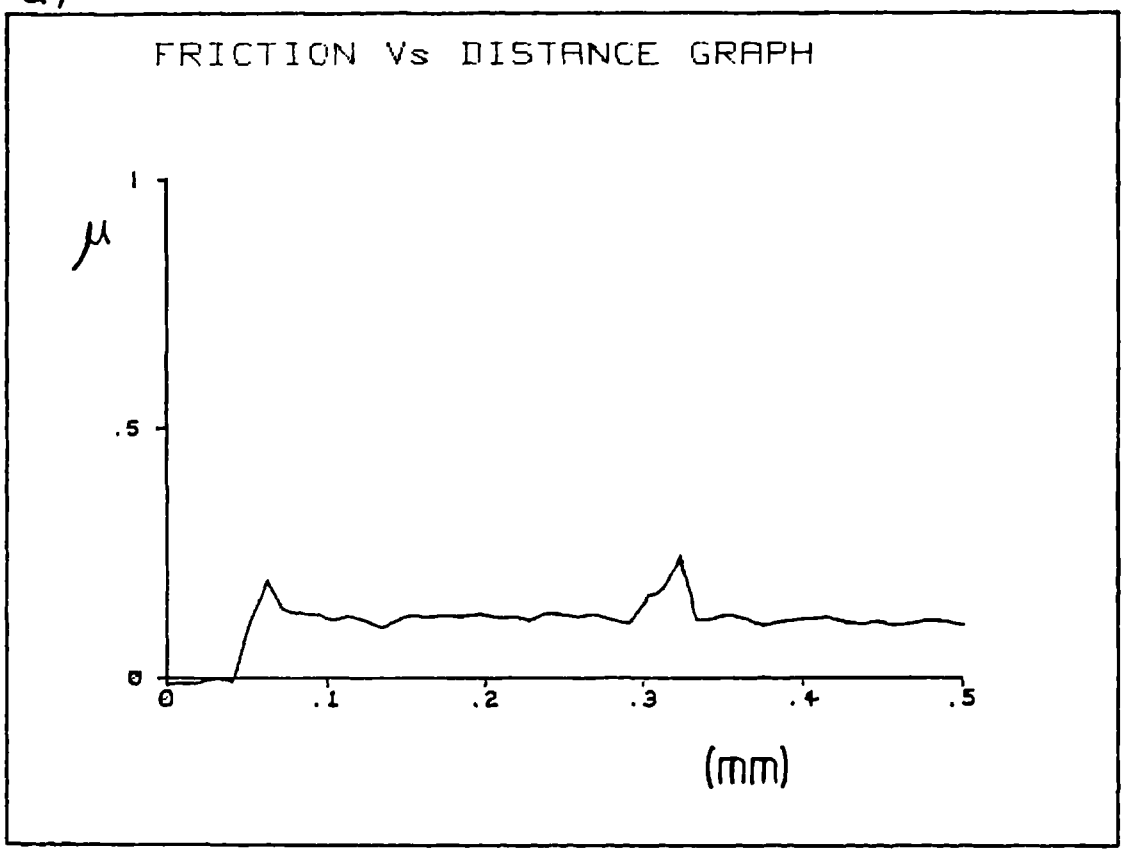

b)

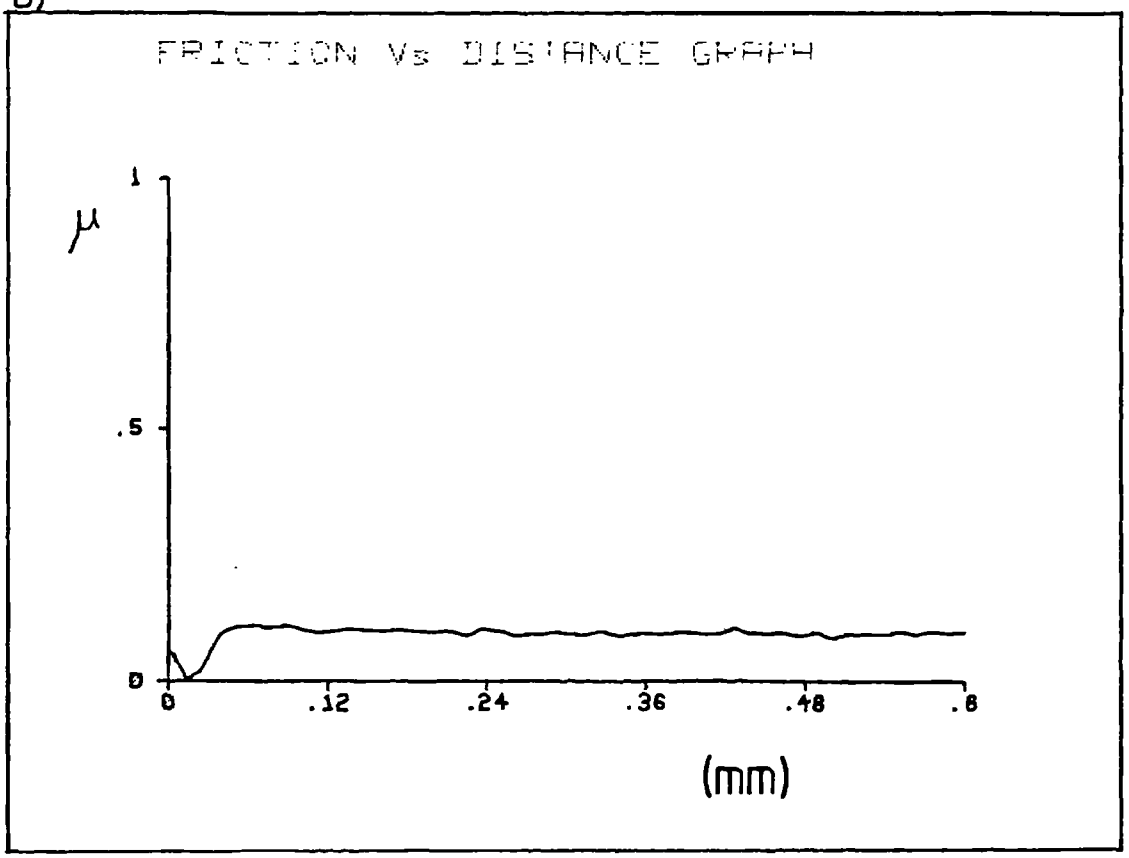

Figure 3.11: Friction characteristics of PTFE at low velocity

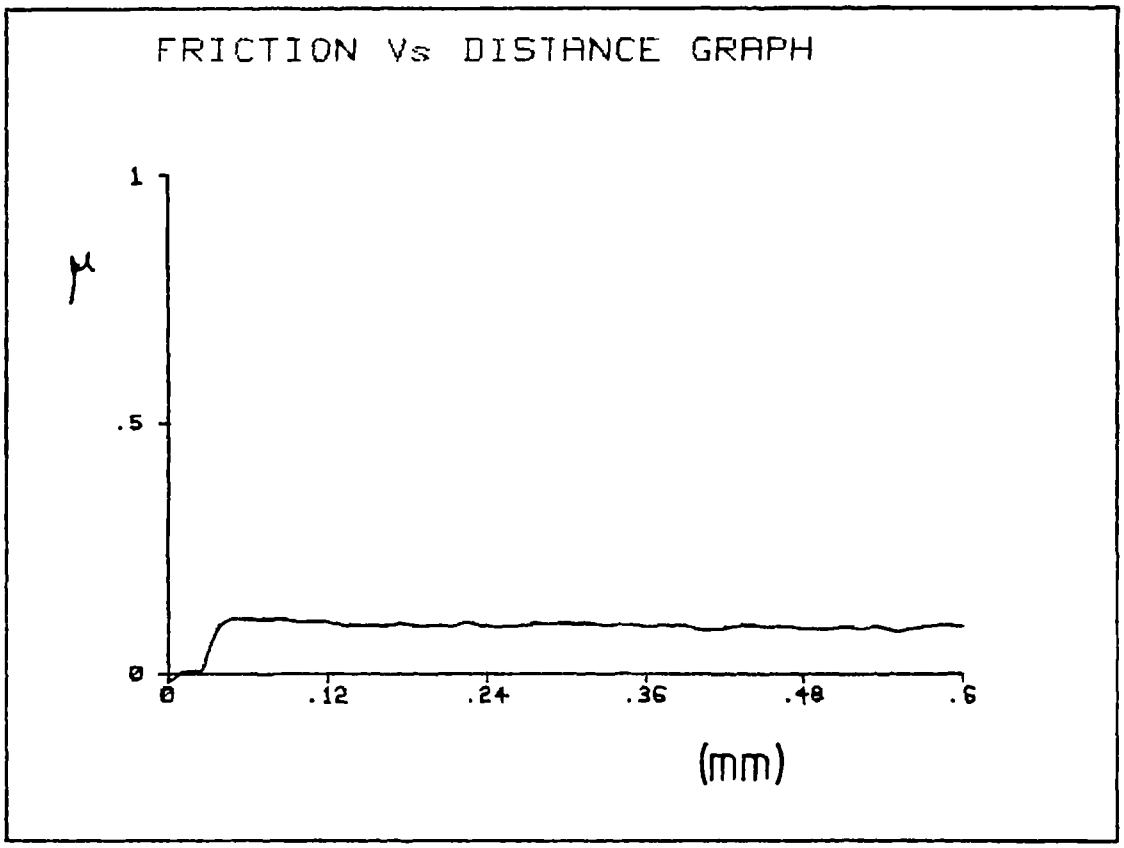

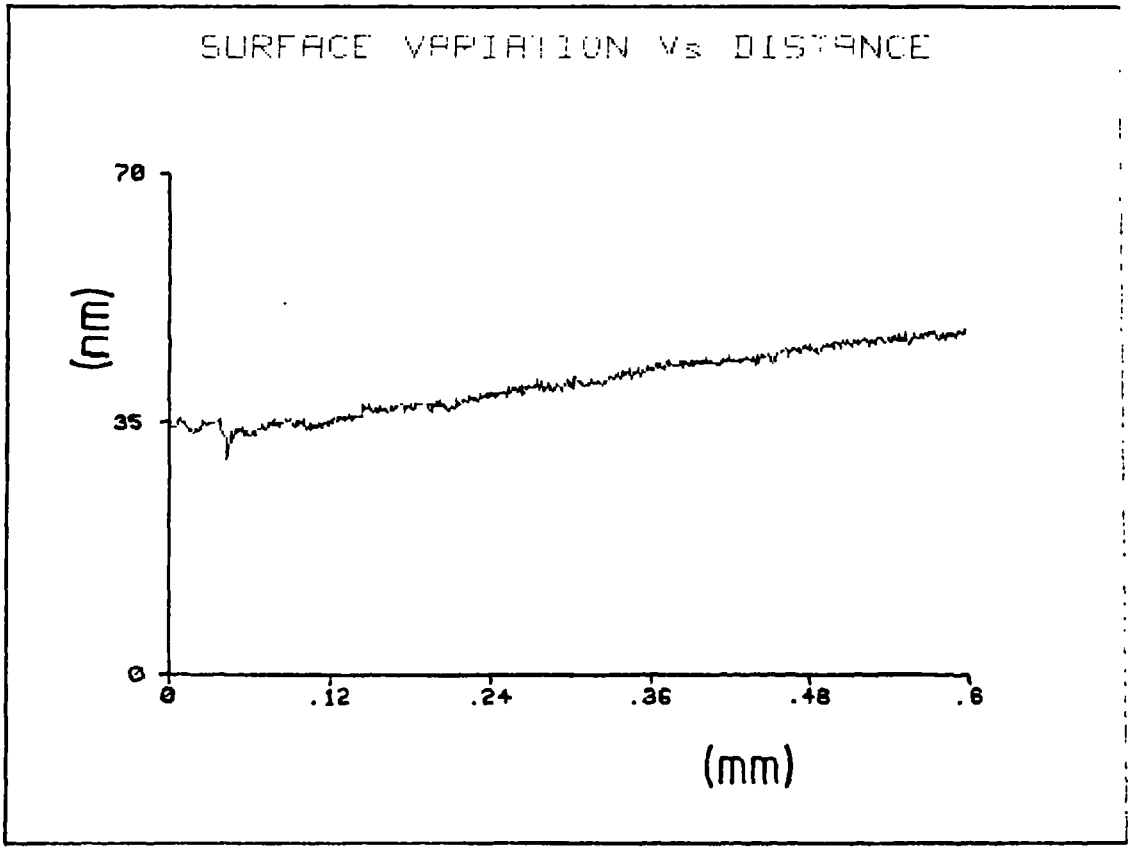

v= 0.005mm/s

Figure 3.12: Typical Talystep trace for super-smooth optical flat

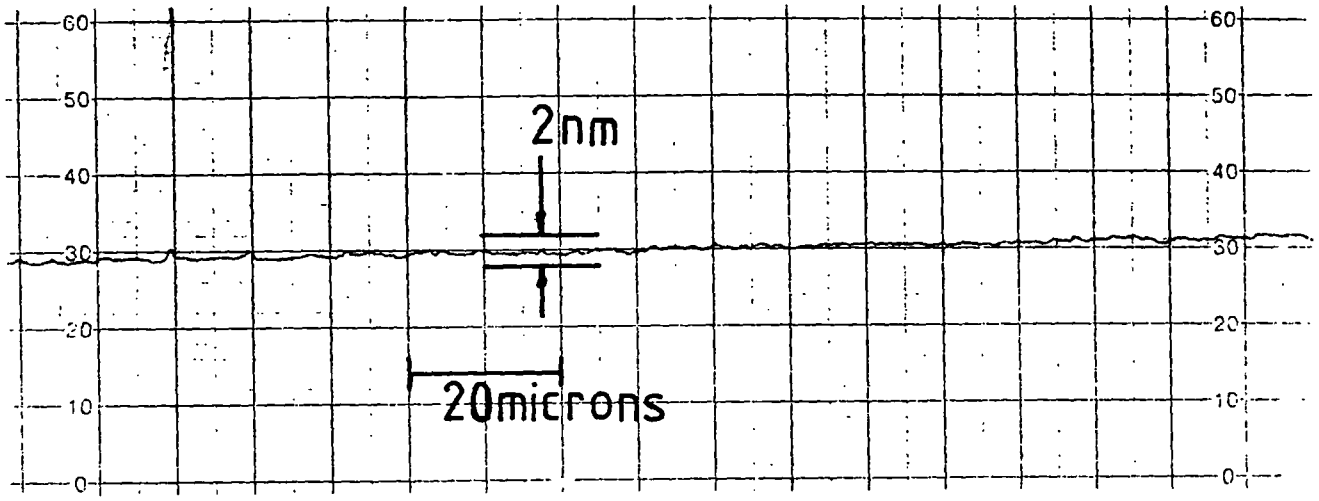

Chapter 4: The design of NPL Nanosurf 2

4.0. Introduction

Nanosurf 2 was designed at NPL during the authors six month tenure there as part of the CASE award scheme. It is a development of the Nanosurf 1 already built at NPL.

Nanosurf 1 was built as an extension of the Rank Taylor Hobson "Talystep" for use in the measurement of the surface characteristics of x-ray optics, Lindsey (1986). This stylus based instrument had been successfully used for the assessment of ultra-smooth surfaces with a spatial wavelength of 1mm or more and accuracy of a few nanometres. Due to this success, it was decided to undergo a development program with the following objectives:-

1. To extend the range to 50μm - 50mm .i.e a lateral range ratio of 1 part in 1000.
2. To obtain accuracies of the order 0.1nm/mm.
3. To create a basic instrument that would be compatible with a wide range of displacement transducers.
4. To increase insensitivity to thermal and mechanical disturbances.
5. To create a data acquisition facility.

4.1. Principle of operation

A labeled photograph of Nanosurf 2 is shown in plate 4.1. The specimen is mounted on a leveling table, T, which is itself mounted on the carriage, C2. This carriage is fitted with dry polymeric bearing pads which interface with the precision linear slideway, SW. Three pads are distributed in a triangular configuration on one side of the carriage with the centroid being coincident with the drive axis. Two more pads are positioned on the opposing side, again in line with the drive axis. This pad system will provide kinematic constraint in the five degrees of freedom

required for a linear motion and will also have a center of friction coincident with the drive axis. The horizontal micrometer, M1, pushes the specimen carriage along the slideway via the slave carriage, C1, which is part of the non-influencing drive coupling arrangement. The micrometer is driven by a remotely mounted DC motor. This has variable speed which enables the setting of continuous micrometer anvil velocities over the range 0.1 to 10mm/min. The stylus/transducer assembly is moved into contact with the specimen via the vertical micrometer, M2. During specimen adjustment, this micrometer and the specimen table tilt-adjusting screw, S, are decoupled from the reference (measurement loop).

The output signal from the transducer is fed into a Hewlett Packard 9836 micro-computer via the Talystep signal conditioning amplifier. This signal is then digitized and various diagnostics are computed using data algorithms developed for this project.

4.2. The measurement loop and materials selection

This instrument is almost entirely constructed from Zerodur. The only non Zerodur components within this instrument are in the transducer and the bearing pads; described in chapter 3. These pads are a mixture of mild steel and brass ≈0.7mm thick coated with an extremely thin layer of PTFE/Pb composite. The thermal expansion of these will be ≈11nm/k. The instrument measurement loop runs downwards through the leveling stage, carriage and bearing pads. It then passes upwards through the transducer support and finally through the transducer itself, see figure 4.1.

To facilitate a calculation of the susceptibility of this loop, it is necessary to look at the thermal characteristic of Zerodur. This material is a ceramic with two phases constituted from crystalline and amorphous glass. These two phases have thermal expansion coefficients of opposite sign. By very carefully annealing this ceramic, the relative proportions of each phase can be adjusted to produce a material with a zero expansion coefficient at a tunable temperature, Otto & Lindig 1986. However, either side of this point Zerodur does have a finite expansion coefficient that rises with increasing departure from this temperature. Additionally, the expansion effects are hysteretic. Commercial Zerodur is annealed to have zero thermal expansion characteristics at

around 294 kelvin. Thus, although this instrument is in a room regulated to this temperature, the conservative value of 5×10^{-8} as given in table 2.1 will be used.

The fused silica tube is calculated to have an expansion of 48nm/k and this can be verified in a rough test. The expansion coefficient of the overall loop is a lot less easy to determine. If all of the components had equal expansion coefficients and thermal capacities then the expansion coefficient would be zero. Observations show that the expansion coefficient is indeed low although quantifying this value was found to be outside of the confidence in the overall system stability.

4.3 The non-influencing drive

The drive system is required to move the carriage over a distance of 50mm without influencing its motion at a level sufficient to induce perturbations that are significant at the 0.1nm/mm level. The technique that has been used to separate the carriage from any drive influences is shown in figure 4.2. The non-influencing drive coupling consists of a tungsten carbide (*WC*) ball sandwiched between two *WC* flat plates. This material was chosen because of its high elastic modulus and advantageous thermal properties (table 2.1). Neglecting rolling resistance and interfacial friction, this configuration is very stiff in one degree of freedom only and will not transmit forces in the five that remain. In the rest state, the ball constrained against the back plate and a conical hole by a spring. When a drive motion is started, the drive must first push the ball out of the conical hole against the spring force until the *WC* plate makes contact with the invar coupling body. It is then a rigid drive. The distance that must be traversed before a positive drive is obtained is dictated by the gap. This can be set with the adjustment screws and was nominally set to 0.025mm.

A more global view of the drive decoupling system is shown in figure 4.3. Because of difficulties encountered with drive alignment, an intermediate slave carriage has been employed. This is on the same slideway as the specimen carriage and will closely follow the same line. This also has a *WC* ball coupling arrangement. The non rotating anvil micrometer is driven by a servo controlled DC motor and gearbox. To reduce the effects of vibrations, the motor is separated from

the micrometer by a sliding coupling and universal joint. The system is stiff only in the one rotational degree of reedom that is required.

4.4 The transducer assembly

The transducer has to be brought accurately into contact with the specimen. This can be adequately performed using a standard micrometer. However, to reduce thermal and mechanical instabilities, it is required that both the measurement loop remain short and interfaces minimal. The tranducer bracket shown in figure 4.4 has been designed with these two points in mind. The stylus transducer (which weighed ≈1kg) is moved into contact with the specimen via a hysteretic coupling. This is achieved by including a large clearance and therefore backlash in the coupling between the micrometer and transducer. When adjustments are completed, the micrometer can be moved clear of the stylus and thus out of the measurement loop. Friction forces created by the leaf springs maintain the transducer in its position. Because of the large mass involved in this particular case, a proportion of the weight is supported by the adjustable tension springs. There is only one interface in the measurement loop. This is between the invar body and Zerodur with a thin epoxy film between the two. The film was deposited onto the invar as a two part epoxy paint.

4.5 The leveling stage

Most transducer systems are limited by their range/resolution ratio. If a ratio of 100(say) is assumed, then for a traverse distance of 50mm, the specimen must be level to an angle of 20nrad if a vertical resolution of 1nm is to be realised. If the specimen is distorted then an angular resolution of considerably better may be required. The technique for leveling the specimen is shown in figure 4.5. All components in the measurement loop are made from Zerodur. The specimen platform is mounted on a three point support and it is free to roll over two spherical pivots at the rear. The point support at the front of the platform is provided by a wedge. This can be driven along a slideway to provide the angular adjustment. The face of the wedge that contacts the platform has been made convex so that a point contact occurs. The slideway is a simple vee rail. To avoid problems associated with ringing, the surface of the vee has been left in the greyed state. Thus the interface is of polished Zerodur onto grey Zerodur. To prevent the platform from moving forward

whilst the wedge is being driven, there is a spring force that can be adjusted to any position acting upon it. The reaction forces (F_1 & F_2) at the wedge and pivots (respectively) are given by

$$F_1=\frac{Fa}{(a+b)} \text{ and } F_2=\frac{Fb}{(a+b)} \text{ or } \frac{F_1}{F_2}=\frac{a}{b} \tag{4.1}$$

It can be seen that the ratio of forces at the reactions are linearly related to the position of the applied force.

The wedge is driven by a feedscrew via a hysteretic coupling which again can be decoupled from the measurement loop once the adjustment has been completed. For a feedscrew of pitch (P), the tilt angle θ for a rotation of the feedscrew ϕ is given by

$$\theta\simeq\frac{P\phi\tan\psi}{(a+b)} \tag{4.2}$$

For the design used, a tilt angle of 2nrad will correspond to a feedscrew rotation of about three degrees. This is easily performed manually. The specimen sits freely on three pads that have been left exposed by etching the surrounding Zerodur. Details of the etching procedure and its stress relieving characteristics are given in Appendix A.

4.6 Data acquisition

Data acquisition has been achieved by using the same instrumentation as that developed for the polymer slideway experiments in chapter 3. The stylus motion is detected as a voltage output from the Talystep amplifier. This voltage is measured using a Hewlett Packard 9836 computer via 98640A ADC.

Plate 4.1

Nanosurf 2

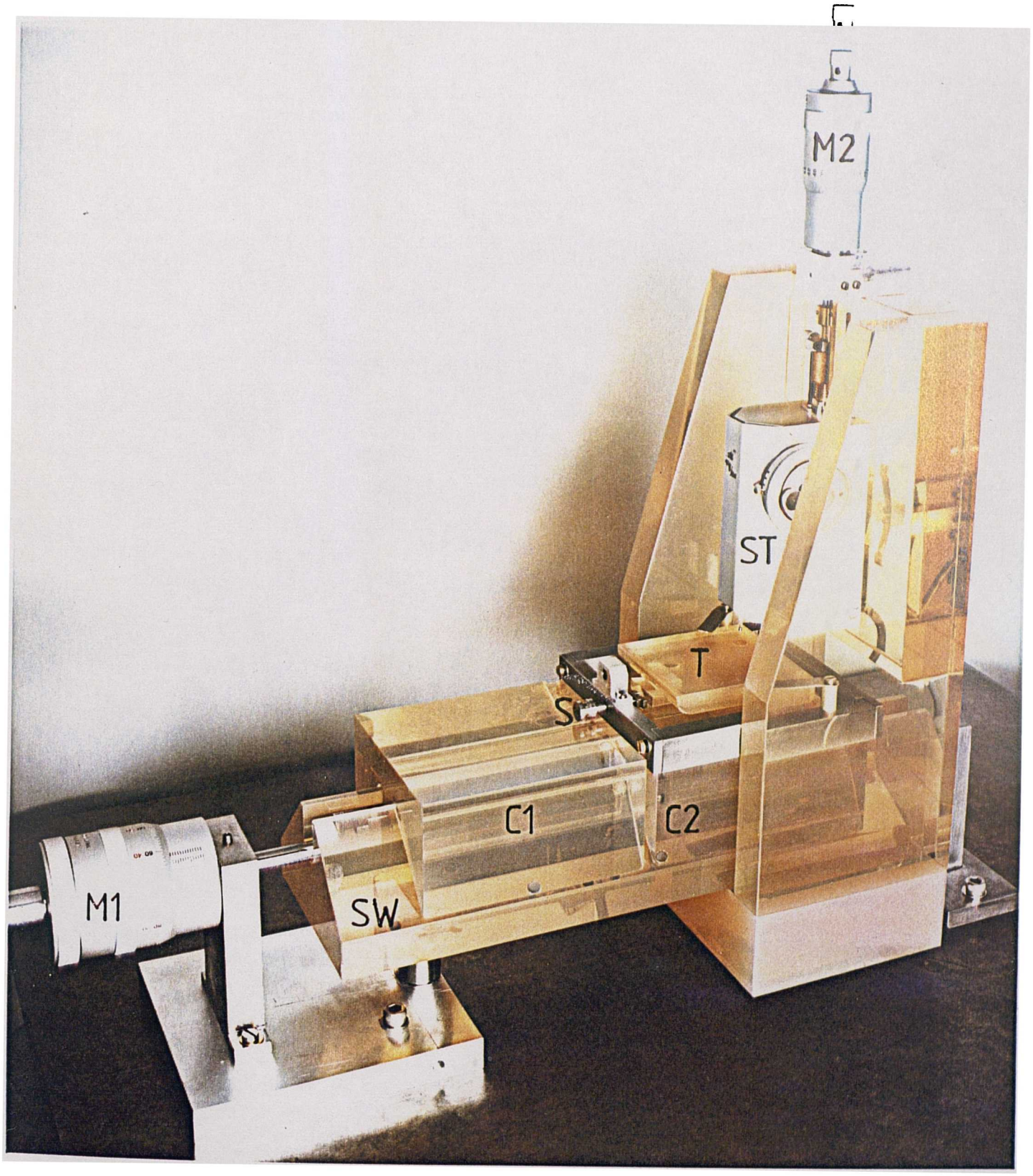

Figure 4.1:Schematic diagram of
Nanosurf 2 measurement loop

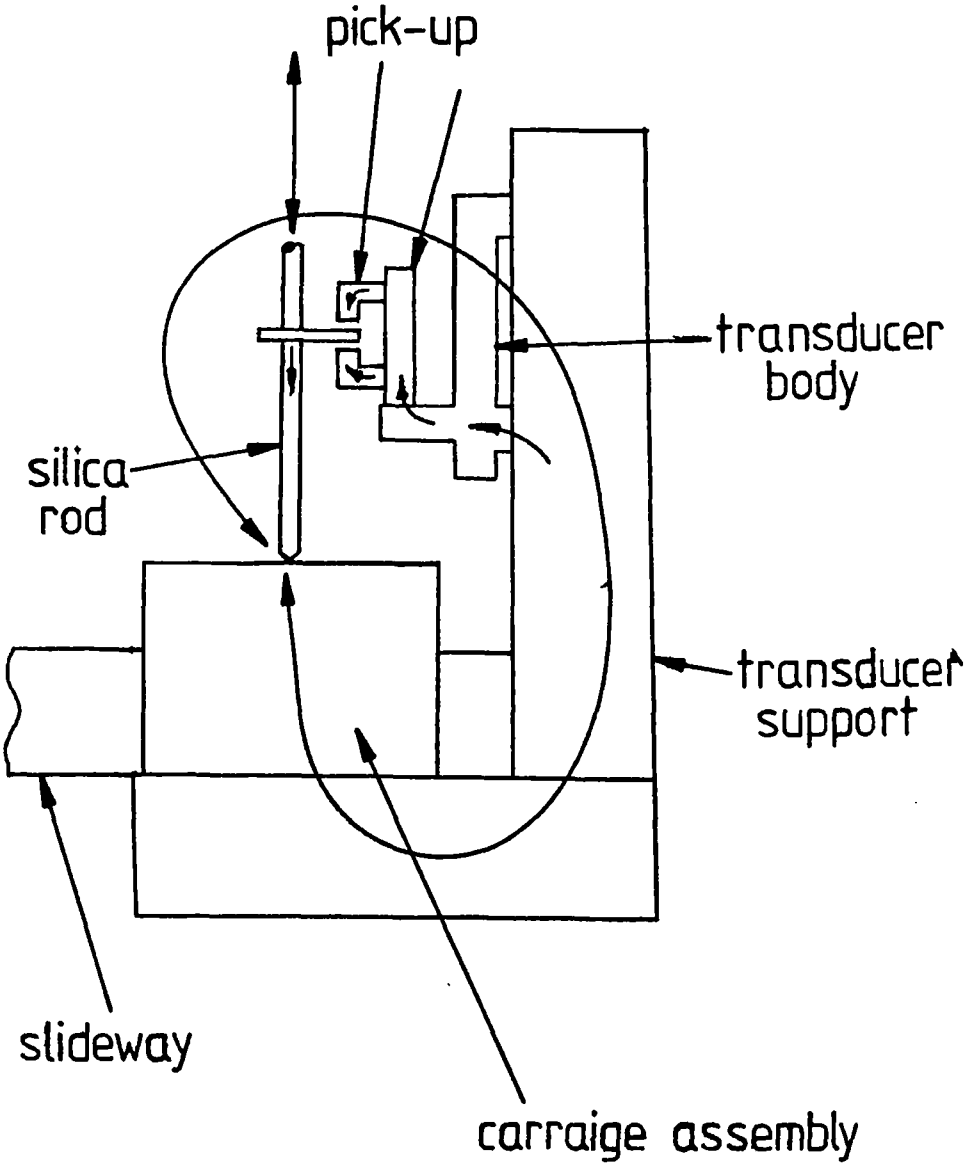

Figure 4.2: Cross-section of non-influencing drive coupling

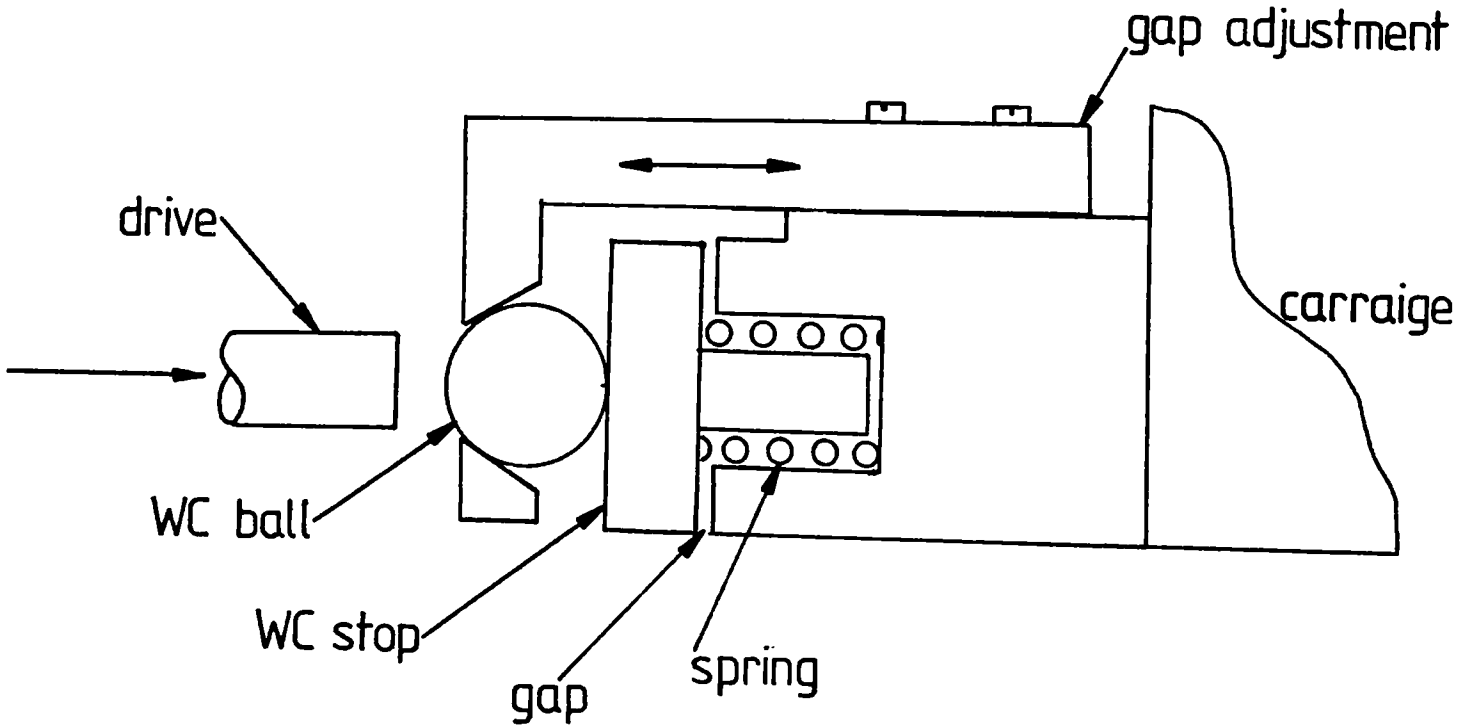

Figure 4.3: Cross section of non-influencing drive

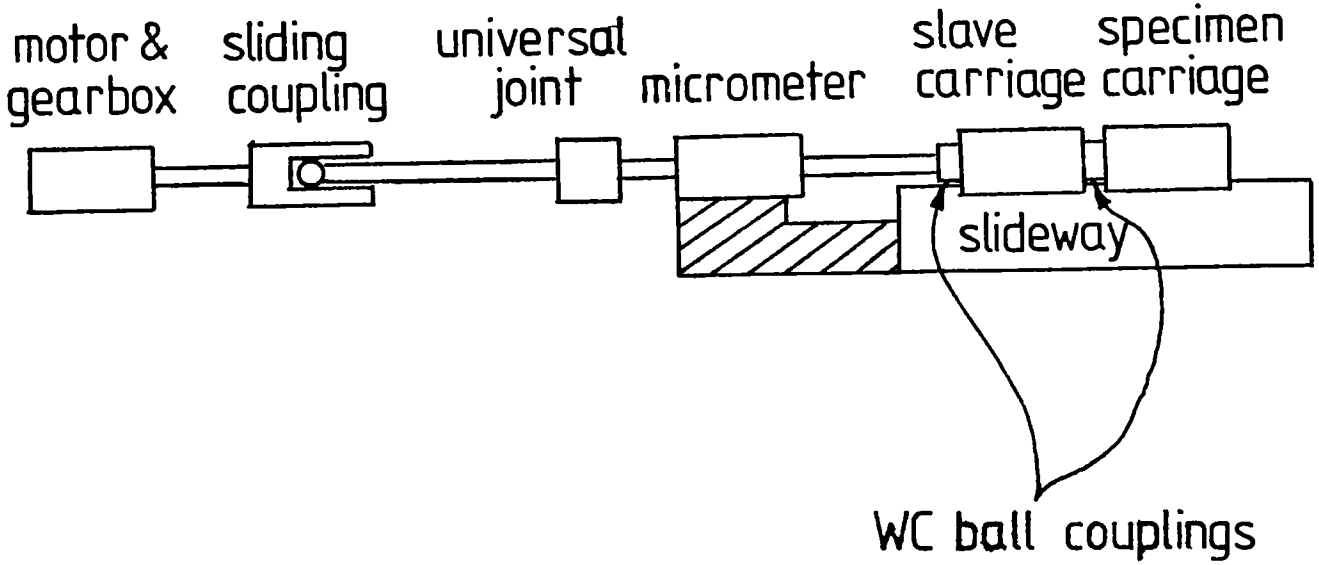

Figure 4.4: Transducer bracket

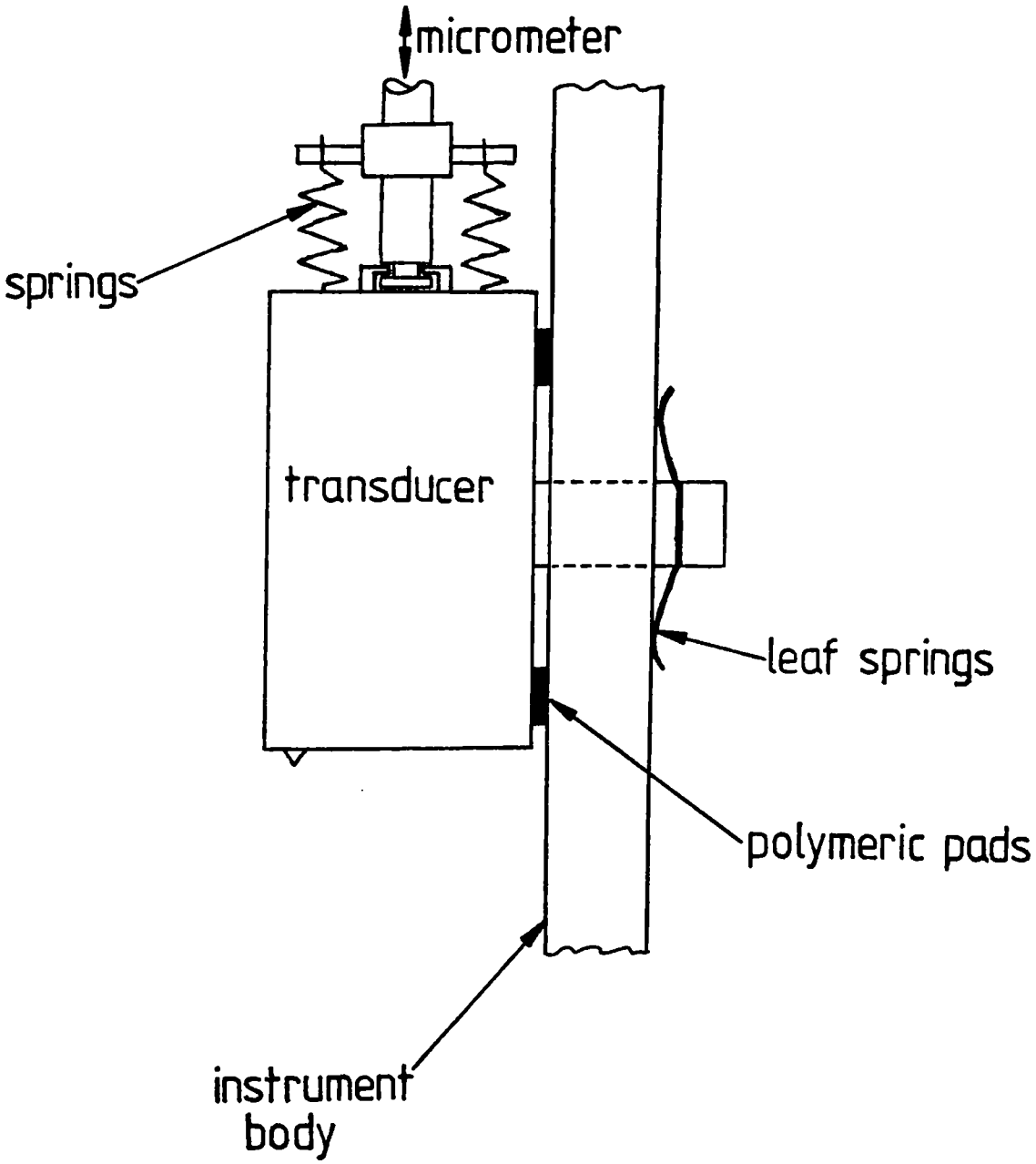

Figure 4.5:The levelling stage

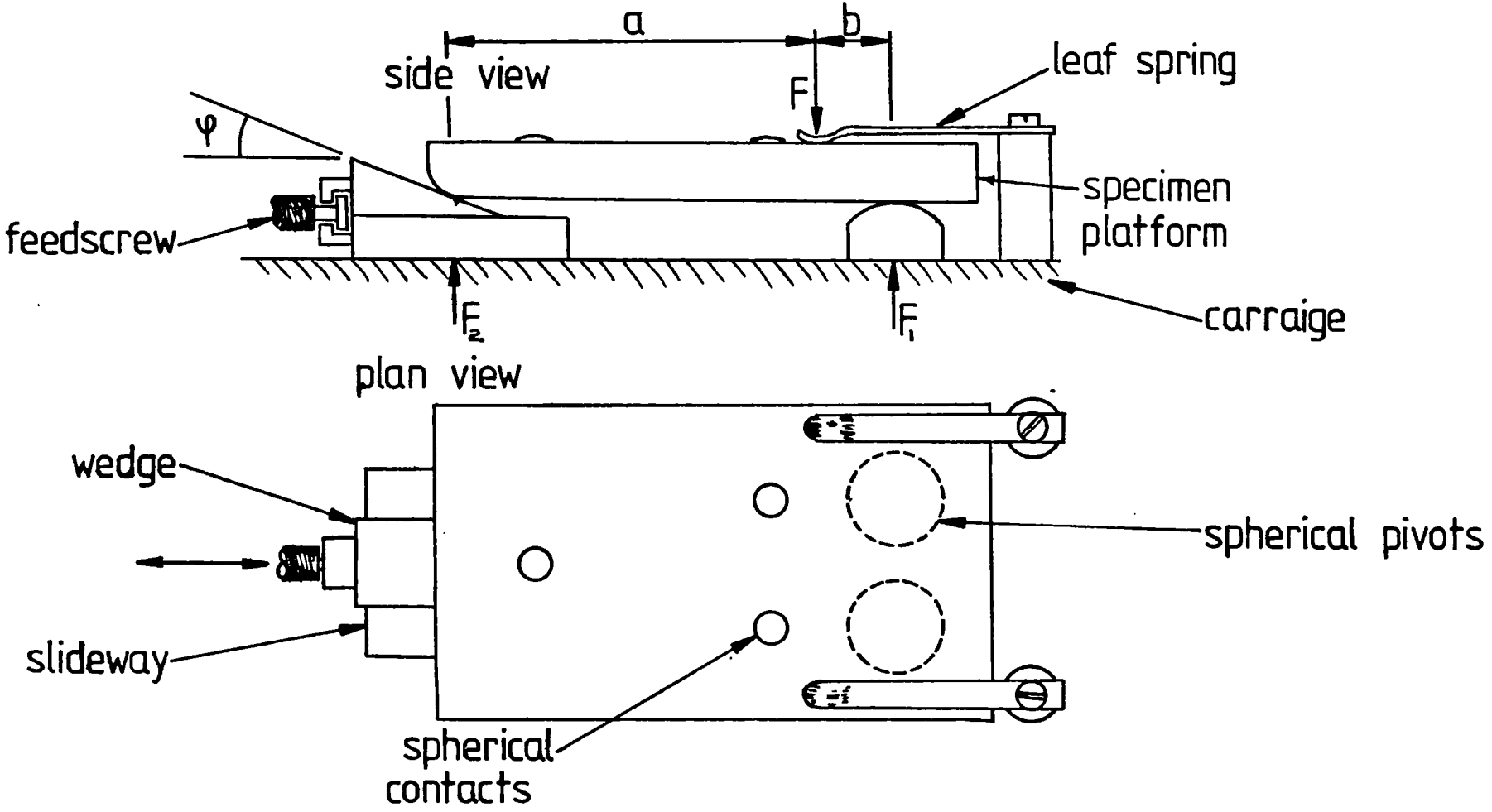

Chapter 5: The characterisation of Nanosurf2

5.0 Experimental method

To characterise Nanosurf 2 a number of its important features have to be assessed. Repeatability is the only possible monitor of the accuracy of this system. This is because the surface measurement is taken relative to the slideway reference. location of the carriage relative to the transducer is obtained from the micrometer drive. This has an accuracy of =±0.1mm. There is no positive specimen location device and thus error evaluation techniques using reversal methods are not achievable, (see Whitehouse, 1976). This is obtained by scanning a specimen twice over a similar portion of its surface and calculating the goodness of fit for these two measurements. The limit on the length of specimen that can be examined is governed by the minimum settling time upon initial start-up and maximum length of stroke. The maximum length of stroke is known (50mm), whereas the start-up characteristic will depend on the quality of the slideway bearing system and indentation (micro-hardness) properties of the specimen under consideration. The main limitation on system resolution is the instrument noise. This arises from both mechanical and electronic sources. Many high precision instruments are limited by their thermal susceptibility. This effect has been considered a prime factor throughout the design process. Consequently, an examination of long term drift and both long and short term thermal expansion characteristics has been undertaken. The influence of any undesirable long term non-linearities can be reduced by increasing the speed of measurement. However, this will be limited by the stylus and slideway dynamics and the nature of the specimen surface. A study of the variation of surface texture parameters with velocity of scan is also presented.

The digital sampling of the stylus output signal is taken over a time interval that is determined by the carriage feedrate, number of data points and length of traverse. The sampling interval is not linearly related to the delay generated by the computer algorithm. Thus, using the com-

puters internal clock, a correction is applied at the end of the data aquisition to compute the true traverse length for the manually set carriage feedrate. This results in a rather peculiar numbering scheme along the x-axis of some of the figures in this chapter.

5.1 Results

5.1.1 Start-up/indentation characteristics for SiC specimen

In this experiment a SiC flat polished specimen has been contacted by the stylus with force of 2mgf. The carriage has then been pushed along by micrometer M1, via the drive motor, at a velocity of 0.15mm/min, figure 4.1. When both carriage and specimen begin motion, perturbations due to high initial acceleration, static/dynamic characteristics of the bearing system and rate dependent indentation of the specimen by the stylus are monitored (these factors are not separable in this type of experiment). If the carriage system has an invariant static/kinetic characteristic, indentation will be indicated by an apparent initial rise in the specimen profile. This reasoning is based on the assumption of the rate dependence of indentation and the independence of dry bearing properties with settling time. A number of tests were performed with settling times ranging from tens of seconds up to an hour. These traces have been obtained by winding the micrometer until it is clear from the carriageway (≈0.4mm). The drive is then advanced until contact and thus traversal of the carriageway is obtained. In each case the transition to motion indicated an apparent rise of the stylus of approximately 1.5nm and there were no observable effects due to the settling times used. This value is in accordance with that expected by extrapolation of the results obtained from a similar investigation into the microhardness of metals, Gane and Cox, 1970. A number of typical stylus traces are shown in figure 5.1. Traces A,B and C represent starting up traces after the stylus has been static on the specimen for periods of 6mins, 10mins and 15mins respectively.

5.1.2 Noise, drift and thermal susceptibility

Instrument noise has been monitored by bringing the stylus into contact with a Zerodur specimen and measuring the transducer output whilst the carriage remains stationary. This output

is then a measure of disturbances caused by vibration transmitted acoustically and via the foundations and also the electronic noise. Another noise source is that of the motor. The plots in figures 5.2 & 5.3 are the noise measurements corresponding to the output with and without the motor running respectively over a period of 100secs. This signal corresponds to an R_a value of approximately 0.03-0.04nm. The flat regions are due to the quantisation limit in the ADC stage of the measurement. This signal has also been passed through an 8Hz low pass analogue filter. The slope of this curve is caused by short term drift due to the thermal shock introduced by a recent manual manipulation of the instrument mechanism. Drift is considered to be the amount by which motion per unit time of the reference from an arbitrary datum is expected for a particular environment. Nanosurf2 is presently being kept in an under ground temperature controlled clean room where fluctuations of the order 0.1 kelvin would be the maximum expected over any 1 hour period. This has also been monitored by measuring the static output from the transducer over the period of about 1 hour. From this test it was observed that after a settling time of a few minutes, there is a steady linear drift of approximately 7nm per hour. This translates to a drift rate of 61 microns per annum. The reason for this drift is very difficult to isolate and could be either mechanical or electronic. From the previous tests it is thought that rate dependent indentation and bearing creep are unlikely to be the source.

The thermal characteristics are more difficult to assess. The various components that make up the complete system are all of different thermal capacitance and expansion coefficients. However, because the transducer consists mainly of relatively small components with a correspondingly low thermal capacitance, it is assumed that the fast thermal response is due to this particular part of the instrument. The rapid thermal response of the instrument has been monitored by measuring static stylus output and temperature (using a thermistor) simultaneously whilst the temperature is rapidly fluctuated by moving ones hand in the vicinity of the stylus and thermistor. The thermistor resistance is measured using a Solartron digital voltmeter. The readout is in kilo ohms with a resolution of 10Ω. This value can be read into the computer via an IEEE488 data bus. The resistance of this bead type thermistor can be considered to be linear over a small temperature range with a temperature coefficient of -4.68kΩ/K. The resolution of this system is

therefore ≈0.002K. The resistance value was compared with an NPL calibrated mercury thermometer having 0.1k divisions. Both were placed in a thermally controlled room which was then adjusted to by a few degrees over a period of about two hours. A graph of thermistor resistance in kilo-ohms against thermometer reading is shown in figure 5.4. From this graph a relationship between the resistance (R) and the temperature (T), is given by the equation

$$R = 207 - 4.68T \quad (k\Omega) \tag{5.1}$$

The time constant for this thermistor is approximately 1 second. A typical result from this sort of test is shown in figure 5.5. Traces A and B represent temperature and stylus output respectively. The relationship between temperature and transducer output can be clearly seen and the rapid temperature coefficient is approximately 50nm per kelvin. This is in close agreement with the value 48nm/k that was predicted for the silica rod in chapter 4. However, the transducer is modified as much as possible for thermal balancing. This means that although localised temperature gradients will effect transducer accuracy it should be less sensitive to environmental temperature changes. A plot of transducer output and temperature over a 1 hour period is shown in figure 5.6. It can be seen that although there has been fluctuations of around 0.1kelvin, the transducer has shown a steady state drift indicating a long term thermal insensitivity.

5.1.3 The variation of surface texture parameters with scan velocity

A change in the surface texture parameters R_a and R_q with the velocity of scan will represent a dynamic characterisation of the instrument. To assess the variation of dry bearing noise with sliding velocity, an ultra-smooth spectrosil specimen has been examined at various feedrates ranging from 0.15 to 2mm/min. A typical plot of both the static and dynamic system noise is shown in figure 5.7. Trace A is the combined instrument noise and surface texture of and NPL polished glass specimen. Trace B represents static system noise and is the stylus output noise with the slideway stationary. This specimen was prepared at NPL and has an R_a roughness between 0.1 and 0.03nm. From these and many other tests it is apparent that dynamic slideway noise is much less than the static noise (this usually gives psuedo R_a values of 0.05nm or more). The results from one set of tests are shown in Table 5.1. It is clear that these two parameters are

invariant over the velocity range. The high values corresponding to the slowest feedrate are a consequence of examining a "rough" portion of the specimen. This result implies that the bearing noise is does not change significantly over this velocity range.

The act of increasing the velocity of the carriage will linearly increase the dynamic spectral bandwidth input to the stylus. For a specimen with a higher roughness value (spatial bandwidth) higher frequency information will be a significant contribution to the surface texture diagnostics. In the above analysis an 8Hz low pass analogue filter was used. As well as the electronic filter, the finite dynamic response of the transducer mechanism will also effect the diagnostic information as the scan rate is varied. This implies that short range information will be lost as the velocity is increased. To assess this effect, the experiment has been repeated with a SiC flat that had an R_a and an R_q roughness of approximately 0.5 and 0.8nm respectively. The results from this test are shown in table 1. The loss of information with increase in velocity can be clearly observed. The instrument noise level was measured and again was observed to have an "R_a" value of approximately 0.05nm.

5.1.4 Repeatability

To assess the repeatability of the instrument a 50mm spectrosil flat polished by ICOS has been measured. This measurement has then been repeated and the two results compared. To avoid the edge roll-off, only a central 40mm portion of the specimen was examined. Because the digital sampling of the stylus is taken at intervals of 40μm with a positional accuracy of ≈20μm (at present), any noise components of wavelength 80μm or less are not an indication of instrument error. Two individual measurements of this specimen profile are shown for comparison in figure 5.7. Using cross-correlation techniques, these two signals have been matched positionally and subtracted to result in the repeatability trace shown in figure 5.9. Apart from the initial discrepancy that is probably due to thermal shock via manual handling, there is an error of less than 4nm over 40mm. The two spikes at the beginning of this trace are caused by dust particles on the surface. The time for each measurement was 8mins. This was the first test to assess the repeatibility of the slideway motion and an example of more recent tests is shown in figure 5.10.

These are two individual traces over a 5mm portion of a Zerodur polished flat. Clearly, in this example, a repeatibility of less than 1nm over this traverse can be observed. Long term ripple has not been observed.

5.2 Discussion

Although verification is rather difficult, the performance has been shown to satisfy the initial requirements to a level that we are capable of assessing. The excellent repeatability is an indication that the wear mechanism is likely to be one of a molecular slip rather than thick (40nm) film delamination, thermal anisotropy or a phase transition effect. This implies that there are three distinct wear regimes. These are low wear due to intermolecular slip followed by an intermediate level resulting from delamination of the surface layer and finally rapid wear caused by the tearing out of large grains.

This repeatability implies that under well controlled conditions, surface profile measurements can be made with nanometer accuracy. This however does not imply that a rectilinear motion is being obtained. After polishing the faces of the reference motion were examined with a Zygo optical interferometer system. The resulting fringe patterns for both sides of two slides are shown in figure 5.11. The screne diameter corresponds to 275mm of rail and the wavelength of the light source is 633nm. The carriage can be modelled as a two point contact moving over an undulating surface. This is shown schematically in figure 5.12. The slideway shape can be described by the functional relationship

$$y = f(x) \tag{5.2}$$

With the carriage positioned at the point x, the hieght of the measuring point y_h is given by, (see fig)

$$y_h = \frac{f(x+d)-f(x)}{d}(s-x) + f(x) + \frac{b}{\cos((f(x+d)-f(x))/d)} \tag{5.3}$$

where

d = carriage length

b = carriage hieght

s = distance along x-axis to the measuring point

From this equation it can be seen that if $f(x)$ is constant or linear, the carriage height will be constant relative to the measuring point. A function that is periodic in d will not have any tilting errors. Assuming a function $f(x)$ of the form $Acos(2\pi x/l)$ the y-axis displacement of the carriage at the measuring point relative to the starting position x_1 can be calculated. Substituting values similar to those expected from the interferograms and instrument dimensions of A=0.00015mm, l=275mm, d=100mm and b=15mm a plot of the deviation from the x-axis over a 50mm traverse has been computed, see figure 5.13. The third axis represents the carriage start position. In each traverse the measuring point covers the central 50mm of the carriage. From this figure it can be seen that the apparent curvature can be of either sign depending on the portion of slideway that is employed although the magnitude of this departure from linearity is in the region 10-30nm. To characterise this fully a reference specimen is required and the position of the carriage relative to the slide must be monitored. It is expected that this will be carried out in the near future.

Table 5.1

specimen	feed ($mm\ min^{-1}$)	filter (Hz)	scan (μm)	R_a (nm)	R_q (nm)
spectrosil glass	0·15	8	8	0·39	0·59
	0·3	"	"	0·12	0·16
	0·6	"	"	0·11	0·16
	1·0	"	"	0·10	0·12
	1·5	"	"	0·14	0·25
	2·0	"	"	0·16	0·20
silicon carbide	0·15	"	"	0·47	0·82
	0·3	"	"	0·37	0·55
	0·6	"	"	0·35	0·45
	1·0	"	"	0·31	0·40
	1·0	25	"	0·40	0·51
	1·5	"	"	0·38	0·46
	2·0	"	"	0·42	0·57
	5·0	"	"	0·43	0·53

Figure 5·1: Start-up /indentation characteristic

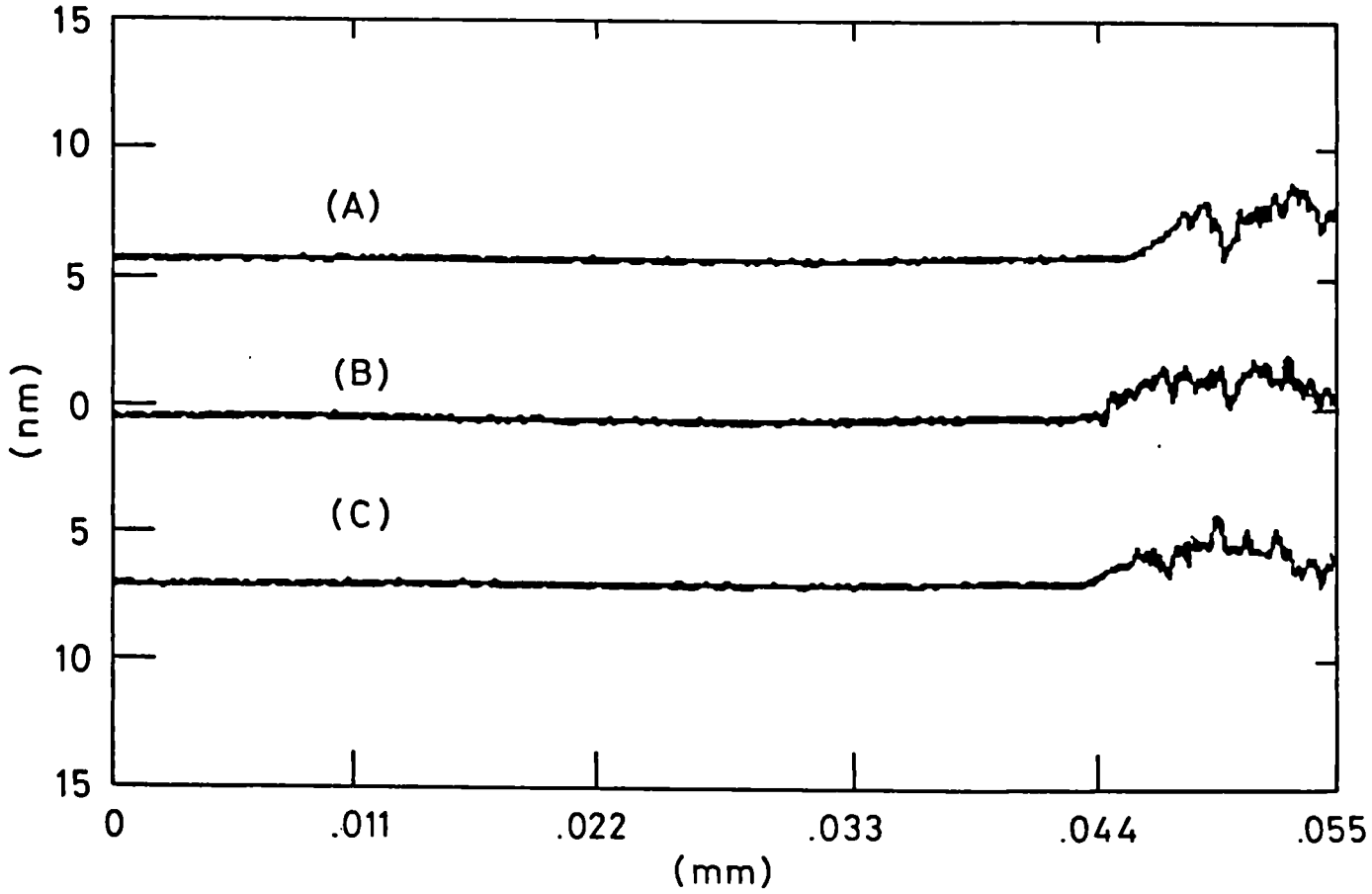

Figure 5·2: Instrument noise with drive motor running

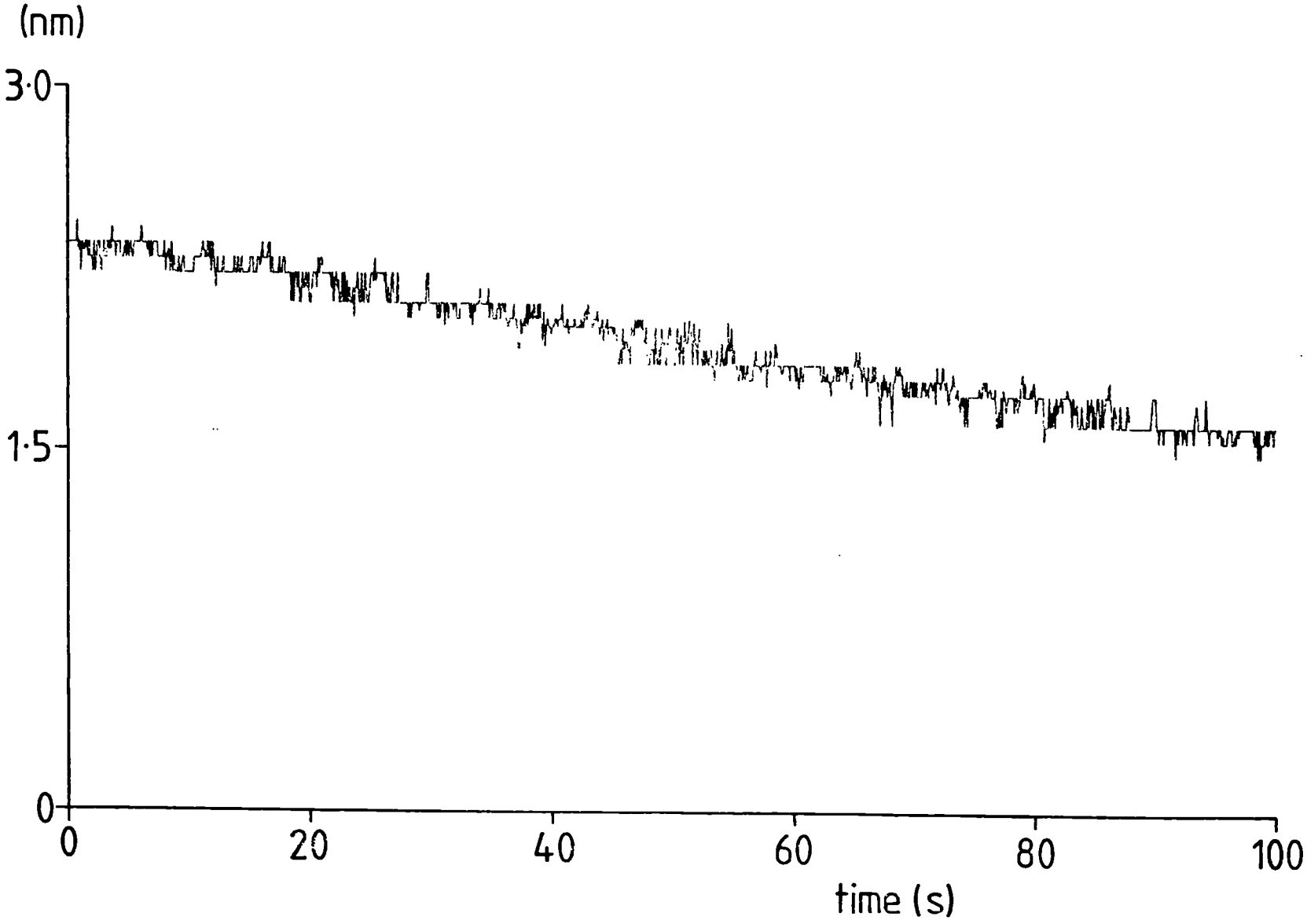

Figure 5·3: Instrument noise with motor stationary

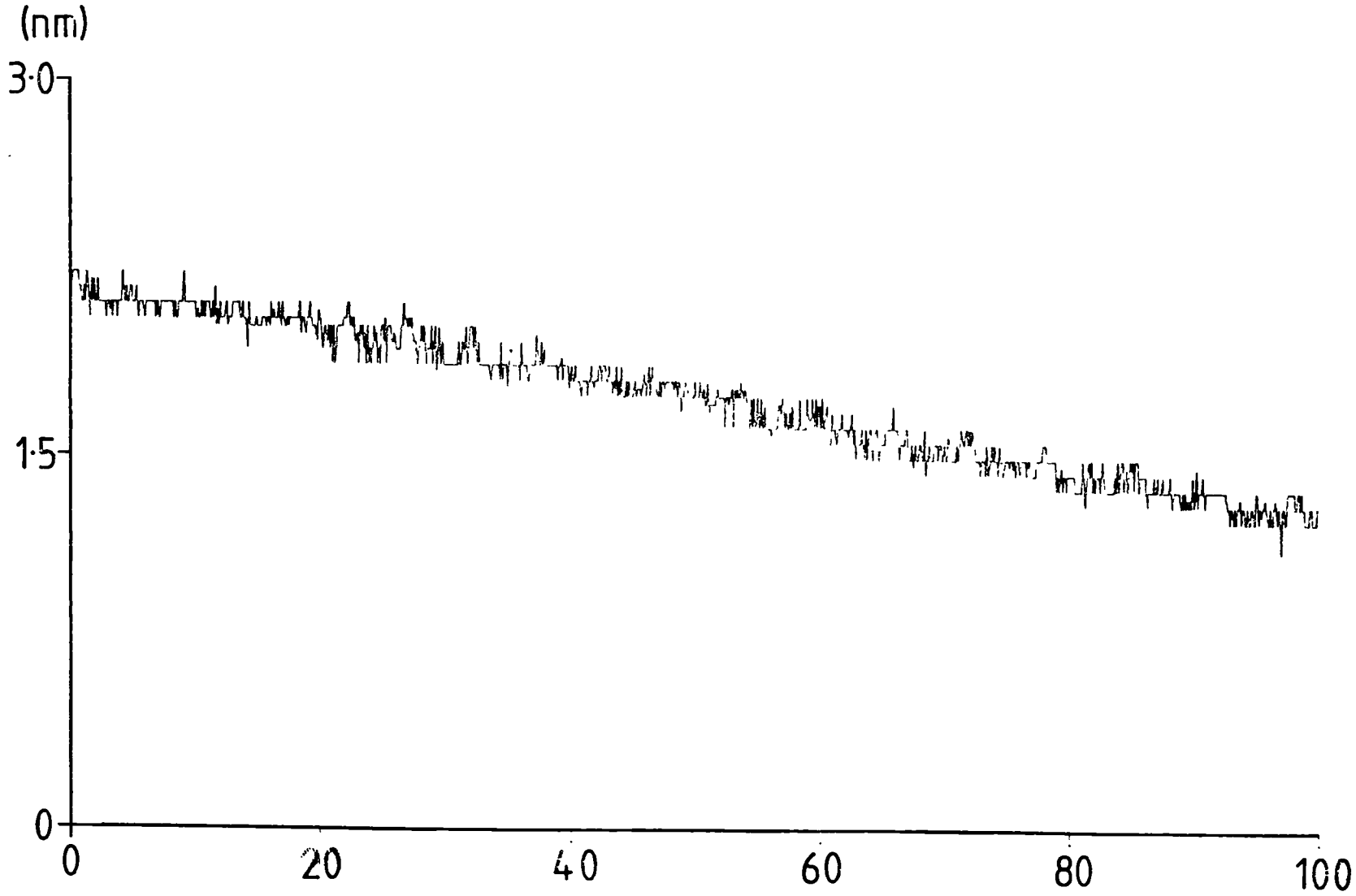

Figure 5.4: Resistance of bead type thermistor (TH B15) against temperature

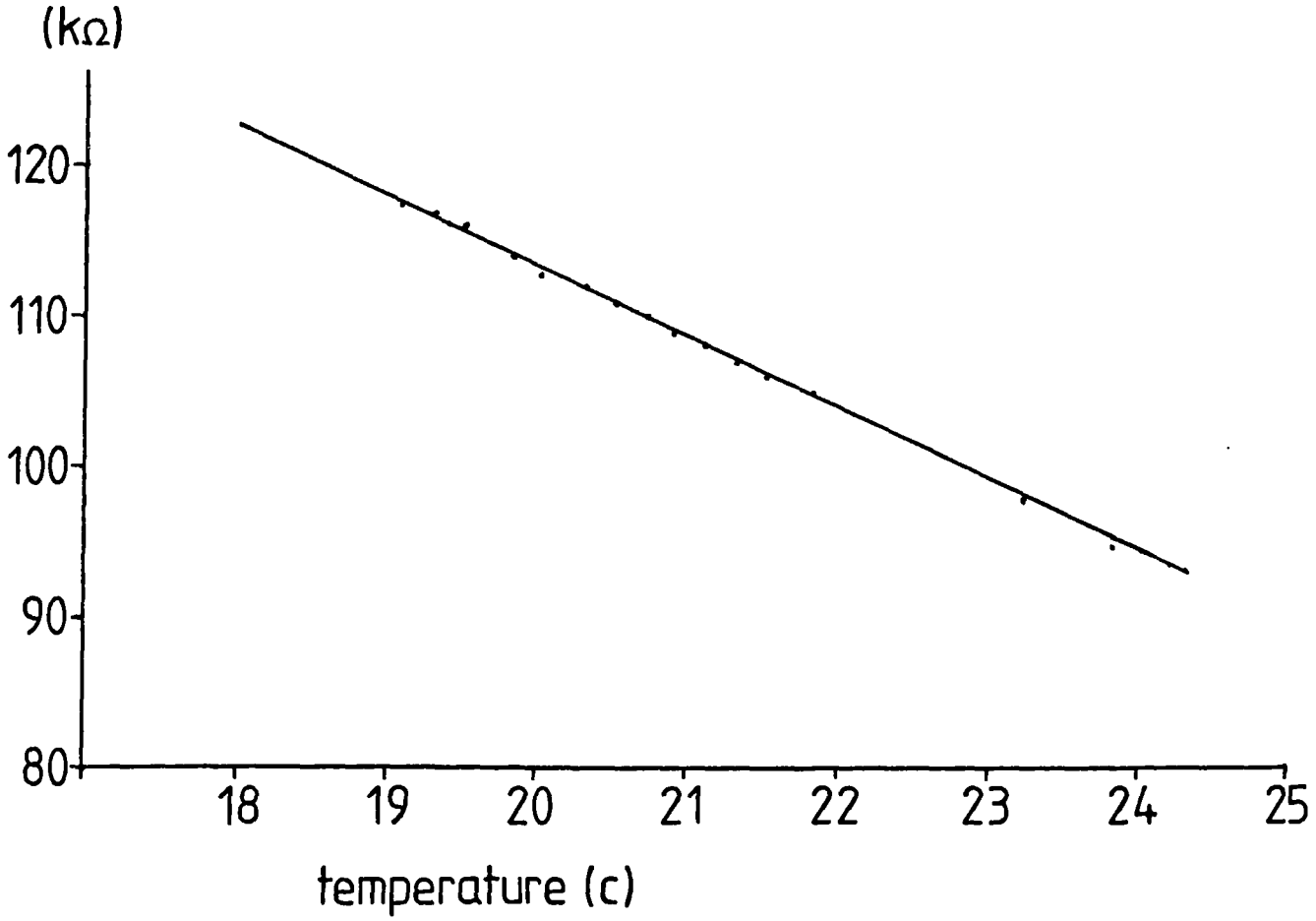

Figure 5·5:Rapid thermal response

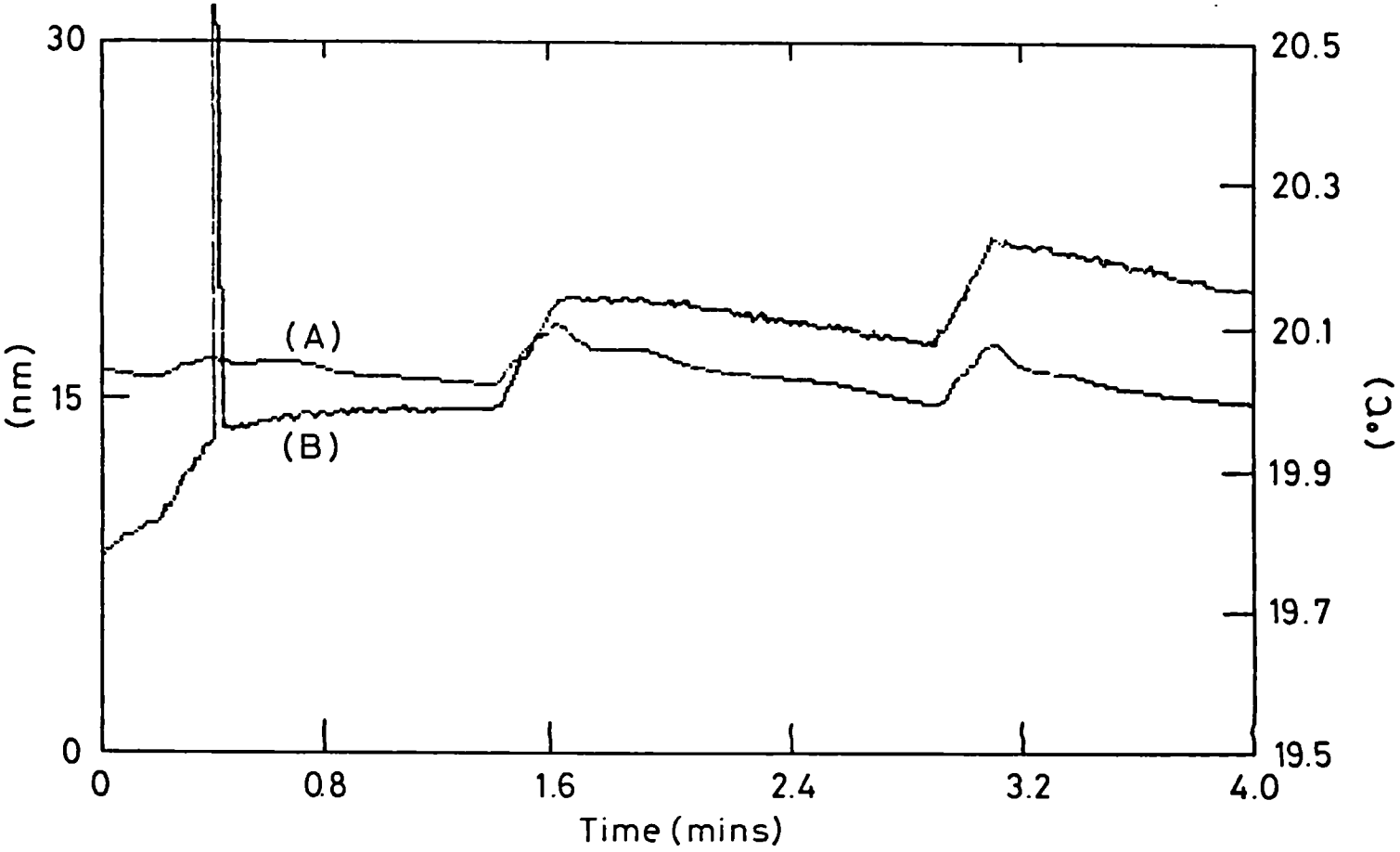

Figure 5·6: Slow thermal response

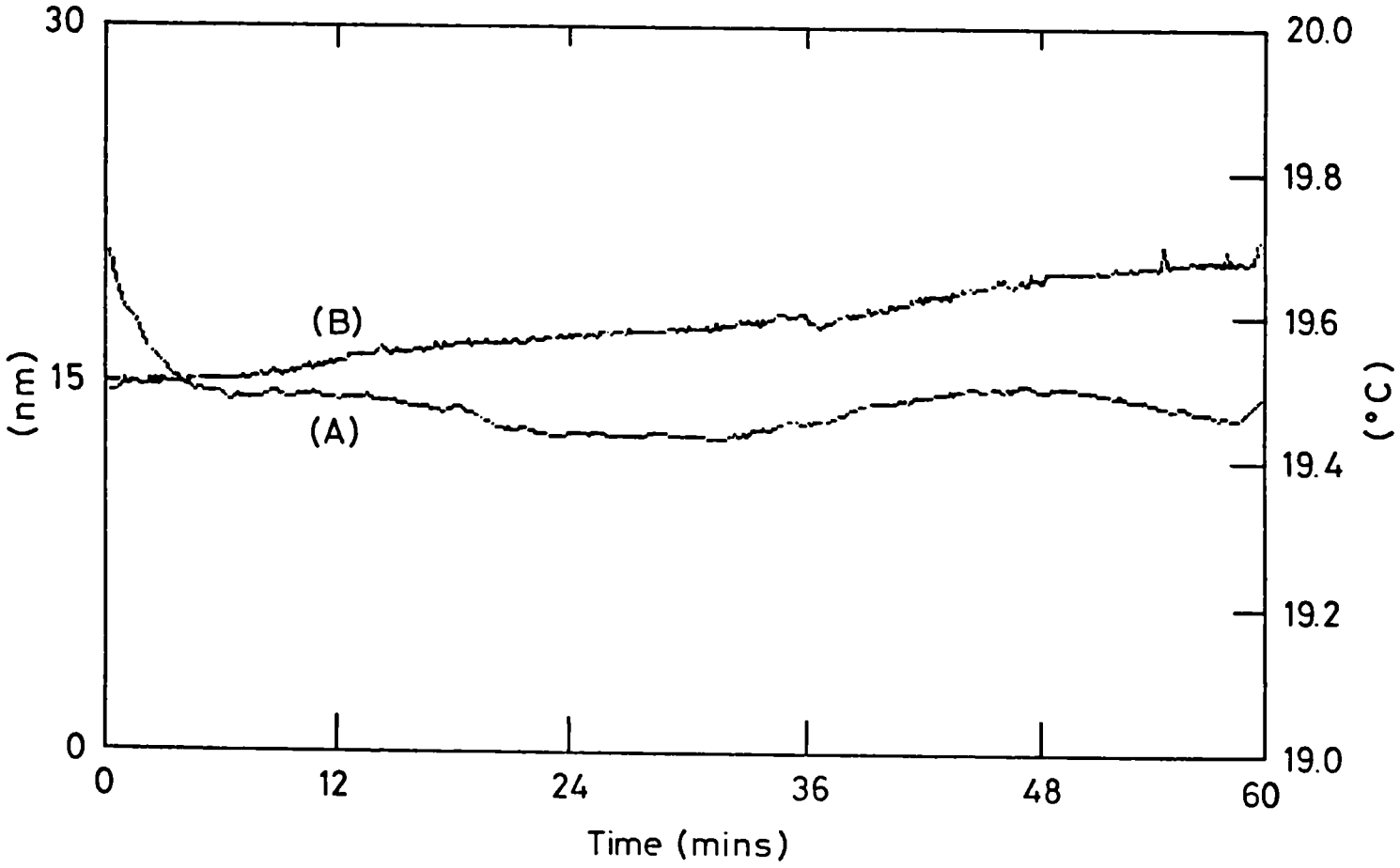

Figure 5.7: Static and dynamic system noise

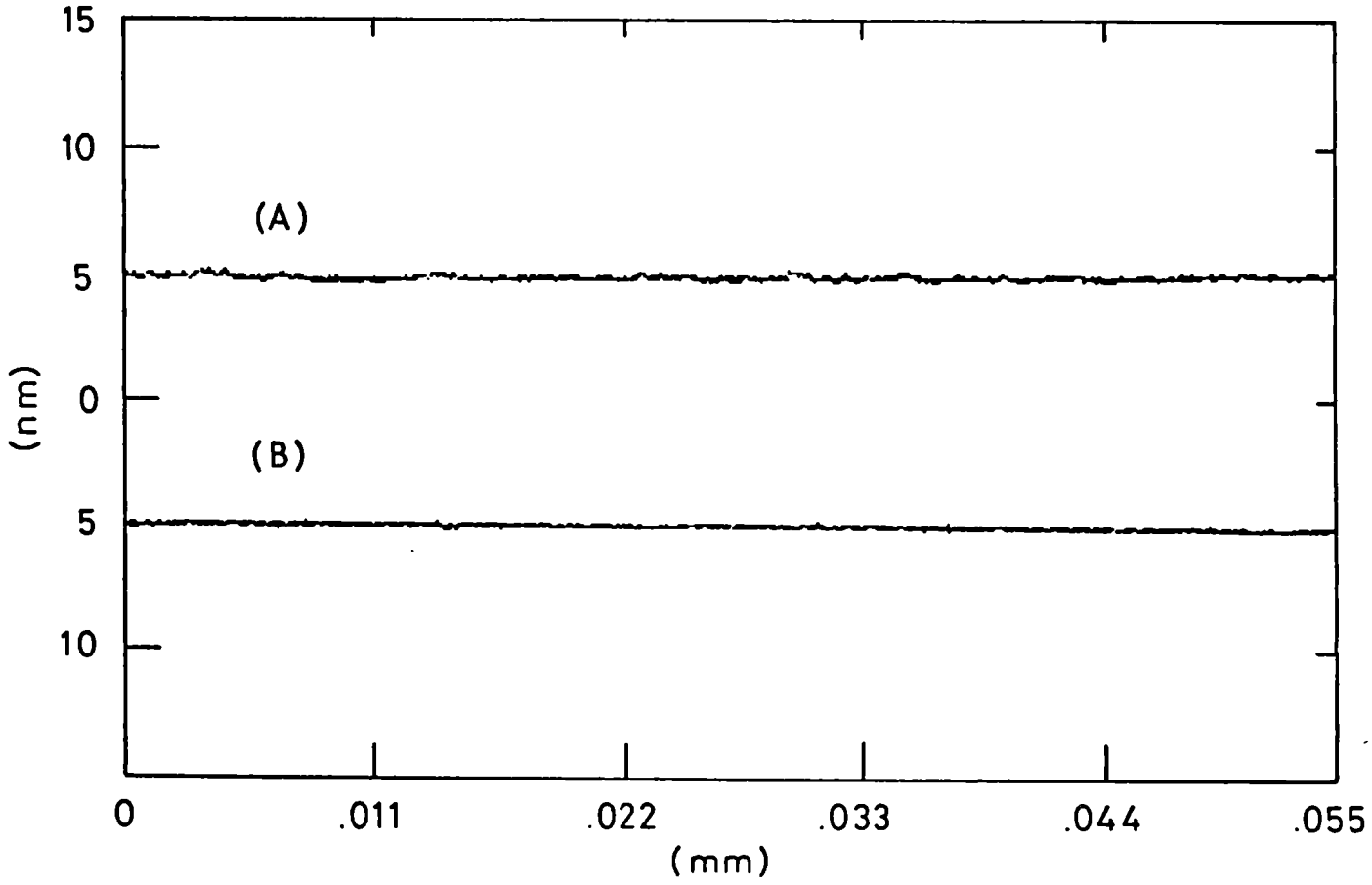

Figure 5·8: Repeat long traces of a pure silica optical flat surface

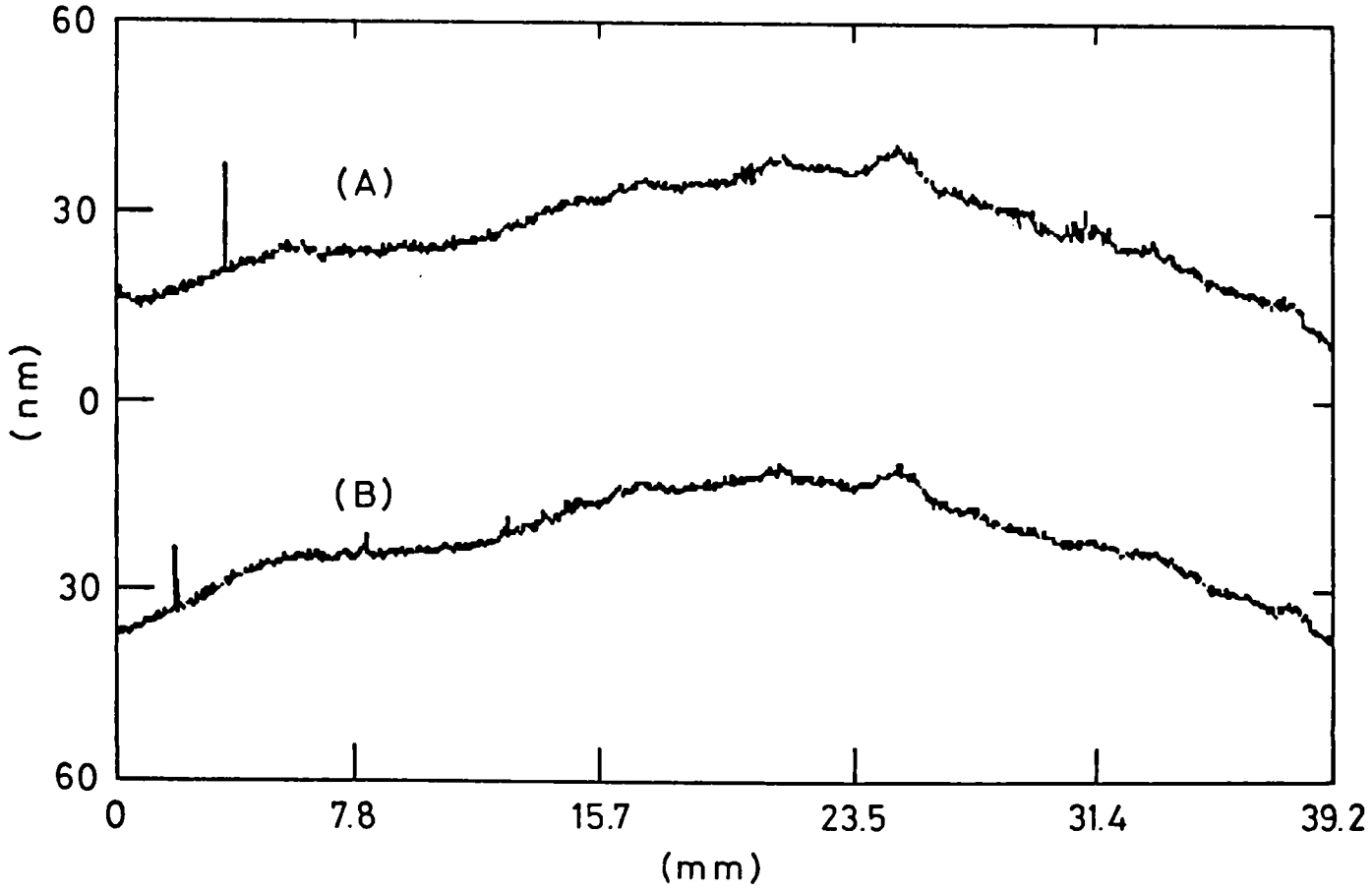

Figure 5.9: Long range repeatibility: trace B-A

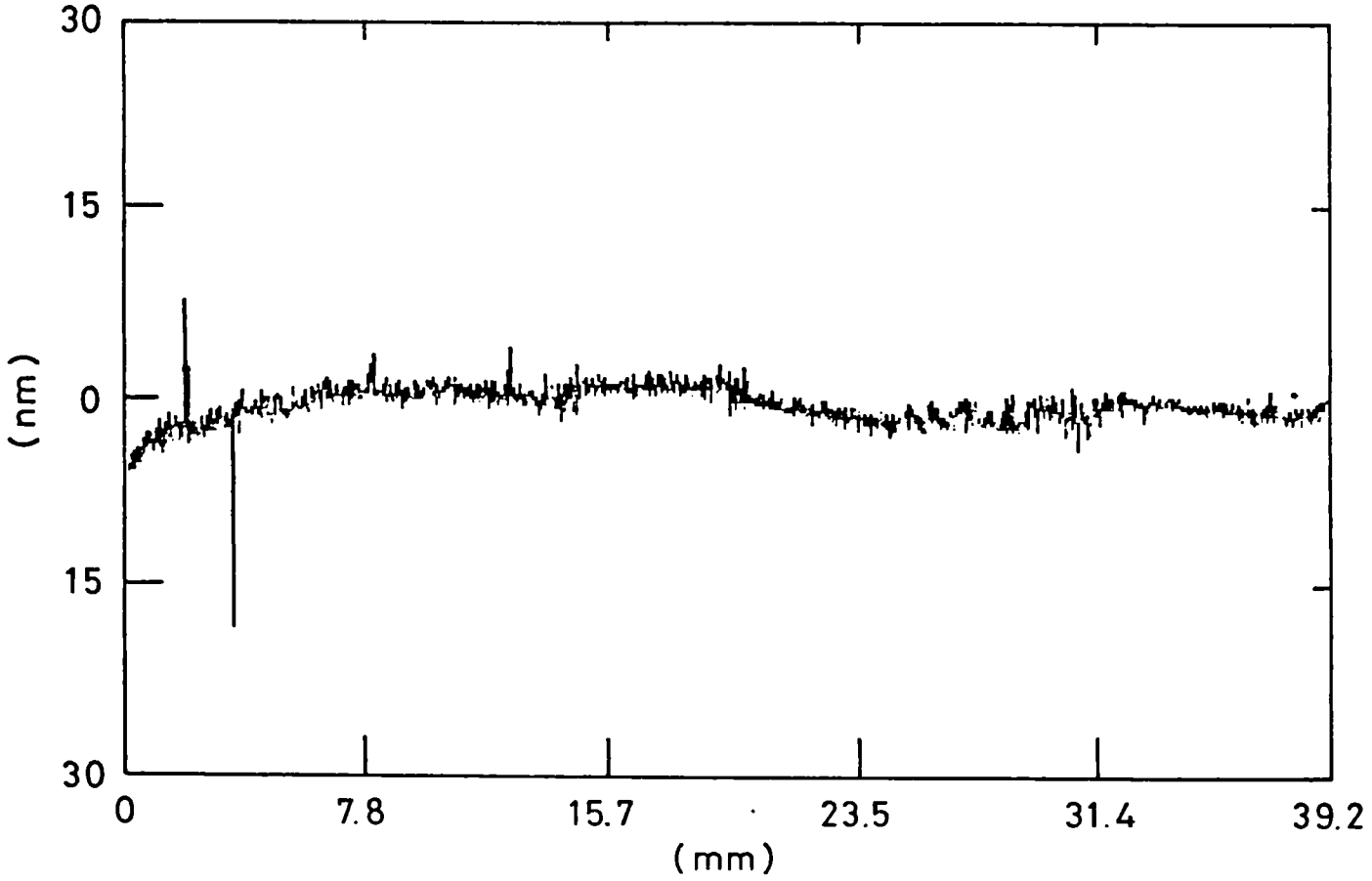

Figure 5.10: Two independent traces over similar region of a super-flat zerodur mirror

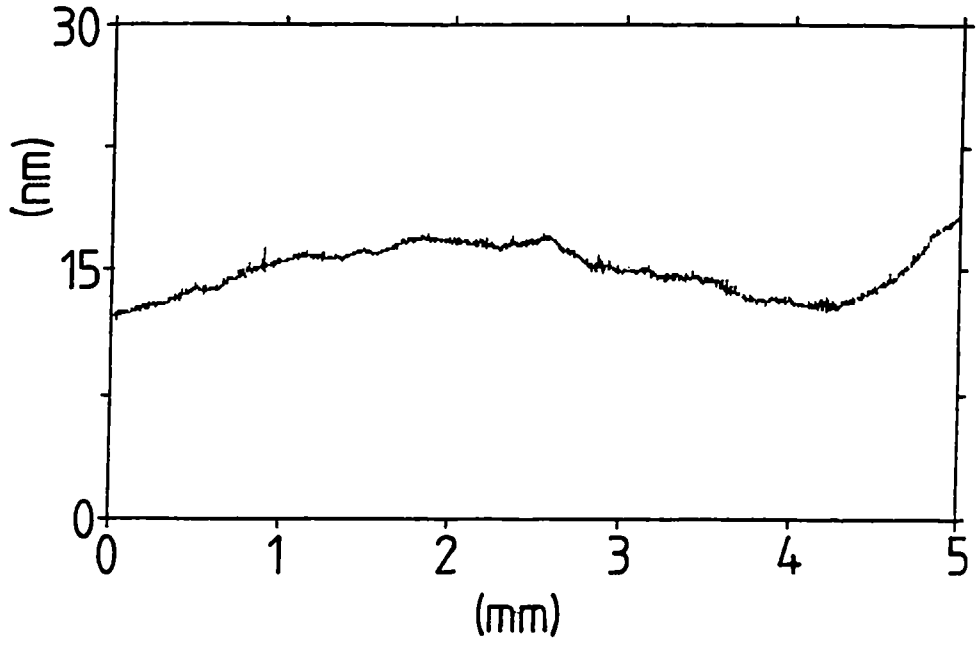

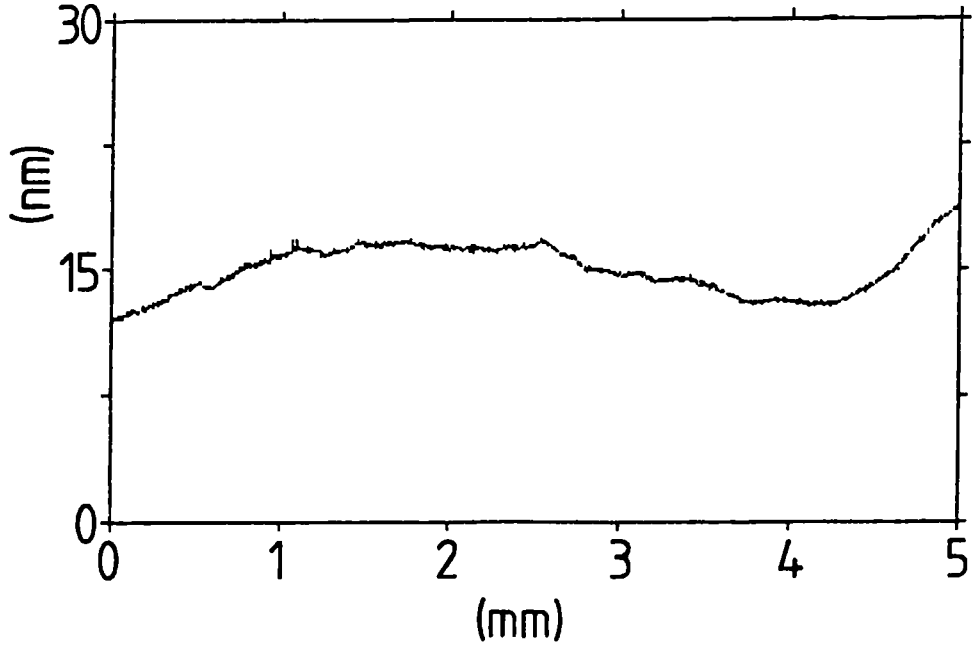

Figure 5.11: Optical interferograms of two slides after polishing

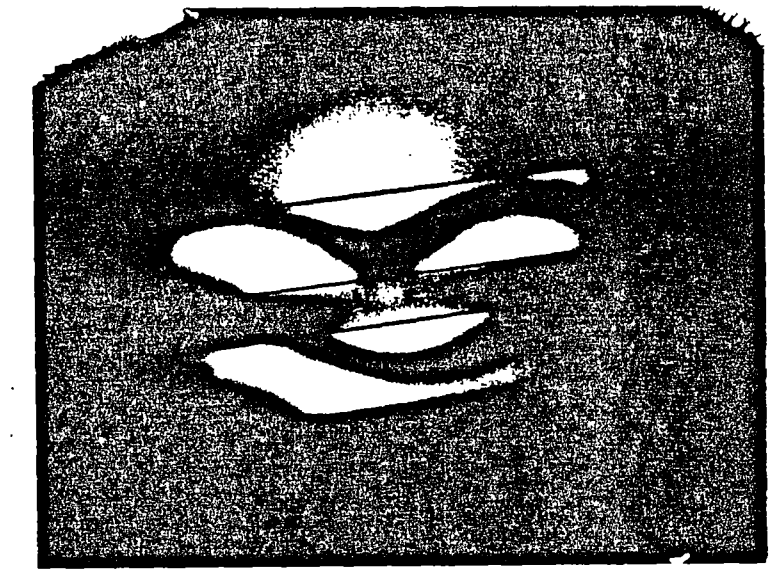

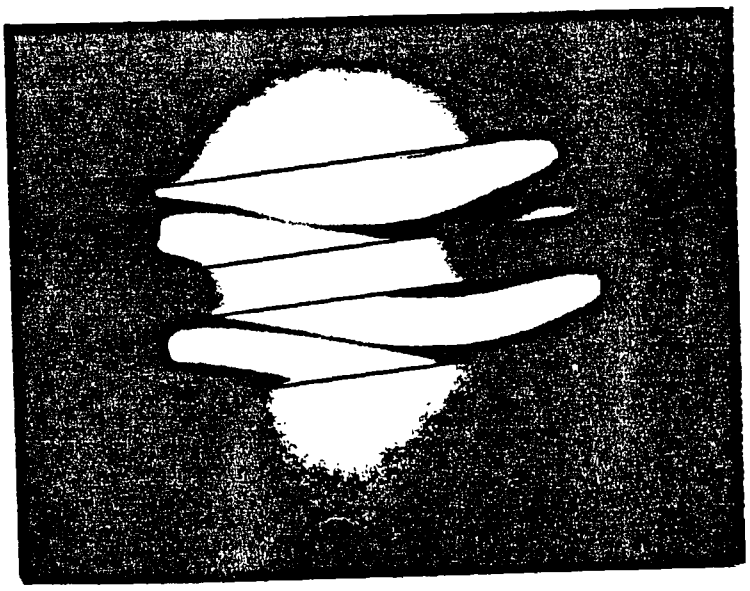

275mm

Figure 5.12: Schematic representation of carriage/slideway configuration

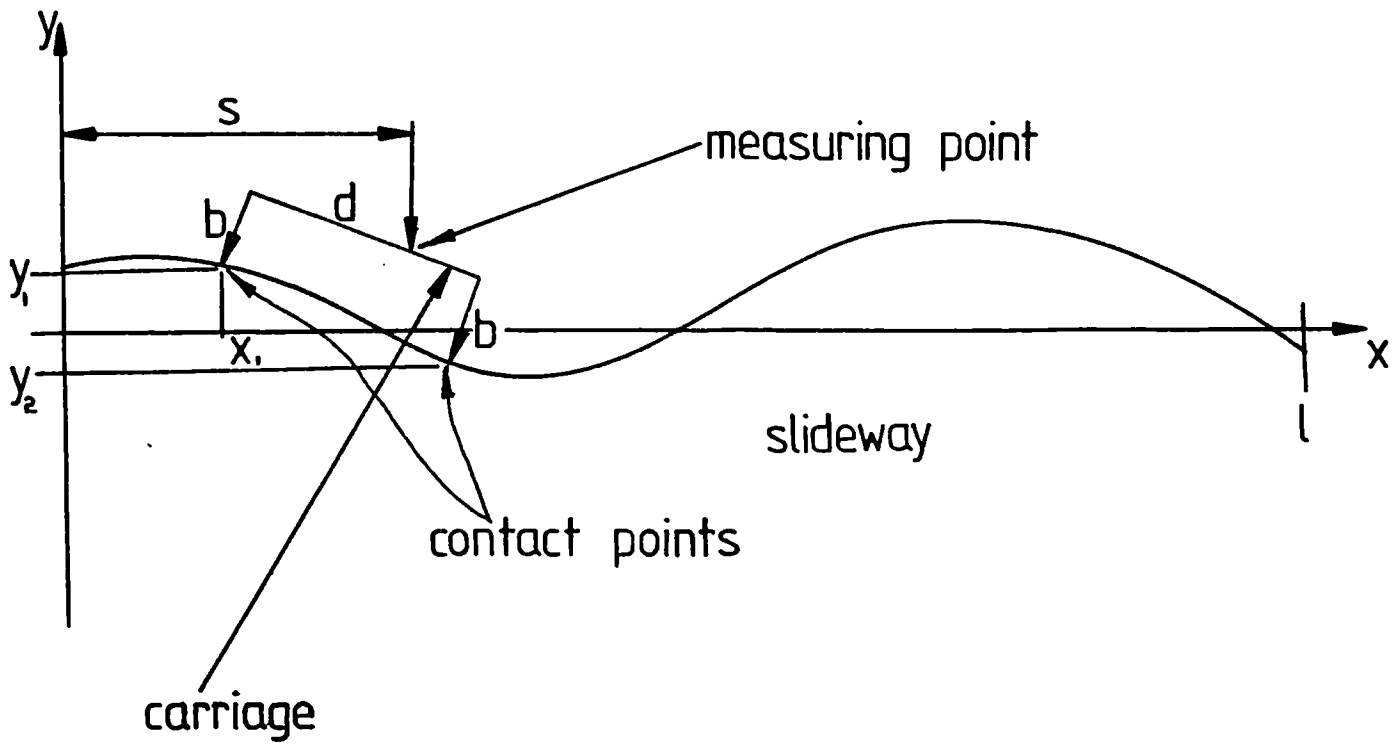

Figure 5.13:Measurement point variation over 50mm traverse for successive start positions

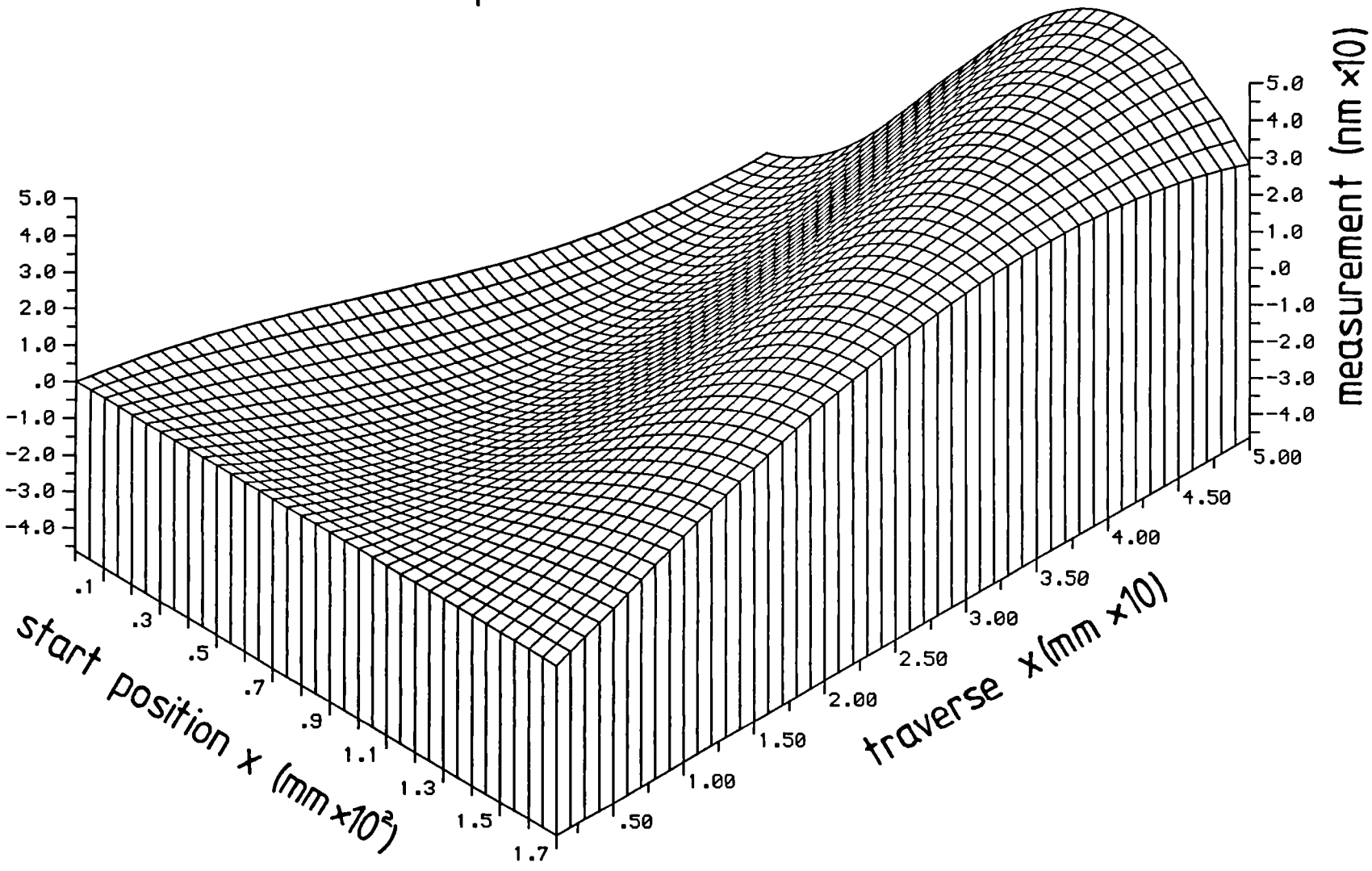

Chapter 6: An assessment of the monolithic linear spring and its application in Scanning Tunneling Microscopy, X-ray Microscopy and X-ray Interferometer systems

6.0 Introduction

Although a lot of useful information relating the performance to the construction of fabricated leaf type linear spring systems exists, little can be found that extends to monolithic web type hinges. To this end a number of experimental investigations have been performed. For comparison, both feedscrew and electro-magnetic drives have been employed in the experiments.

The results from these tests and the analysis of chapter 2 imply that rectilinear displacement mechanisms utilizing the above design principles will adequately satisfy the requirements for a number of precision instruments. The later sections in this chapter describe the use of these mechanisms in STM/X-ray interferometry and X-ray Microscopy. Particular attention will be paid to the integration of the linear spring system into a complete STM design.

6.1 Experimentation

The objective of the initial experiments was to translate a number of monolithic web hinge rectilinear spring configurations and monitor any parasitic errors that may occur. The source of these errors is also of great interest. A schematic diagram of the experimental procedure is shown in figure 6.1. The linear spring is firmly attached to the mounting block and driven by a feedscrew and wobble-pin arrangement similarly held. All of the experiments were performed in a temperature-controlled laboratory and the results presented are representative of a large number of tests over a period of about two months. Problems associated with mechanical hysteresis have been avoided by driving away from the rest position of the springs and keeping stress levels well

below the yield value. Linear platform displacements were measured by a Hewlett Packard 5526A laser measurement system that had a realisable accuracy of 50nm in stable thermal conditions. Rotations about the three principal axes were measured using a Hilger & Watts simultaneous two-dimensional autocollimator. This had a realisable accuracy of 0.5 seconds of arc. The feedscrew drive was accurate to 0.005mm. The coordinate system for these measurements is shown in figure 6.1. The depth of the webs (h of equation 2.3) was 10mm for the springs used in these tests. A discussion of the three types of spring on which these experiments are based can be found in section 2.2.

6.2 Results

6.2.1 The simple compound monolithic spring

Primary platform rotations (α) and (γ), representing yaw and roll, could not be detected over 0.5mm of traverse. There was, however, a pitch (β) of 3", figure 6.2a. By adjusting the angle and position of the wobble-pin it was possible to alter or even reverse this rotation. This suggests that the pitching motion is caused by forces due to errors in parallelism and rectilinearity. An eccentricity of the recess in which the wobble pin is located at the drive will cause the pin to follow a circular path about the drive axis. This may result in a periodic pitching error. The torsional stiffness of the systems can be increased without altering any of the other design parameters by joining two springs together in the x-y plane at a fixed distance. For monolithic devices this presents alignment difficulties that are not present in fabricated springs and thus has not been investigated. The primary/secondary platform displacement ratio, corrected for elastic effects of the drive mechanism, is around 1.94, figure 6.2b. The variations about this value correspond to an error standard deviation of 0.33μm in the drive device. This is similar to that quoted in section 6.1. This ratio error will correspond to a parasitic y-axis error of 5×10^{-8} over the traverse considered and is beyond the measurement capability. Variations in y-axis motion were small (≈100nm) and irregular suggesting that external influences (i.e temperature gradients and mechanical vibrations) are dominant.

6.2.2 The slaved compound rectilinear spring

Parasitic errors of this mechanism were significantly greater than those observed in the unconstrained springs. Over a displacement of 0.5mm a pitch and roll motion of nearly 30″ was measured. A yawing motion of 8.5″ was also measured. These large parasitic errors are caused by a couple introduced by the slaving mechanism itself. The difference between the monolithic and the more conventional slaving device is the fact that the hinge in the former has stiffness in the rotation axes whilst the latter only possesses a small and constant angular resistance. With the mechanism removed, the performance became comparable to that of the unslaved spring.

6.2.3 The double compound monolithic spring

The principle of operation of this device is similar to that of the simple compound spring and it exhibits a corresponding rectilinearity (figure 6.2). The main increase is in the stiffness and volume. As with previous devices, there was a slight pitching error that is mainly attributed to influencing by the drive. Errors in y-axis motion, roll and yaw are not detectable over 0.35mm of travel.

Remounting the laser measurement system parallel to the z-axis, parasitic deflections are again undetectable over 0.3mm of travel. These results could only be obtained after considerable manual manipulation of the feedscrew drive mechanism, further indicating the limitations of such a device.

The double compound spring was manufactured on a Kunzmann CNC vertical milling machine. Measurement of manufacturing errors on this relatively inexpensive machine using the CSIP universal measuring machine gave typical values of δ=0.02mm and $\phi=3\times10^{-3}$ for use in equations (2.8) and (2.9). For worst case conditions with these values, individual hinges could vary in stiffness by up to 50%. The primary/secondary platform displacement ratio of 1.97 (figure 6.2b) shows the favourable effects of averaging and kinematic overconstraint.

6.3 The electromagnetic translator

Having determined the parametric design considerations for linear elastic springs and drive

techniques in chapter 2, an electromagnetic drive system was matched to a stage . This stage (courtesy NPL Teddington) was a low stiffness large traverse design based on folded simple parallel springs. This provided an opposite extreme to the high stiffness short range drives that have been amply proved on x-ray interferometers, Bowen et al, 1985. The analysis procedure was similar to the previous experiment in that drift, out of plane motion and translation have been monitored using laser interferometry. The coil drive and measurement system were controlled using a BBC model B microcomputer, IEEE 488 data bus and Bede Minicam interface module.

The graphs of figure 6.3(a-f) are representative of results obtained from these tests. A magnet/coil force transducer was mounted to form an x-axis drive whilst the y-axis was left to "free float". The device used a 5mm × 5mm samarium/cobalt magnet positioned along the axis of a 500 turn coil 12mm long and 6mm internal diameter. This gave a force of 1.6×10^{-4} corresponding, with this slide, to a displacement of 50nm mA^{-1}. The x-axis drift has been monitored in both the free mode (no coil current) and with the coil energised, figure 6.3(a & b). Note that the fluctuations observed are near to the 50nm resolution of the measurement system, so the details of the curves should not be taken as definitive. Inductive vibration damping can be clearly observed. The major perturbations in this system occurred in the y direction, figure 6.3(c). This is because it is the most compliant axis with the least damping. The x-axis motion and y axis drift were monitored for input forces corresponding to displacements ranging from 1 to 50μm. The y-axis drift during an x-axis traverse of 4μm is shown in figure 6.3(d). This is similar to graphs obtained for free drift and thus is not significantly influenced to the measurement resolution. The x-axis motions under different forces are shown in figures 6.3(e & f). Figure 6.3(e) is an initial uncalibrated motion of approximately 5.4μm and 6.3(f) is a 3μm calibrated translation. The linearity of x-axis translation is excellent and departures could not be detected over a 50μm translation, which also includes contributions to the errors from the electronics. Whilst the coil/magnet contains some damping it is clearly necessary to design a stiff drive to minimise errors induced by vibration. However, figures 6.3(a - f) show that biasing influences of the electromagnetic drive are undetectable at system resolution whereas they were a serious problem with the feedscrew and wobble-pin arrangement.

The force on the magnet at the optimum position (usually with the magnet positioned such that its centriod is coincident with the end of the coil) can be obtained from solutions to equations 2.25 to 2.32. The general characteristics of this magnet and solenoid transducer are shown in figure 6.4(a and b). This shows graphs of the field and force between magnet and solenoid along the axis from the centroid of the coil. It is clear from figure 6.4b) that as long as the magnet is positioned close to the end of the coil, the force will remain constant even if small fluctuations in the this position do occur. This demonstrates the important property that the drive force is independent of dimensional stability.

6.4 The design applications of linear spring systems

6.4.1 An X-ray Microscope XY specimen stage

As mentioned in chapter 1, to obtain an x-ray microscope image, the specimen must be raster scanned in the focal region. A scan range of 100μm is required with parasitic deviations of less than 10nm. It is clear from previous discussions that this requirement can be satisfied using the linear spring systems of the above analysis. For this purpose, an experimental aluminium XY stage, based on the folded notch type simple spring, was produced. This is driven by an electromagnetic pusher via a computer and 16-bit digital to analogue converter (DAC) giving a range to resolution of 1 part in 65,536. This will adequately satisfy the design specification. The design parameters for the complete system have been calculated using the computer program of Appendix B. The stiffness of the stage in each individual axis is $1.3\times10^{4}N/m$ and a lowest natural frequency of ≈100Hz is predicted. In accordance with the the analysis of section 2.5, all the following coils for these devices have geometry factors (α_c and β_c) of 2.0 and 1.0 respectively. The coil consists of 1500 turns of copper wire and has an internal radius of 6mm. The magnet is a samarium/cobalt rod, 10mm diameter by 5mm long. For a remanence value of 1.08Tesla a magnetic moment of $\approx4.23\times10^{-7}$ is calculated from equation (2.30). This will give a force constant K_1 of 2.47N/A. For an input power of 2.8W, an displacement range of 103μm has been calculated. The required voltage of 14v is obtained from a precision power amplifier capable of up to 30v. Because this is a trial stage and will be operating at relatively low velocities, a dynamic analysis

has not been carried out.

6.4.2 The design of a combined Scanning Tunnelling Microscope and X-ray Interferometer instrument

6.4.2.1 The specimen translation mechanism

The philosophy of having an XY raster scan for the specimen and following by a servo system in the Z plane has been adopted in this design. To fully utilise the resolution of the tunnelling probe, an accuracy and stability of <0.05nm over a range of 10μm is required. Over a range of 0.1μm this criterion has been adequately satisfied using a monolithic parallel spring manufactured from single crystal silicon, Hart, 1968. The use of this material has the two distinct advantages of favourable material properties and the ability to form an x-ray interferometer. A diagram of the XY stage is shown in figure 6.4. This stage is again based on the folded simple parallel spring arrangement with leaf type springs. The electromagnetic drive is identical to that used with the x-ray microscope. The stiffness of these springs is 2.37×10^5 which will correspond to a displacement of ≈14nm/mA. The depth of these springs is 10mm. A fundamental mode natural frequency of approximately 400Hz has been calculated.

The dynamic characteristics of the raster scan can be computed from equations (2.46 - 2.49). A voltage ramp of 1v/s has been applied to the coil, figure 6.6, resulting in a displacement of 200nm, figure 6.7. The plots of figure 6.8(a & b) are the inherent dynamic errors that will result from an open loop system using current and voltage respectively as a monitor of position. The values for the inductance and the critical damping factor that have been used are 0.024h and 0.03. It can be seen that parasitic errors of less than 0.2nm transient and 0.01nm steady state are encountered for this fast rate of 1 scan per second and the relatively large scan distance. The stresses incurred by the platform support legs are plotted in figure 6.9. These are an order of magnitude within the safe stresses assumed for flawed silicon, Lawn, 1981. A stress concentration factor of 1 has been used for this calculation as obtained from Peterson, 1977.

6.4.2.2 Probe control

The probe displacement spring is shown in figure 6.10. This has three interferometer blades as a part of the monolithic structure. The analyser blade is in the line of action of the force transducer and the probe. This will enable secondary monitoring of probe position to an accuracy of 10pm or less. The tunnelling probe is made from a 1mm diameter tungsten wire and the sharp tip is produced by electrochemical etching. This will be described in chapter 7. This is held by an aluminium holder that is clamped to the z-axis platform, figure 6.11. This mechanism is similar to that sued for securing the leads in a common drawing compass. Because of the reduced mass of this stage, a fundamental frequency of ≈550Hz has been calculated. This spring is bonded to the x-y stage in a perpendicular plane to form the complete x-y-z mechanism, figure 6.12. The bonding of silicon is discussed in section 7.6.

The probe is required to follow the surface contour and be thus capable of dynamically reproducing displacement patterns of unknown characteristic. This very linear system can be analysed using simple control theories.

The servo system for probe control is represented schematically in figure 6.13. The change in probe/specimen separation during traverse is monitored as a change in the tunnelling current. This current is amplified logarithmically to give an output of ≈1v/decade giving a sensitivity of $\approx 1\times10^{10}$v/m. This output is fed through a power amplifier to the coil/magnet/spring system with a unity gain, steady state sensitivity of $\approx 1\times10^{-3}$m/v. A control theory representation is shown in figure 6.14. The stability of the system can be determined by the Routh-Hurwitz criterion and, for this system, is governed by the relationship

$$K_1K_2<LM\left[\frac{2c\,\omega_n R_c^2}{L^2}+4c^2\omega_n^2\frac{R}{L}+2c\,\omega_n^3\right] \tag{6.1}$$

Substituting values into this equation it is found that the gain can be increased three orders of magnitude before instability begins. A Nyquist plot of the system transfer function is plotted in figure 6.15. The phase angle/frequency relationship for this system is shown in figure 6.16. The design parameters are; L=0.024h, m=0.02kg, ω_n=3456rad/s, c=0.1, $\lambda=2.37\times10^5$, R_c=69.4Ω. For example, to restrict phase shifts to less than 10 degrees it will be necessary to operate at

frequences of less than 80Hz. A 90 degree shift occurs at a frequency of around 500Hz.

6.4.2.3 Specimen positioning

Specimen position is obtained by moving a sliding platform towards the probe using a differential micrometer. This is driven by a 200 step stepper motor and gearbox arrangement, figure 6.17. The gearbox has a ratio of 60:1 giving a displacement of ≈4.2nm/step. Having obtained a tunnelling current, the micrometer is withdrawn from the platform and the specimen is maintained in position by a friction grip. This grip is similar to that used for the transducer mount in Nanosurf 2 which displayed a stability of <7nm/hr. It consists of an aluminium rod inside of a tube of similar material. The friction force is supplied by PTFE that is sprung between the two surfaces, figure 6.18. Material interface separation is maintained by a layer of high vacuum grease.

Figure 6.1

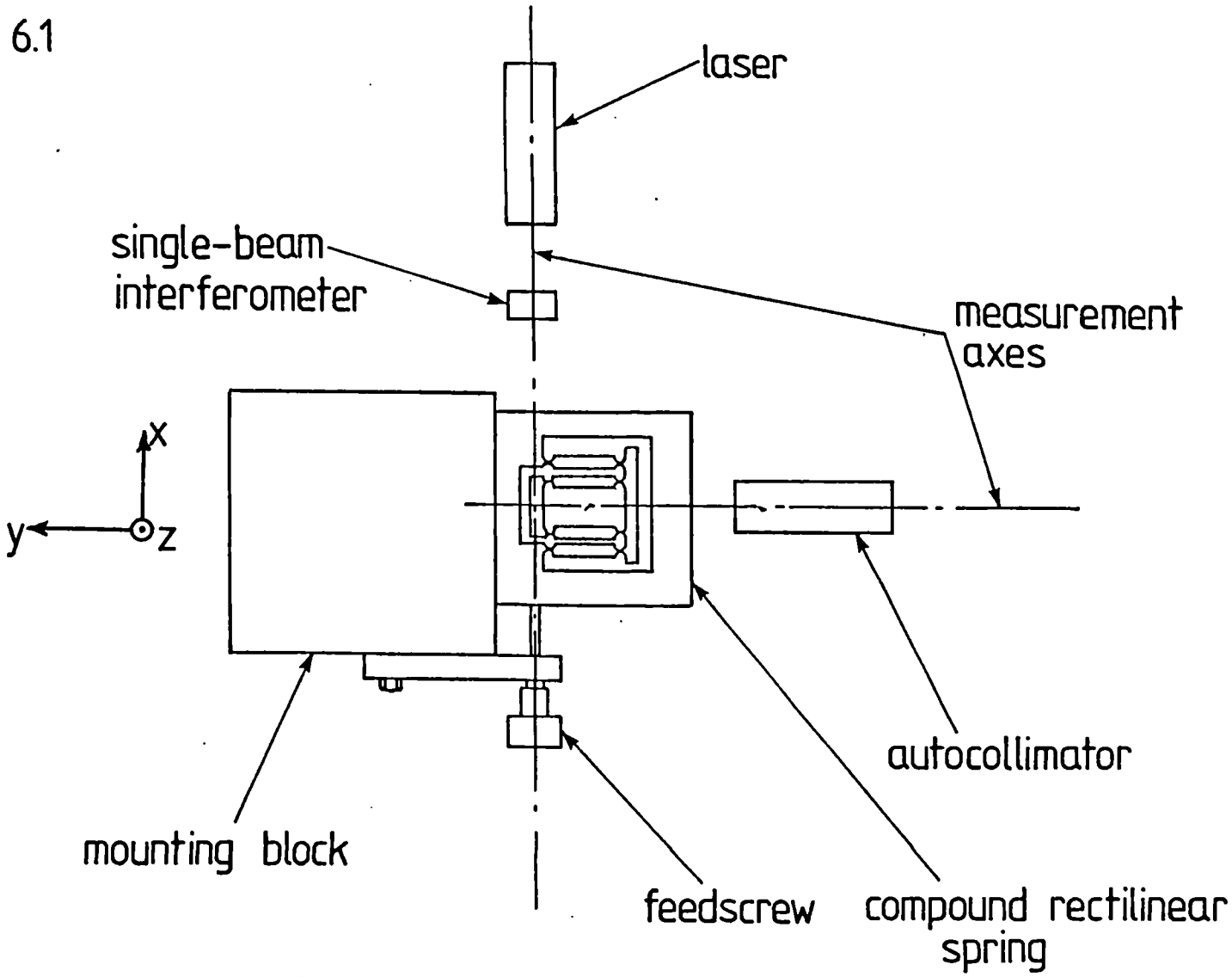
laser
single-beam
interferometer
measurement
axes
x
y
z
autocollimator
mounting block
feedscrew
compound rectilinear
spring

Figure 6.2a: Pitching of the primary platforms

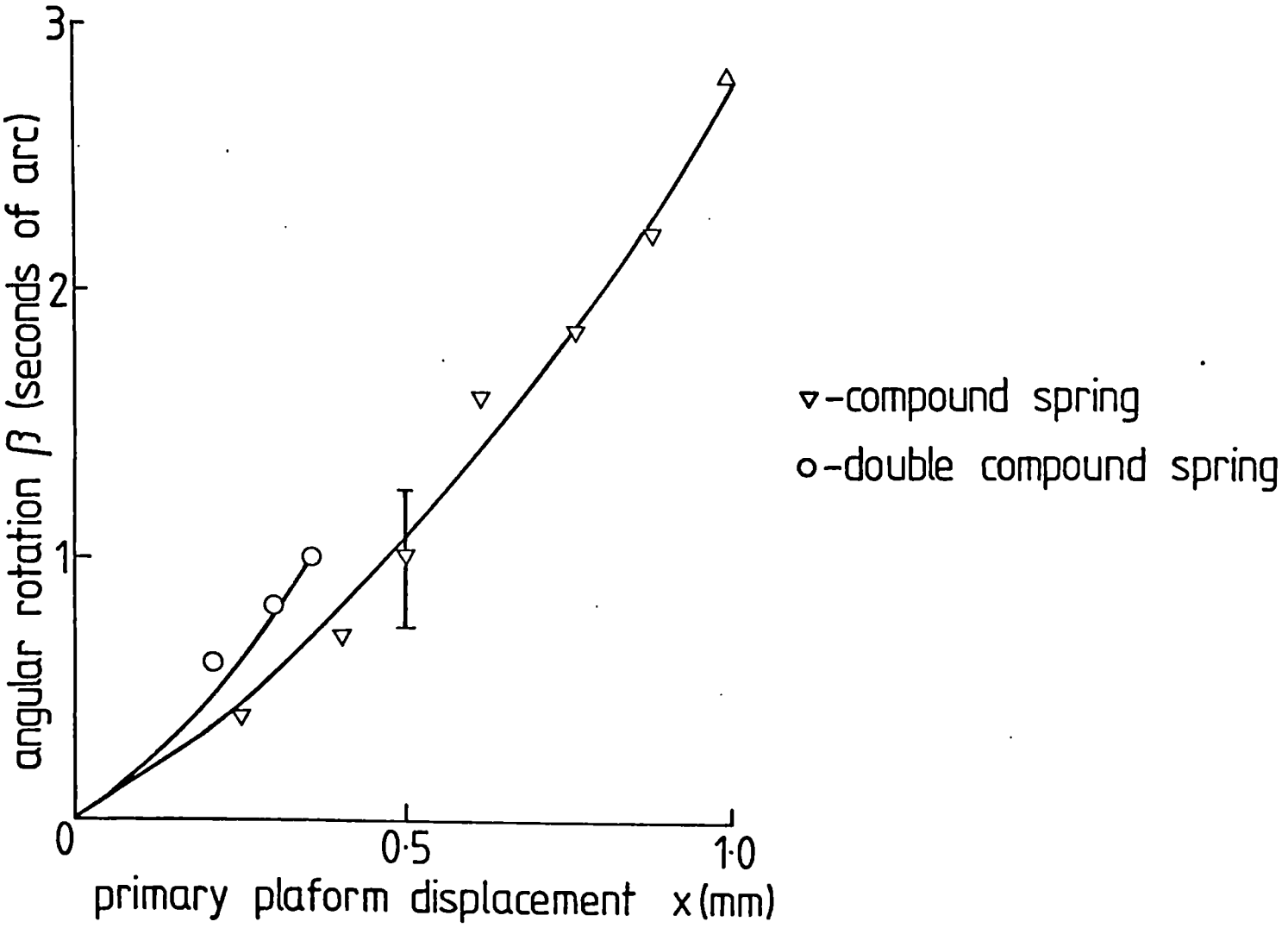

Figure 6.2b:Deviation of primary/secondary platform displacement ratio from the ideal value of 2

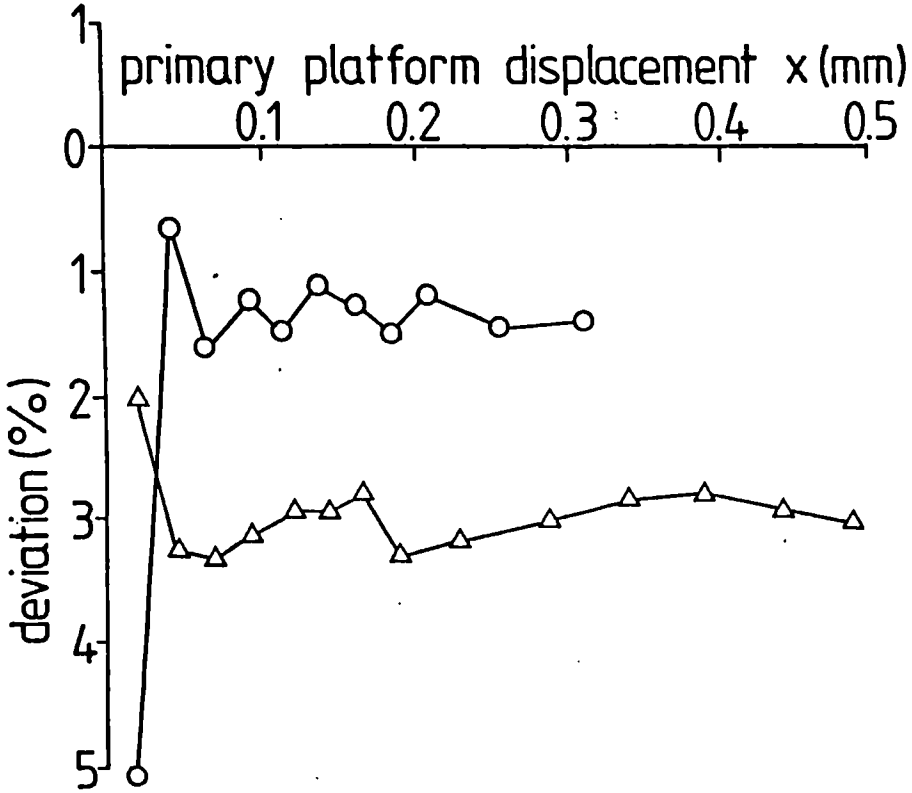

Figure 6.3:Displacement characteristics of an electromagnetically driven linear spring

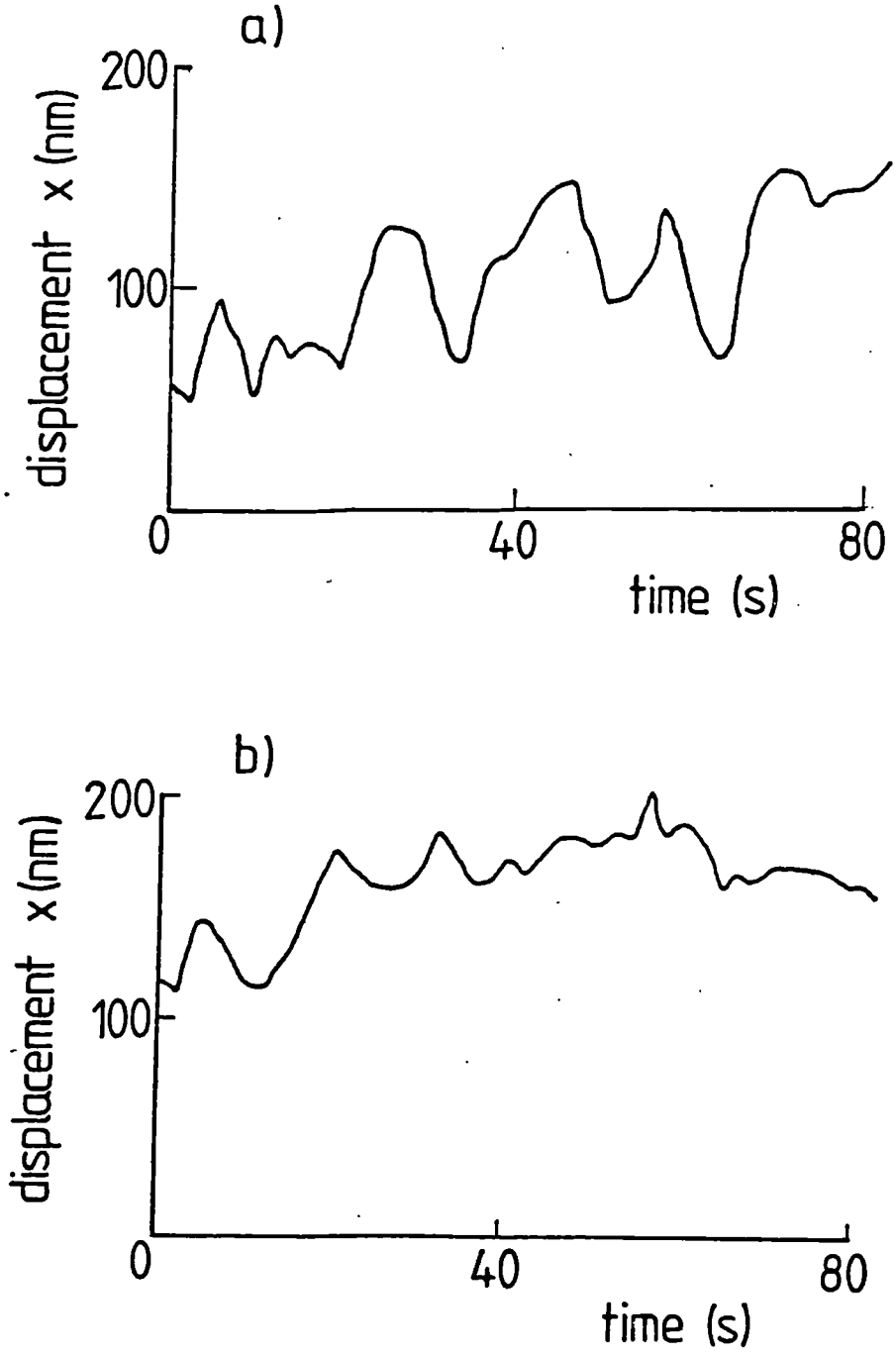

Figure 6.3

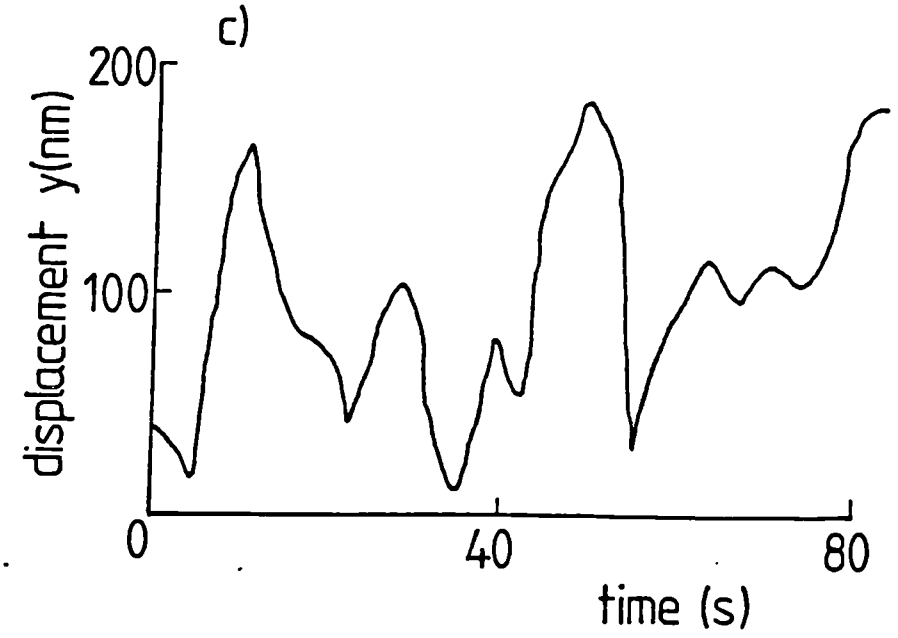
c)
200
100
0
displacement y(nm)
40
80
time (s)

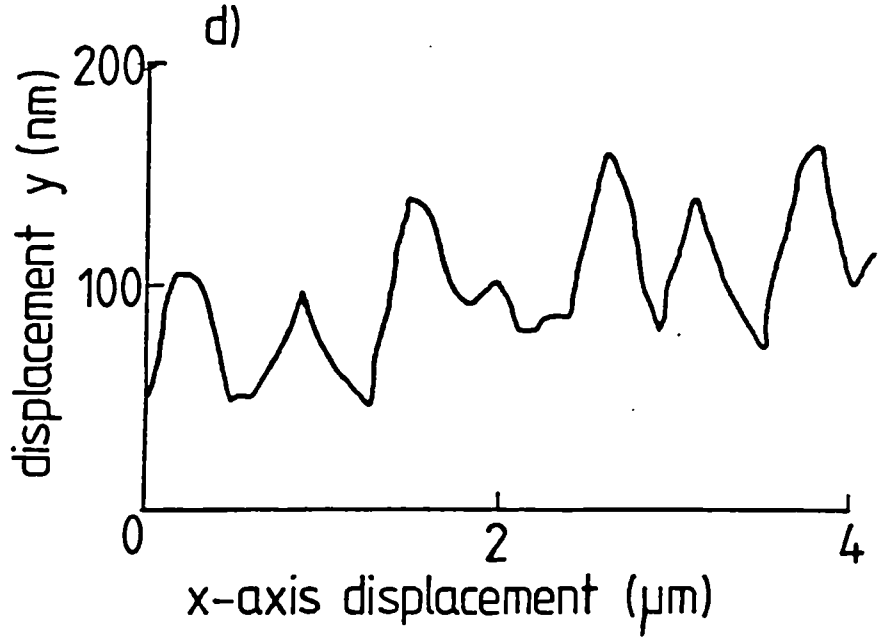
d)
200
100
0
displacement y (nm)
2
4
x-axis displacement (μm)

Figure 6.3

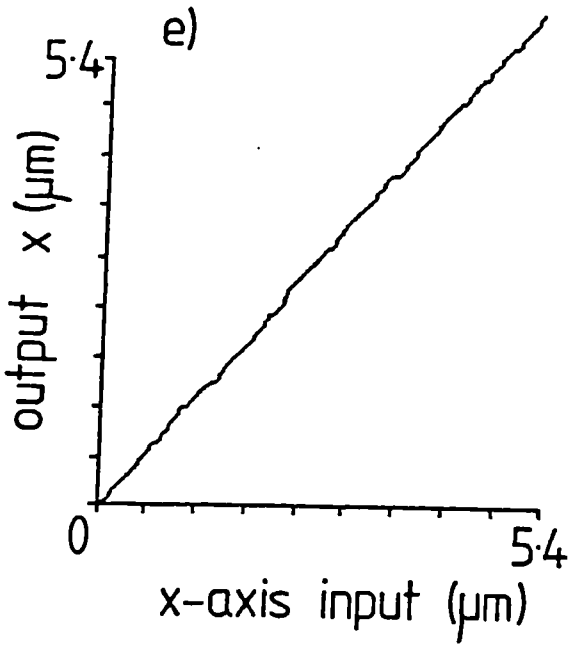
e)
5·4
output x (μm)
0
5·4
x-axis input (μm)

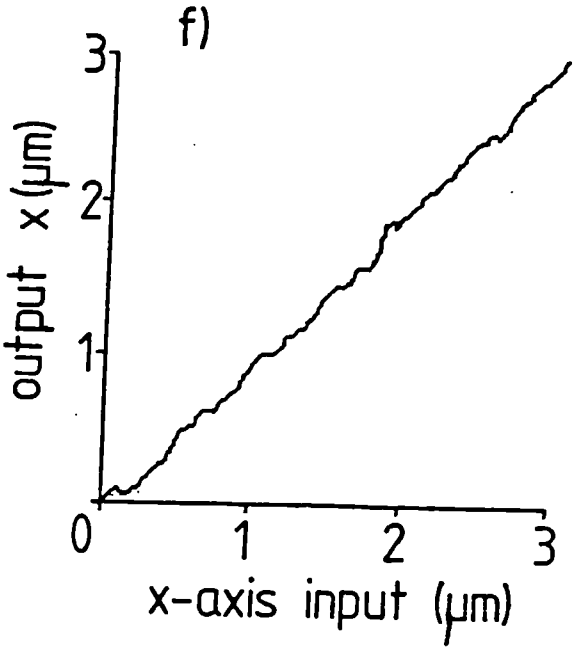
f)
3
2
1
output x (μm)
0
1
2
3
x-axis input (μm)

Figure 6.4: The characteristics of a solenoid coil with a magnet positioned along its axis

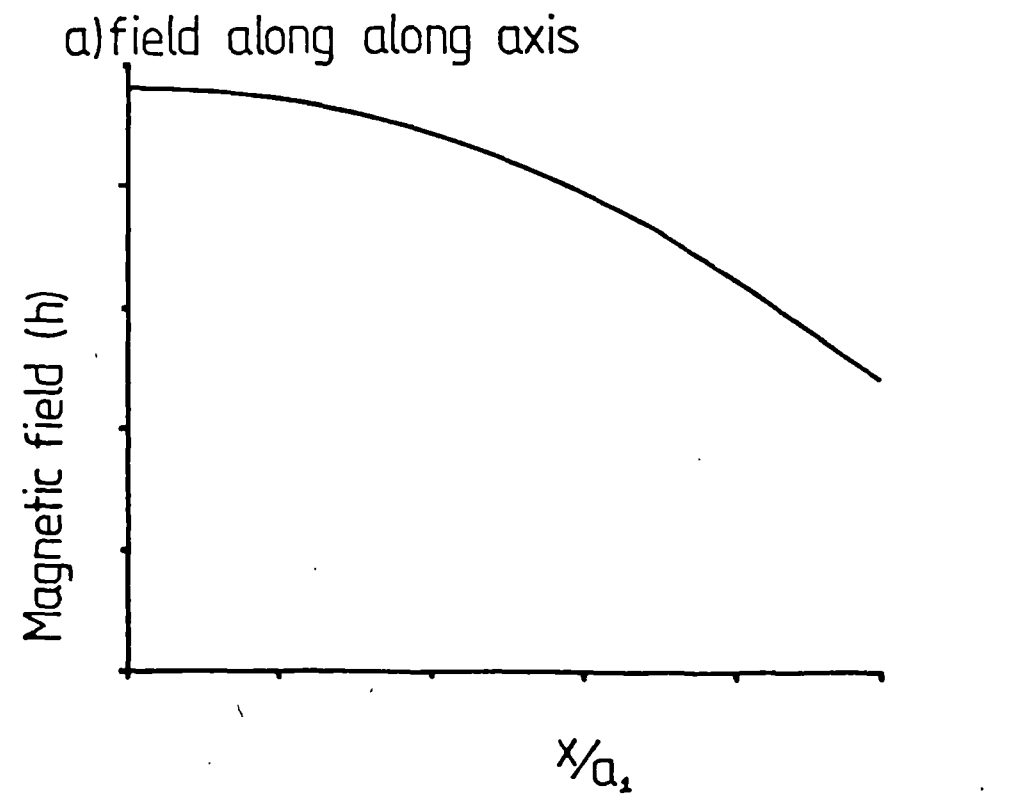

Figure 6.5:Specimen translation stage

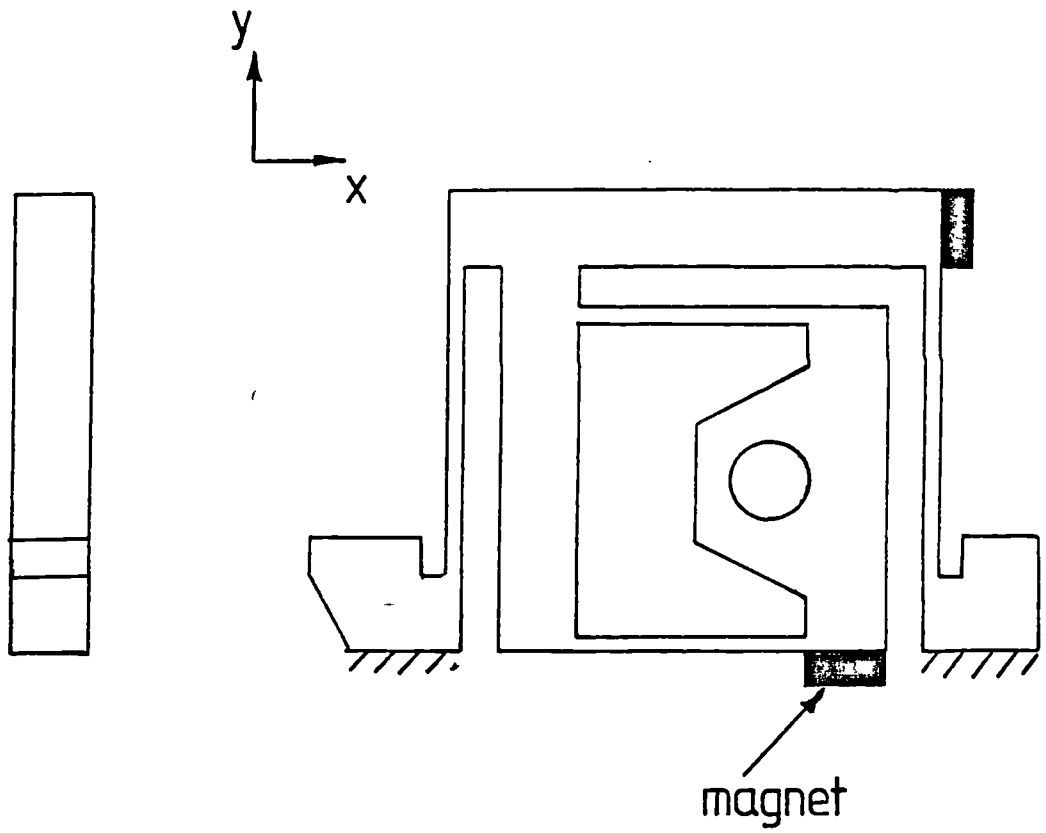

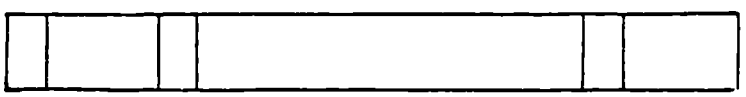

Full Scale

Figure 6.6:Input voltage waveform to coil

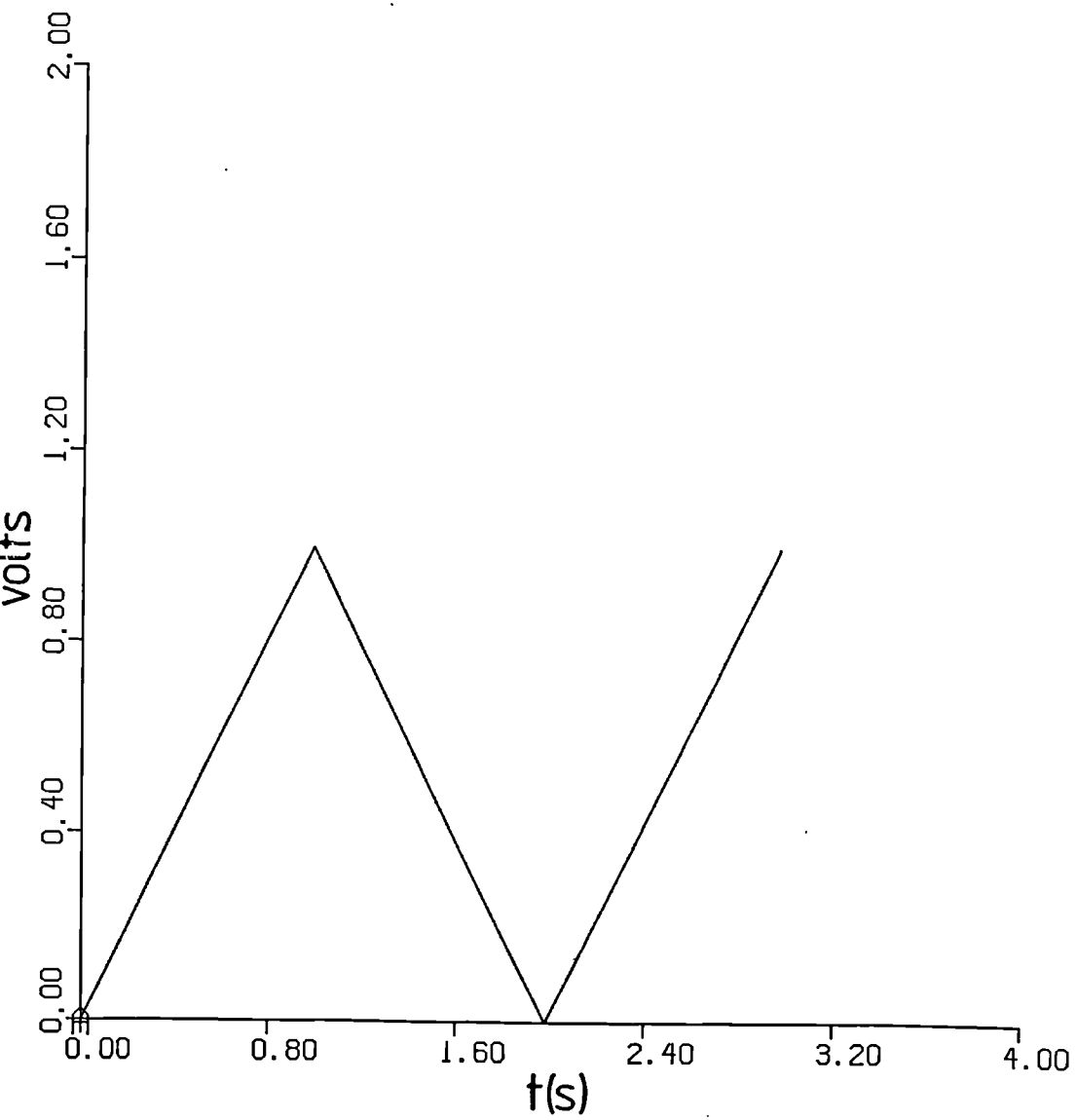

Figure 6.7:Platform displacement

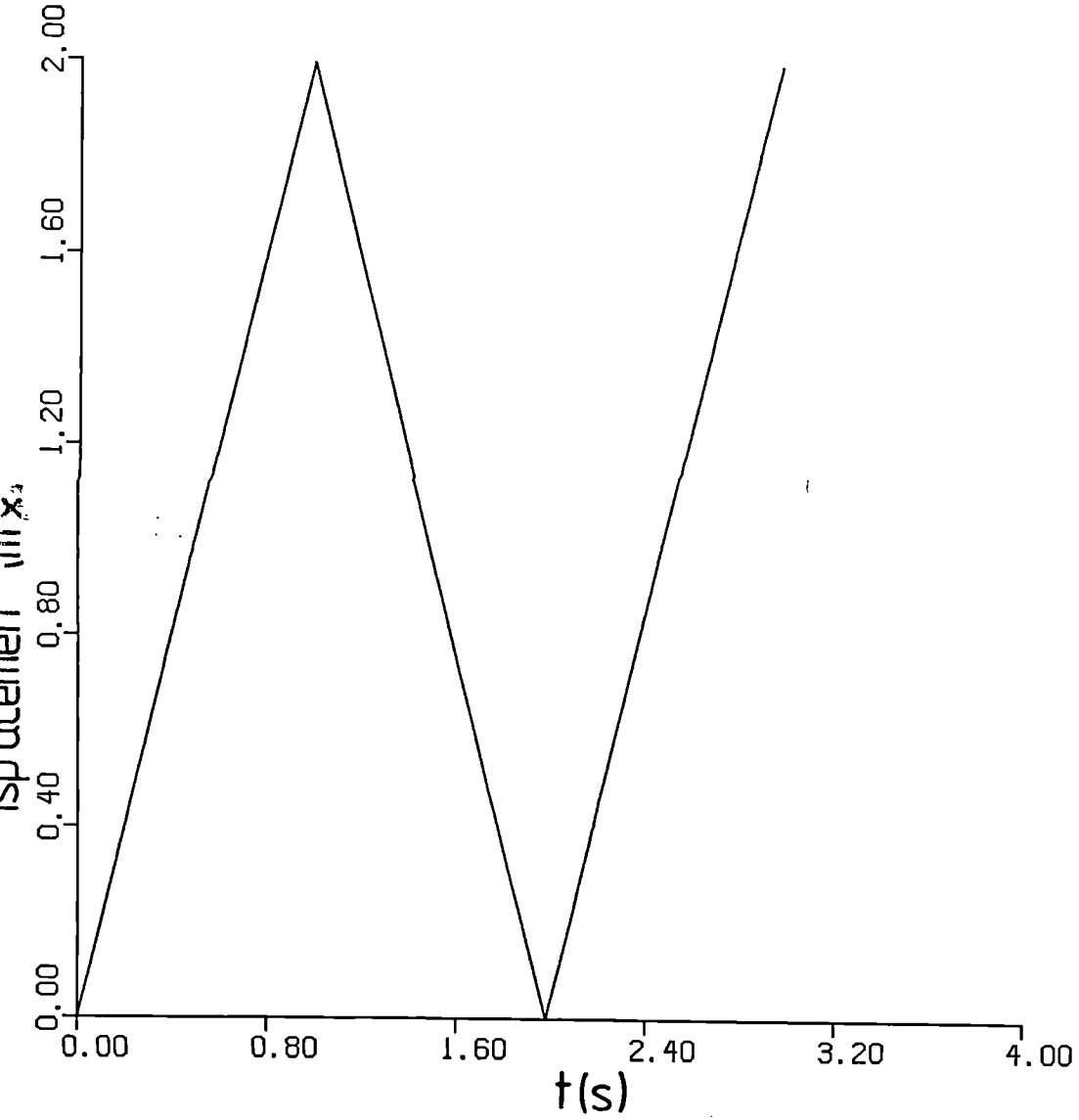

Figure 6.8:Open loop dynamic error

a)monitoring current

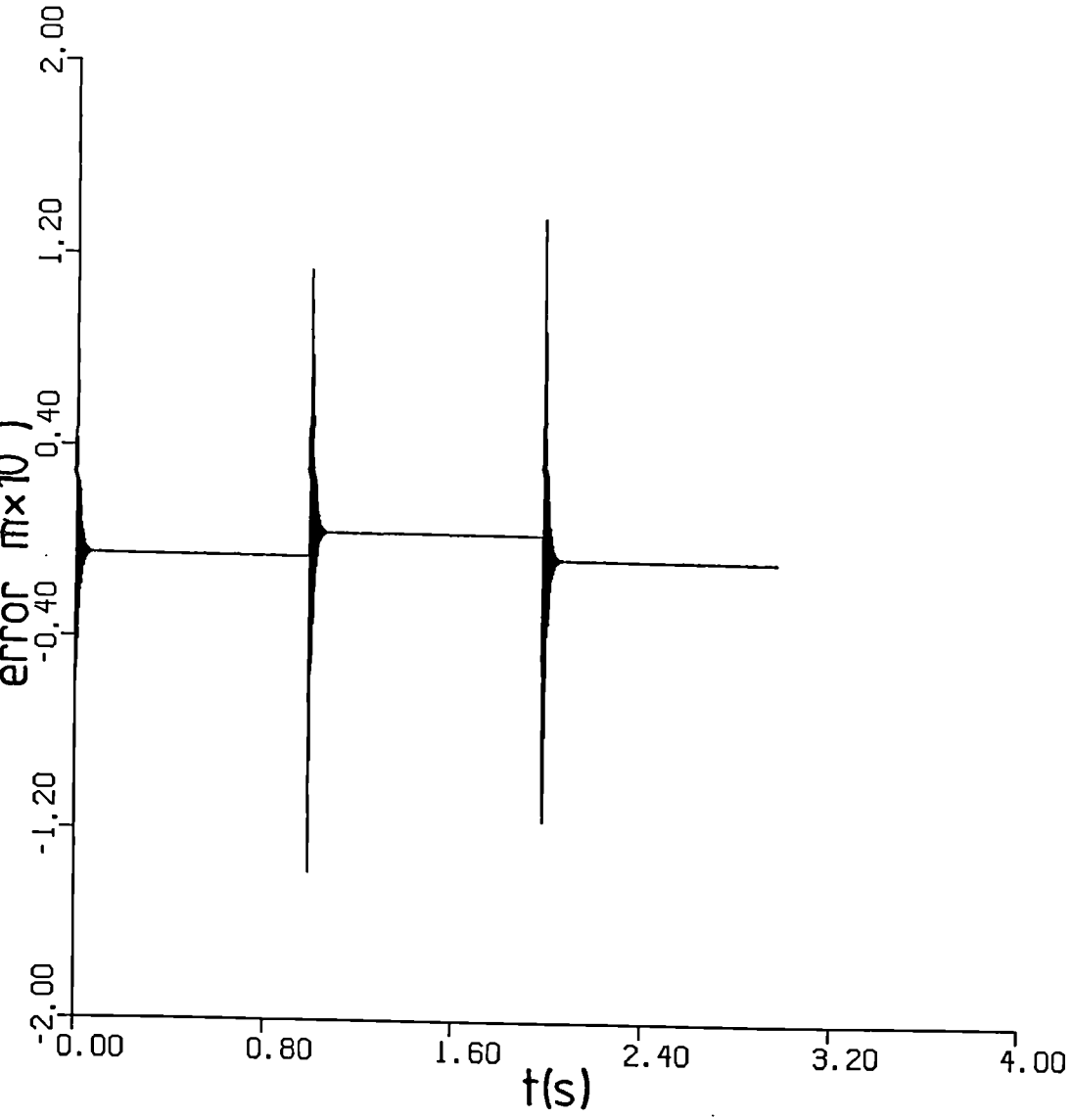

b)monitoring voltage

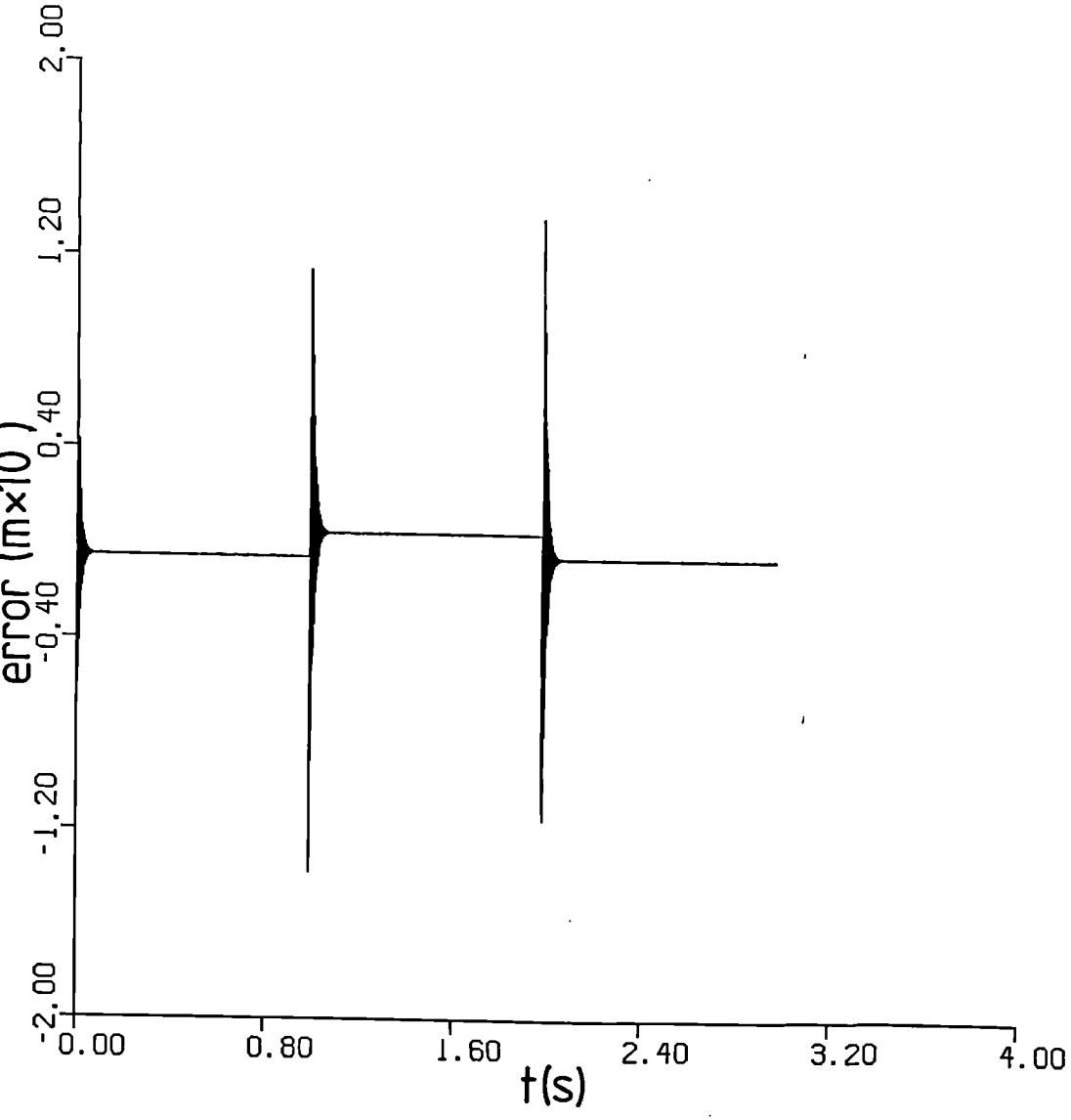

Figure 6.9:The maximum stress within the springs

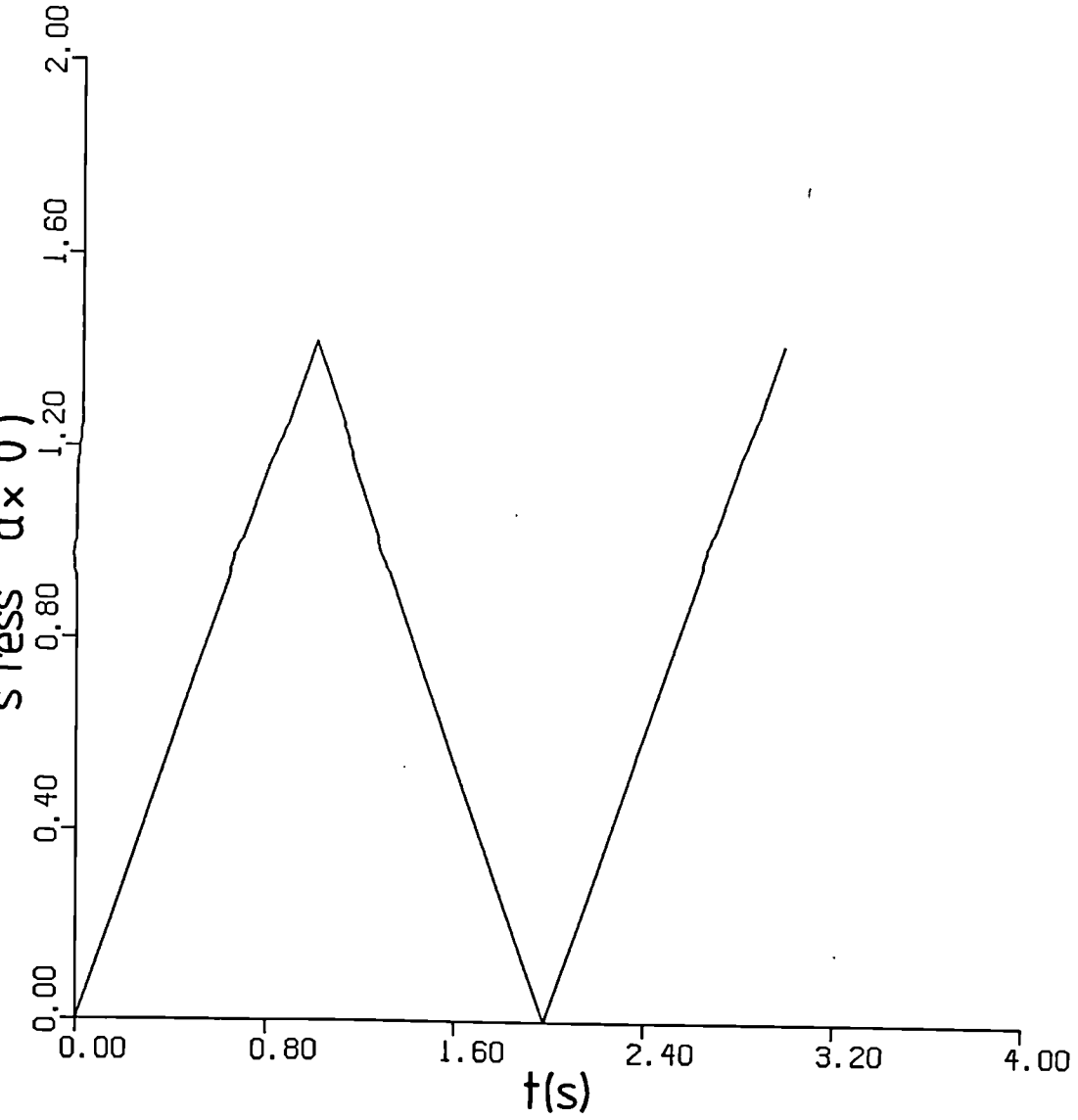

Figure 6.10: Z-axis stage

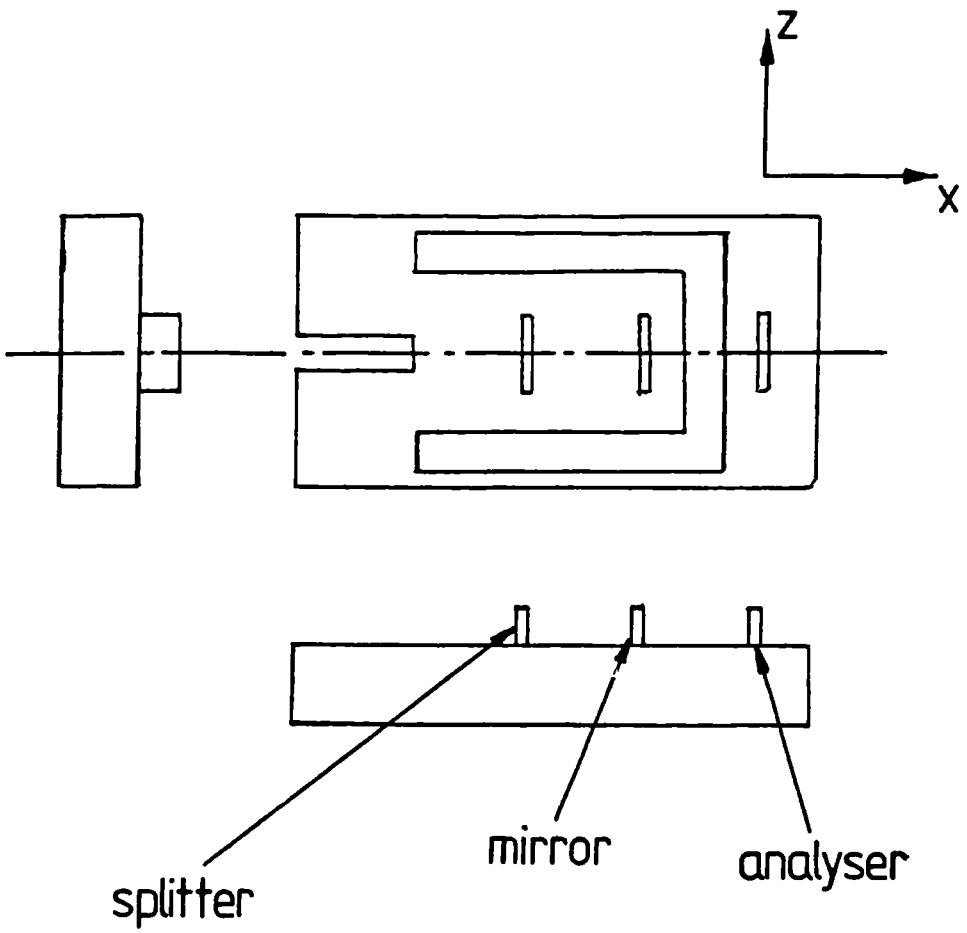

FULL Scale

Figure 6.11:STM probe clamp

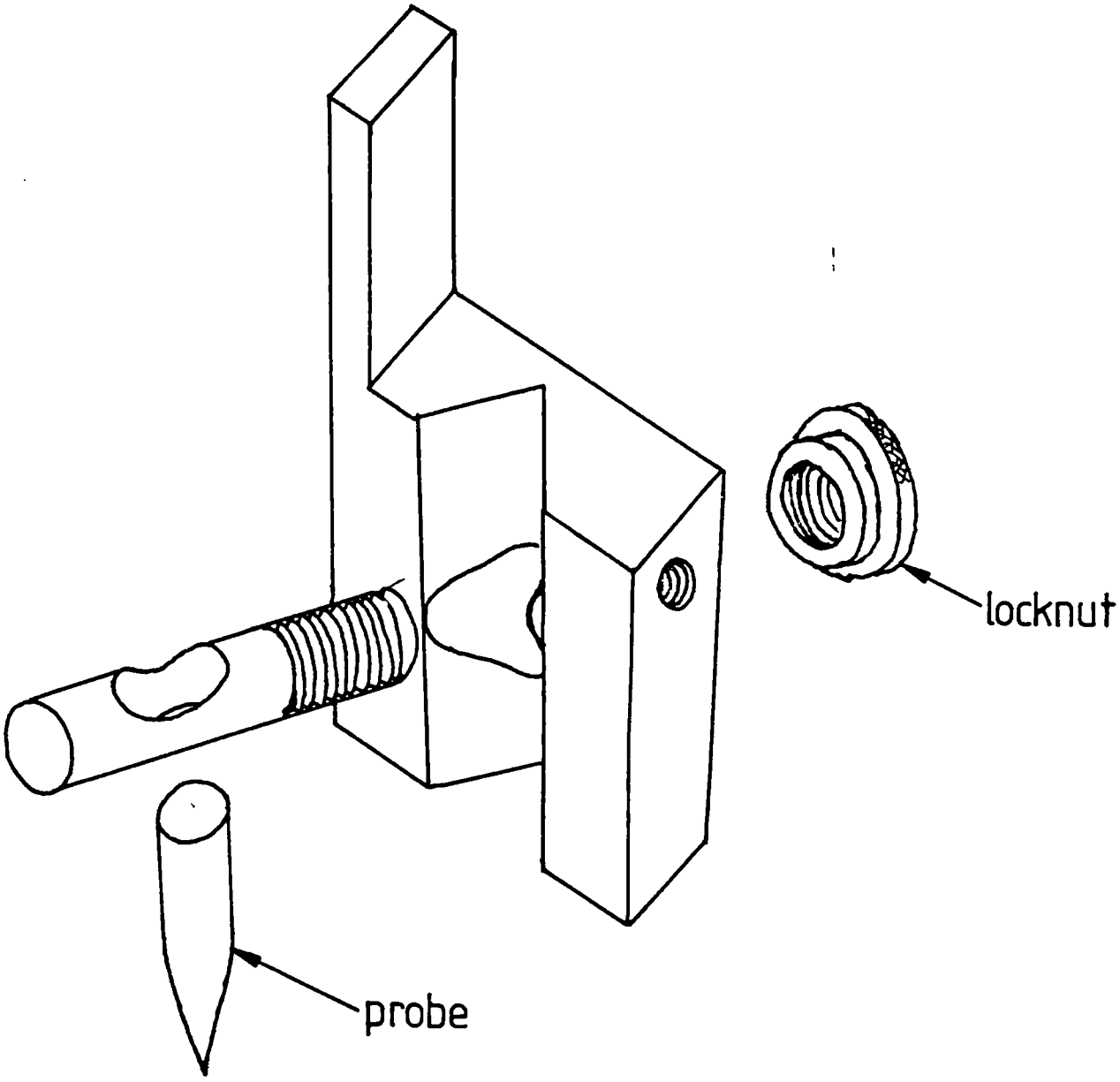

Figure 6.12:STM system schematic

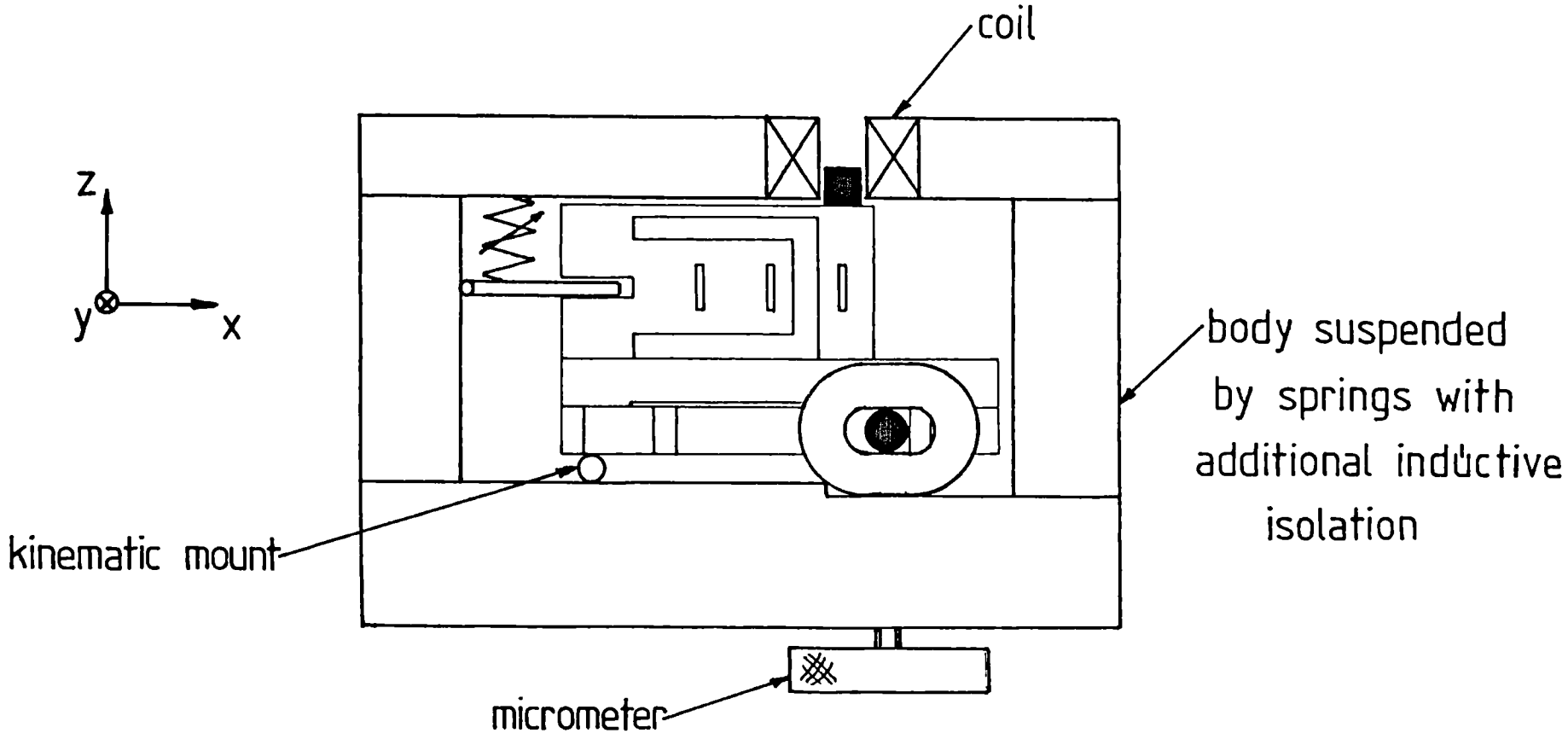

Figure 6.13:Schematic diagram of probe servo system

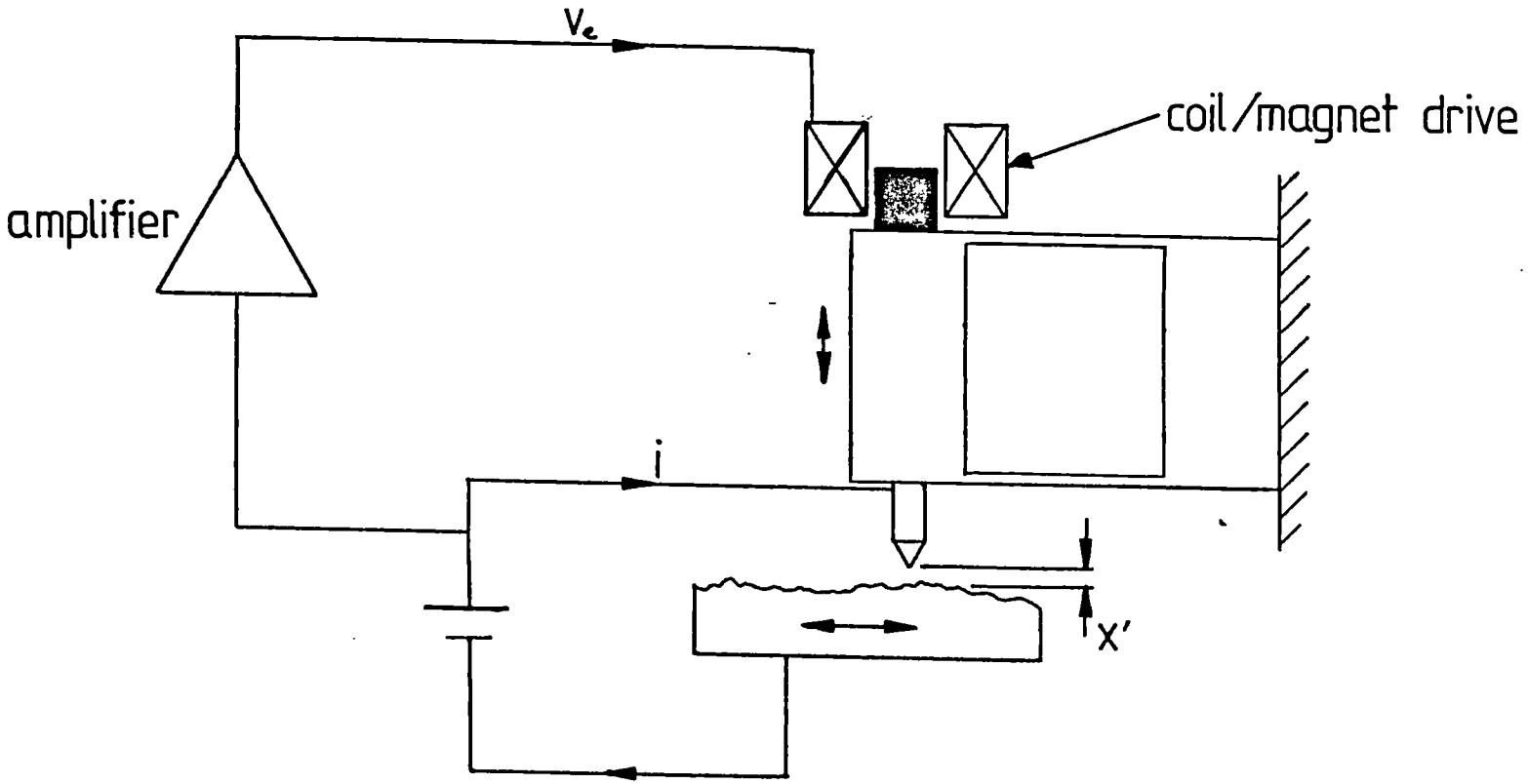

Figure 6.14:Tunnelling probe control system

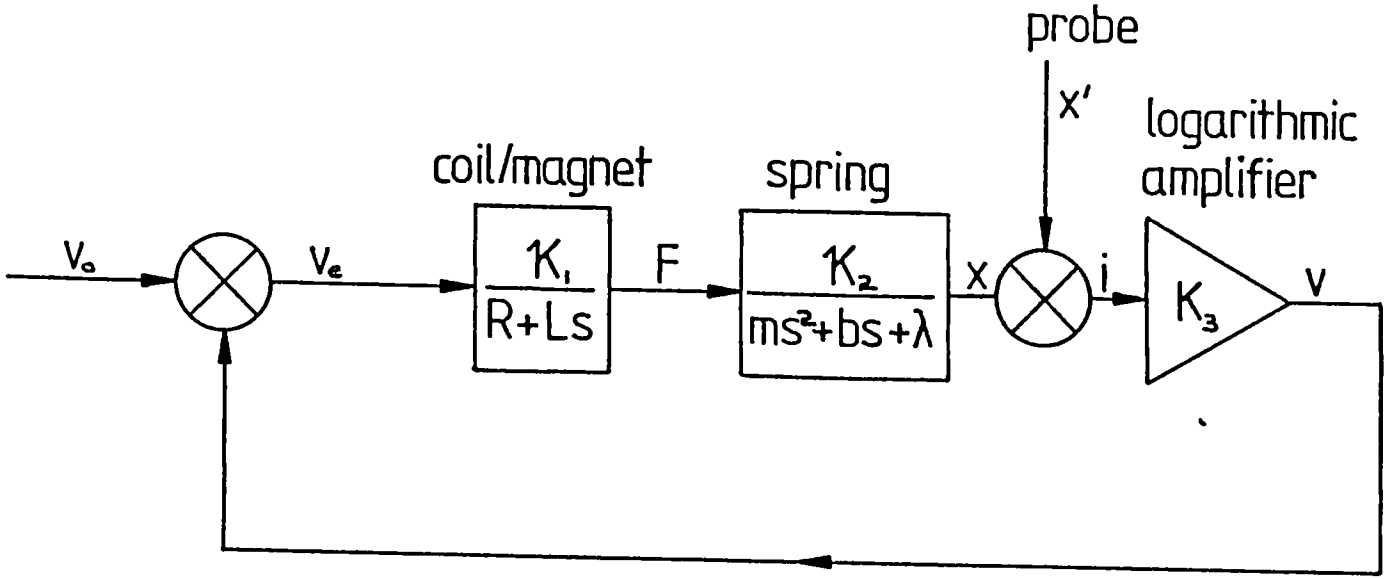

Figure 6.15:Polar plot of probe transfer function

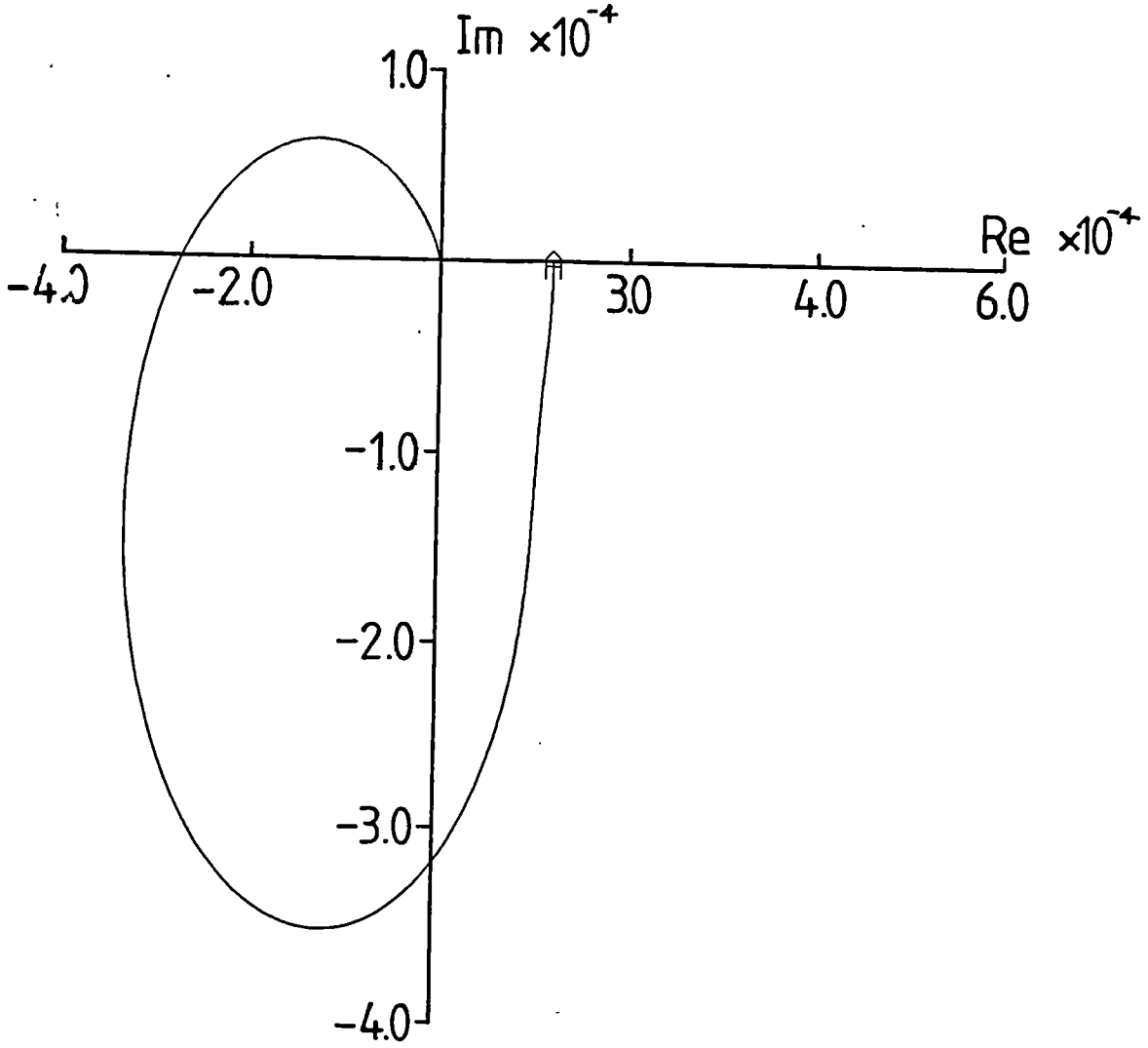

Figure 6.16:Phase angle of control system as a function of frequency

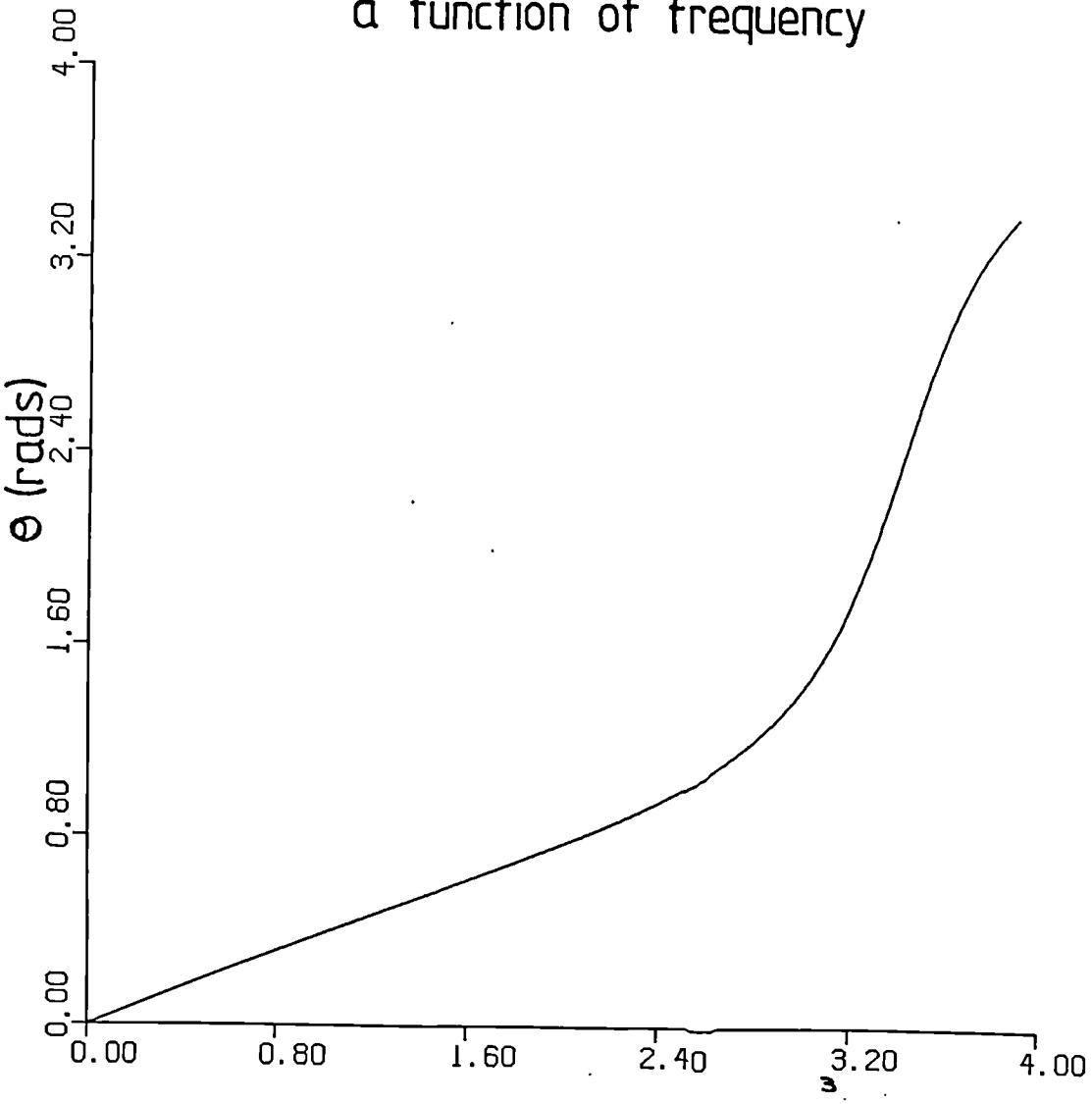

Figure 6.17: Specimen positioning stage

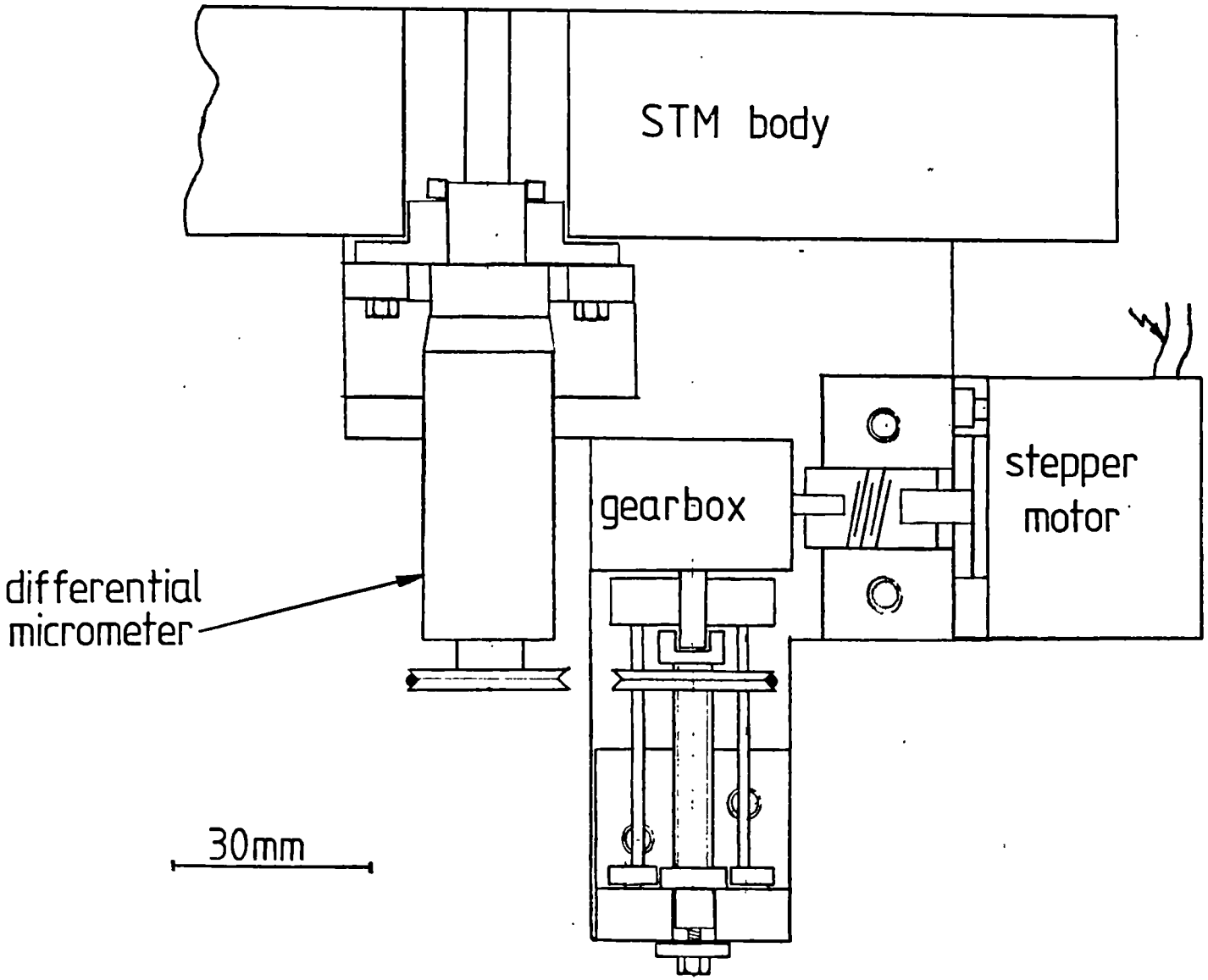

Chapter 7: The manufacture of the combined Scanning Tunneling Microscope and X-ray Interferometer

7.0 Introduction

This chapter will describe some of the novel techniques that are required for the production of various components within the combined STM/X-ray interferometer system. The following sections will include; large scale shaping of single crystal silicon, manufacture of the tungsten STM probe and the bonding of silicon. Because of the implications of machining processes in this material, particular attention will be paid to the current speculations on mechanisms of the various bulk removal processes. Some experimental results of grinding this material with small diameter, high speed, diamond end mills will be presented.

7.1 An overview of mechanisms for the manufacture of large, complex shapes in brittle materials

As described in the previous chapter, the main x-y-z stage for the STM is a three dimensional spring manufactured from single crystal silicon. This material is both extremely hard and brittle and does not lend itself readily to those processes commonly used in a traditional engineering workshop. It has, however, been successfully diamond turned with subsurface damage less than a few microns in depth, Gani et al, 1984. It is also unusual for a glass workshop to produce shapes that are both complex and may involve reentrant angles. To create these shapes, a purpose built machining station had to be developed. Firstly, a material removal process had to be identified. The three considerations were

Etching

Polishing

Grinding

7.1.1 Etching

Etching is a standard process for the removal of surface damage after rough grinding operations. A standard isotropic etchant is HNO_3, HF and H_2O with or without $HC_2H_3O_2$. A mixture of 1 part in 20 of 40%HF in 90%HNO_3 is likely to give an etch rate of approximately 4μm/min at 300k and will produce a smooth surface, Schwartz and Robbins, 1976. This is an exothermic process and thus it is necessary to maintain this temperature by continuous intermittent quenching in clean water for optimum results. Because the removal rate is temperature dependent, it is difficult to maintain consistent results and in experiments this could vary from 4-8μm under apparently similar conditions. Measurement and control of temperature is not practical for a component having complex shapes and varying thermal capacitance over its geometry. This is further complicated by the rather hostile and toxic environment. Using some anisotropic etchants, such as KOH, mechanical devices have been produced using masking techniques similar to those of the silicon integrated circuit industry, Petersen, 1982. The devices are only in a region of *mm's* to fractions of a mm and this process is, as yet, unsuitable for manufacture of components having dimensions in the region of centimetres.

7.1.2 Polishing and/or grinding

The common distinction between grinding and polishing is that, for brittle materials, the former is considered to be a fracture process whilst the later is thought to involve a certain degree of plastic flow, Preston, 1920. The phenomena of the polishing of glass has received a considerable amount of attention over the years and a fairly comprehensive viewpoint on the process is beginning to develop. This suggests that the surface becomes liquid due to a combined chemical/mechanical effect, allowing the surface molecules to flow quite readily, Brown, 1987. This flowed surface layer has been recognised for many years and was first postulated in 1909 and is known as the "Beilby" layer, Beilby, 1909. It is possible that a similar process will occur with Si although it would be expected that the flowed layer would be very much smaller. It can be

noted that after polishing it is necessary to subject semiconductors to a final etch before depositing masks and forming integrated circuits.

The act of polishing must, by definition, break atomic bonds and thus create a temporarily ionised state. Clearly from this simplified outlook, chemical effects will be expected to play a role in the material removal process. Brown suggests that there is both a softening of the surface by tensile strain induced hydrolysis and an increase in the surface reaction due to compressive strain, Nogami, 1984. Both stress conditions are likely to occur over the period of a particle traverse. Another consequence of this surface chemical interaction is that there will be extensive penetration of hydrogen ions required to maintain charge equilibrium. These protons will impose a tensile strain in the glass and thus increase its fracture sensitivity. Thus it can be seen that there is a key role played by the interaction between the liquid and the stress regime imposed by the particulates. Although water has the desired effect of enhancing surface flow, it will also cause hydrogen embrittlement. It is also apparent that for this process to take place coplanar with the surface, adhesion and thus friction between surface and machine tool must occur.

The plasticisation of Si has been investigated and there is evidence to suggest that softening does occur as a diffusion process, Cutherell, 1979. In these studies a 2mm ball was pressed onto a number of materials, including Si, with a load of 1500g and rotated at a speed of 10rpm. It is shown that ductile flow did occur after long duration in an aprotic fluid (CCL_4) whilst a predominantly brittle wear mechanism occurred with hydrogen bearing fluids (H_2O). This process appeared to be diffusion dependent and full plasticity occurred only after approximately a 1hr soak in the fluid. This effect varied for different materials but it was observed that "silicon exhibits one of the largest observed hydrogen dependent changes in mechanical properties". The drilling speed and loads that were used are very different than that encountered during drilling or polishing and can only be viewed as evidence of a chemomechanical softening and hydrogen embrittlement. Grinding may produce a similar effect if localised thermal changes increase the surface permeation rate.

Grinding is a dynamic process that may influence the elastic coefficient or because of these

high strain rates induce regelation. The surface speeds encountered in a typical grinding operation will be in the region v = 1-100m/s. If we consider that the tool will encounter the material, adhere to it and then proceed to distort the surface, then the strain rate will be dependent upon the distance into the material at which displacements will occur (δ). The depth of distortion can be expected to be in the region of the depth of damage that is normally observed, ≈1–30μm, Gani et al, 1984. The strain rate ($\dot{\eta}$) is given by

$$\dot{\eta} = \frac{v}{\delta} \tag{7.1}$$

Substituting in the above values gives a strain rate in the region of 3×10^4 to 1×10^8. These calculations are not intended as an accurate assessment of the conditions that are expected at localised areas on a surface during grinding but they do serve to indicate that the dynamic effects are not insignificant. These high strain rates may lead to adiabatic heating as mentioned previously and may also effect the dislocation generation processes. A dislocation will exhibit pure mechanical slip if a stress wave front of sufficiently small wavelength is generated (1-40nm) or will have to multiply if the rate of stress becomes equal to the speed of sound of the material (≈10^4m/s for silicon), Cottrell, unknown, Von Karman and Duwez, 1950. These conditions are unlikely to occur in the experiments of the proceeding sections.

In the preceding paragraphs it has been assumed that plasticity is an essential property for the production of a damage free surface. A technique that is commonly used to measure a materials yield strain is the indentation hardness test, Johnson, 1970. This is performed by forcing an indenter of conical, pyramidal or spherical shape into the surface of a material and analysing the resulting indentation. This technique was originally developed for the testing of plastic materials but can be readily adapted for micro-hardness measurements with "brittle" materials, Gane and Cox, 1970, Pethica, 1983. To this authors knowledge there has not been any attempt to use hardness testing techniques to study the surface characteristics of brittle materials under different liquids. Such a study may yield useful information about the environment dependence of deformation and fracture of surface and sub surface regions in these solids (known as the Rebinder-Westwood effect). A study has been made that shows a reduction in the hardness of both Si and

Ge if a current is passed through the material for indenter depths of less than 2μm, Westbrook and Gilman, 1962. The mechanism by which this occurs is uncertain although it may be connected with the carrier charge associated with dislocations. Neither current time dependence or polarity had any influence on this effect.

For higher volume removal rates it is likely that the bulk material properties are of more significance. The first experiments employing the standard hardness test on brittle materials were performed on glass, Taylor, 1949. A number of reasons for this plastic flow have since been postulated, Marsh, 1964, Roesler, 1956. The effect of adiabatic heating was observed to give erroneous hardness figures due to the large thermoelastic coefficient and low thermal conductivity. For the relatively slow hardness tests the favourable properties of silicon, mentioned in chapter 2, will tend to preclude this effect. Another distortion mechanism common to a number of glasses is densification, Ernsberger, 1968. This indicates that large compressible distortions may occur although this is contradicted by a piling up of material observed around hardness indentations. Additional mechanisms are the rate dependent viscous deformations and dislocation movement in the crystalline regions. All of these can occur in a purely plastic distortion or may accompany brittle fracture. This will require an additional term for internal energy in the Griffiths energy balance equation. These mechanisms and probably many others combine to produce a microplasticity that is comparable to that of ductile metals. Joos, 1958, has shown a curly swarf produced by sliding a diamond stylus across a glass surface. This could only occur in a plastic material.

Tabor, 1951, has shown that for a wide range of plastic materials the ratio of the hardness (H) to the yield stress (σ_y) is constant and approximately equal to 3. However, for materials having a high yield strain, a different law relating these parameters has been derived independently by Marsh, 1964, and Perrott, 1977. This relationship is given by

$$\frac{H}{\sigma_y} = A + B \ln Z \quad (GPa) \tag{7.2}$$

The value Z is related to the yield stress, elastic modulus (E) and the indenter geometry. A and B are constants. This has been found to accurately predict the hardness of a wide variety of materials. For a Vickers pyramidal indenter it has been found that A=0.07, B=0.6 and $Z=E/\sigma_y$, Johnson,

1970. Pethica, 1983, has shown quite conclusively that a purely plastic indentation does occur for penetration depths less than 1μm. He also notes that silicon undergoes an αSn phase transformation at 20GPa which is within the pressures that are likely to have occurred during the hardness test. From all of the above considerations it is apparent that for very small depths of cut (<1μm) it is reasonable to expect a significant degree of ductile behaviour, even in the most brittle of materials. This is indeed the philosophy of current research into the new "ductile machining" technologies, Puttick et al, 1979, Miyashita, 1982.

Having established the finite degree of plasticity in silicon under certain conditions it is important to identify the brittle fracture mechanisms that occur due to the stresses that are likely to be generated during a grinding process . To do this, it is necessary to look at the stress patterns produced by a distortion of the surface. The grit indentation geometries are going to be either pointed or curved corresponding to sharp new grits and worn cutters respectively. The wear of diamond will be discussed in a later section. The stress distribution under a point contact is known as a "Boussinesq" field, Lawn and Swain, 1975. This calculates a tensile stress contour extending into the surface in a hoop that is parallel to the axis of indentation with the circumference passing through the point of contact. From this analysis it is predicted that a penny shaped crack will form below the surface of indentation. However, because of the point contact, an infinite pressure is predicted. This cannot be sustained and a finite amount of deformation must take place. Once formed, this penny shaped crack, known as a median vent, will expand upon further loading. Removing this indenter will allow this crack to close but not heal. Healing would only occur if the surface free energy created during fracture were equal to the relaxation of elastic (as opposed to plastic, viscous, dislocation dissipation etc..) internal energy and in the absence of environmental, thermal or chemical effects. The plastically deformed zone will then create a near surface tensile stress that will initiate circumferential cracking perpendicular to the indenter axis. Upon further removal of the load this crack, known as a lateral vent, will grow and may eventually break through to the surface, creating a familiar oyster shell shaped chip. This sequence of events is shown schematically in figure 7.1 and an excellent scanning electron micrograph of this phenomena can be found in Lawn and Swain, 1975. These vents extend well into the

region that is assumed to undergo a plastic distortion and the size of the cracks is measured in the region of tens of micrometers to millimeters. Using the Griffith fracture hypotheses, it has been shown that for large cracks sizes the ratio of load to crack size is constant, Lawn and Swain, 1975. The load at which cracks will begin is not yet possible to calculate because there is no knowledge of the flaw size created by this "plastic" region. A number of people have examined silicon for the onset of cracking and can usually detect cracks at a load of 5-30gms, Puttick et al, 1979, Lankford and Davidson, 1979, and Lawn et al, 1981. Having once formed, these cracks are likely to be atomically sharp with a drastic degradation in the strength of the material, Lawn et al, 1980. This will also leave residual stresses in the material that are related to the indenter load (P), crack length (c) and a material indenter geometry factor (χ_r) by the equation

$$K_r = \chi_r \frac{P}{c^{2/3}} \tag{7.3}$$

Where K_r is the residual stress intensity factor. It must be noted that Perrott, 1977, presents an analysis of crack formation in the plastic zone (Palmqvist cracks) of tougher ceramic materials that could be relevant to this problem.

The stress distribution under an area contact can be computed by either integrating the Boussinesq field or using Hertzian analysis. This results in the familiar "Hertzian" field. This is markedly different to the Boussinesq field in that there is no tensile stress component in the region immediately below the indenter. The highest tensile stress (σ_m) is calculated at the edge of the contact zone. This stress can be calculated from the well known equations

$$\sigma_m = \frac{1}{2}(1 - 2\nu)\frac{P}{2\pi a^2} \tag{7.4}$$

$$a^3 = \frac{4}{3}\frac{kPr}{E} \tag{7.5}$$

$$k = \frac{9}{16}\left[(1 - \nu^2) + (1 - \nu'^2)E/E'\right] \tag{7.6}$$

where E, E', ν and ν' are the modulus and Poissons ratio of specimen and indenter respectively, r is the indenter radius and a is the contact radius. This gives rise to circular ring cracking just outside of the circle of contact and parallel to the indenter axis. Upon further loading, this crack will move into the surface forming a truncated cone. The dimensions of this cone have been measured, in glass, under different loads and the results used to calculate the surface tension,

Roesler, 1956. It was also found that the crack angle is independent of indenter radius and the cone base diameter (s) is related to the load (P) by the equation

$$\frac{s}{P^{2/3}} = n = constant \tag{7.7}$$

The base diameter could be readily measured in glass using a travelling microscope. It was found that $n=1.57\times10^{-2}$ and the cone half angle was $68^{o}30'$. An excellent photograph of cone cracking in fused silica can be found in the paper of Benbow, 1960. A principal stress trajectory in this Hertzian field is also a cone of half angle $\approx68^{o}$, Frank and Lawn, 1967. Thus it is assumed that the crack will follow a principle stress trajectory as long as sharp deviations in direction do not occur. This is because cracks are known to exhibit a psuedo-inertia causing them to swing wide around any sudden change. The onset of cracking has been found to be a constant ratio of the load and radius of indenter. This is known as Auerbach's law and remains consistent over a wide range of indenter radii. For larger radii this law breaks down and the crack initiation threshold becomes proportional to the square of the radius. This effect has been found to begin in glass at a radius of approximately 2cm. The initiation and growth of cracks under a spherical indenter is analysed in the paper of Frank and Lawn, 1967. From this analysis, the upper limit to which Auerbach's law remains valid is given by the equation

$$r_u = 66\left[\frac{E}{k^2\gamma}\right]^{1/2} c_f^{3/2} \tag{7.8}$$

where c_f is the flaw size and γ is the surface tension. Putting the values $E=1.9\times10^{11}N/m^2$, $\gamma=2.5\ Jm^{-2}$, k=2/3 and $c_f=10^{-6}$ a limit on the indenter radius r_u of 1mm is obtained. This is the limit at which the load tolerance is likely to increase in the presence of flaws of approximately 1μm. In the grinding process these contact forces will also be sliding across the surface. The stress field created by a sliding circular contact has been solved by Hamilton and Goodman, 1966. This analysis indicates that the greatest tensile stress σ_m will occur at the trailing edge of the contact zone and can be calculated from the equation

$$\sigma_m = (1+15.5\mu)(\tfrac{1}{2}-\nu)\frac{P}{\pi a^2} \tag{7.9}$$

where μ is the coefficient of friction. From equation (7.9) it can be seen that the coefficient

of friction will have a large effect on the stress encountered by the surface. An introduction of a coefficient of 0.5 will increase the stress approximately eight fold. It was also shown previously that polishing processes must and will involve adhesion so that frictional forces may even be higher than this value. It is also noted that this frictional stress may also influence the damage induced by stylus measuring techniques. The stress at the leading edge is similarly reduced by a friction increase. This makes it less likely that a crack will propagate around the full circumference giving rise to a series of half moon shaped cracks following an indenter as it is drawn across a surface. Excellent examples of this phenomena can be found in the papers of Preston, 1922, and Lawn and Wilshaw, 1975. This analysis forms the basis of an analytical study into the initiation and propagation of cracks due to a sliding contact, Lawn, 1967. Also, material properties are probably not the same at the surface as they are in the bulk. He predicts that the ratio of the load required to produce a crack (P_c) with a sliding contact to that required in the static case (P_o) is, within the realms of Auerbach's law, given by

$$\frac{P_c}{P_o}=6.7\times10^{-3}\frac{k(\gamma/E)^{1/2}r}{(1-\nu^2)^{1/2}(1-2\nu)(1+15.5\mu)^3 I_f^3 c_f^{3/2}} \tag{7.10}$$

Where I_f can be obtained from Lawn, 1967. The outcome of this analysis is to show that for small radius indenters the crack initiation threshold can be reduced by a factor of 100 for even a low coefficient of friction ≈0.1.

Because silicon can be single crystal, it is expected that some anisotropy will result. The act of abrading this material in different orientations has been assessed by Puttick and Shahid, 1977. Even under loads of 3gms and less the scraping of a Vickers pyramidal indenter across the surface of silicon was found to induce dislocation densities of $\approx 10^{10} mm^{-2}$. No evidence was found for cracking at loads of 3 and 5gms. For higher loads (50-100gms) the scratches induced predominantly brittle fracture. It was also found that the extent of the fracture was also anisotropic. These results were obtained using TEM, SEM and x-ray topographic techniques. During scratching, no measurements of the frictional forces were made. However, frictional anisotropies in other materials have been measured, Seal, 1958, Bowden and Brookes, 1966, and Bowden and Hanwell, 1966. In these studies, loads in the range 10-1000gms were employed with a varying

radii of indenter. In all cases frictional anisotropy was found to increase with the load and reduction in indenter radius. If the anisotropy is due to ploughing, then in view of Auerbach's law this result would be expected. At low loads anisotropy was undetectable whilst at higher fracture thresholds this value could vary by up to 300%. Sliding speeds were low in comparison to those expected during grinding. Examination of some wear tracks frequently revealed the familiar half moon cracking with foci in the direction of traverse. Ploughing forces were calculated to be greater than the yield strength of the respective crystals.

If minimal surface cracking is required, then it is clear that sharp fixed abrasives are least desirable. Thus it is better to blunt the grits before use. Because of the large directional variation in wear rate for diamond (up to 500:1) under certain conditions, cutting scrap material or dressing is unlikely to create smooth asperities and may even result in sharpening favourably oriented grits. A reasonably isotropic wear rate is found to exist at during high speed cutting (≈20-30m/s) and/or under water based coolants, Seal, 1958 and 1967. Under these conditions, carbon like powders (dry wear) waxy deposits have been found. This would again imply a chemomechanical and/or thermal effect (diamond exhibits rapid burning at $\approx 800^{o}c$ and a rapid graphitization at $\approx 1000^{o}c$). Thus it would be expected that a heavy cut at high speeds would both remove and smooth sharp asperities and this will be shown in a later section.

7.2 Experimentation

The equipment that is used for grinding complex shapes in silicon has been chosen for its flexibility. It comprises a Bridgeport series 1 CNC vertical milling machine and NSK Planet air turbine high speed spindles. The diamond speed pins attached to these spindles were of two varieties. These differed in the type of bond and the shank material on which the diamonds are deposited. They shall be distinguished as type A and type B. The type A pins are mounted on to a steel mandrel with the diamond grits held in place by a nickel bond. In both cases the grit size could be specified. The type B pins are mounted onto a tungsten carbide mandrel with the grits moulded onto the shank in the form of a paste of high tin bronze (up to 90% Sn). Because of the depth of the grits these wheels can be dressed. The shank and grinding head diameters were

chosen to be 3mm. The standard grit size is 100μm although a fine grit of 40μm has been assessed.

It is important to note that this procedure differs in a number of ways from that of conventional grinding processes. The most common silicon grinding process is that of sawing into wafers using large diameter cutting wheels, Meek and Huffstutler, 1969. As the wafer is being removed from the boule, it is exposed in a manner analogous to a cantilever beam. Any vibration, hydrodynamic effects and/or vibrations will cause cracking and large dislocation build up. This is related to the amount of time that the wheel is in contact with the wafer and thus the feedrate. So in these processes the faster the feed the better. In the case of side cutting with an end mill, it is more likely that the greatest stresses will be those incurred by the cutting action. The effects of vibration will be attenuated in proportion to the stiffness of the system. The air turbines are mounted in roller bearings and the stiffness is proportional to the cube root of the load. This preloading is a part of the bearing manufacture. The stiffness of the speed pins for a given geometry is dependent on the material. An increase in stiffness of 300% would be expected with a transition from steel to tungsten carbide. The machine stiffness is fixed but may be ignored if the resonant frequency is low and the inertias are high. Another difference is that the grits are likely to be in contact with the material for a very short time period. For a speed pin of radius (r_p) rotating at an angular speed (ω [rad/s]), the maximum time (t_m) that an individual grit will be in contact with the surface is given by

$$t_m=\frac{\cos^{-1}(1-\delta/r_p)}{\omega}=\frac{\xi}{\omega} \tag{7.11}$$

where δ is the depth of cut and ξ is the proportion of the circumference in contact with the surface. Inserting values of δ=0.1, r_p=1.5mm and ω=8400 gives a contact time of 44μs. This is also very different to the diamond turning of silicon assessed by Gani et al, 1984. The depth of cut per grit per pass is approximately the product of the feedrate and contact time (t_m). For a feedrate of 0.1mm/s and the the above contact time, the depth of cut becomes ≈4.4nm. In reality this is likely to be a lot higher due to vibrations, eccentricities, etc..

In these following experiments a number of assessment techniques were employed to exam-

ine the surfaces formed during grinding. Both the scanning electron microscope and optical microscopy have been used to visually examine any features. The more quantifyable methods are stylus and x-ray rocking curve techniques. A number of difficulties arise in the use of conventional stylus techniques for the assessment of surface damage. The main problem is that of the surface contour of the cutter. This is superimposed on the machined surface and will be conventionally measured as the surface finish. This value does not necessarily relate to the surface damage and gives a heavily anisotropic value. The degree of anisotropy was variable and was found to range from 2:1 to 16:1. Although this effect may be related to surface damage for a given process, this has not been pursued. The strength degrading mechanism for brittle materials is dominated by micro-cracking and internal stresses (due to plastic distortion, Rehbinder-Westwood effects or the Twyman effect). Microcracks are not detectable if they have considerably less root radius and slope than the stylus itself and this is in general the case for brittle materials. The rocking curve technique is related to surface and sub-surface strains. This operates by diffracting x-rays at the surface at the appropriate Bragg angle. Braggs law states that for a given x-ray wavelength, there is only one angle at which diffraction will occur for a given crystal orientation. If lattice strains are present, this diffraction angle will effectively blur and vary over a range of rotation. Thus by rocking the surface about this angle a diffraction intensity curve can be recorded. The full width of this curve at half height maximum (FWHM) is used as a monitor of the amount and depth of surface damage. By etching the surface whilst recording a series of rocking curves a plot of damage against surface depth can be produced and used to assess the damage depth. By masking the material and etching away the surrounding surface for a given time, a step will develop. The resulting step can be measured to determine the etch rate. A typical measurement of the step produced on an Si(111) surface after a 5min etch in 10%HF/90%HNO_3 for a period of 5mins is shown in figure 7.3. From this figure an etch rate of ≈4μm/min has been calculated.

7.3 Results

An SEM micrograph of a type A tool is shown in figure 7.4. It can be clearly seen that the

grinding surface consists of large grits having many sharp asperities. After machining with these tools observations of the surface indicate a predominantly brittle removal process with a depth of damage measured to be in the region 10-40μm. The findings from these experiments indicate that the depth of damage, as measured using rocking curve methods, is reduced by both an increase in the density and a reduction in the size of the grits. An optical micrograph of a ground silicon (111) surface using a fine grade (≈100μm), 3mm diameter spindle rotating at 89000rpm is shown in figure 7.5(a). The estimated depth of damage for this specimen was ≈15μm. After the etching process, the surface has been reexamined under an optical microscope. Preston, 1922, has shown that, for glass, etch pits will originate from flaws in the surface. From the optical micrograph of figure 7.5(b), a regular array of linear hollows are clearly observed. These would be expected for the half moon shaped cracks or median vents predicted in the previous section. The etch depth may have removed some useful information.

Because of the high stiffness, thick matrix and small grit size (≈40-100μm) of the type B tools, less damage is expected during the grinding process in this case. An SEM micrograph of a 3mm used tool is shown in figure 7.6(a). After considerable heavy cutting the diamond grits will become worn with removal of the sharp asperities. Both SEM and optical micrographs of the worn surface are shown in figure 7.6(b and c). This surface comprises worn diamonds that are flush to the surface. The micrograph of figure 7.6(c) reveals a site where a grit has been completely removed from the tool due to high forces encountered during the grinding process or poor keying/adhesion. This implies that the wear process is mainly isotropic and thus a thermal or chemical effect, Seal, 1967. This 3mm cutter has been used to grind the face of a Si(111) surface at a feedrate of 15mm/min with a depth of cut of 0.02mm and at a rotational speed of 89000rpm. From equation (7.11) this corresponds to a removal rate of 5000μm^2/s and 17nm/cut. The surfaces produced by this cutter, with the same cutting conditions, in both the as new and worn state are shown in the micrographs of figure 7.7(a,b and c). It can be clearly seen that a transition from brittle fracture to a smoother finish does in fact occur with the possible appearance of plastic flow in the latter case. A closer look at these two surfaces using the SEM highlights the differences. Figure 7.8(a) shows a typical brittle failure crack according to the model of figure 7.1. This shows

a characteristic lateral vent with pitting in the central region of the indenter (grit) contact. Adjacent to this region is a smoother region characteristic of plastic or ductile machining. Figure 7.8(b) shows a portion of the smooth surface having a similar magnification. No brittle failure can be observed although some pitting or tearing can be seen that indicates strong adhesion a thus a high friction coefficient. The surface finish values across the machining marks and along the grains have a ratio of ≈16:1. The rocking half width for this specimen is approximately 70secs of arc. This is between 50% to 30% of the value usually measured for a ground Si surface. The rocking curve for this specimen and for the same crystal orientation (111) ground with a fine grade type A tool are shown in figure 7.9. The count rate on the y-axis being in arbitrary units. The lattice strains are thus considerably less in the smooth machine surface. This specimen has then been etch and the FWHM plotted as a function of the depth of surface removed, figure 7.10. This curve indicates an almost complete recovery from the strained condition after the first 2μm have been removed. Additionally, the etched surface shows no evidence of the perpendicular pits that could be observed in the previous specimens.

The influence of the stress distribution between the grinding wheel and surface has been shown to greatly influence effect the surface damage and possibly even the removal mechanism itself. This implies that a quasi ductile machining mechanism can be obtained for relatively large depths of cut to those normally employed, Miyashita, 1982. The possibility that this is due to a thermal softening under high contact friction conditions is backed up by the isotropic wear of the diamond grits. However, it is unlikely to occur during the very small contact time and with the high conductivity of silicon. This would favour a chemical effect. This technique can clearly produce smooth surfaces requiring little etching to create mechanically useful devices of almost arbitrary complexity.

7.4 The manufacture of STM tungsten probes

A variety of techniques have been successfully used to produce tunnelling probes. Early probes were ground or simply cut with engineers snips from a 1mm diameter wire. Because of the ragged surface produced by this process, a single sharp asperity becomes likely and it is this that

forms the tip. There is considerable doubt that the same asperity is in operation when these are used to scan rough surfaces. Later tips have been electrochemically etched in a KOH solution to produce a better defined tip and thus avoid the above problem, Dragoset et al, 1986. Tips having asperities of atomic dimensions can be produced by field evaporation and monitoring this with a field ion microscope, Yuk and Silverman, 1986. It has recently been shown that reliable probes can be manufactured by electrochemically etching followed by ion beam milling, Biegelsen et al, 1987. The etching process consists of a carbon anode placed in a 1N KOH solution. The tungsten cathode is placed in the solution with all but a 1mm wide band covered by an insulator, see figure 7.12(a). An electrode is applied to the top of the W rod and a current pulse is applied. When the exposed band of the rod has eroded through, the lower portion of the rod will drop to the bottom of the container and the etching process will cease. An SEM micrograph of a probe produced by this process is shown in figure 7.13. This probe has been produced by applying a 50Hz, 25mA square wave with an electrode potential of ≈1.8v. For this configuration an effective resistance of ≈60Ω has been measured across the electrodes. There is a slight increase with frequency (≈50Ω at 0Hz to ≈80Ω at 500Hz) although there is difficulty in measuring accurately due to the formation of bubbles around the W probe causing considerable noise. This etching process will produce an oxide layer (WO_3) surrounding the tip. This can be removed by rotating the tip under an ion beam. Figure 7.14 shows an SEM micrograph of the same tip after machining for 60mins in an argon ion beam with an energy of 1kV and a current density of ≈1.5mA/cm^2. This process shows little sharpening of the tips at any angle of beam incidence (positive or negative) and enhancement of the reliability is considered to be caused by contaminant removal.

7.5 The bonding of silicon

To create a three dimensional translation using silicon spring mechanisms requires the bonding of the z-axis stage perpendicular to the x-y stage. Three methods of achieving this have been considered. These are

1. Optical wringing

2. Direct bonding

3. Anodic bonding

7.5.1 Optical wringing

This process is often used with glass optics to obtain a very strong and stable bond. The usual procedure is to polish the two surfaces flat to ≈1/10-1/50λ. The two surfaces are then cleaned and contacted. This contacting is performed by applying a considerable manual force whilst the interface thickness is observed as a change in the colour of the diffracted light. This process is undesirable due to the opaqueness of silicon in visible light and the possibility of damaging the springs during application of high contacting forces. It is also unknown to this author whether the above flatness can be achieved with silicon.

7.5.2 Silicon-silicon direct bonding

In this method the mating interface is initially created by the formation of silanol (Si-OH) groups. This is achieved by polishing the two faces to be mated followed by cleaning in a hydrogen peroxide, sulphuric acid mixture (H_2O_2–H_2SO_4) and dipped in a dilute HF solution. A hydrophilic layer is then created by an H_2SO_4 soak. Following a water rinse or exposure to vapor, the two surfaces are then brought into contact. This results in a bond without any applied pressure and has been measured in the range 2-5kg/cm^2, Shimbo et al, 1986. It was found that subsequent heating in a nitrogen ambient to 1273K for ≈1hr increases this strength up to ≈100-200kg/cm^2. The postulated mechanism resulting in such a bond is shown in figure 7.15. The initial contact causes the formation of the silanol interface. Heating will then induce a condensation reaction leaving the Si-O-Si interface. Finally diffusion of the oxygen into the bulk of the material results in a Si-Si bond, Shimbo et al, 1986. Similar results has been obtained for thin oxidized wafers contacted and heated in a steam ambient to ≈930 celcius, Kimura et al, 1983.

7.5.3 Anodic bonding

An alternative to the direct bonding method is that of anodic bonding. In this process a thin insulating layer (1-5μm) is formed on the surfaces to be bonded. This layer is usually sputtered

borosilicate glass or a thermally grown oxide. After contacting the surfaces are heated and a potential of 30-50v applied across the insulating barrier. This results in electrostatic forces creating a better contact as well as enhancing any thermochemical effects. Although Brooks et al, 1972, were able to obtain hermetic seals with furnace temperatures of less than 500c, this could not be reproduced by Anthony, 1985. In this paper the optimum bonding conditions for a two micron SiO_2 isolating layer were at furnace temperatures and applied voltages in the range 850–950°c and 30-50v respectively. For this process, a flatness considerably better than the thickness of the isolating layer is required if the surfaces are not to be subjected to distorting forces during bonding.

7.5.4 Experimentation

To examine the above bonding methods, four silicon blocks were lapped and polished. These were in the form of discs of approximately 100mm diameter and 18mm thickness. The polishing of these large blocks was carried out by an initial optical finish diamond lap followed by a "Syton" polish on a polyurethane bed. There were no checks on the flatness of the surfaces and thus it must be assumed that form errors are similar to those encountered with a standard optical polished. These form errors are usually in the region of 1 micron for this size of disc. The optical finish diamond lap was carried out at NPL. This then had to be transported to Monsanto Industries Limited (Milton Keynes), where Syton polishing on a polyurethane mat completed the process. The use of a polyurethane mat precludes any control of the flatness of the surface being generated. Because the production equipment used in the polishing of wafers for integrated circuits was not compatible with thick discs, polishing was carried out on a Logitech 400. Each disc face was polished for half an hour. The subsequent surface finish was examined using a Talystep and was estimated to have a roughness (R_a) value of around 1-2nm.

From the discussion in section 7.6.1 that the form errors due to this uncontrolled polish preclude any optical wringing. Thus the direct bonding method has been tested. First the polished discs were cleaned in a 1,1,3 solution of H_2SO_4, H_2O_2 and H_2O for 15 minutes. These were then dipped in a 1,9 solution of HF and H_2O for 15 minutes followed by a one and a quarter hour soak

in H_2SO_4. Finally the surfaces were given a distilled water rinse and manually contacted. Two sets of specimen were then placed in a furnace that had been preheated to 1000°c and left for an hour. After this treatment it was found that only one specimen pair could sustain a force. Upon soaking the specimen in an HF solution the bond failed. This implies that the bonding was predominantly an oxide fusion.

It is thought that the processes of both direct and anodic bonding require a high degree of conformity if they are to be successful. In the case of a wafer, this is provided by the very high degree of polishing and its large compliance. Thus it is considered that form errors of less than a tenth of a fringe and sub nanometre surface finish values are required to enhance the feasibility of further testing. These two parameters can only be manipulated at the required level by an improved finishing process. The generation of super-flat, polished silicon blocks may be achievable using pitch polishing technologies. This has not, as yet, been attempted.

Figure 7.1: Schematic representation of crack formation under point load

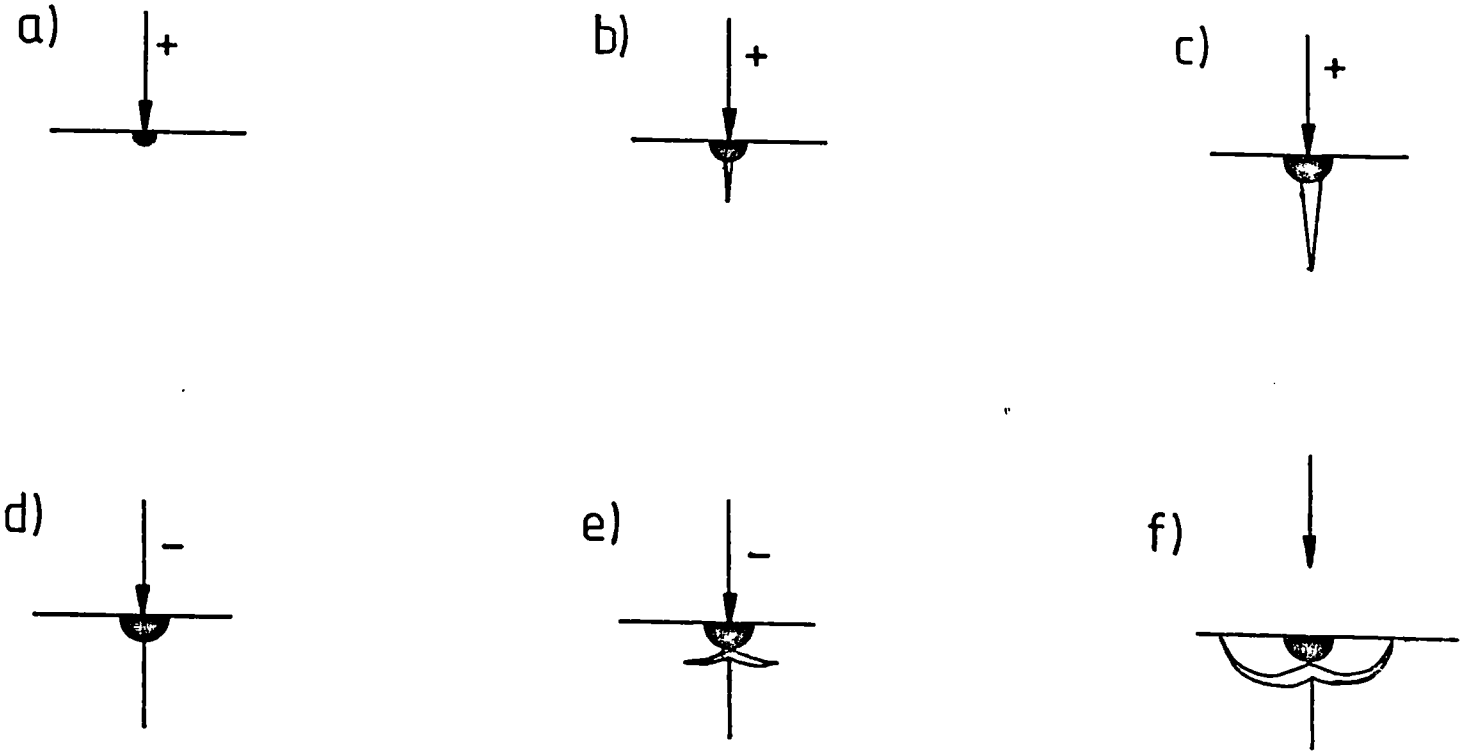

Figure 7.2:Proportion of grit contact time as a function of depth of cut and radius of cutter

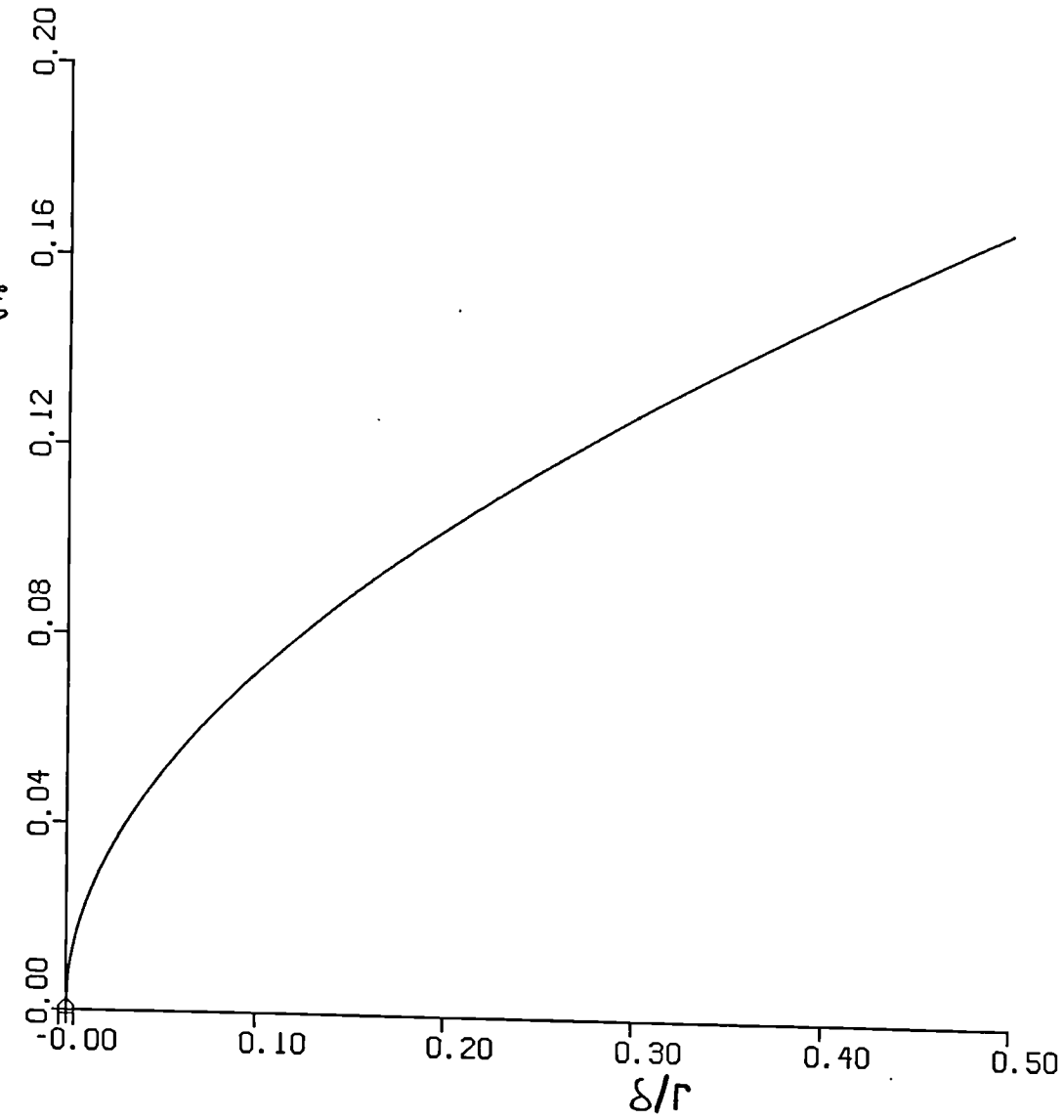

Figure 7.3:Step indicating masked region of an etched Si(111) specimen

Figure 7.4: A nickel bonded diamond end-mill

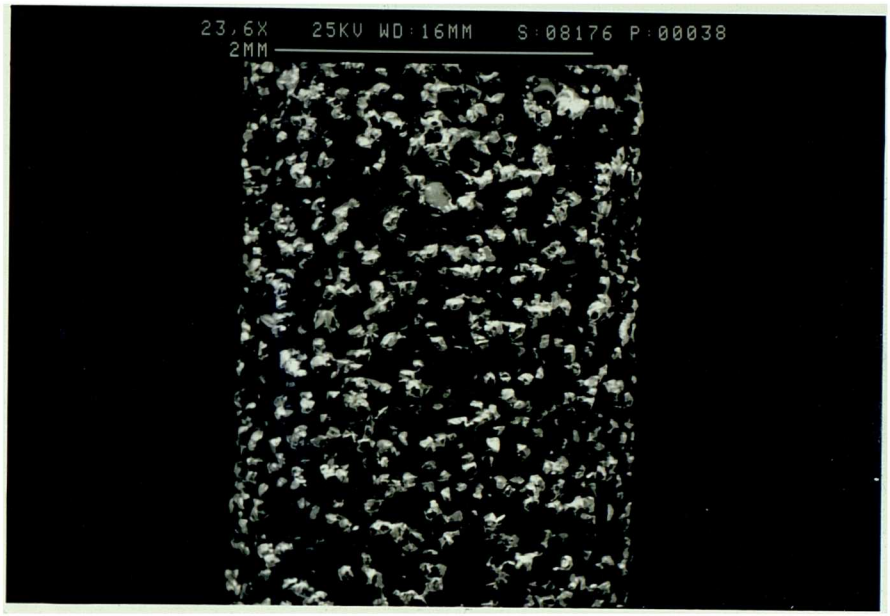

Figure 7.5

a)Optical micrograph of as-ground S_i(111) (×200)

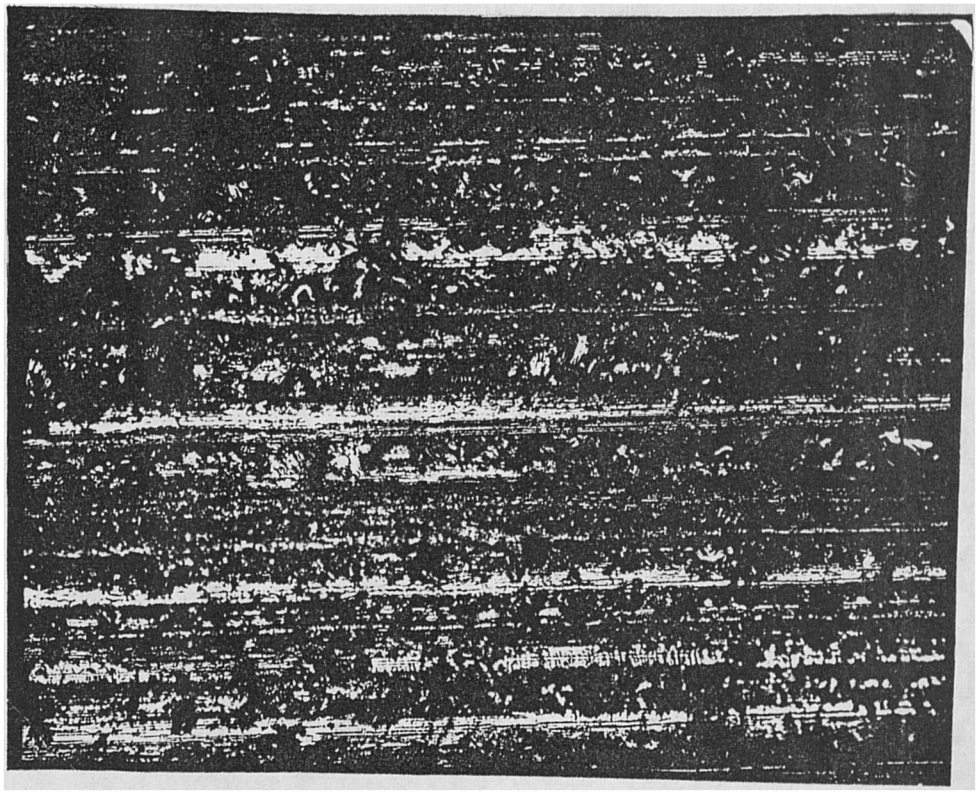

b)The same surface after etching

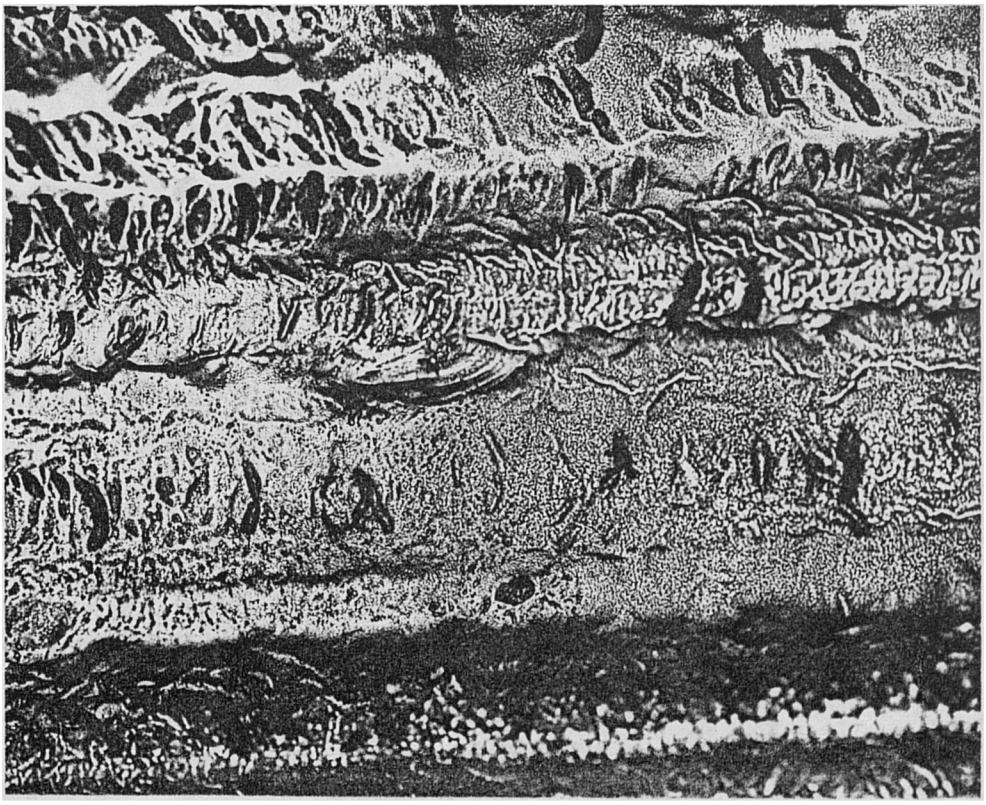

Figure 7.6:The tin-bonded diamond end mill

a)SEM micrograph (×23.6)

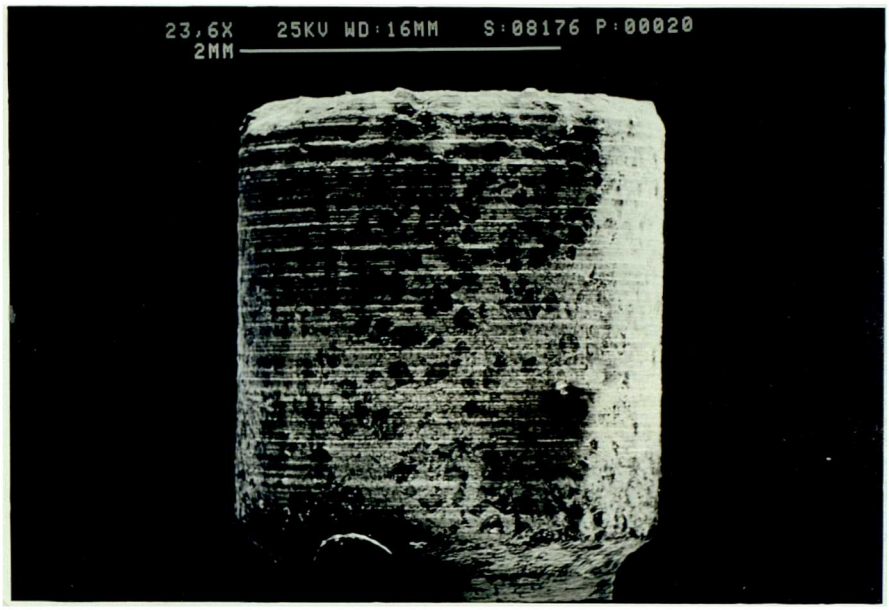

b)SEM micrograph (×146)

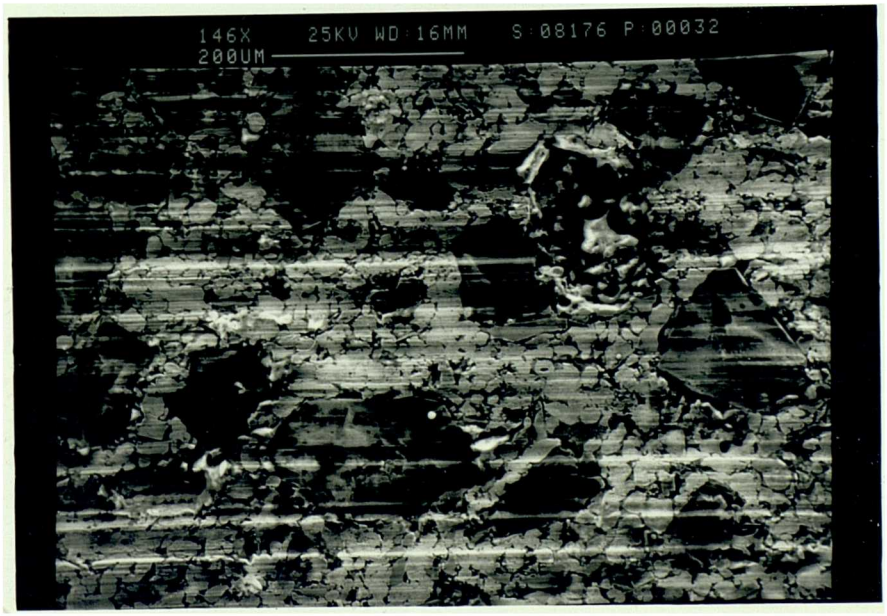

c)optical micrograph (×240)

Figure 7.7: Si(111) surfaces as ground by a high speed diamond end-mill

a)new tool

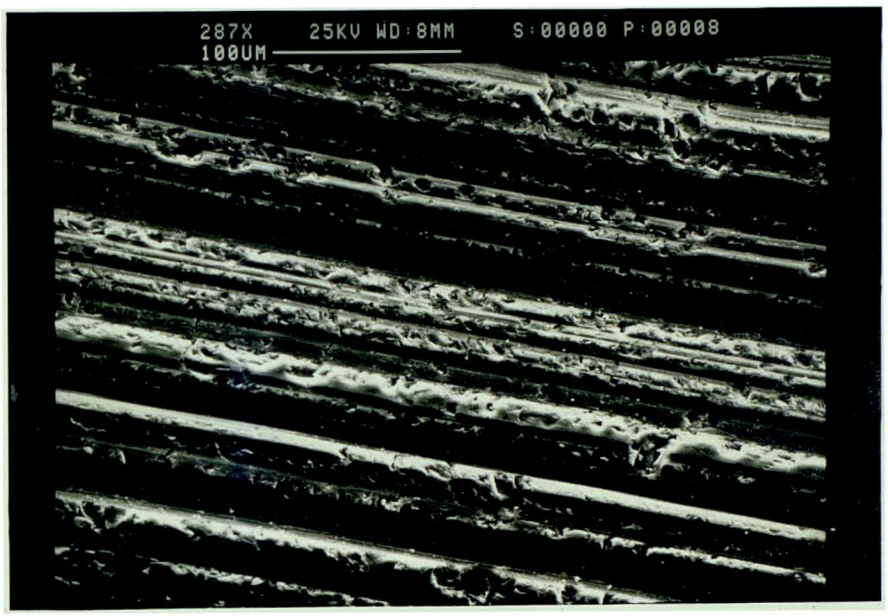

b)worn tool

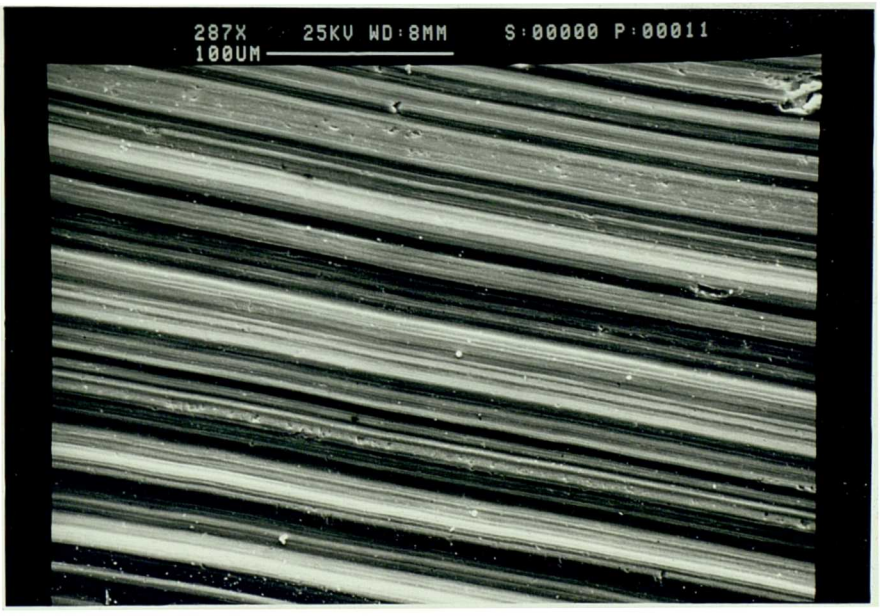

Figure 7.8:Si(111) ground surfaces

a)brittle fracture surface

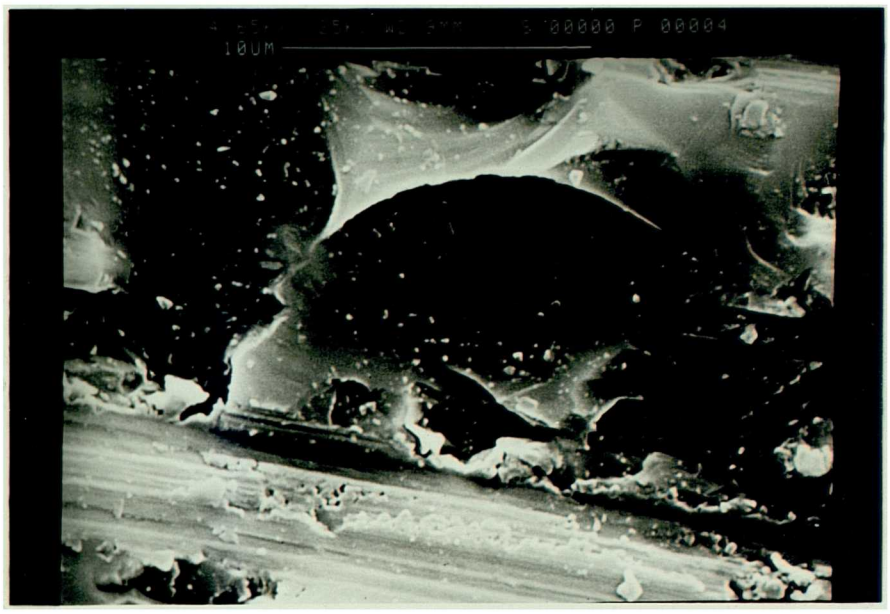

b)smooth surface

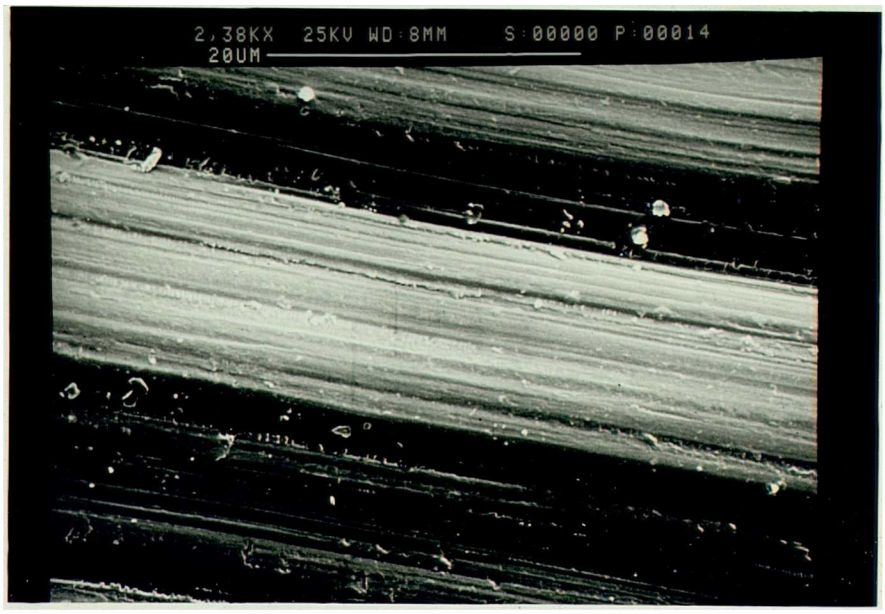

c)optical micrograph of (b) overleaf (×200)

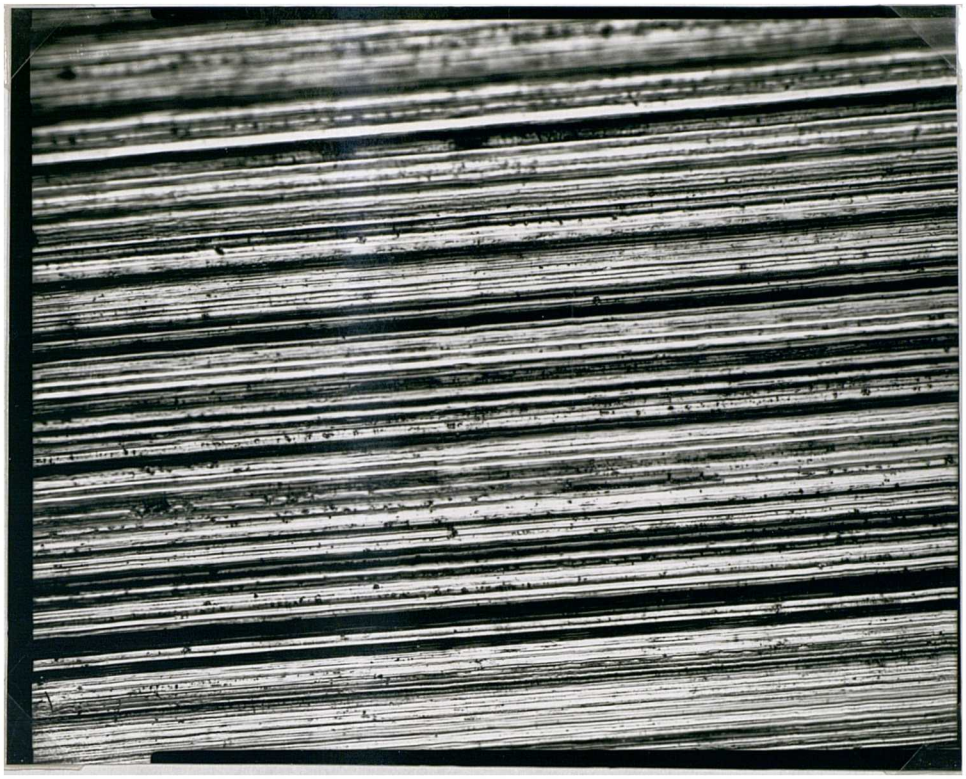

Figure 7.9:Rocking curves for as-machined silicon

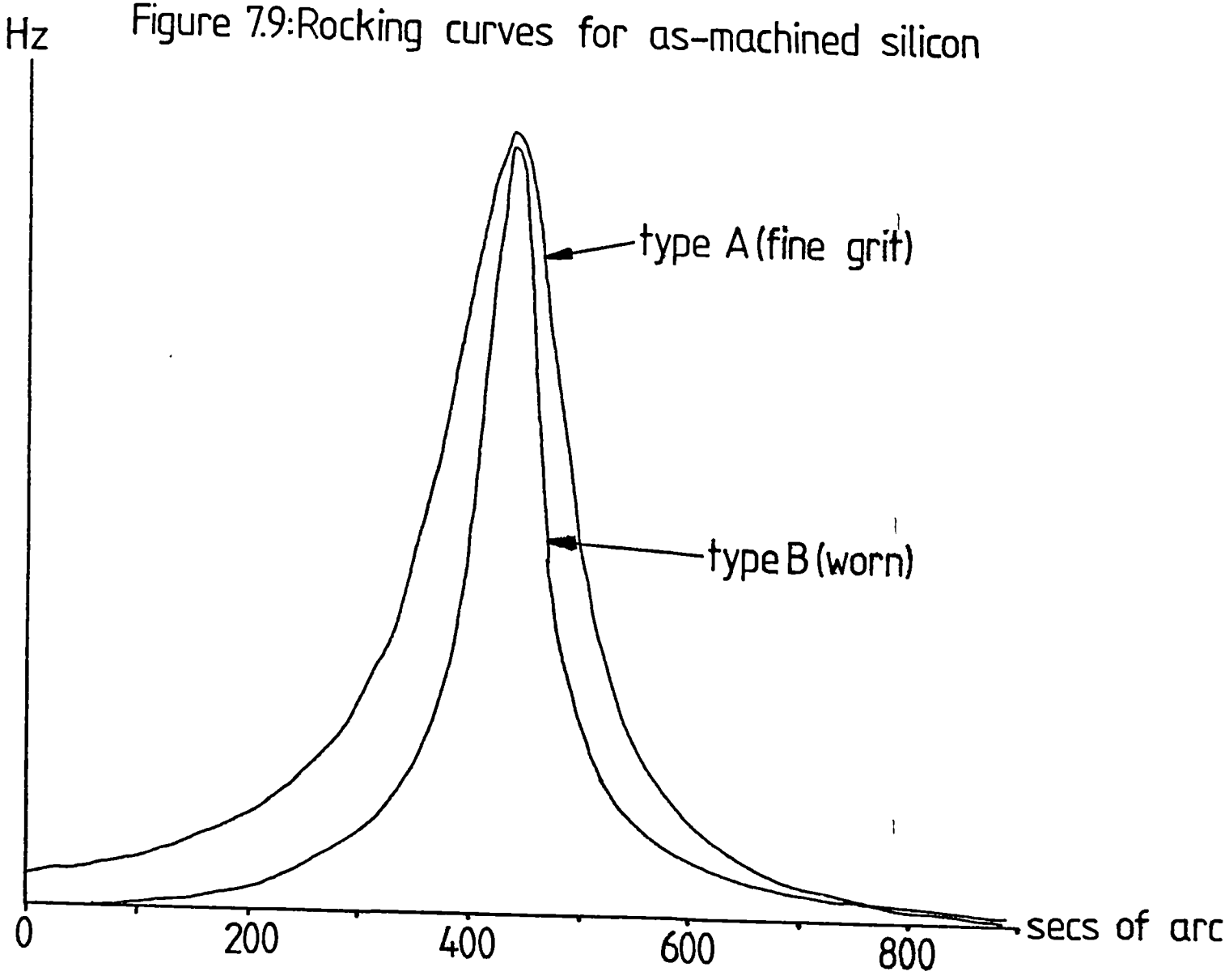

Figure 7.10:FWHM as a function of depth removed

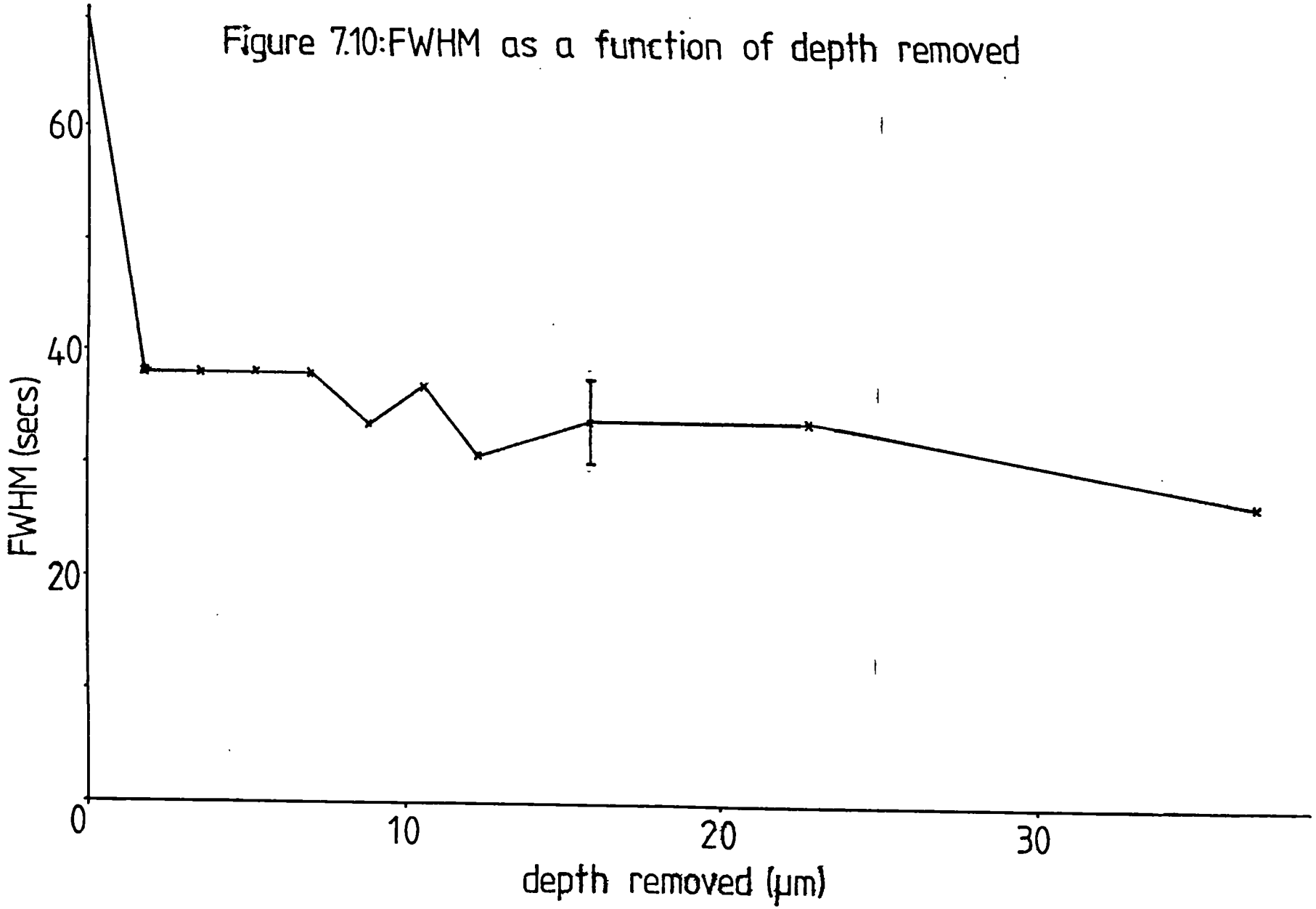

Figure 7.11: Optical micrograph of etched silicon having low initial surface damage (×200)

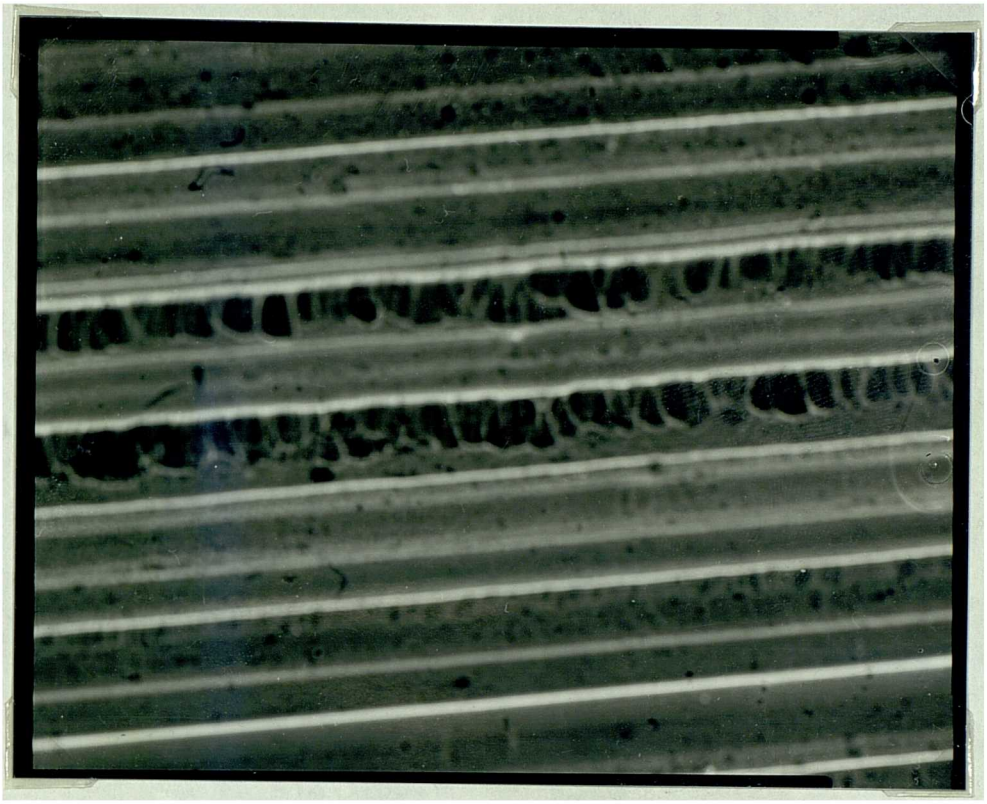

Figure 7.12

a)Electrochemical etching proceedure

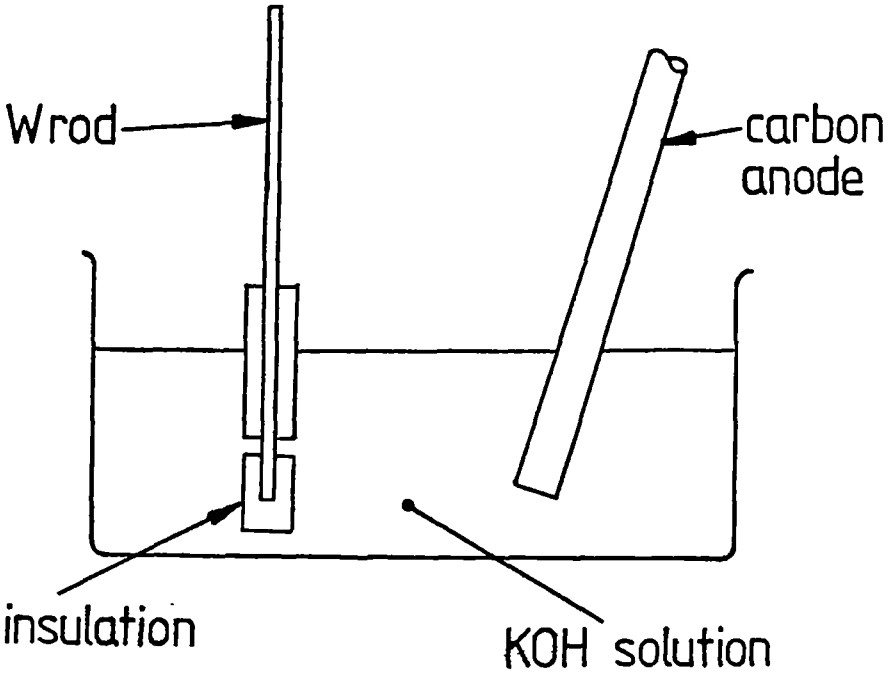

b)Ion beam machining procedure

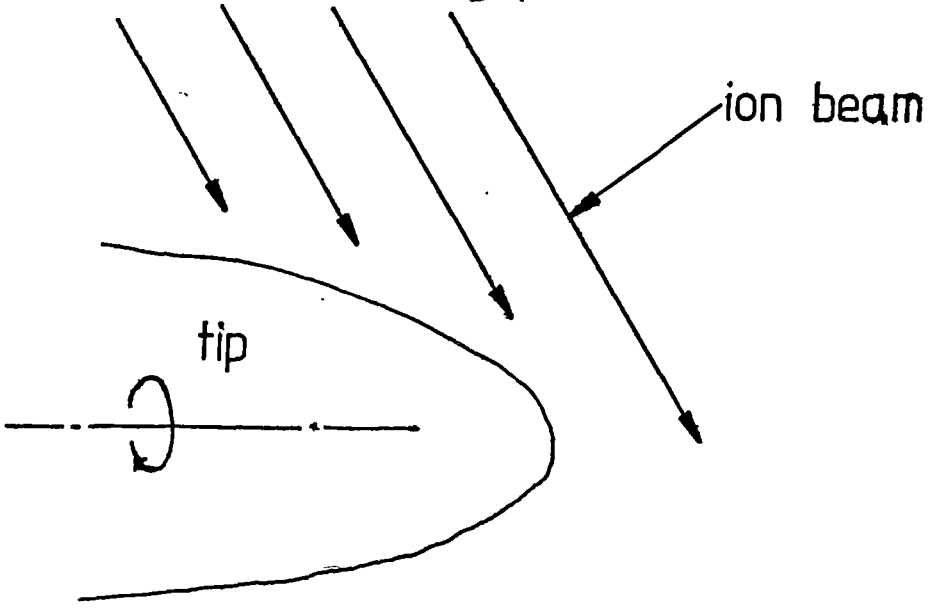

Figure 7.13:SEM micrographs of electrochemically etched tungsten probes

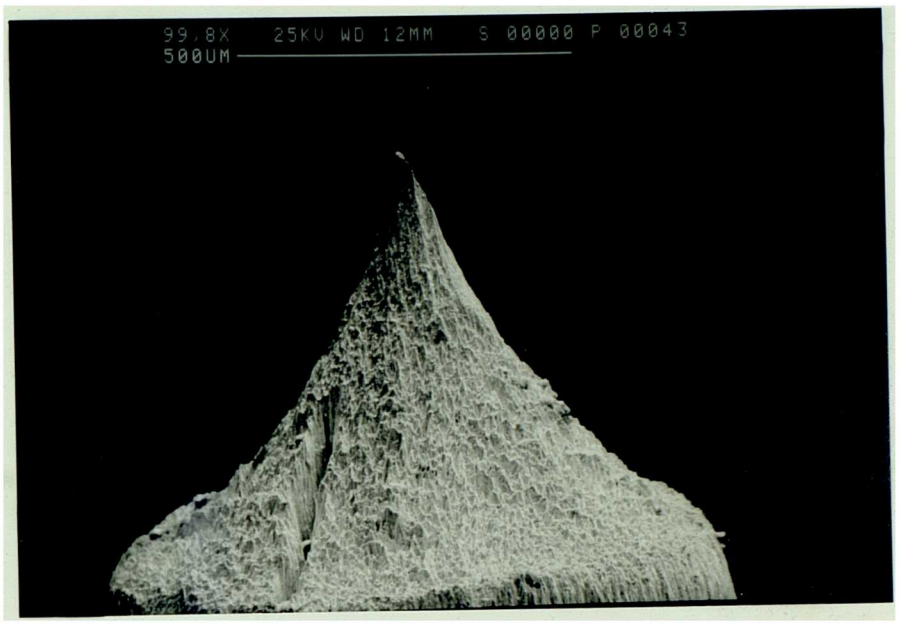

Figure 7.14:SEM micrographs of a tungsten probe after ion beam machining

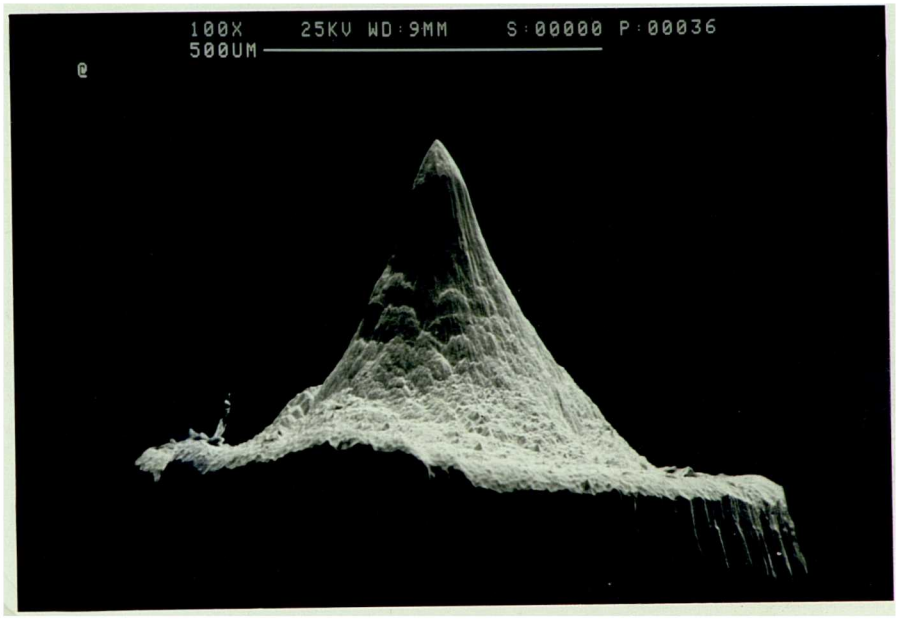

Figure 7.15: The water bonding process

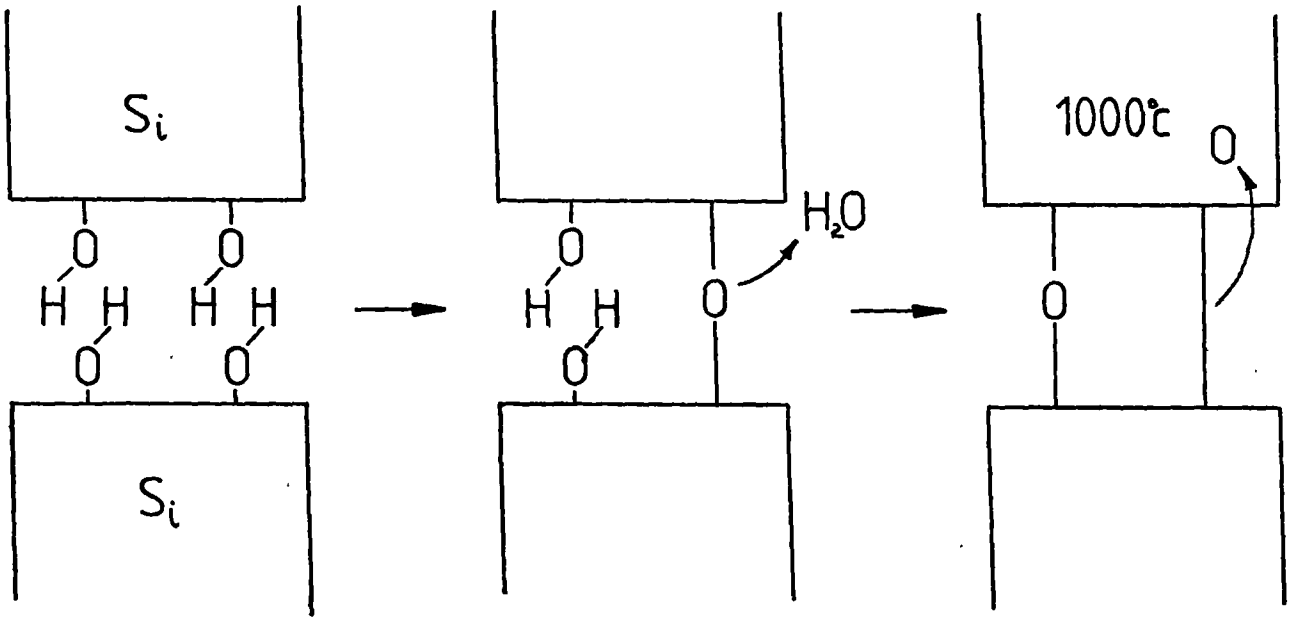

Chapter 8: Current status of the combined Scanning Tunnelling Microscope/X-ray interferometer system

8.0 Introduction

A complete STM system has been designed that operates on the principles described in chapter 6. A full evaluation of the limitations of such a system are beyond the scope of the work presented in this thesis and constitute a rather extensive research project. In this chapter some preliminary experimentation and a theoretical analysis of the initial results will be described. A labelled photograph of this system is shown in figure 8.1 and is described fully in chapter 6. A photograph of the auxiliary electronic monitoring and control is shown in figure 8.2. The method of control has been represented schematically in figure 8.3. This outlines the various interfacing such as the analogue to digital converters for computer control, power amplifiers for the coil drives, a sensitive current amplifier for monitoring tip currents and a logarithmic amplifier to linearise the control loop. All of these components are under the direct control of an IBM PC microcomputer. This controls the rest of the system via a Metrabyte Dash 16 and a Bede Minicam interface board. Because of its high speed, the Dash 16 is used to control the probe displacements and micrometer drive motor as well as monitoring the tunnelling current. The DAC range of this board is 0-5v and thus a differential amplifier and power amplifier have been used to convert this to -5 to 5v. Having a bipolar output allows both forward and reverse motor control and effectively doubles the probe displacement range. The specimen is advanced at a speed of ≈15nm/s, although a wide range of approach speeds can be employed. Upon the monitoring of a tunnelling current, the probe is retracted and the micrometer drive reversed. The required response time of ≈50ms can be easily achieved by the software and probe spring. Reversing of the micrometer serves to completely decouple this hardware from the scanning system. This decou-

pling is represented as a switch in figure 8.3. The x and y-axis drives are controlled by a Bede Minicam 4-channel DAC via an RS232 serial interface. This has bipolar output that simply requires power amplification to the drive coils. All of these DAC's are 12 bit giving a range resolution of 4000-1. A 16 bit DAC and power amplifier having monotonic accuracy has been manufactured and tested to extend this range.

The tunnelling current is amplified and converted to a voltage signal by two M117 FET transistors connected as a long tailed pair to the virtual earth of a standard 741 voltage amplifier. This output voltage is then fed into an Analogue Devices 755N logarithmic amplifier. This amplifier was kindly supplied by The National Physical Laboratory, Teddington.

8.1 Calibration

This section presents the calibration of the electronic and mechanical components. The ohmic tunnelling junction has been simulated using fixed value resistors. The settings that are referred to in this section relate directly to the numbers indicated on the front panel dials.

8.1.1 Three dimensional coil drive stage

The voltage delivered to the coil drives from the power amplifiers due to a given digital output have been monitored with a Phillips PM2519 digital voltmeter. The voltages for a single step requirement in the three axes were found to be v_x=7.7mv/step, v_y=1.4mv/step and v_z=1.36mv/step. From the analyses of section 2.3, the stiffnesses (λ) of the springs in the three axes have been calculated to have the values $\lambda_y=5.63\times10^5$N/m, $\lambda_x=8.02\times10^5$ N/m and $\lambda_z=2.37\times10^5$N/m. The electromagnetic drives for all three configurations are all the same and have a value for the force constant (K) of 2.84N/A. Resistances have been added to these coils such that R_y=120Ω, R_x=275Ω and R_z=163Ω. The output displacement (δ) for a unit DAC step is given by

$$\delta_x=\delta_y=\delta_z=\frac{v\,K}{R\,\lambda}=0.1nm/step \qquad (8.1)$$

The values for K and λ are dependent upon the geometry of the coil and spring arrangement. The displacement per unit step can be readily altered by varying the resistance (R) or amplifying the

DAC step voltage (v).

8.1.2 The logarithmic amplifier

The overall amplifier consists of three stages. These are the tip voltage supply, the current voltage amplifier and the logarithmic amplifying stage. The tip supply voltage is set via a ten turn helicoil potentiometer with the choice of polarity being set by a switch. A graph of the tip voltage as a function of the potentiometer setting over the range 0-0.3 is shown in figure 8.4. This voltage was found to be rather uncertain at the lowest settings.

The current amplifier has a number of gain settings. This has presently been used only with preset gain that corresponds to the zero setting on the gain potentiometer. The voltage output from this amplifier for a given input current has been calibrated by connecting the tip supply voltage to the current amplifier via a number of different resistances. The voltage output from the amplifier as a function of input current was found to closely follow the equation

$$v_{out} = 0.047\, I_{in}(nA) \qquad (v) \tag{8.2}$$

The output from the current amplifier passes into a logarithmic amplifier. This has an offset facility that allows an output voltage to be referenced to a particular input voltage. The offset setting for a required input current (I_{req}) can be calculated from the approximate equation

$$offset \approx 2.54 - 0.070 I_{req}(nA) \quad (1 < offset < 2) \tag{8.3}$$

This setting is that at which a zero output voltage is obtained at a given current into the initial amplification stage and acts as the reference tunnelling current.

Connecting a resistor across the tip supply to the current amplifier can be used as a calibration method. Using a ten mega-ohm resistor, a current range of approximately 10 to 75nA can be generated. A graph of the output voltage against the input current for the complete amplification system is shown in figure 8.5(a). This graph shows the transfer characteristics with a unity offset. Replotting these points with a logarithmic abscissa does not produce a straight line as expected for the amplifier, figure 8.5(b).

8.1.3 Micrometer advance calibration

The discrete action of the stepper motor drive was found to produce unacceptable vibrations in the microscope. The amplitude of this vibration was large enough to be sensed with the hand and the motor action was clearly audible. Consequently, this has been replaced by a geared DC motor and servo control unit. The angular speed of the motor drive system has been calibrated by timing a number of revolutions of the coupling for a specific voltage applied to the servo-control unit. The gearbox and micrometer were also connected during this calibration. The output angular velocity (ω_{out}) was linearly related to the input voltage over the range 0.5 to 5rpm and can be determined from the equation

$$\omega_{out}=2.7v_{in}\ \ (rpm) \tag{8.4}$$

The micrometer advance velocity in microns per minute for the gearing of this rig is 5/6 of the angular velocity in revolutions per minute.

8.1.4 Verification of probe axis displacement

To verify that the displacements specified by the DAC output correspond to those predicted by the theory, z-axis displacements have been monitored by a Talysurf 5 stylus measurement system. The stylus was contacted onto the piece of aluminium that normally houses the tunnelling probe. A potential of 1v was applied to the coil magnet force transducer and the stylus output voltage measured by a Schlumberger DVM. Drift problems and an excessively large measurement loop restricted the measurement accuracy to probably no better than 20-30%. The accuracy of the stylus may also introduce further errors. Repeated trials implied a motion of approximately 50nm. The calculated value of 73nm is outside of the specified accuracy although the added stiffness of the stylus system imply a conservative estimate. This exercise, although imprecise, confirms the displacements predicted from the theory of chapter 2.

8.2 Preliminary experimental results

8.2.1 Experimental method

The complete STM system, as described in chapter 6, has been manufactured and is mounted on a vibration isolated table inside a lead lined, wooden cabinet, Bowen et al, 1985. Vibration isolation is carried out by two stages. The complete instrument is mounted onto a concrete block that is supported by an airspring suspension. This servo controlled system has a fundamental frequency of less than 1Hz and is overdamped for large amplitude vibration. The working stage of the instrument is mounted onto an optical bench that is filled with sand and is further isolated against higher frequency vibrations by three viton of thermal perturbations and airborne noise. Cable connections are made via the concrete block to the cabinet. The specimen consisted of a piece of polished silicon 4mm by 4mm by 1mm, having a thin sputtered layer of gold on its surface. The probe has been electrochemically etched and ion-beam milled as described in section 7.5.

8.2.2 Results

An initial experiment has been conducted to establish the feasibility of this mechanism for STM analysis. The specimen was positioned close to the probe by monitoring the amplifier output whilst advancing the micrometer. Upon measuring a small current, both the probe and micrometer were retracted. Repeating this procedure a number of times under computer control enabled the probe to maintain a current with the micrometer retracted clear from the specimen mounting stage. An offset of 1.35 was found to null the amplifier output. This corresponds to a junction current of approximately 17nA with a tip potential of 122mv.

The output from the logarithmic amplifier was then monitored with the probe incremented backwards and forwards in a linear path. A plot of the amplifier output voltage as a function of the calculated probe displacement is shown in figure 8.6. It can be seen from this figure that the motion far exceeds that which would normally be expected to be due to the tunnelling mechanism. The fact that the curve is approximately linear implies that the junction current is exponentially related to the probe displacement. This is characteristic of tunnelling mechanisms. The mechanism encountered in this instance may well be a consequence of contact with the specimen as described by Coombs and Pethica, 1985.

At this point in the study, the ADC circuit used in this experiment behaved erratically. All subsequent measurements of amplifier voltages have been obtained using a Phillips PM2516.

The amplifier output voltage has been monitored as the tip potential has been varied. This is shown in figure 8.7. The amplifier output voltage against a linearly changing input current is expected to exhibit a logarithmic characteristic for a purely ohmic junction. Correcting the raw data of figure 8.7(a) for the true tip potential and plotting this with a logarthmic abscissa results in the graph of figure 8.7(b). Although this curve is not linear, it does have a similar form to that of figure 8.5(b). This implies that there is an ohmic junction between the tip and sample. The resistance of this junction has been calculated to be approximately 6MΩ. Upon completion of these experiments the probe was manually contacted with the specimen a resistance of approximately 10ohms was measured across the input and output leads.

Finally, a plot of the z-axis input required to maintain a constant amplifier output voltage as the specimen was scanned in the x-direction has been plotted in figure 8.8. The profile has been produced by manually inputing coil values and observing the output voltage on the DVM. This output voltage could be maintained at level of around 15mv. This corresponds to the background noise level. This plot was produced in approximately twenty minutes. A number of move and return settings were performed and it was found that the variance of the displacement value applied to the probe coil corresponded to approximately 0.4nm.

The effect on the instrument of people entering the room and speaking outside of the cabinet was not detectable. This implies a very low noise susceptibility under the conditions prevailing in this experiment. Upon completion of the tests, opening and closing the cabinet resulted in a marked shift and the specimen moved outside of its displacement range.

8.3 Discussion

These results pose a number of questions as to the nature of the tip-surface interface throughout this experiment. The most obvious question is whether the tip is actually in contact with the surface and if so what is the nature of the interface. From the graph of figure 8.6, it can be seen that a force has been applied to the z-axis linear spring that would correspond to a free

motion of 100nm. The apparent probe to specimen separation characteristic does however have an exponential relationship as predicted by tunnelling theory. The force required for this motion is approximately 20mN. Although this is the force experienced by the linear spring mechanism, it is not necessarily transmitted to the specimen surface. This will depend on the overall measurement loop stiffness. This has not been quantified as yet. From the work of Durig et al, 1986, a high junction stiffness of say 50N/m cannot possibly support this force.

This phenomena of contacting the specimen whilst maintaining a tunnelling characteristic has been an issue since the very first STM work and apparently continues to this day, Pethica, 1986. This mechanism whereby tunnelling occurs around in intermediate particle or through a crack in a surface oxide is discussed on page 12. The low noise and excellent repeatability shown in figures 8.6-8.8 are also characteristic of this mechanism. That an ohmic junction having an exponential dependence upon apparent separation has been shown to be not only a function of the tip-sample properties but also the mechanical fidelity of the measurement system. The advantage with this particular system is that, because of its open loop linear characteristics, any inconsistencies with the theoretical predictions can be identified. This may prove to be of primary importance in the complete evaluation of scanning tunnelling microscopy for surface physics and metrological applications.

8.4 Summary and further work

In this thesis the design and assessment of linear elastic and polymeric displacement mechanisms for use as a reference motion has been presented in chapters 2 and 3. Analysis of a polymeric bearing slideway system has been shown to exhibit repeatabilities of a few nanometres or less over motions of around 40mm. More recent investigations have demonstrated that better performance figures are achievable.The estimated slideway noise is better than 50pm.This system has, as yet, a lateral resolution of 50μm. Results from the investigation of the polymeric slideway system were used in the design and development of a stylus based measuring instrument called Nanosurf 2. The design and evaluation of this instrument is presented in chapters 4 and 5 respectively. The design and manufacture of a novel STM system based on linear spring mechanisms

and an electromagnetic force transducer are presented in chapters 6 and 7. It has been shown that the elastic displacement devices can control rectilinear displacements having parasitic errors of better than 1 part in 10,000. The accuracy of this displacement can be controlled in open loop fashion and the range resolution ratio is mainly a function of the electronic drive. This range resolution ratio has been shown to be unimpaired at a resolution of better than 10pm if single crystal silicon is used for the elastic members. An analysis of the electromagnetic force transducer and optimisation of its performance is presented in chapter 2. Analyses of both of the reference motion configurations indicate that consistent operation may be expected at the sub-nanometre level. It is expected that a dedicated experimental analysis procedure having enhanced measurement resolution will be required to establish the dimensional fidelity of both of these systems.

In chapter 7 a manufacturing technique for the production of intricate shapes such as the linear elastic spring mechanisms has been presented. In the process of generating these shapes in this material, a number of methods have been identified that have the potential for the generation of smooth surfaces having low surface damage as assessed using x-ray diffraction techniques. Further characterisation of this process will be useful for the understanding of the "ductile" or "gentle" grinding of this very useful semiconductor material. The ability both to directly bond silicon and to machine it into intricate shapes will lead to the possibility of producing large, quasi-monolithic silicon crystal components. These would be able to exploit the stable and predictable mechanical, electronic and thermal properties of this material. To verify the feasibility of this idea, the direct water bonding of very high quality bulk silicon flats in a well defined environment must be examined.

This final chapter has outlined the preliminary investigations into a novel STM system. Although imaging has not yet been achieved, the instrument has been shown to produce repeatable motion having nanometre resolution. Because of its linear characteristic, it is able to diagnose tip-specimen contact and any departures from theoretical expectations. Having produced this instrument it is recomended that an assessment program be developed with a view to quantifying the mechanical and electronic characteristics of this instrument and developing it as a future complement to existing systems.

Figure 8.1

a)Three-axis silicon linear spring

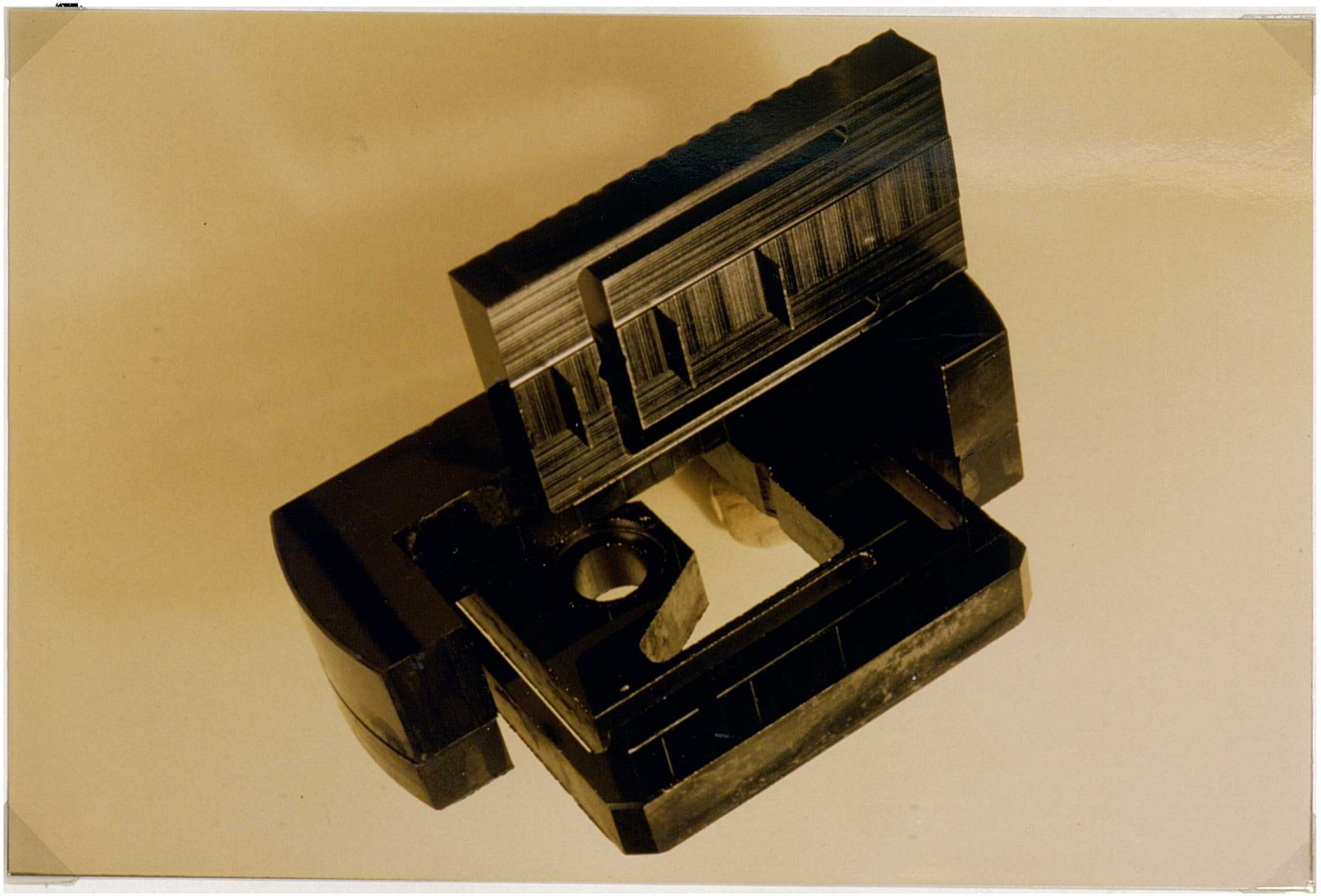

b)STM assembly

Figure 8.2: STM control hardware

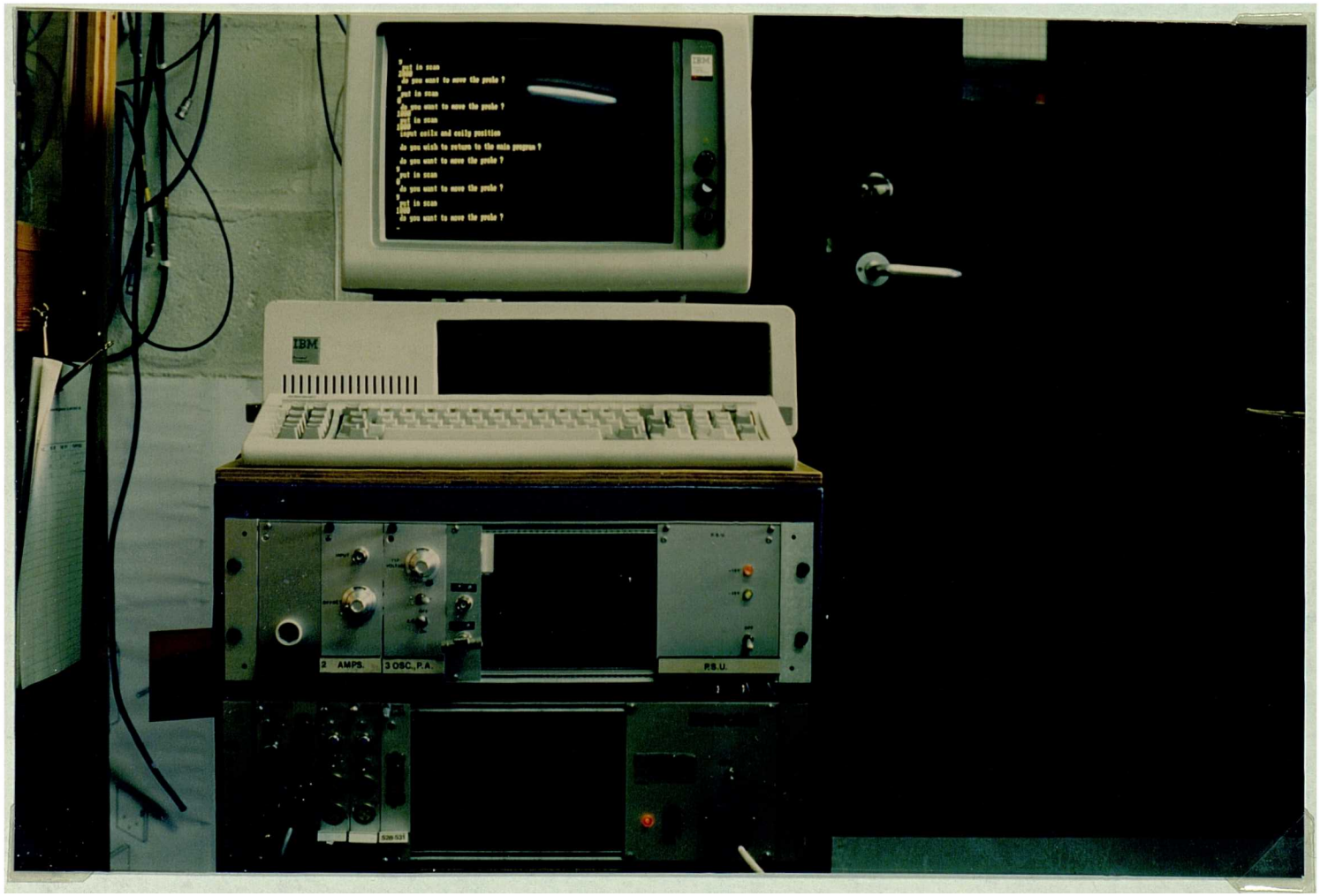

Figure 8.3: Schematic diagram of STM control system

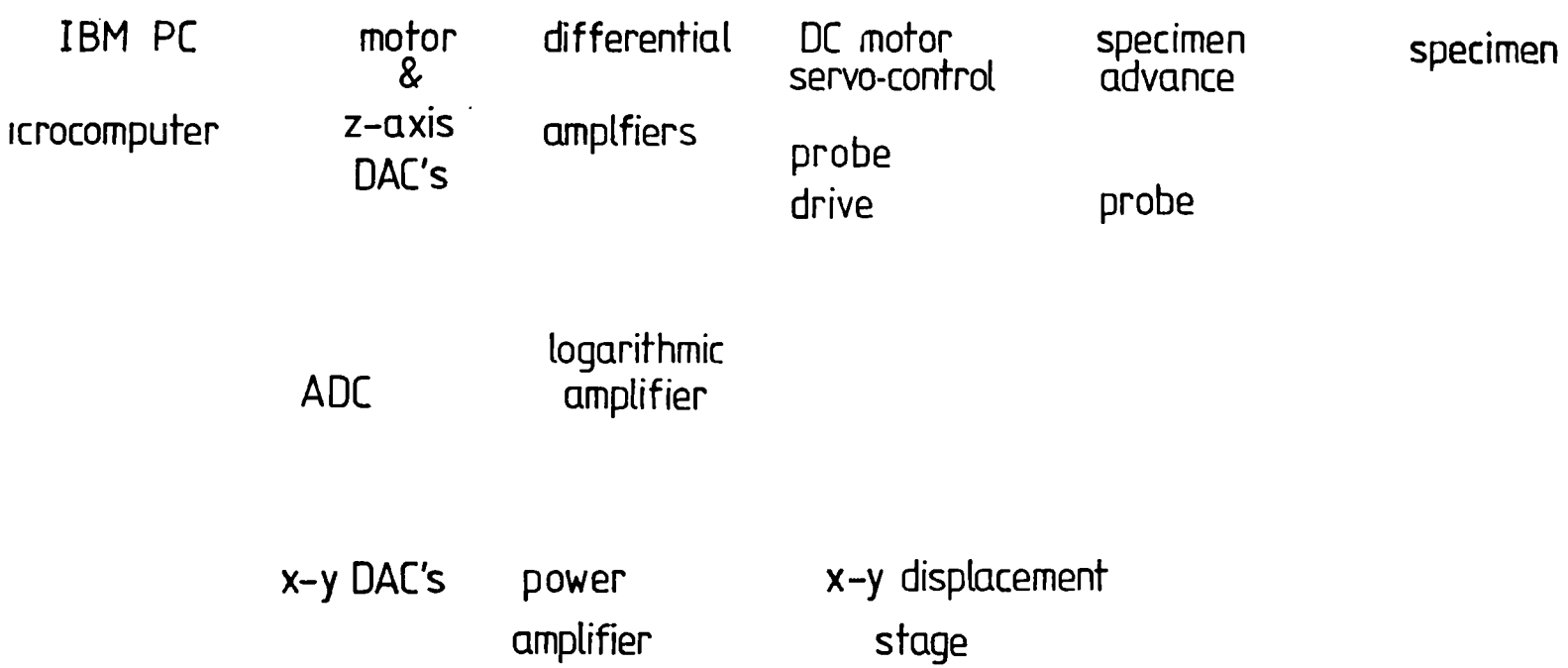

Figure 8.4:Tip supply voltage against potentiometer setting

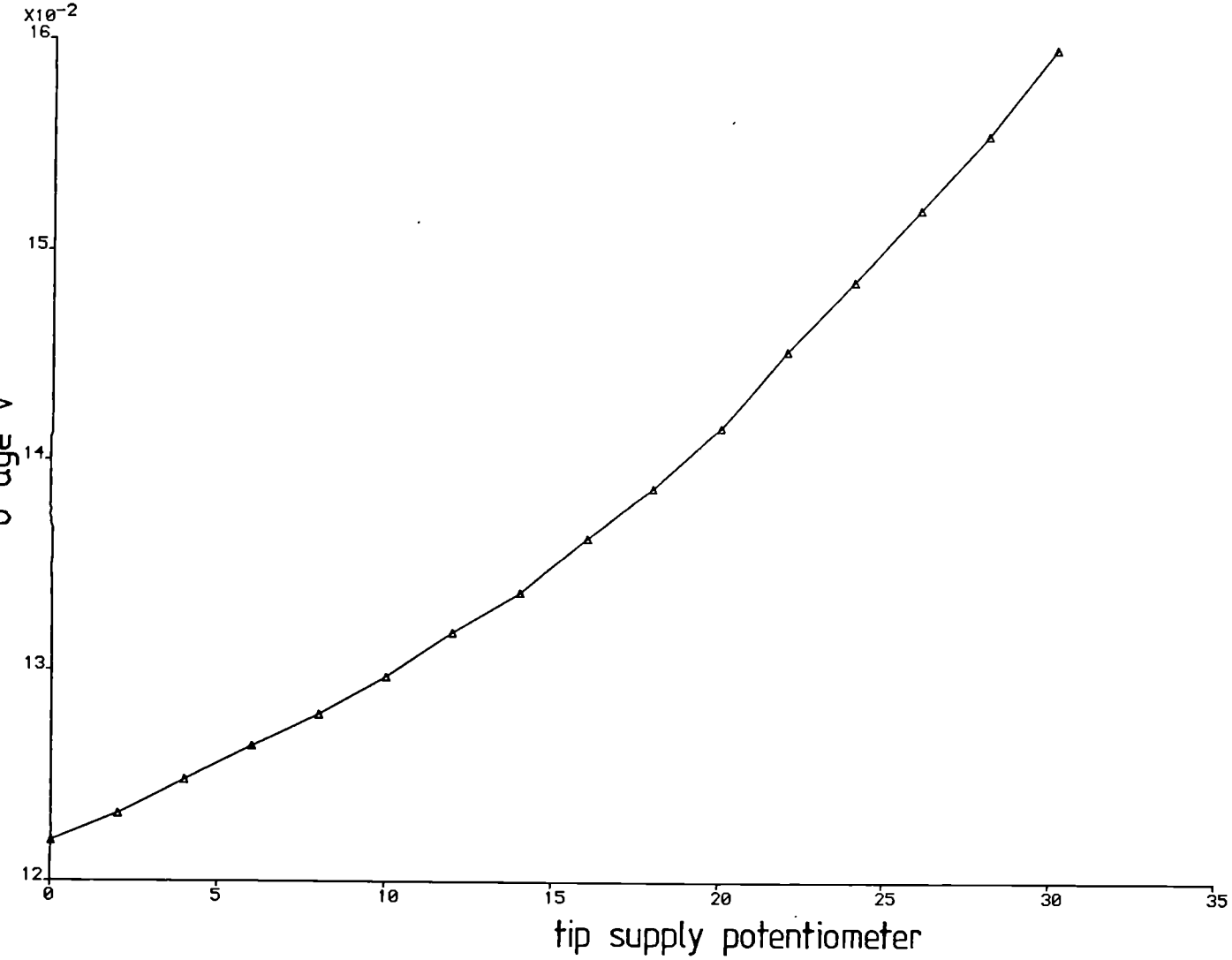

Figure 8.5:Voltage/current characteristic of tunnelling amplifier

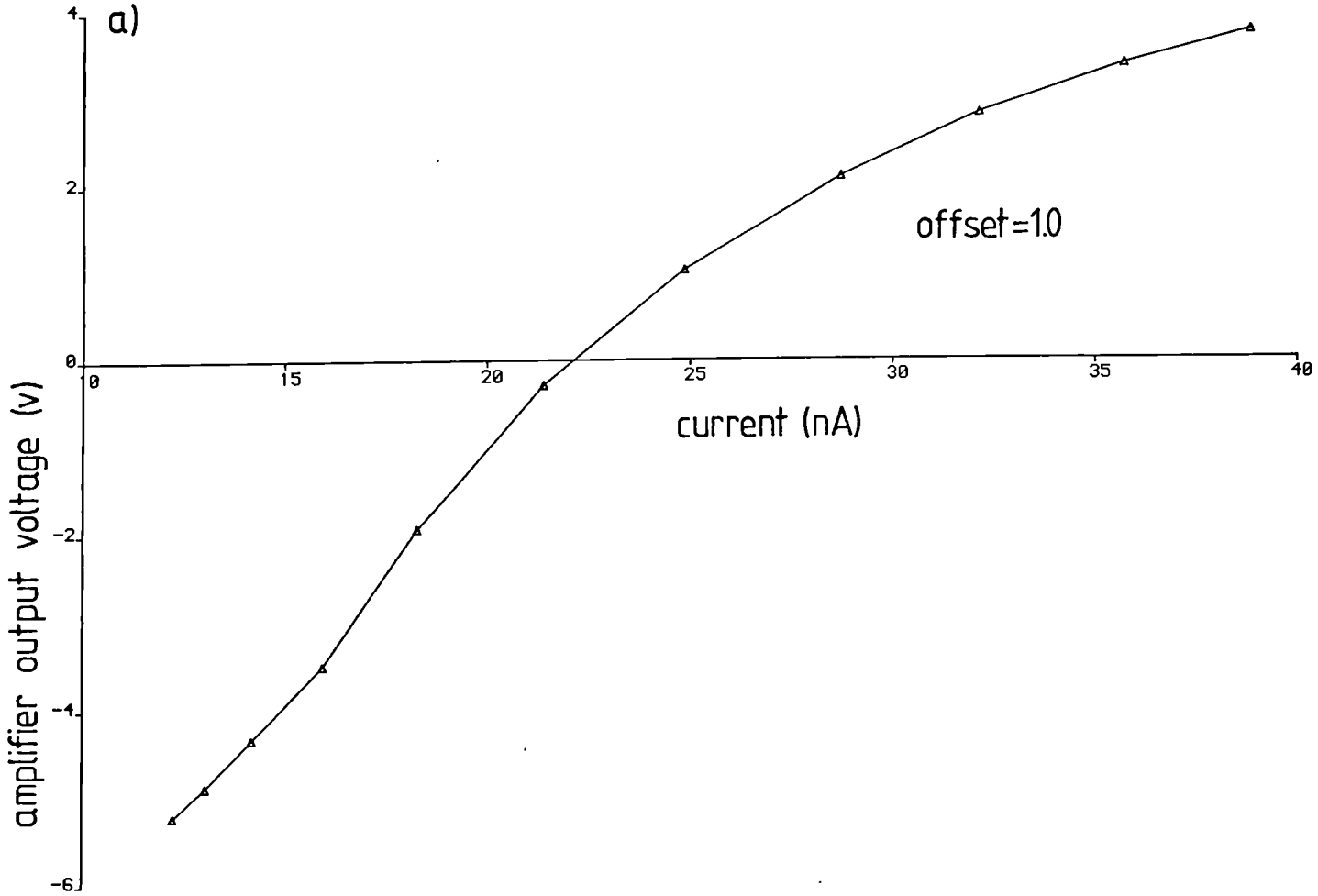

b)current plotted on a logarithmic axis

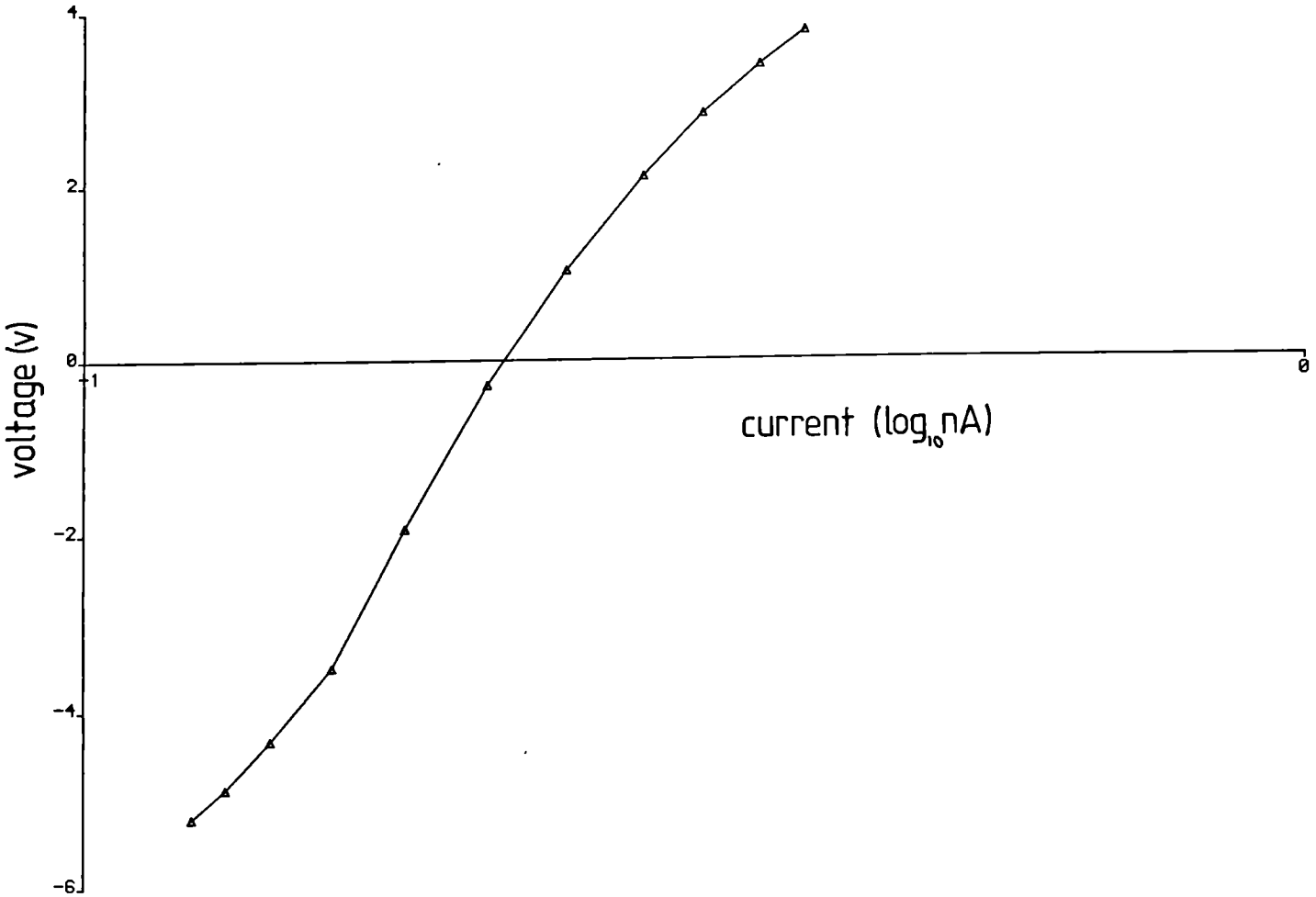

Figure 8.6: Amplifier output voltage against probe displacement setting

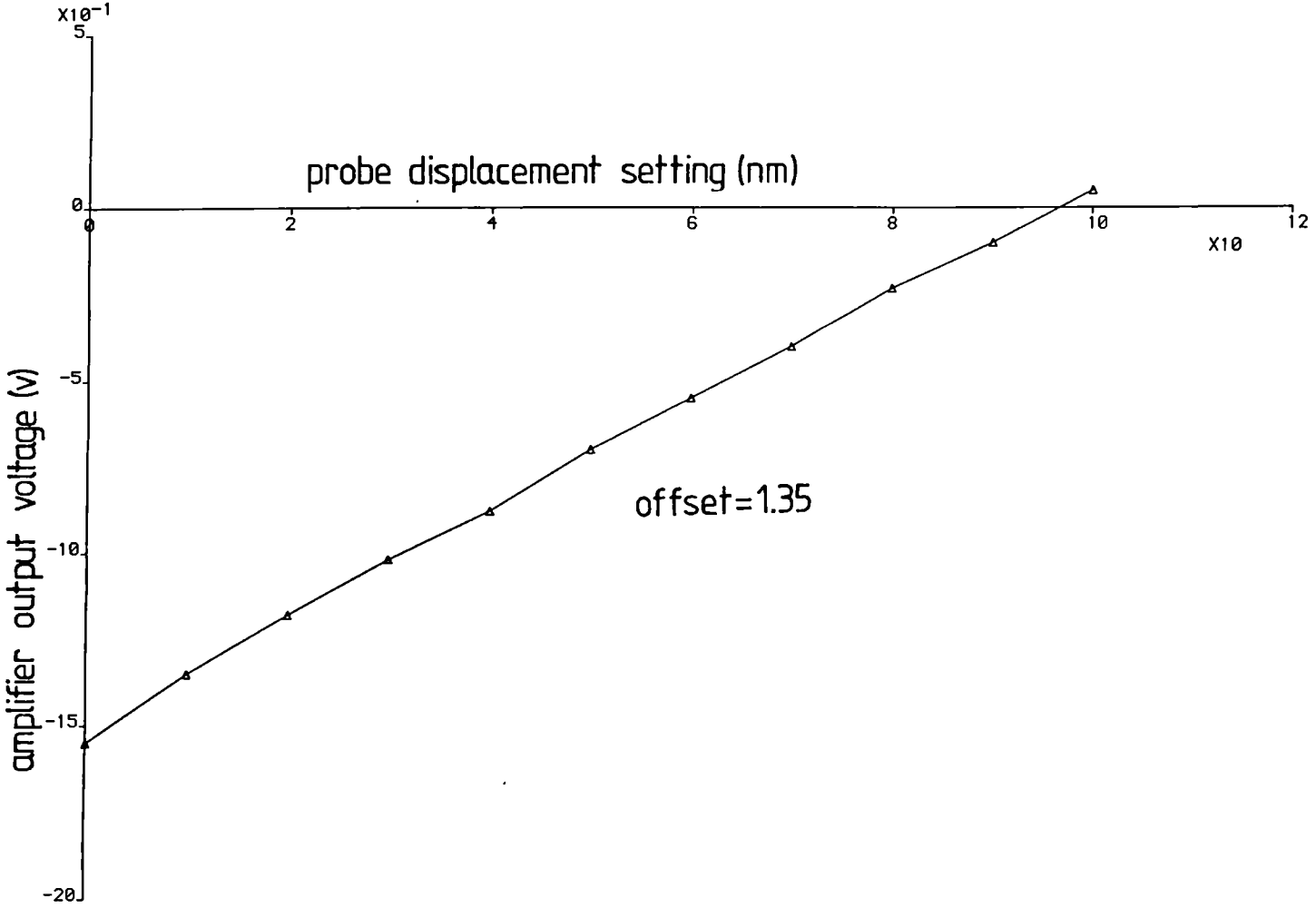

Figure 8.7:Amplifier output voltage against the tip voltage setting

a)raw data

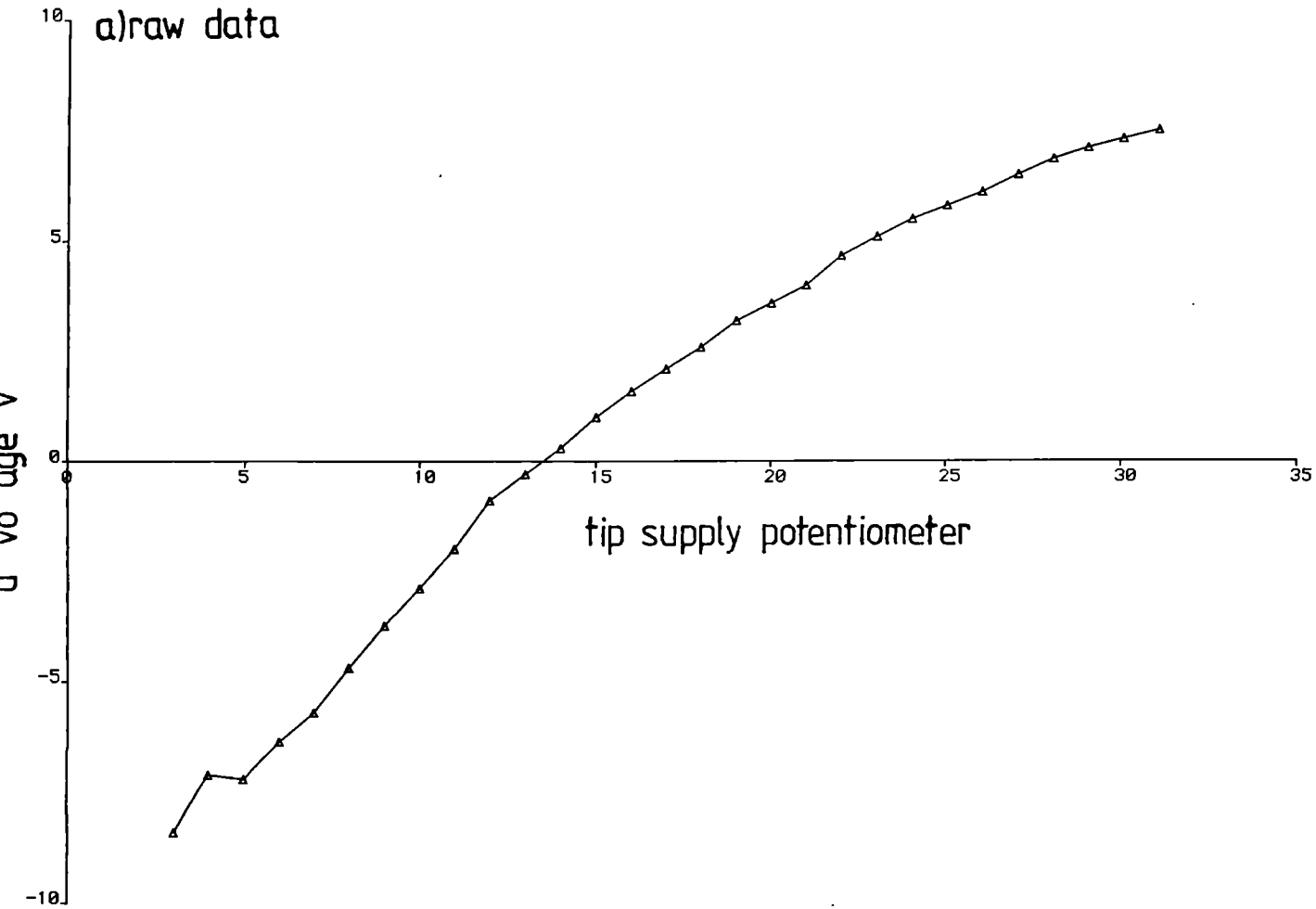

b) amplifier output voltage against the logarithm of tip potential

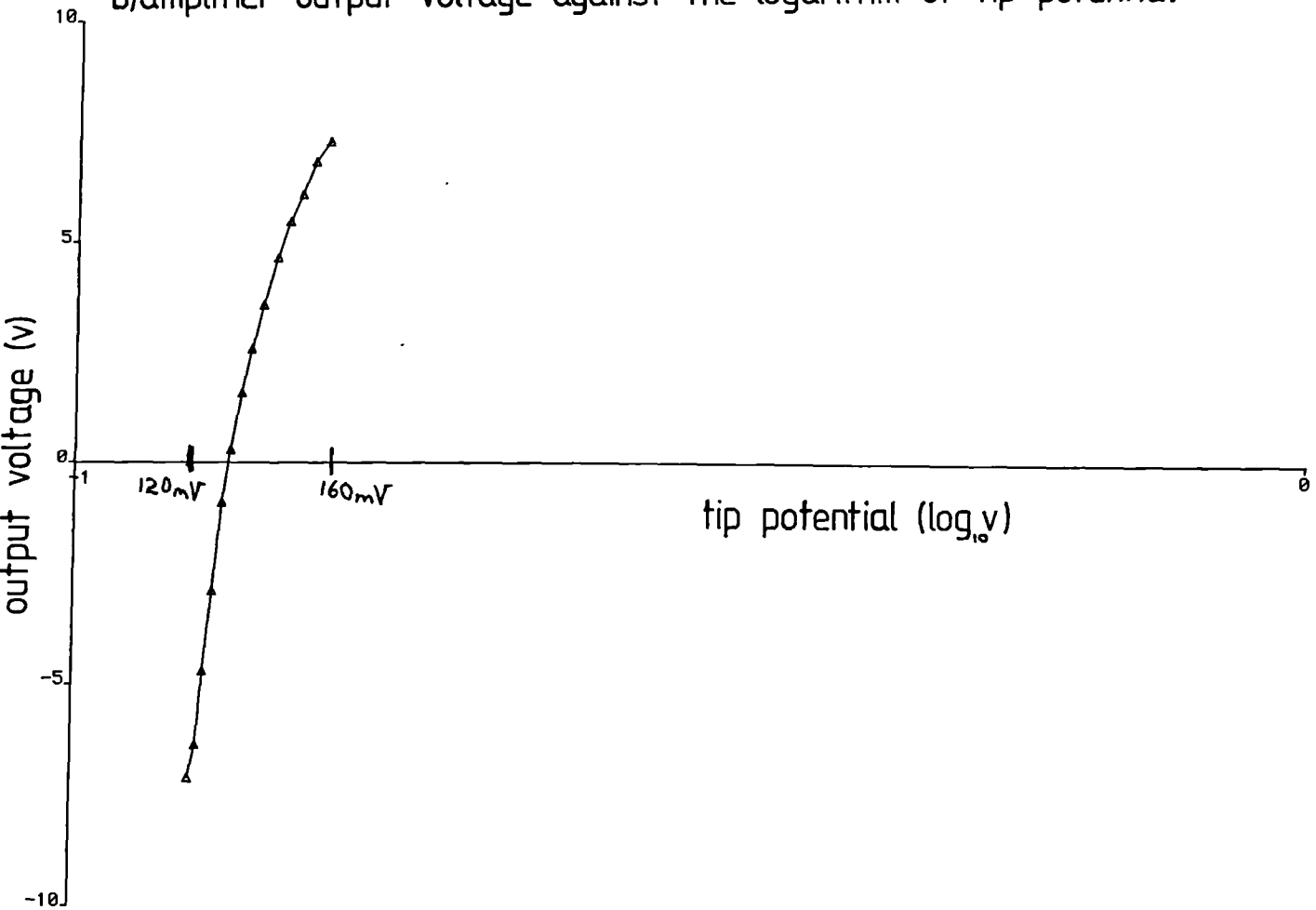

Figure 8.8: Z-axis output required to maintain a constant current over specimen scan of 100nm

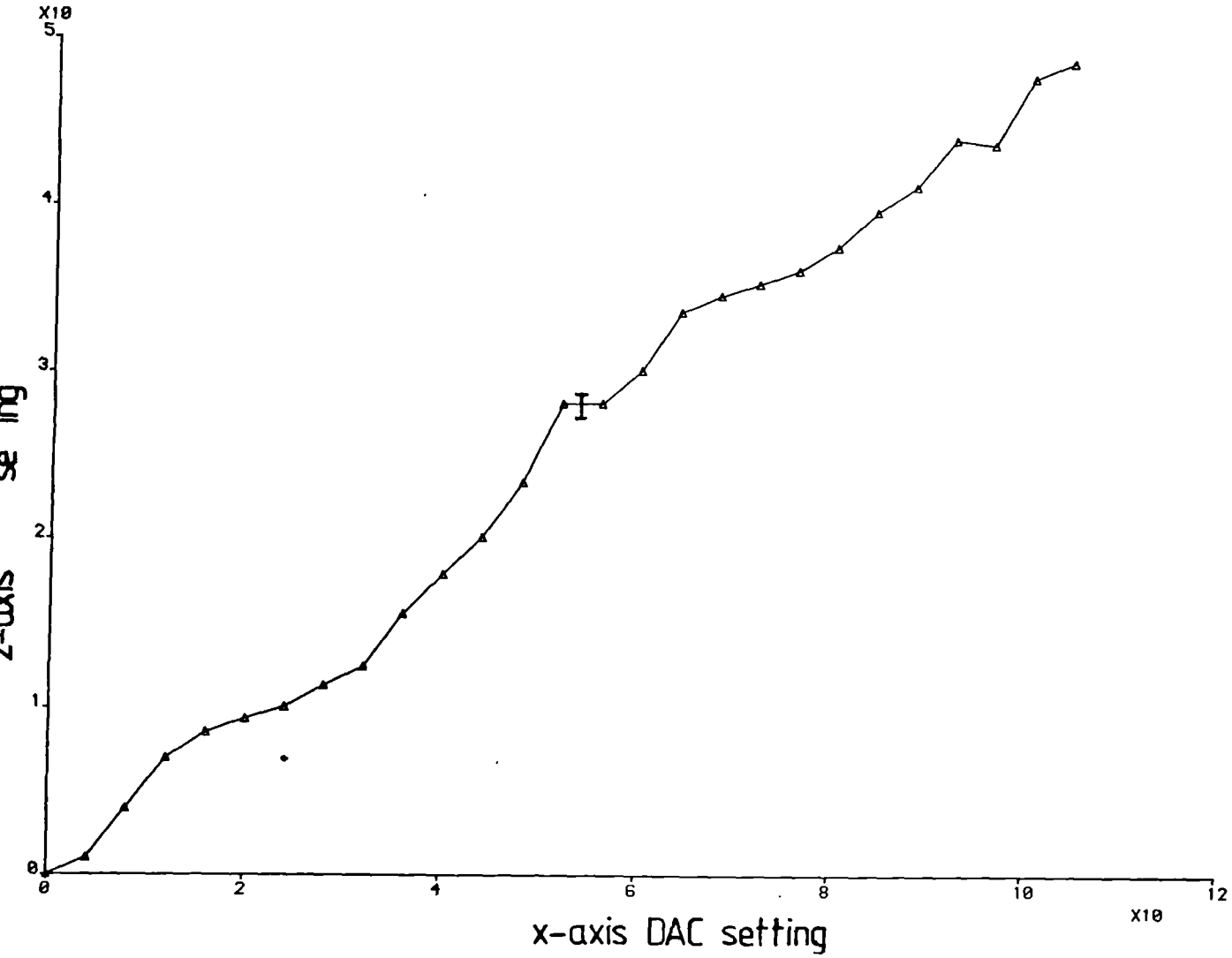

1. References

Adams N., 1963, "Friction and deformation of nylon.I Experimental", J. Appl. Polymer Sci., Vol. 7, pp. 2075-2103.

Alemanni M., Mana G., Pedrotti G., Strona P.P. and Zosi G., 1986, "On the construction of a Zerodur translation devic for x-ray interferometric scanning", Metrologia, Vol. 22, pp. 55-63.

Anthony T.R., 1985, "Dielectric isolation of silicon by anodic bonding", J. Appl. Phys., Vol. 58, No. 3, pp. 1240-1247.

Archard J.F. and Baglin K.P., 1975, "Nondimensional presentation of frictional tractions in elastohydrodynamic lubrication:Part I; Fully flooded conditions",Trans. ASME, pp. 398-411.

Archard J.F. and Baglin K.P., 1975, "Nondimensional presentation of frictional tractions in elastohydrodynamic lubrication:Part II; Starved conditions",Trans. ASME, pp. 412-423.

Atkins A.G., Omar M.K. and Lancaster J.K., 1984, "Wear of polymers", J. Mater. Sci. Letts.,Vol. 3, pp. 779-782.

Baro A.M., Miranda R., Alaman J., Garcia N., Binnig G., Rohrer H., Gerber Ch. and Carrascosa J.L., 1985, "Determination of surface topography of biological specimens at high resolution by scanning tunnelling microscopy", Nature, Vol. 315, pp. 253-254.

Becker P., Dorenwendt K., Ebeling G., Lauer R., Lucas W., Probst R., Rademeacher H.J., Reim G., Seyfried P. and Helmut S., 1981, "Absolute measurement of the (220) lattice plane spacing in a silicon crystal", Phys. Rev. Letts., Vol. 46, No. 23, pp. 1540-1543.

Becker P., Seyfried P. and Siegert H., 1982, "The lattice parameter of highly pure silicon single crystals", Z. Phys. B, Vol. 48, pp. 17-12.

Becker P., Seyfried P. and Siegert H., 1987, "Translation stage for a scanning x-ray optical interferometer", Rev. Sci. Instrum. Vol. 58, No. 2, pp. 207-211.

Becker R.S., Golovchenko J.A. and Swartzentruber B.S., 1985, "Electron interferometry at

crystal surfaces", Phys. Rev. Letts., Vol. 55, No. 9, pp. 987-990.

Becker R.S, Golovchenko J.A. and Swartzentruber B.S., 1987, "Atomic scale surface modifications using a tunnelling microscope", Nature, Vol. 325, pp. 419-421.

Beilby, 1909, Proc. Roy. Soc., Vol. A82, p599.

Benbow J.J., 1960, "Cone cracks in fused silica", Proc. Phys. Soc., Vol. B75, pp. 697-699.

Bennett.J.M., 1985, "Comparison of instruments for measuring step heights and surface profiles", Applied Optics, 24(22), pp. 3766-3772.

Biegelsen D.K., Ponce F.A. and Tramontana J.C., 1987, "Ion milled tips for scanning tunneling microscopy", Appl. Phys. Letts., Vol. 50, No. 11, pp. 696-698.

Binnig G., Rohrer H., Gerber Ch. and Weibel E., 1982, "Tunneling through a controllable vacuum gap", Appl. Phys. Letts., Vol. 40, No. 2, pp. 178-180.

Binnig G. and Rohrer H., 1982, "Scanning tunneling microscopy", Helv. Phys. Acta, Vol. 55, p 726-735.

Binnig G., Rohrer H., Gerber Ch. and Weibel E., 1982, "Surface studies by scanning tunnelling microscopy", Phys. Rev. Letts., Vol. 49, No. 1, pp. 57-60.

Binnig G. and Rohrer H., 1983, "Surface imaging by scanning tunnelling microscopy", Ultramicroscopy, Vol. 11, pp. 157-160.

Binnig G., Rohrer H., Gerber Ch. and Weibel E., 1983, "7 × 7 Reconstruction on Si(111) resolved in real space", Phys. Rev. Letts., Vol. 50, No. 2, pp. 120-123.

Binnig G., Garcia N., Rohrer H., Soler J.M. and Flores F., 1984, "Electron-metal-surface interaction potential with vacuum tunneling: Observation of the image force", Phys. Rev. B, Vol. 30, No. 8, pp. 4816-4818.

Binnig G., Quate C.F. and Gerber Ch., 1986, "Atomic force microscope", Phys. Rev. Letts., Vol. 56, No. 9, pp. 930-933.

Bonse U. and Hart M., 1965, "An x-ray interferometer", App. Phys. Letts., Vol. 6, No. 8, pp. 155-156.

Bowden F.P. and Tabor D., 1964, "The Friction & Lubrication Of Solids:Vol II", Clarendon Press.

Bowden F.P. and Brookes C.A., 1966, "Frictional anisotropy in nonmetallic crystals", Proc. Roy. Soc, Vol. A295, pp. 244-258.

Bowden F.P. and Hanwell A.E., 1966, "The friction of clean crystal surfaces", Proc. Roy. Soc., Vol. A295, pp. 233-243.

Bowen D.K, Chetwynd D.G. and Davies S.T., 1985, "Calibration of surface roughness transducers at Angstrom levels using x-ray interferometry", Proc. SPIE, San Diego, 563, pp. 412-419

Bowers R.C., Clinton W.C. and Zisman W.A., 1953, J. Appl. Phys., Vol. 24, pp. 1066-1067.

Brooks A.D., Donovan R.P. and Hardesty C.A., 1972, "Low-temperature electrostatic silicon to silicon seals using sputtered borosilicate glass", J. Electrochem. Soc., Vol. 119, No. 4, pp. 545-546.

Brown N.J., 1987, "Some speculations on the mechanisms of abrasive grinding and polishing", Precision Engineering.

Bruinsma R. and Bak P., 1986, "Quantum tunneling, dissipation and fluctuations", Phys. Rev. Letts., Vol. 56, No. 5, pp. 420-423.

Chetwynd D.G., Siddons D.P. and Bowen D.K., 1983, "X-ray interferometer calibration of microdiplacement transducers", J. Phys. E., Vol. 16, pp. 871-874.

Chetwynd D.G., 1987, "Structural materials for percision devices", Precision Engineering, in press.

Cohen S.C. and Tabor D., 1966, "The friction and lubrication of polymers", Proc. Roy. Soc.(Lond.), Vol. A291, pp. 186-207.

Coombs J.H. and Pethica J.B., 1985, "Properties of vacuum tunnel currents: Anomalous barrier hieghts", IBM/STM Workshop, Oberlech, Austria, July 1-5.

Corb B.W., Ringger M., Guntherodt H.-J. and Pinkerton F.E., 1987, "Microstrucural investigation of Nd-Fe-B with the scanning tunneling Microscope", Appl. Phys. Letts., Vol. 50, No. 6, pp. 353-355.

Cottrell A.H. and Kelly A., 1966, "The design of strong materials", Endeavour, Vol. 25, pp. 27-32.

Cottrell A.H., "Deformation of solids at high rates of strain", unknown.

Cudworth C.J. and Higginson G.R., 1976, "Friction of lubricated soft surface layers", Wear, Vol. 37, pp. 299-312.

Cutherell R.E., 1979, "The influence of hydrogen on the deformation and fracture of the near surface region of solids: proposed origin of the Rebinder-Westwood effect", J. Matl. Sci., Vol. 14, pp. 612-618.

Danyluk S. and Reaves R., 1982, "Influence of fluids on the abrasion of silicon by diamond", Wear, Vol. 77, pp. 81-87.

Deslattes R.D., 1969, "Optical and x-ray interferometry of a silicon lattice spacing", Appl. Phys. Letts., Vol. 15, No. 11, pp. 386-388.

Deslattes R.D., Henins A., Schoonover R.M., Carroll C.L. and Bowman H.A., 1976, "Avagadro constant- corrections to an earlier report", Phys. Rev. Letts., Vol. 36, No. 15, pp. 898-900.

Dragoset R.A., Young R.D., Layer H.P., Mielczarek S.R.,Teague E.C. and Celotta R.J., 1986, "Scanning tunneling microscopy applied to optical surfaces", Optics Letts., Vol. 11, No. 9, pp. 560-562.

Drake B., Sonnenfeld R., Schneir J., Hansma P.K., Slough G., Coleman R.V., 1986, "Tunnelling microscope for operation in air or fluids", Rev. Sci. Instrum., 57(3), pp. 441-445.

Durig U., Gimzewski J.K. and Pohl D.W., 1986, "Experimental observation of the forces acting during Scanning Tunnelling Microscopy", Phys. Rev. Letts., Vol. 57, No. 19, pp.2403-2406.

Dyer H.B., "Diamond grits -Their increasing specialisation", Science and Technology of Industrial Diamonds, Vol. 2, 1967, pp. 83-91, Grovesenor Press.

Dyson J., 1960, "Optical diffusing screens of high efficiency", J. Optical Soc. Am., 50(6), pp. 519-520.

Eastman F.S., 1937, "The design of flexure pivots", J. Aeronautical Sciences, Vol. 5, No. 1, pp. 16-20

Ellison A.E. and Zisman W.A., 1954, "Wettability of halogenated organic solid surfaces", J. Phys. Chem., Vol. 58, pp. 260-265.

Elrod S.A., de Lozanne A.L. and Quate C.F., 1984, "Low temperature vacuum tunneling microscopy", Appl. Phys. Letts., Vol. 45, No. 11, pp. 1240-1242

Ennos A.E. and Virdee M.S., 1983, "Precision measurement of surface form by laser auto-collimation", Proc. SPIE, 398, pp. 252-257.

Ernsberger F.M., 1968, "Role of densification in the deformation of glass under point loading", J. Am. Ceram. Soc., Vol. 51, No. 10, pp. 545-547.

Feuchtwang T.E., Cutler P.H. and Miskovsky N.M., 1983, "A theory of vacuum tunneling microscopy", Phys. Letts., Vol. 99A, No. 4, pp. 167-171.

Fischer J.C. and Giaever I., 1961, "Tunneling through thin insulating layers", J. Appl. Phys., Vol. 32, No. 2, pp. 172-177.

Fort T., 1962, "Adsorption and boundary friction on polymer surfaces", J. Phys. Chem., Vol. 66, pp. 1136-1143.

Fowler R.H. and Nordheim L., 1928, "Electron emission in intense electric fields", Proc. Roy. Soc., pp. 173-181.

Frank F.C. and Lawn B.R., 1967, "On the theory of Hertzian fracture", Proc. Roy. Soc., Vol. A299, pp. 291-306.

Franks A., "X-ray optics - a challenge to precision engineering". Department of Mechanical and Optical Metrology, National Physical Laboratory, Teddington, Middlesex. TW11

OLW.

Franks. A., 1977, "X-ray optics", Sci. Prog., Oxf., 64, pp. 371-422.

Gane N. and Cox J.M., 1970, "The micro-hardness of metals at very low loads", Phil. Mag., Vol. 22., pp. 881-891.

Gani S.M.A., Tanner B.K., McKenny T.G., Hingle H.T. and Bowen D.K., 1984, "An assessment of diamond turning for the production of silicon x-ray optical elements", J. Appl. Cryst., Vol. 17, pp. 111-117.

Garratt J.D., 1979, "Survey of displacement transducers below 50mm", J. Phys. E.: Sci. Instrum., Vol. 12, .pp 563-573.

Garcia N., Ocal C. and Flores F., 1983, "Model theory for scanning tunneling microscopy: Application to Au(110)(1 x 2) surfaces", Phys. Rev. Letts., Vol. 50, No. 25, pp. 2002-2005.

Garcia N., Baro A.M., Miranda R., Rohrer H., Gerber Ch., Cantu R.G. and Pena J.L., 1985, "Surface roughness standards, obtained with the scanning tunneling microscope operated at atmospheric air pressure", Metrologia, Vol. 23, No. 3, pp. 135-138.

Geary P.J., 1954, B.S.I.R.A. Research Report M18. - 1960, B.S.I.R.A. Research Report R249.

Gerber Ch., Binnig G., Fuchs H., Marti O. and Rohrer H., 1986, "Scanning tunneling microscope combined with a scanning electron microscope", Rev. Sci. Instrum., Vol. 57, No. 2, pp. 221-224.

Gibbons C.H., 1935 , "Materials Testing Machines", Instruments, Vol.8, No.3, pp. 76-78.

Greenwood J.A. and Williamson J.B.P., 1966, "Contact of nominally flat surfaces", Proc. Roy. Soc.(London), Vol. A295, pp. 300-319.

Griffith A.A., 1920, "VI. The phenomena of rupture and flow in solids", Proc. Roy. Soc., A221, pp. 163-198.

Gross W.A., 1962, "Gas Film Lubrication",John Wiley & Sons,Inc.

Guerrero J.L. and Black J.T., 1972, "Stylus tracer resolution and surface damage as determined by scanning electron microscopy", Trans. ASME B, Vol. 94, pp. 1087-1093.

Hadfield D., 1962, "Permanent Magnets", J. Wiley & Sons.

Hamilton G.M. and Goodman L.E, 1966, "The stress field created by a circular sliding contact", Trans. ASME, J. Appl. Mech., Vol. 33, pp. 371-375.

Hart M., 1968, "An angstrom ruler", Brit. J. Appl. Phys. (J. Phys. D), 1968, Ser. 2, Vol. 1, pp. 1405-1408.

Hill R.M. and Bruce C.M., 1961, "Limiting precision in a scanning optical interferometer", Aust. J. Phys., Vol. 14, pp. 194-222.

Holm R., 1951, "The electric tunnel effect across thin insulator films in contacts", J. Appl. Phys., Vol. 22, No. 5, pp. 569-574.

Hooke C.J. and O'Donoghue J.P., 1972, "Elastohydrodynamic lubrication of soft highly deformed contacts", J. Mech. Eng. Sci., Vol 14, No. 1, pp. 34-48.

Hornbogen E. and Karsch U.A., 1983, "Frictional wear of polytetrafluoroethylene", J. Mater. Sci. Letts., Vol. 2, pp. 777-780.

Huerta M. and Malkin S., 1976, "Grinding of glass: The mechanics of the process", J. Engg. Ind., pp. 459-473.

Ido S., Tsuyuzaki H., Takamoto K. and Omata F., 1981, " Accurate positioning stage driven by hydraulic cylinder ", Bull. Japan Soc. of Prec. Engg., Vol. 15, No. 2, pp. 123-127.

Johnson K.L., 1970, "The correlation of indentation experiments", J. Mech. Phys. Solids, Vol. 18, pp. 115-126.

Jones R.V., 1951, "Parallel and rectilinear spring movements", J. Sci. Instrum., Vol. 28, pp. 38-41.

Jones R.V., 1952, "An optical slit mechanism", J. Sci. Instrum., Vol. 29, pp. 345-350.

Jones R.V., 1956, "Some parasitic deflexions in parallel spring movements", J. Sci. Instrum., Vol. 33, pp. 11-15.

Jones R.V., 1962, "Some uses of elasticity in instrument design", J. Sci. Instrum., Vol. 39, pp. 193-203.

Jones R.V., 1967, "The measurement and control of small displacements", Physics Bulletin, Vol. 18, pp.325-336.

R.V. Jones, 1968, "More and more about less and less", Proc. R. Instn. Gt. Br., Vol. 43, No. 202, pp. 323-345.

Jones R.V. and Richards J.C.S., 1973, "The design and some applications of sensitive capacitance micrometers", J. Phys. E., Vol. 6, pp. 589-600.

Joos P., 1957, "Uber die mikroharte von glasoberflachen", Z. f. Angew. Physik., Vol. 9, No. 11, pp. 556-561.

Kelly A., 1973, "Strong Solids", Clarendon Press, Oxford.

Kimura M., Egami K., Kanamori M. and Hamaguchi T., 1983, "Epitaxial film transfer technique for producing single crystal silicon film on an insulating substrate", Appl. Phys. Lett., Vol. 43, No. 3, pp. 263-265.

Kuk Y. and Silverman P.J., 1986, "Role of tip structure in scanning tunneling microscopy", Appl. Phys. Letts., Vol. 48, No. 23, pp. 1597-1599.

Lancaster J.K., 1984, "The lubricated wear of polymers", 11^{th} Leeds-Lyons Symposium on "Mixed Lubrication and Lubricated Wear", Leeds 4^{th}–7^{th} Sept' 1984.

Lankford J. and Davidson D.L., 1979, "The crack-initiation threshold in ceramic materials subject to elastic/plastic indentation", J. Matls. Sci., Vol. 14, pp. 1662-1668.

Lawn B.R., 1967, "Partial cone crack formation in a brittle material loaded with a sliding spherical indenter", Proc. Roy. Soc., Vol. A299, pp. 307-316.

Lawn B.R. and Swain M.V., 1975, "Microfracture beneath point indentations in brittle solids", J. Matls. Sci., Vol. 10, pp. 113-122.

Lawn B.R. and Wilshaw R., 1975, "Review; Indentation fracture: principles and applications", J. Matls. Sci., Vol. 10, pp. 1049-1081.

Lawn B.R., Hockey B.J. and Wiederhorn S.M., 1980, "Atomically sharp cracks in brittle solids: an electron microscopy study", J. Matls. Sci., Vol. 15, pp. 1207-1223.

Lawn B.R., Marshall D.B. and Chantikul P., 1981, "Mechanics of strength-degrading contact flaws in silicon", J. Matl. Sci., Vol. 16, pp. 1769-1775.

Lindig O. and Pannhorst W., 1985, "Thermal expansion and length stability of Zerodur in dependence on temperature and time", Applied Optics, 24(20), pp. 3330-3334.

Lindsey K., 1986, "The assessment of ultra smooth substrates and overcoatings", Vacuum, 35(10-11), pp. 499-502.

Lindsey K., 1973, Proc. Conf. on X-ray Optics in Astronomy(ed by P.W.Sandford), p101. The University Of London: Mullard Space Science Laboratory.

Ling C.B., 1952, "On the stresses in a notched strip", Journal of Applied Mechanics, Trans. ASME, Vol. 74, pp. 141-146.

Lhymn C., 1986, "Microscopy study of the frictional wear of polytetrafluoroethylene", Wear, Vol. 107, pp. 95-105.

Mackinson K.R. and Tabor D., 1964, "The friction and wear of polytetrafluoroethylene", Proc. Roy. Soc.(Lond.), Vol. A281, pp. 49-61.

Mairlot H., 1969, "Parametres influencant le rendement du travail du verre a la meule diamantee", Verres et Refractaires, Vol. 23 (4/5), pp. 493-502.

McLaren K.G. and Tabor D., 1965, "The friction and deformation properties of irradiated polytetrafluoroethylene (PTFE)", Wear, Vol. 8, pp. 3-7.

Mamin H.J., Abraham D.W., Ganz E. and Clarke J., 1985, "Two dimensional, remote micropositioner for a scanning tunneling microscope", Rev. Sci. Instrum., Vol. 56, No. 11, pp. 2168-2170.

Marsh D.M., 1961, "Micro-tensile testing machine", J. Sci. Instrum., Vol. 38, pp. 229-234.

Marsh D.M., 1964, "Plastic flow in glass", Proc. Roy. Soc., A279, pp. 420-435.

Marshall D.B. and Lawn B.R., 1979, "Residual stress effects in sharp contact cracking: Part 1, Indentation fracture mechanics", J. Matls. Sci., Vol. 14, pp. 2001-2012.

Marshall D.B., Lawn B.R. and Chantikul P., 1979, "Residual stress effects in sharp contact cracking: Part 2, Strength degradation", J. Matls. Sci., Vol. 14, pp. 2225-2235.

Maxwell J.C., 1897, Kensington Museum Science Handbook, 1 (London: Chapman and Hall).

McCord M.A. and Pease R.F.W., 1987, "Scanning tunneling microscope as a mechanical tool", Appl. Phys. Letts., Vol. 50, No. 10, pp. 569-570.

McScimin H.J., 1953, "Measurement of elastic constants at low temperature by means of ultrasonic waves - data for silicon and germanium single crystals, and for fused silica", J. Appl. Phys., Vol. 24, No. 8, pp. 988-997.

Meek R.L. and Huffstutler M.C., 1969, "ID-diamond-sawing damage to germanium and silicon", J. Electrochem. Soc., Vol. 116, No. 6, pp. 893-898.

Miyashita M. and Yoshioka J., 1982, "Development of ultra-precision machine tools for micro-cutting of brittle materials", Bull. Japan. Soc. of Prec. Engg., Vol. 16, No. 1, pp. 43-50.

Montgomery D.B., 1963, "The generation of high magnetic fields", Rept. Prog. Phys., Vol. 26, pp. 69-104.

Montgomery D.B., 1969, "Solenoid Magnet Design", Wiley Interscience.

Moreland J. and Hansma P.K., 1984, "Electromagnetic squeezer for compressing squeezable electron tunneling junctions", Rev. Sci. Instrum., Vol. 55, No. 3, pp. 399-403.

Nakayama K., Tanaka M. and Morimura M., 1982, "Observation of x-ray interference signals from a two crystal x-ray interferometer", Bull. of NRLM, Vol. 31, No. 3, pp. 3-8.

Nogami M. and Tomozawa M., 1984, "Effect of stress on water diffusion in silica glass", J. Am. Ceram. Soc., Vol. 67, pp. 151-154.

O'Leary K. and Geil P.H., 1967, "Polytetrafluoroethylene fibril structure", J. Appl. Phys.,

Vol. 8, pp. 4169-4181.

Paros J.M. and Weisbord L., 1965, "Flexure hinges", Machine Design, Nov. 25, pp. 151-156.

Pascoe M.W. and Tabor D., 1956, "The friction and deformation of polymers", Proc. Roy. Soc.(Lond.), Vol. A235, pp. 210-224.

Pashley M.D., Pethica J.B. and Coombs J., 1985, "Scanning tunnelling microscope studies", Surface Science, Vol. 152/153, pp. 27-32.

Perrott C.M., 1977, "Elastic-plastic indentation: Hardness and fracture", Wear, Vol. 45, pp. 293-309.

Petersen K.E., 1982, "Silicon as a mechanical material", Proc. IEEE, Vol. 70, No. 5, pp. 420-456.

Peterson R.E., 1974, "Stress Concentration Factors", J. Wiley & Sons.

Pethica J.B., Hutchings R. and Oliver W.C., 1983, "Hardness measurement at penetration depths as small as 20nm", Phil. Mag., Vol. 48, No. 4, pp. 593-606.

Pethica J.B., 1986, "Comment on "Interatomic forces in Scanning Tunnelling Microscopy: Giant corrugations of the graphite surface", Phys. Rev. Letts., Vol. 57 No. 25, pp. 3235.

Plainevaux J.E., 1956, "Mouvement de tangage d'une suspension elementaire sur lames elastiques", Nuovo Cimento, Vol. 4, No. 5, pp. 1133-1141.

Plainevaux J.E., 1956, "Etude de deformations d'une lame de suspension elastique", Nuovo Cimento, Vol. 4, No. 5, pp. 922-928.

Pohl D.W., 1987, "Dynamic piezo electric translation devices", Rev. Sci. Instrum., Vol. 58, No. 1, pp. 54-57.

Pooley C.M. and Tabor D., 1972, "Friction and molecular structure: the behaviour of some thermoplastics", Proc. Roy. Soc.(Lond), Vol A329, pp. 251-274.

Preston F.W., 1921-22, "The structure of abraded glass surfaces", Trans. Optical Soc., Vol. 23, No. 3, pp. 141-164.

Puttick K.E., Shahid M.A. and Hosseini M.M., 1979, "Size effects in abrasion of brittle materials", J. Phys. D: Appl. Phys., Vol. 12, pp. 195-202.

Puttick K.E. and Shahid M. A., 1977, "Abrasion of silicon by diamond", Ind. Diamond Rev., pp. 223-237.

Radhakrishnan V., 1970, "Effect of stylus radius on the roughness values measured with tracing stylus instruments", Wear, Vol. 16, pp. 325-335.

Reeds J., Hansen S. and Otto O., 1985, " High speed precision x-y stage", J. Vac. Sci. Technol., B3(1), pp. 112-116.

Roesler F.C., 1956, "Brittle fractures near equilibrium", Proc. Phys. Soc., B69, pp. 981-992.

Rubenstein C., 1961, "Lubrication of polymers", J. Appl. Phys., Vol. 32, No. 8, pp. 1445-1450.

Sayles R.S. and Thomas T.R., 1976, "Mapping a small area of a surface", J. Phys. E, Vol. 9, pp. 855-861.

Scire F.E. and Teague E.C., 1978, "Piezodriven 50-μm range stage with subnanometer resolution", Rev. Sci. Instrum., Vol. 49, No. 12, pp. 1735-1740.

Schwartz B. and Robbins H., 1976, "Chemical etching of silicon: IV. Etching technology", J. Electrochem. Soc., Vol. 123, No. 12, pp. 1903-1909.

Shimbo M., Furukawa K., Fukuda K. and Tanzawa K., 1986, "Silicon-to-silicon direct bonding method", J. Appl. Phys., Vol. 60, No. 8, pp. 2987-2989.

Simmons J.G., 1963, "Generalised formula for the electric tunnel effect between similar electrodes separated by a thin insulating film", J. Appl. Phys., Vol. 34, No. 6, pp. 1793-1803.

Seal M., "The abrasion of diamond", Proc. Roy. Soc., Vol. A248, pp. 379-393.

Seal M., "The wear of diamond", Science and Technology of Industrial Diamonds, Vol. 1, 1967, pp. 145-159, Grovesenor Press.

Senior J.M. and West G.H., 1971, "Interaction between lubricants and plastic bearing surfaces", Wear, Vol. 18, pp. 311-323.

Siddons D.P., 1978, Ph.D. Thesis, Univ. of London.

Slough C.G., McNairy W.W., Coleman R.V., Drake B. and Hansma P.K., 1986, "Charge density waves studied with the use of a scanning tunneling microscope", Phys. Rev. B, Vol. 34, No. 2, pp. 994-1005.

Smith D.P.E. and Elrod S.A., 1985, "Magnetically driven micropositioners", Rev. Sci. Instrum., Vol. 56, No. 10, pp. 1970-1971.

Smith D.P.E. and Binnig G., 1986, "Ultrasmall scanning tunneling microscope for use in liquid helium storage Dewar", Rev. Sci. Instrum., Vol. 57, No. 10, pp.2630-2631.

Smith S.T., Chetwynd D.G. and Bowen D.K., 1987, "Design and assessment of monolithic high precision translation mechanisms", J. Phys. E, In press.

Smythe, 1950, Static and Dynamic Electricity, McGraw-Hill, New York. Chap IV.

Sonnenfeld R., Moreland J., Hansma P.K., Adams A. and Kvaas R., 1985, " Contacless tunneling to semiconductors", J. Appl. Phys., Vol. 58, No. 11, pp. 392-395.

Sonnenfeld R., Schneir J., Drake B.,Hansma P.K. and Aspnes D.E., 1987, "Semiconductor topography in aqueous environments: Tunneling microscopy of chemomechanically polished (001) GaAs", Appl. Phys. Letts., Vol. 50, No. 24, pp. 1742-1744.

Spreadbury G., 1949, "Permanent Magnets", Pitman.

Stanley V.W., Franks A. and Lindsey K., 1968, " A simple ruling engine for x-ray gratings", J. Phys. E, Vol. 1, Ser. 2, pp. 643-645.

Stedman M., 1987, "Basis for comparing the performance of surface measuring machines", Precision engineering.

Steijn R.P., 1968, "The sliding surface of polytetrafluoroethylene; An investigation with the electron microscope", Wear, Vol. 12, pp. 193-212.

Sydenham P.H., 1981, "Mechanical design of instruments: Putting elasticity to use (parts A & B)", Meas. and Cont., Vol. 14,

Sydenham P.H., 1984, "Elastic design of fine mechanism in instruments", J. Phys. E: Sci. Instrum., Vol. 17, .pp 922-930.

Tabor D., 1957/58, "Friction,lubrication and wear of synthetic fibres", Wear, Vol. 1, pp. 5-24.

Tabor D., 1969, "The direct measurement of normal and retarded van der Waals forces", Proc. Roy. Soc., Vol. A312, pp. 435-450.

Tanaka K., 1984, "Kinetic friction and dynamic elastic contact behaviour of polymers", Wear, Vol. 100, pp. 243-262.

Tanaka K., Uchiyama Y. and Toyooka S., 1973, "The mechanism of wear of polytetrafluoroethylene", Wear, Vol. 23, pp. 153-172.

Tanaka M., 1983, "The dynamic properties of a monolithic mechanism with notch flexure hinges for precision control of orientation and position", Japan. J. Appl. Phys., 22, pp. 193-200.

Taylor E.W., 1949, "Plastic deformation of optical glass", Nature, Vol. 163, p323.

Tersoff J. and Hamann D.R., 1985, Theory of the scanning tunneling microscope", Phys. Rev. B, Vol. 31, No. 2, pp. 805-813.

Thomas T.R., 1975, "Recent advances in the measurement and analysis of surface micro-geometry", Wear, Vol. 33, pp. 205-233.

Thompson W.A. and Hanrahan S.F., 1976, "Thermal drive apparatus for direct vacuum tunnelling experiments", Rev. Sci. Instrum., Vol. 47, No. 10, pp. 1303-1304.

Van der Walle G.F.A., Gerritsen J.W., van Kempen H. and Wyder P., 1985, "High stability scanning tunneling microscope", Rev. Sci. Instrum., Vol. 56, No. 8, pp. 1573-1576.

Van de Walle G.F.A., van Kempen H., Wyder P. and Davidsson P., 1987, "Scanning tunneling microscopy on photoconductive semi-insulating GaAs", Appl. Phys Letts., Vol. 50, No.

1, pp. 22-24.

Von Karman T. and Duwez P, 1950, "The propogation of plastic deformation in solids", J. Appl. Phys., Vol. 21, pp. 987-994.

Westbrook J.H. and Gilmen J.J., 1962, "An electromechanical effect in semiconductors", J. Appl. Phys., Vol. 33, No. 7, pp. 2360-2369.

Whitehouse D.J., 1974, "Stylus techniques", from "Characterization of Solid Surfaces", ed. Kane P.F. and Larrabee G.B., Plenum Press.

Whitehouse D.J., 1985, "Assessment of surface finish profiles produced by multi-process manufacture", Proc. Instn. Mech. Engrs., Vol. 199, No. B4, pp. 263-270.

Willis R.F., Payne M.C., Pethica J.B., Pashley M.D. and Coombs J.H., 1985, "Vacuum tunnelling microscopy- a status report", Festkorperprobleme (Advances in Solid State Physics), Vol. XXV, pp. 699-709.

Young R.D., 1966, "Field emission ultramicrometer", Rev. Sci. Instrum., Vol. 37 No. 3, pp. 275-278.

Young R., Ward J. and Scire F., 1972, "The Topographiner: An instrument for measuring surface microtopography", Rev. Sci. Instrum., Vol. 43, No. 7, pp. 999-1011.

Appendix A: The Etching Of "Zerodur" With $HF/HCl/H_2O$ Concentrates

1. Introduction

As modern technologies have developed, there has arisen the awareness of a need for miniaturisation in the production of many components and devices. This will invariably require the development of measurement systems of ever increasing resolution, accuracy and thus stability. One material that promises to suit this requirement is the ultra low expansivity glass ceramic "Zerodur", Otto & Lindig, 1985. This can have a room temperature linear expansion coefficient of $5\times10^{-8}/K$.

The mechanical applications for this hard, brittle material are mainly limited by insufficient machine tools and the prohibitively high labour costs that are incurred in the process of forming complex shapes. Glass workshops are traditionally concerned with the generation of flat or curved geometries of excellent form and finish but restricted to optical applications. Engineering workshops, on the other hand, are restricted to machining relatively soft and ductile materials.

Presently, glass components are "roughed" out using a grinding or lapping system. These surfaces contain a high density of cracks and locked-in stress concentrations. This can induce additional instabilities caused by relaxation and/or the hydrophillic nature of the surface as well as reducing the components load resisting capabilities.

In an effort to reduce the labour costs of these components, it is proposed that dimensionally non-critical surfaces may be roughed out and subsequent surface and sub-surface damage removed by a HF or $HF/HCl/H_2O$ etchant. This report will outline the physical etching characteristics of "Zerodur" with the aforementioned etchant.

2. Experimental Method

Specimens were produced using the various processes available in the average glass workshop. These were; slotting, grinding, drilling and polishing. These were then examined by optical microscope using polarised light to assess surface texture and sub-surface damage.

The specimens were then immersed in two different etchant concentrations and agitated for a specified period of time. After etching, the specimens were weighed to determine the etch rate and reexamined under the microscope.

3. Results

The surface texture of both polished and ground specimens have been measured using a "Talysurf" stylus system, figure A1. The surface of ground Zerodur has an rms roughness of 4μm whilst that of the polished specimen was undetectable in the sub-micron region with the rather old equipment that was used. The surface texture of the ground surface is clearly very irregular with frequency components probably well above the filter characteristic of a stylus tip. Plate A1 shows the edge of a ground specimen after a few days in a normal laboratory atmosphere. Water retension is clearly visible and can be seen with the naked eye as less opaque regions on the surface.

Sub-surface damage, assessed using a polarimeter, is prominent in holes and slots. Plate A2(a & b) shows the stress pattern along the side of a hole and around a crack at the root. The stain at the root was measured as 22$\mu\eta$. This would cause a significant reduction in the stamina (often referred to as fatigue life) of a component having undergone this process. Internal stresses were not observed within polished surfaces.

After etching in a dilute solution of HF(40%)/HCl(36%) etchant, the stresses in the region of the same hole were reassessed. Plate A3(a & b) are views of the same regions as shown in plate A2 after etching. It can be seen that the crack has etched into a vee groove and the tip has become considerably blunted. Internal stresses have also reduced to a levels below measurement resolution. The edge of the hole (Plate A3(b)) shows characteristic concave spherical regions that give the surface an orange peel appearance.

Plate A4(a & b) shows two views of the surface of the etched Zerodur. One of the surfaces is clean A4(a) whilst the other A4(b) has a crazed appearance. This coating is probably the result of impurities present in the water that was used to dilute the etchant.

The average surface grain size is approximately $4\mu m$. It has been found in similar experiments that grain size will increase in an exponentially decaying manner with time, Dyson, 1960. It can be seen in the Talysurf traces (figure A2) that macro ripple is of the order $50\mu m$ (initially polished region) to $60\mu m$ (initially ground region). Micro ripple is undetectable with the measurement system that was used.

The linear etch rates are listed in Table A1. These were linear over the time period considered and depend on the initial surface crack density and internal stress levels. The effects of temperature were not investigated in these experiments but was monitored at a constant 296k.

Finally, similar specimens have been etched in a bath of undiluted HF/HCl etchant. After a period of 6mins the surface is as shown in Plate A5. The average grain size for this etchant is $\approx 3\mu m$. The surface also appears clean and free from contamination, thus enhancing the opinion that impurities in the dilution medium can leave undesirable deposits that are difficult to remove. The Talysurf plots of figure A3(a & b) indicate a macro ripple of between 10 and $20\mu m$ with a micro ripple that is again undetectable.

4. Conclusions

The objective of etching Zerodur is to remove the hydrophyllic surface and relieve internal stresses. The above results indicate that this is so. The resultant surface finish is opaque and looks similar to that of a dry, ground surface. It is considered that for a good optical transmission, polishing is the only viable route. However, in some cases (such as holes slots etc..) polishing may be prohibitively expensive and etching will be the most economical method of improving the life expectancy of components.

Table A1

Etching Time (mins)	Initial Surface Texture	Removal Rate (μm/min)	Etchant Recipe	
			Parts	Etchant
6	Polished	8.42	2	HF
	Ground	18.70	1	HCl
25	Polished	2.10	2 1	HF HCl
	Ground	4.76	3	H_2O

Plate A1

Ground Zerodur

10µm

Plate A2

Stress pattern in the region of a hole

a)Side of hole

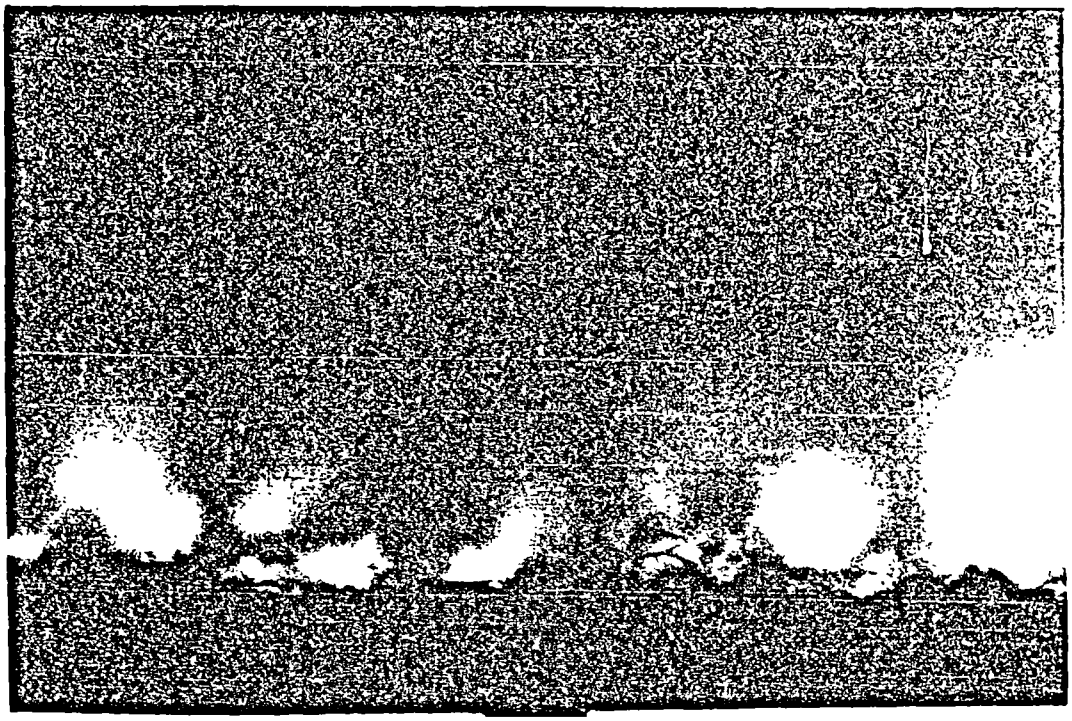

b)Root of hole

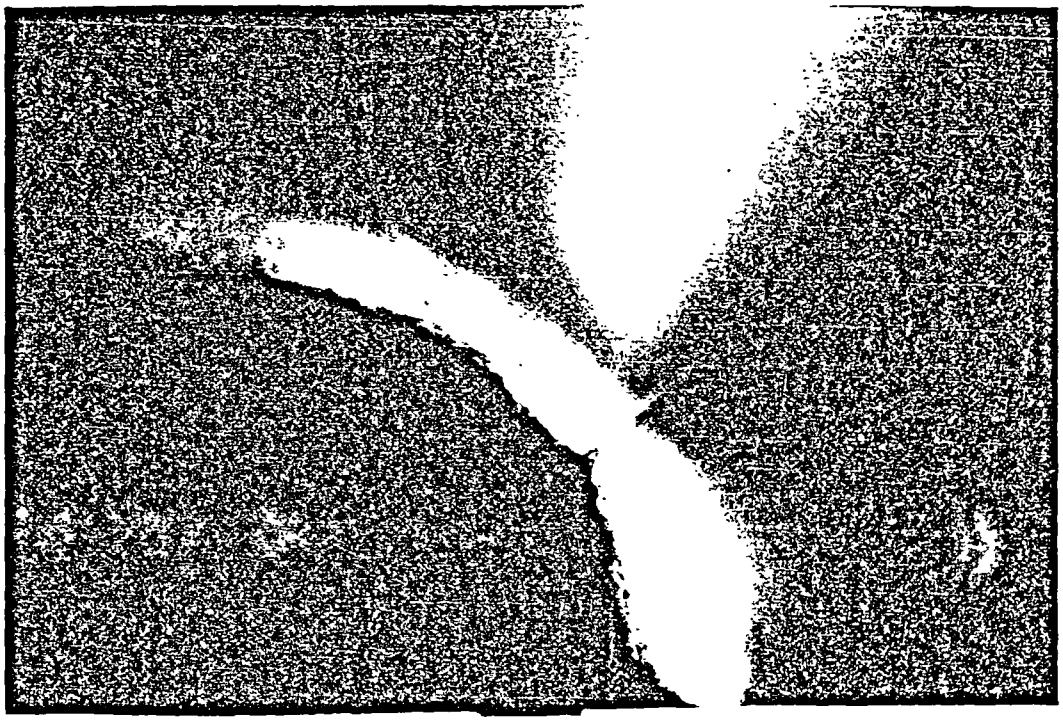

10 µm

Plate A3

Stress pattern in the region of an etched hole

a)Side of hole

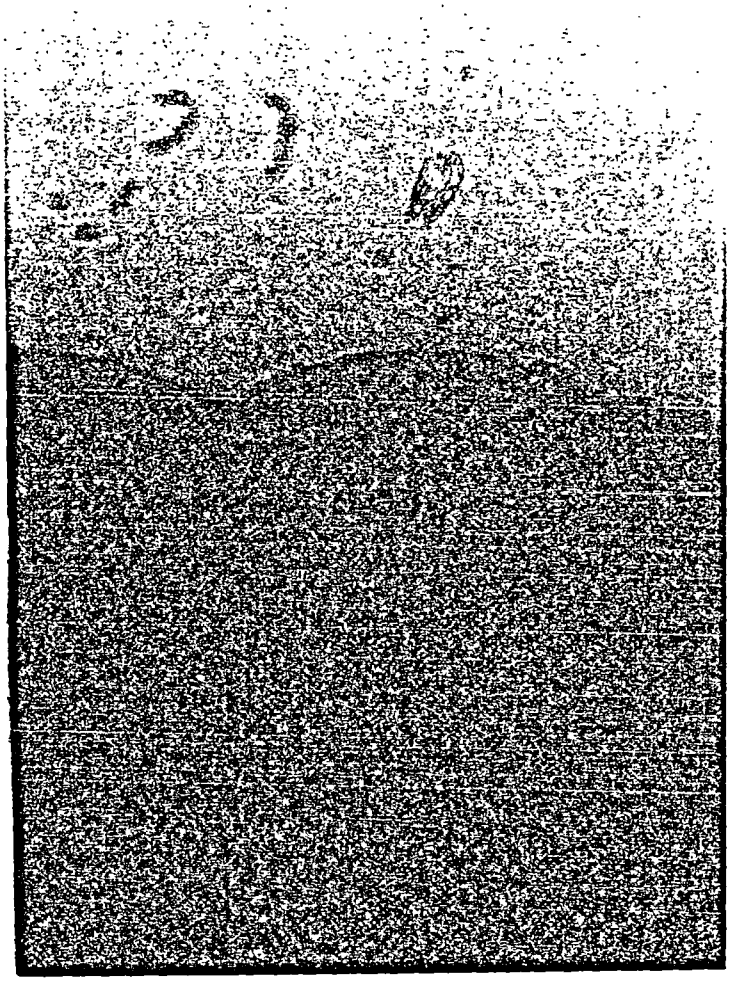

10μm

b) Root of hole

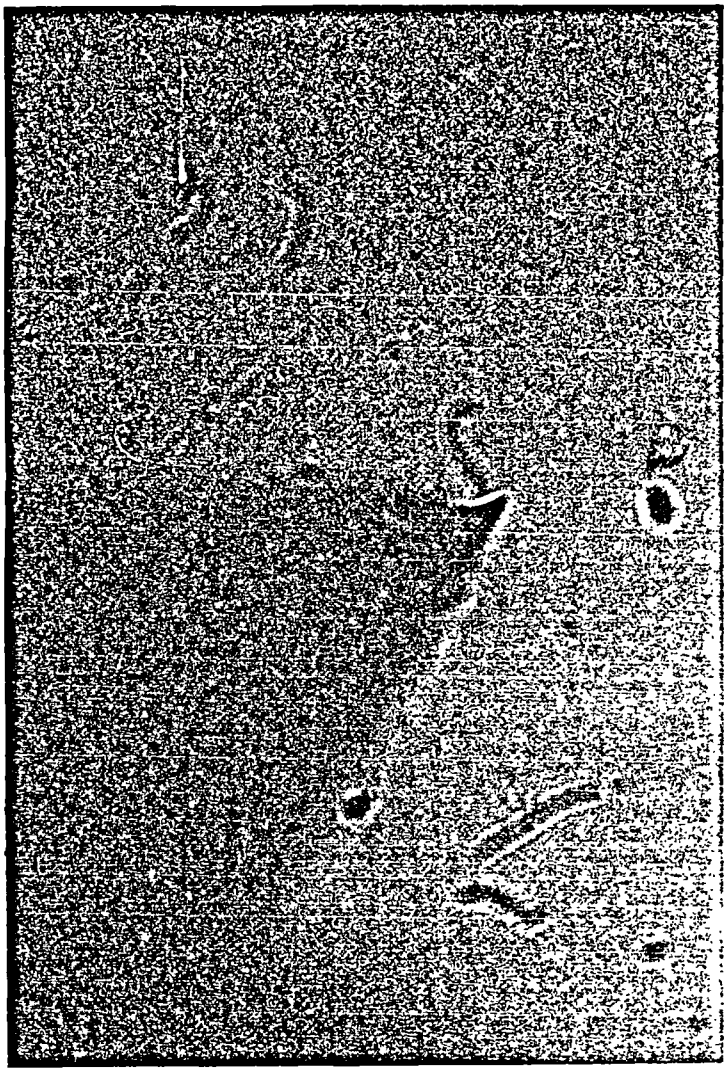

20μm

Plate A4

Surface of etched Zerodur in dilute HF/HCl etchant

a) Clean

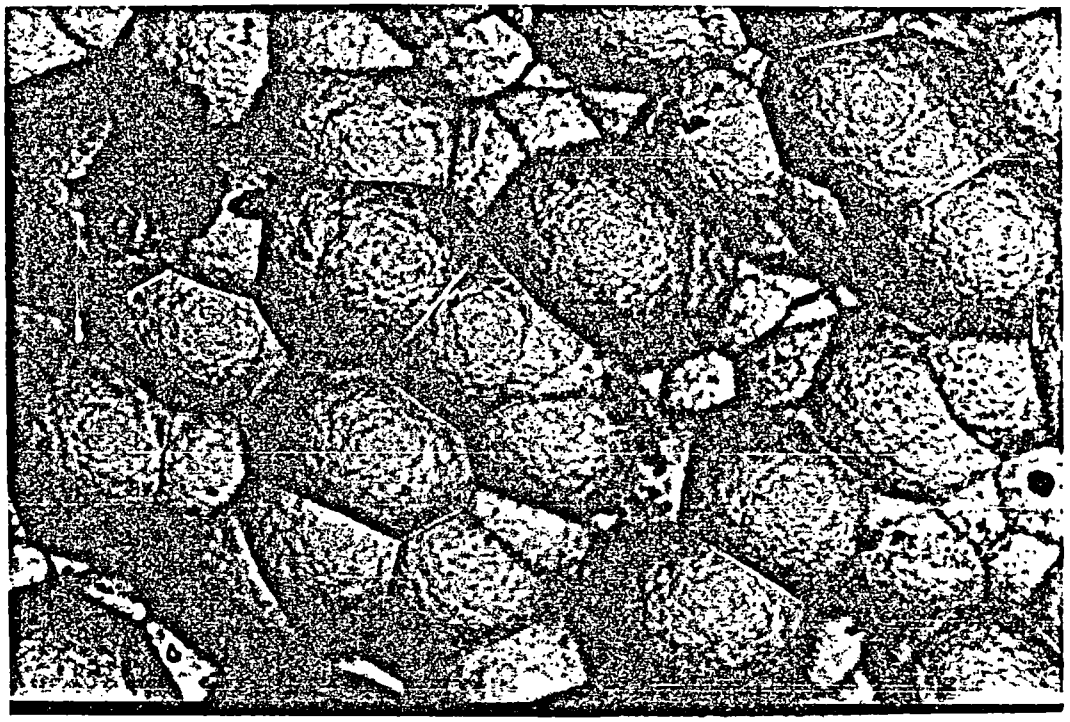

b) Contaminated

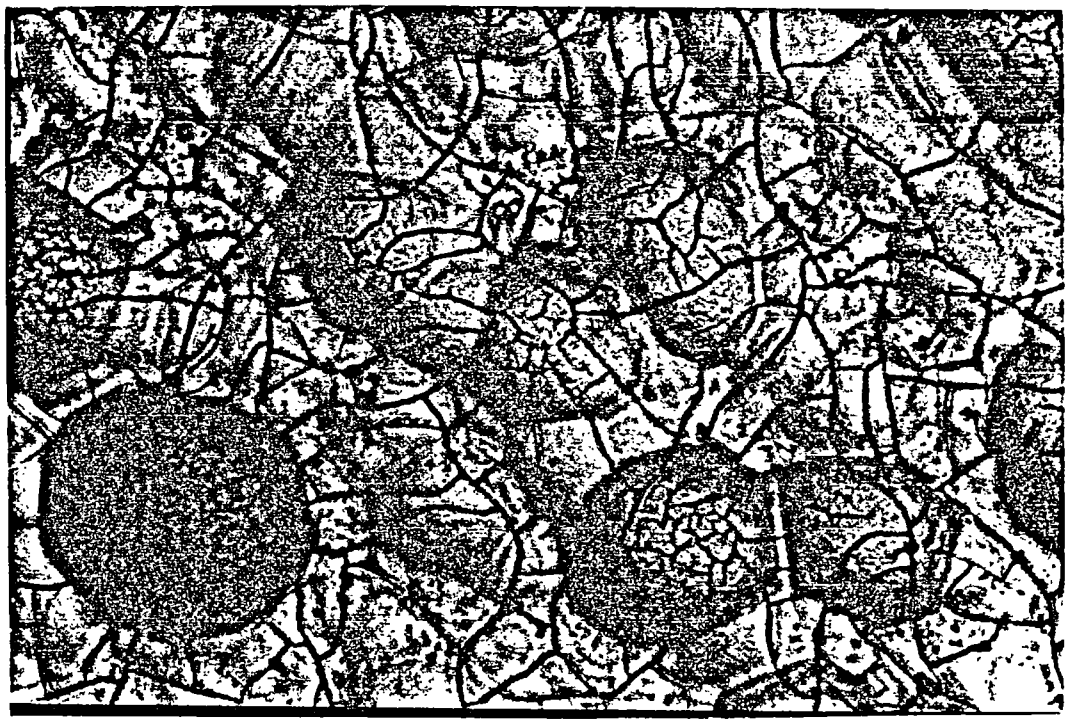

10 µm

Plate A5

Surface of Zerodur etched in HF/HCl solution

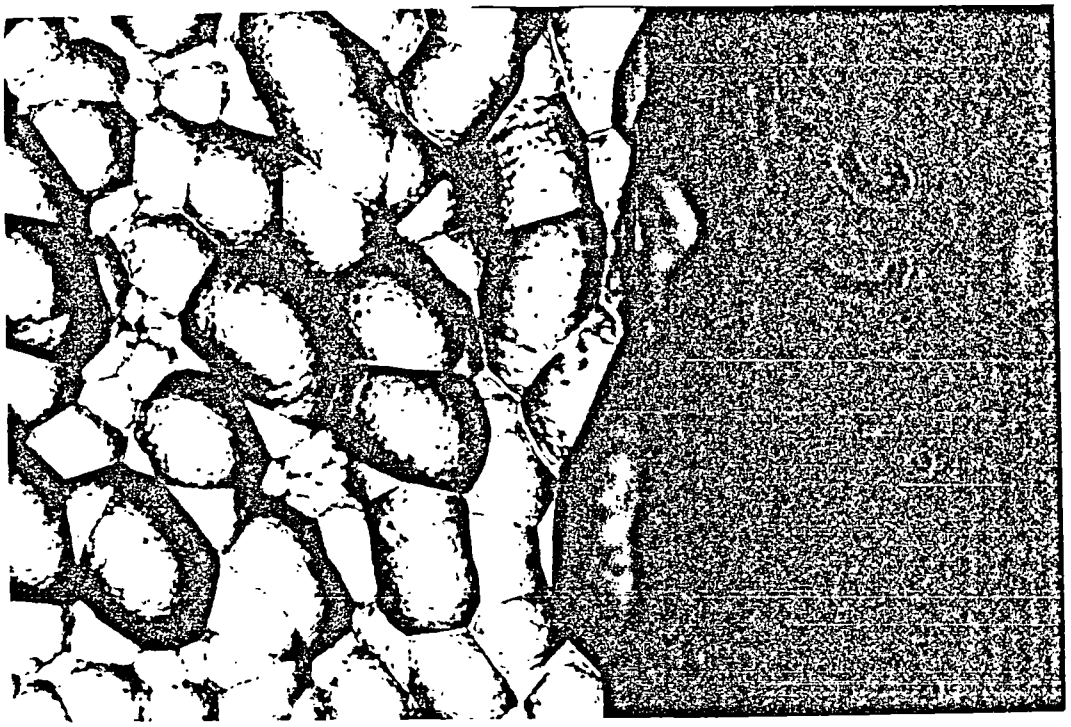

10µm

Figure A1:Talysurf traces of glass surfaces prior to etching

a)Polished

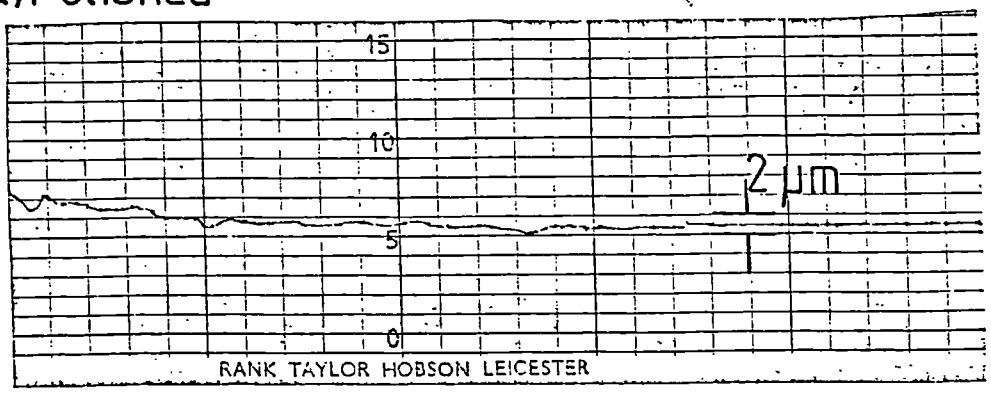

b)Ground

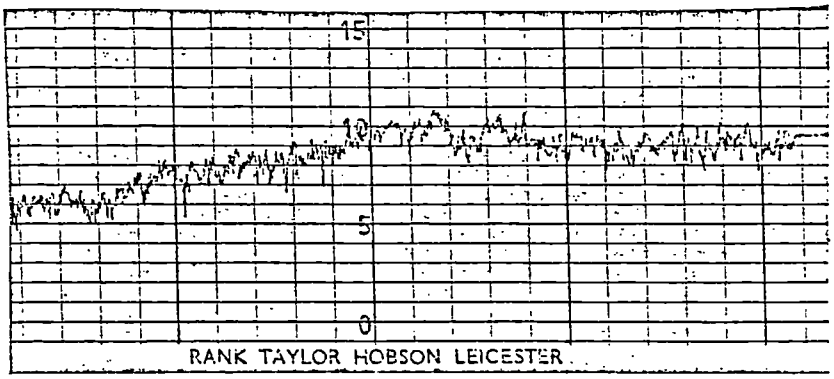

c)Instrument noise

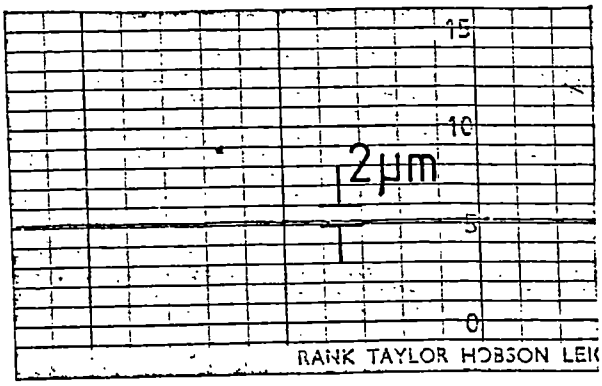

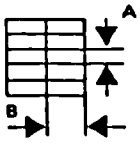

VERT. MAG. A = 5000

HORIZ. MAG. B = 100

Figure A2: Talysurf traces of glass after etching in dilute HF/HCL solution

a) Polished

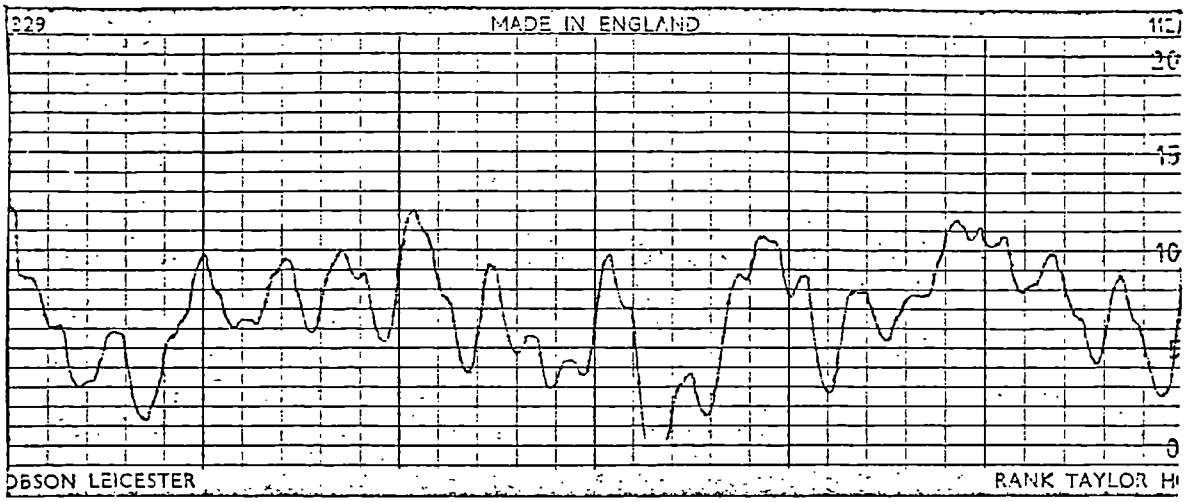

b) Ground

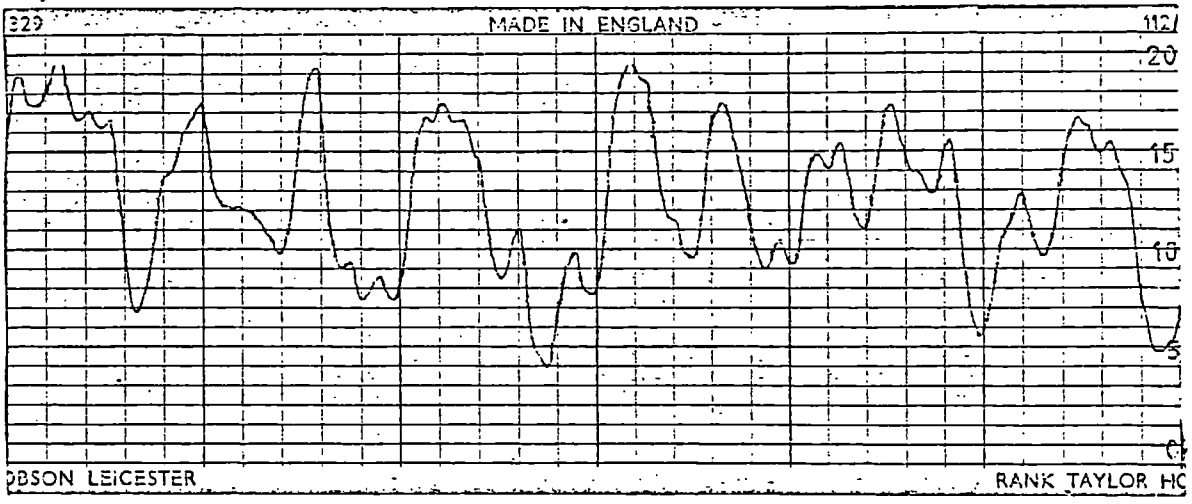

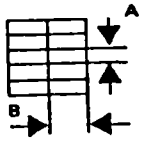

VERT. MAG. A = 2000

HORIZ. MAG. B = 20

Figure A3: Talysurf traces of glass after etching in undiluted HF/HCL solution

a) Polished

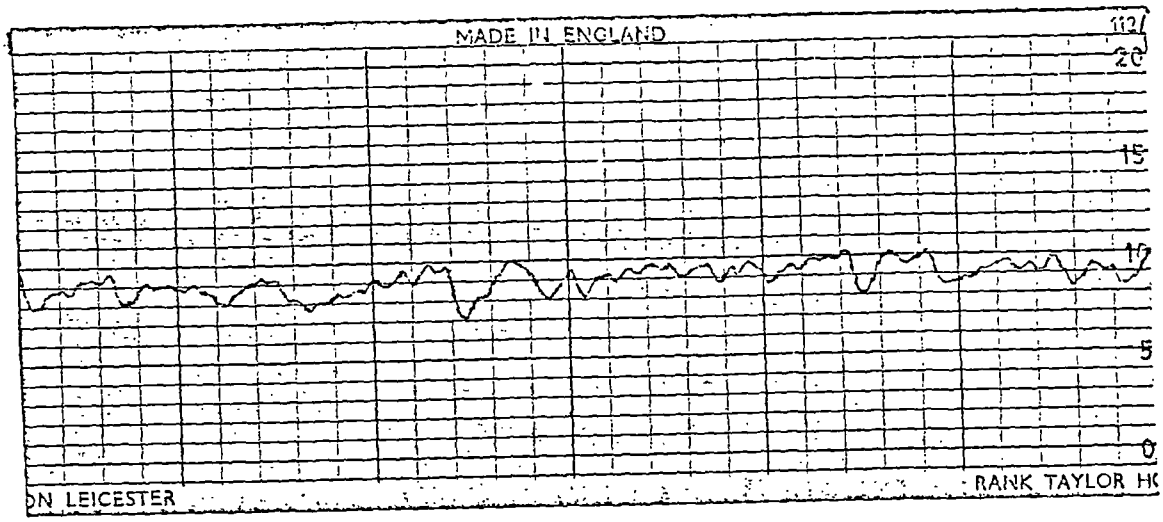

b) Ground

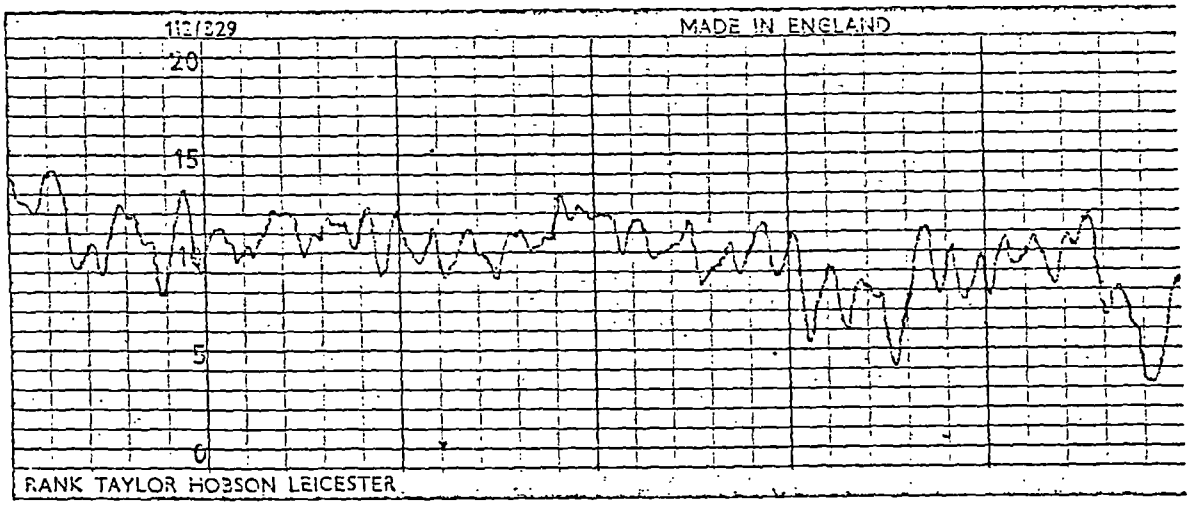

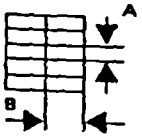

VERT. MAG. A = 2000

HORIZ. MAG. B = 20

Appendix B: Computer algorithm to calculate the design parameters for an electromagnetically driven simple linear spring system

```
      PROGRAM CRUNCH
```


```
      PROGRAM CRUNCH
```


```
C       This is a general program to compute the design
C     parameters for an electromagnetically driven
C     linear spring mechanism. The linear spring can be
C     either the common leaf spring or the notch type
C     spring.
C
C
C
C       A notch type spring can be selected by
C     assigning a value of 1 to the parameter
C     labelled NOTCH.
C
C
C       The parameters required by this program for
C     calculation are modulus of elasticity of the
C     spring (E), thickness of spring (TH), depth of
C     spring (DEPTH), length of leaf springs or pitch
C     of notches (LGTH), mass supported by springs(MASS)
C     , critical damping factor (C), ratio of radius of
C     notch to thickness of webb (ROVERT), current
C     through coil (AMPS), number of coil turns
C     (TURNS), resistivity of windings matl' (RHO),
C     inside radius of coil (A1), ratio of outside radius
C     to inside radius (>1!)(ALPHA), ratio of coil
C     half length to inside radius (BETA) and the
C     moment of the magnet to be used (VMOM). The
C     value of VMOM for small soleniod fields is
C     given by the product of remanence and volume
C     of the permanent magnet.
C
C
C
C      Input character names and assign them to the array V
C
C
C
      REAL LAMBDA,LGTH,MASS,K,L,NOTCH,LAMB1,LAMB2
      DIMENSION H(0:170),HDOT(170),FNORM(0:170),X(170),V(64)
      CHARACTER*6 NAME(24)
      EQUIVALENCE(NOTCH,V(1))
      EQUIVALENCE(ROVERT,V(2))
      EQUIVALENCE(RESIST,V(3))
      EQUIVALENCE(E,V(4))
      EQUIVALENCE(C,V(5))
      EQUIVALENCE(MASS,V(6))
      EQUIVALENCE(TH,V(7))
      EQUIVALENCE(DEPTH,V(8))
      EQUIVALENCE(LGTH,V(9))
      EQUIVALENCE(K,V(10))
      EQUIVALENCE(AMPS,V(11))
      EQUIVALENCE(L,V(12))
      EQUIVALENCE(OMEGA,V(13))
      EQUIVALENCE(STRESS,V(14))
      EQUIVALENCE(DISP,V(15))
      EQUIVALENCE(FREQ,V(16))
      EQUIVALENCE(LAMBDA,V(17))
      EQUIVALENCE(TURNS,V(18))
      EQUIVALENCE(A1,V(19))
      EQUIVALENCE(ALPHA,V(20))
```

```
      PROGRAM CRUNCH



      EQUIVALENCE(BETA,V(21))
      EQUIVALENCE(RHO,V(22))
      EQUIVALENCE(POWER,V(23))
      EQUIVALENCE(VMOM,V(24))
C
C
C
C     Give values corresponding to array V
C
C
C
      DATA (V(I),I=1,2)/0.0,6.0/
      DATA(V(I),I=3,8)/4.0,1.9E11,0.03,0.04,0.002,0.01/
      DATA(V(I),I=16,24)/0.0,0.0,2000,0.006,2.0,1.0,17E-9,0.0,4.23E-7/
      DATA(V(I),I=9,15)/0.04,1.28,0.2,0.0005,0.0,0.0,0.0/
      DATA (NAME(I),I=1,2)/'NOTCH','ROVERT'/
      DATA (NAME(I),I=3,8)/'RESIST','E','C','MASS','TH','DEPTH'/
      DATA (NAME(I),I=9,14)/'LGTH','K','AMPS','L','OMEGA'
     C,'STRESS'/
       DATA (NAME(I),I=15,24)/'DISP','FREQ','LAMBDA','TURNS','A1',
     C'ALPHA','BETA','RHO','POWER','VMOM'/
C
C
      OPEN(6,FILE='NUMOUT',STATUS='MODIFY')
100   DO 10 N=1,8
       WRITE(1,5)N,NAME(N),V(N),N+8,NAME(N+8),V(N+8),N+16,
     CNAME(N+16),V(N+16)
10     CONTINUE
C
C
C
C      Section of program to enable user to change
C      values, work out design parameters or stop
C      the program.
C
C
C
      WRITE(1,*)
      WRITE(1,*)'TO CHANGE A VALUE TYPE NUMBER'
      WRITE(1,*)'USE ALL SI UNITS'
      WRITE(1,*)'TO RUN PROGRAM TYPE 99'
      WRITE(1,*)'TO STOP PROGRAM TYPE 101'
      WRITE(1,*)'TO LIST VALUES TYPE 777'
      WRITE(1,*)'TO CHANGE ALL VALUES TYPE NO OF VALUES*100'
      WRITE(1,*)
      READ(1,*)I
      IF (I.EQ.99) GO TO 250
      IF (I.EQ.777) GO TO 100
      IF (I.EQ.101) GO TO 300
      IF (I.GT.24)GO TO 400
      WRITE(1,*)
      WRITE(1,*)'PRESENT VALUE OF ',NAME(I), V(I)
      WRITE(1,*)'INPUT NEW VALUE'
      READ(1,*) V(I)
      GO TO 100
400   DO 20 N=1,I/100
       WRITE(1,*)'INPUT VALUE OF ',NAME(N)
       READ(1,*) V(N)
20     CONTINUE
      GO TO 100
```

```
      PROGRAM CRUNCH



C
C
C
C      Program to calculate the system characteristics.
C
C
C
250   CONTINUE
C
      ROOTRT=SQRT(ROVERT)
      WRITE(*,*)' OK'
      LAMB1=(E*(1.0-NOTCH)*TH**3*DEPTH)/(LGTH**3)
      LAMB2=NOTCH*E*DEPTH*TH**2*0.283/(LGTH**2*ROOTRT)
      LAMBDA=LAMB1+LAMB2
      OMEGA=SQRT(LAMBDA/MASS)
       RES=(3.14159*RHO*(ALPHA+1.0))/(A1*0.77*(ALPHA-1.0)*2*BETA)
       L=1.0E-6*TURNS**2*A1
       RESIST=RES*TURNS**2
      POWER=AMPS*AMPS*RESIST
      FREQ=OMEGA/(2*3.1429)
C
C
C
C     This section will compute the force/distance
C     characteristic for a magnet situated along the
C     axis of a uniform current density soleniod coil
C
C
C
       A=F(ALPHA,BETA)
       AL=ALPHA
      A2=ALPHA*A1
      B =BETA*A1
       BE=BETA
       H(0)=(TURNS*AMPS*F(AL,BE))/(A1*2*BE*(AL-1.0))
      WRITE(*,*)H(0)
       FNORM(0)=0.0
       DO 17 J=1,170
       T=J
       P=(A1*T)/57
       D=BE+P/A1
       IF(P/A1.GT.BE)THEN
       EC=P/A1-BE
       S=-1.0
       ELSE
       EC=BE-P/A1
       S=1.0
       END IF
       H(J)=H(0)*((F(AL,D)+S*F(AL,EC))/(2.0*F(AL,BE)))
       HDOT(J)=57*(H(J-1)-H(J))/A1
      WRITE (*,*)HDOT(J)
       FNORM(J)=VMOM*HDOT(J)
       X(J)=(T-1.0)/57
      IF(FNORM(J).LT.FNORM(J-1))GOTO 18
   17  CONTINUE
   18 CONTINUE
C
C
C
C       K is the maximum force current constant for
```

```
      PROGRAM CRUNCH


C       this magnet/coil system.
C
C
C
      K=FNORM(J-1)/AMPS
      STRESS=K*AMPS*3.0*E*TH/(LGTH**2*LAMBDA)
      DISP=K*AMPS/LAMBDA
      GOTO 100
300   CONTINUE
      DO 30 N=1,8
       WRITE(6,5)N,NAME(N),V(N),N+8,NAME(N+8),V(N+8),N+16,
     CNAME(N+16),V(N+16)
30    CONTINUE
5     FORMAT(1X,I2,A7,E11.3,8X,I2,A7,E11.3,8X,I2,A7,E11.3)
       WRITE(6,15)A1,A2,B,TURNS,AMPS,VMOM
   15 FORMAT(1X, ' THE INSIDE AND OUTSIDE RADII OF COIL ARE',2X,2F10.4
     1,/,' THE HALF LENGTH OF THE COIL IS',F10.4,/,' THE TOTAL NUMBER
     1OF TURNS ARE',2X,F7.0,/,' THE CURRENT THROUGH THE COIL IS',2X,
     1F10.4,/,' THE FORCE CONSTANT IS',2X,E10.3)
      CLOSE(6)
       STOP
       END
C
C
C
C       This function computes the fabry factor for
C       this geometry of coil.
C
C
C
       FUNCTION F(FAL,FBE)
       R=SQRT(FAL*FAL+FBE*FBE)
       T=1.0+SQRT(1.0+FBE*FBE)
       F=FBE*ALOG((FAL+R)/T)
       RETURN
       END
```